FLUX-COUPLING LOW-POLE FLUX-SWITCHING PERMANENT MAGNET MACHINES

by

Yingjie Li

A dissertation submitted in partial fulfillment of

the requirements for the degree of

Doctor of Philosophy

(Electrical Engineering)

at the

UNIVERSITY OF WISCONSIN – MADISON

2017

Date of final oral examination: 04/27/2017

The dissertation is approved by the following members of the Final Oral Committee:

Sarlioglu, Bulent, Assistant Professor, Electrical Engineering

Jahns, Thomas, Professor, Electrical Engineering

Lorenz, Robert, Professor, Mechanical Engineering

Venkataramanan, V., Professor, Electrical Engineering

Blasko, Vladimir, IEEE Fellow, Electrical Engineering

Abstract

The purpose of this research is to investigate a novel family of flux-switching permanent magnet (FSPM) machines that have a low number of rotor poles. The low-pole topology is favorable for the medium to high-speed operation to minimize fundamental frequency requirement and associated losses. The conventional six stator slots and four rotor poles (6/4) FSPM machine has inherent large harmonic distortion in the flux linkage and severe cogging torque. The proposed flux-coupling dual-stator structure eliminates the even order harmonics in the flux linkage. Harmonic distortion and cogging torque are notably reduced in the proposed machine. The principle of operation, design methodologies, sizing equations, and multiple alternative topologies are investigated for the proposed dual-stator 6/4 FSPM machine. The performance of proposed machine is compared to 12/10 FSPM machine to show benefits of reduced losses and improved efficiency. Various scalable designs are compared and the principle of scalability is summarized. Torque ripple reduction techniques including rotor pole shaping and step skew are implemented. Mechanical tolerance analysis including deviation of offset angle, rotor static and dynamic eccentricities are presented to show the importance of tolerance control. Rotor dynamic properties such as natural frequencies and vibration modes are studied for the medium-speed machine. Structural stress distribution is evaluated to show the machine operates at safe margin within material strength. Dynamometer experimental tests are performed to validate the performance of the proposed machine.

Acknowledgements

This thesis represents the essence of my Ph.D. research project over the length of my graduate program. The past few years that I spent here in Madison Wisconsin provide me with tremendous enlightenment and enjoyment that I will always cherish. I was profoundly inspired by the wisdom and generosity of the people around me. Therefore, I would like to express my sincere gratitude to all that helped me along the way.

First, I am in debt to my advisor Professor Bulent Sarlioglu for his continuous support and guidance throughout my graduate study. My personal grow has benefited so much from his experience and patience over the years. I am grateful not only for his research advice but also for the everyday lessons he taught me, including the optimism towards the difficulties and the agility in uncertainties. I am very fortunate to work and learn from him, and the intangible asests he passed on to me will deeply influence my future career path and decision making.

I would like to extend my thanks to Professor Robert Lorenz, Professor Thomas Jahns, Professor Giri Venkataramanan, and Dr. Vladimir Blasko for serving as my Ph.D. committees for both preliminary exam and final defense. The valuable recommendations they provided for me help improve my research quality. I also would like to thank all the other faculties from the Wisconsin Electric Machines and Power Electronics Consortium (WEMPEC) for their valuable interactions with me on different occasions.

My thanks extend to our WEMPEC administrative staff and lab managers, Helene Demont, Raymond Marion, and Kyle Hanson for their kind support in the student logistics and lab experiments. I would like to thank David Farnia for his professional technical support for JMAG, and Paul Larson for his timely support in ANSYS. My appreciation is also expressed to Arnold

Magnetic Technologies for their help in fabrication of the prototype research electric machine, and to Rockwell Automation for their generous donation of the servo drive used for my experiments. My thanks also extent to Jagadeesh Tangudu from United Technologies Research Center for the collaboration on my project. I would like to thank all the WEMPEC sponsors that provide the research software, the informative Friday seminars and symposiums.

My gratitudes also goes to Wisconsin Alumni Research Foundation (WARF) who provides financial support for my early years of the Ph.D. program. I would like to thank National Science Foundation (NSF) for offering funding support from the Grant Opportunities for Academic Liaison with Industry (GOALI) project for the rest of my research program.

My special thanks extend to the entire WEMPEC graduate student community for making my life so wonderful here in Madison. I benefited from their diversity and inspiring personality, as I can learn something from each of them. I would like to acknowledge my friends and current fellow WEMPECKERs (in alphabetical order), Apoorva Athavale, Dheeraj Bobba, Le Chang, Parikshith Channegowda, Zhe Chen, Susie Wooyoung Choi, Hao Ding, Hang Dai, Jiejian Dai, Zhentao Du, Huthaifa Flieh, Baoyun Ge, Aditya Ghule, Skyler Hagen, Di Han, Phillip Hart, Ryoko Imamura, Hao Jiang, Ye Gu Kang, Ju Hyung Kim, Matt Woongkul Lee, Shang-Chuan Lee, Silong Li, Mingda Liu, Jianyang Liu, Wenbo Liu, Seth McElhinney, Seun Guy Min, Hung-Yen Ou Yang, Pablo Castro Palavicino, Dinesh Pattabiraman, Tim Polom, Michael Rios, Adam Shea, Minghao Sheng, Yuying Shi, Boru Wang, Kang Wang, Yujiang Wu, Yang Xu, Ruxiu Zhao, Bo Zhu, Guangqi Zhu and many others.

I would also like to thank my friends who already graduated at this moment (in alphabetical order), Gilsu Choi, Cong Deng, Shun Feng, Minjie Jiang, Wenying Jiang, Larry Juang, Phillip Kollmeyer, Jin Li, Ye Li, James McFarland, Casey Morris, He Niu, Jukkrit Noppakunkajorn, Di

Pan, Erik Schubert, Caleb Secrest, Jiyao Wang, Yukai Wang, Fan Wu, Wei Xu, Yinghan Xu, Yida Yang, Chen-Yen Yu, Wanjun Zhang, Yichao Zhang, Junjian Zhao, Honghao Zheng, Guozhen Zhou, Huimin Zhou, Ruonan Zhou, and Yutong Zhu.

Finally, I would like to express my greatest gratitudes to my parents and other family members for their love and support. They give me the courage to pursuit my dreams. They make me understood what genuine happiness and meaningful life look like.

Table of Contents

Nomenclature

Symbol	Description
V_{tip}	Tip speed of the rotor
N_s	Number of stator slots
N_r	Number of rotor poles
k_p	Pitch factor
k_d	Distribution factor
k_w	Winding factor
h	Harmonic order
F_{mx}	Force on the x-axis
F_{my}	Force on the y-axis
μ_0	Permeability of free space
B_c	Circumferential component of magnetic flux density
B_r	Radial component of magnetic flux density
f_e	Fundamental excitation frequency
n	Rotational speed in RPM
λ	Magnetic flux linkage in the winding
θ_e	Rotor position in electric angle
θ_m	Rotor position in mechanical angle
n_w	Winding function
n_h	Winding function harmonic amplitude for h^{th} order
N_c	Number of turns per winding coil
I_m	Amplitude of phase current
ω_e	Rotor angular rotational speed
F_c	Winding magnetomotive force
F_{pm}	Permanent magnet magnetomotive force
$F_{pm,h}$	Amplitude of hth harmonic of permanent magnet MMF
N_m	Number of permanent magnets
$P_{r,front}(\theta_m,t)$	Front rotor permeance function
$P_{r,h}$	Amplitude of hth harmonic of rotor permeance

$P_s(\theta_m)$	Stator permeance function
$P_{s,h}$	Amplitude of hth harmonic of stator permeance
$P_{g,front}(\theta_m)$	Front airgap permeance
$B_{g,front}(\theta_m)$	Front airgap magnetic flux density
$B_{g,sta}(\theta_m)$	Stationary component of airgap flux density
$B_{g,rot}(\theta_m)$	Rotational component of airgap flux density
$B_{g,mod}(\theta_m)$	Modulation component of airgap flux density
θ_{max}	Rotor position electric angle to achieve maximum flux linkage
N_t	Number of turns connected in series per phase
$B_{g,pk}$	Peak airgap magnetic flux density
K_m	The magnetization coefficient
K_t	Ratio of stator tooth width over stator pole pitch width
D_{is}	Stator inner diameter
D_{os}	Stator outer diameter
L_e	Effective stack length of electric machine
K_{fund}	Fundamental flux coefficient
E_{pk1}	Amplitude of fundamental back-EMF
P_{out}	Output power
I_{pk}	Amplitude of phase current
$A_{s,rms}$	Electrical loading
η	Efficiency
T_{out}	Output torque
g	Airgap length
B_r	Magnet remnant flux density
d_m	Magnet width
J_s	Current density in the winding
K_{cu}	Slot fill factor
L_d	d-axis inductance
L_q	q-axis inductance
R_s	Resistance per phase
P_c	Copper loss
P_{fe}	Iron loss
P_{mag}	Magnet eddy current loss

d_{gap}	Gap distance between two stators
λ_{split}	Split ratio of electric machine
$R_{mag,in}$	Magnet inner radius
$R_{mag,out}$	Magnet outer radius
R_{slot}	Stator slot bottom radius
d_{teeth}	Stator teeth width
$d_{mag,half}$	Half of the magnet thickness
$d_{s,tip}$	Stator teeth tip length
R_{shaft}	Rotor shaft radius
R_{ir}	Rotor inner radius
$R_{r,tip}$	Rotor pole tip bottom radius
R_{or}	Rotor outer radius
$d_{pole,half}$	Half width of rotor pole
$d_{r,tip}$	Rotor pole tip length
Φ_p	Magnetic flux per pole
C_d	Skin friction coefficient
R_e	Reynolds coefficient
M_{stator}	Mass of stator iron
M_{rotor}	Mass of rotor iron
M_{copper}	Mass of copper with end winding
M_{mag}	Mass of permanent magnets
ξ_T	Specific torque density
ξ_P	Specific power density
λ_{pm}	Magnet flux linkage
L_d*	Per unit d-axis inductance
L_q*	Per unit q-axis inductance
T_{ripple}	Torque ripple
ζ_{cu}	Copper loss density
ζ_{fe}	Iron loss density
ζ_{mag}	Magnet eddy current loss density

Abbreviations

IM	Induction Machine
IPM	Interior Permanent Magnet machine
SPM	Surface Permanent Magnet machine
SRM	Switched Reluctance Machine
DSPM	Doubly Salient Permanent Magnet machine
FRPM	Flux Reversal Permanent Magnet machine
FSPM	Flux-Switching Permanent Magnet machine
b-EMF	Back-Electromotive Force
PM	Permanent Magnet
BLDC	Brushless Direct-Current machine
MMF	Magnetomotive Force
FEA	Finite Element Analysis
HCF	Highest Common Factor
UMF	Unbalanced Magnetic Force
UBEMF	Unbalanced Back Electromotive Force
NdFeB	Neodymium Iron Boron permanent magnet
HEV	Hybrid Electric Vehicle
EV	Electric Vehicle
U.S. DRIVE	United States Driving Research and Innovation for Vehicle efficiency and Energy sustainability
PWM	Pulse Width Modulation
SiC	Silicon Carbide
FFT	Fast Fourier Transformation
THD	Total Harmonic Distortion
LCM	Least Common Multiplier
DOE	Design of Experiments

List of Figures

List of Tables

Introduction

Research Motivation

The flux-switching permanent magnet (FSPM) machine topology has the potential for medium and high-speed operation as proposed by previous researchers, but one of the biggest challenges that constrain the upper-speed limit is the high fundamental frequency required by the available high-pole FSPM machine topologies. Using high-pole FSPM machine for medium or high-speed operation has the disadvantages of possibly producing excessive high-frequency associated losses in the copper, lamination steel, and permanent magnets. It is also challenging to dissipate the heat generated by the various losses. From the perspectives of power electronic drives, the switching frequency of the devices is multiple times higher than the fundamental frequency, and the conventional Si-based devices may have difficulty in achieving such a high switching frequency. The medium or high-speed machines typically have a small number of rotor poles such as two pole or four poles if the rotational speed is very high. The low-pole configurations of flux-switching topology have not been fully investigated, and there are opportunities to develop viable low-pole flux-switching machine topologies especially for those high-speed operating conditions.

Thus, the motivation of this research is to investigate a viable FSPM machine topology with a low number of rotor poles to reduce the required fundamental frequency. The proposed FSPM machine topology has a dual-stator structure with six stator slots and four rotor poles that significantly reduces the fundamental frequency by 60% compared to the widely used twelve stator slots and ten rotor poles FSPM machine topology. In return, various losses such as iron loss,

permanent magnet loss, and inverter loss will be prominently reduced, and the total efficiency will be drastically higher than high-pole-count FSPM machines. The outcome of this research is expected to be a design methodology that maximizes the performance of the proposed novel low-pole flux-switching permanent magnet machine at medium and high-speed operations. This novel flux-coupling low-pole FSPM machine topology will be a compelling candidate for many emerging applications that require medium to high-speed motors and generators.

Research Overview

The primary research objective is to investigate the design and performance of the proposed flux-coupling dual-stator 6/4 FSPM machines and the advantages compared to other existing topologies, especially at medium and high-speed operating condition. The low-pole topology for the medium to high-speed machine is favorable to minimize the fundamental frequency requirement. Viable stator slot/rotor pole combinations of low-pole count FSPM machines are studied. The lowest possible three-phase topology of FSPM machine, with six stator slots and four rotor poles (6/4), has unacceptably large 2^{nd} order harmonic distortion in the flux linkage and severe cogging torque in its conventional single-stator-single-rotor form. To resolve these challenges, a novel dual-stator structure for the 6/4 FSPM machine is proposed that eliminates the even order harmonics in the flux linkage. Harmonic distortion and cogging torque are notably reduced in the proposed machine. Thus, the 6/4 combination becomes feasible for the FSPM machine.

The proposed dual-stator structure concept applies to multiple topology variations of 6/4 FSPM machine that achieve the same effect of even harmonic cancellation. The differences

between these alternative topologies regarding manufacturability and performances are studied to determine which configuration should be chosen appropriately. To understand the principle of operation for the proposed dual-stator 6/4 FSPM machine, fundamental theories such as winding function, magnetomotive forces generated by the winding currents, and the harmonics in the airgap produced by the stationary permanent magnets in the stators are studied in detail. To perform initial geometrical design of the dual-stator 6/4 FSPM machine, the sizing equations are developed to quantify the key dimensions of the machine when a specific design rating is given. The sizing equations also provide design insights on how to improve the output torque or power of the machine. The principle of scalability of the dual-stator 6/4 FSPM machine is verified by four designs with different power and speed ratings.

To demonstrate the novelty of the proposed dual-stator 6/4 FSPM machine, its performances are characterized and compared with other existing FSPM machines. The proposed flux-coupling dual-stator 6/4 FSPM machine is compared with the conventional 6/4 FSPM machine to show the reduction of harmonic distortion in the flux linkage and back-EMF, and reduction of cogging torque and torque ripple. More accurate performances of the proposed machine are investigated by both 2-dimentional (2D), and especially 3-dimentional (3D) finite element analysis. The high-speed operating capabilities of the proposed dual-stator 6/4 FSPM machine are also studied in comparison with the 12/10 FSPM machine. Both parametric analysis and optimization are investigated for dual-stator 6/4 and 12/10 FSPM machines. The electromagnetic properties including torque and power density, loss distribution, and efficiency are compared for the low-pole 6/4 and high-pole 12/10 FSPM machines.

The performance of the proposed machine is improved by torque ripple minimization technique including stator tooth rotor pole shaping and rotor step skew. Mechanical tolerances in the airgap region including the deviation of rotor offset angles, rotor static eccentricity, and rotor dynamic eccentricity are investigated to demonstrate their influence to machine performances. Structural dynamic analysis including the natural frequencies, rotor dynamic mode shapes, and critical speeds are studied for the medium-speed dual-stator 6/4 FSPM machine. Mechanical stress on the rotor is evaluated to ensure the machine operates within a safe mechanical margin. A prototype proof-of-concept machine is designed and fabricated, and the dynamometer test setup is built for experimental study. The torque production capability and various losses of the prototype machine are measured. Results obtained from the experiments show reasonably good agreement with the analytical studies. The validity of the dual-stator 6/4 FSPM machine concept is proved.

Primary Contributions

The key contributions of this research study are to propose and develop the analytical methodology for a novel flux-coupling dual-stator 6/4 flux-switching permanent magnet machine. The following paragraphs concisely summarize the key contributions from this research. More detailed discussion of each contribution can be found in Chapter 9.

A novel concept of dual-stator structure is proposed for the 6/4 FSPM machine to address the unbalanced back-EMF challenges of the conventional 6/4 FSPM machine. Analytical equations are studied to explain the reason why the novel dual-stator structure can achieve even order harmonic cancellation in the flux linkage. Multiple alternative topologies of the dual-stator 6/4 FSPM machines are proposed and studied for the performance differences.

Fundamental principles of operation are analytically investigated for the dual-stator 6/4 FSPM machine, primarily by harmonic analysis of the winding magnetomotive forces and airgap flux density harmonic contents. The multi-harmonic operating nature of the proposed 6/4 FSPM machine and the torque producing principles are explained. Sizing equations for the dual-stator 6/4 FSPM machine are derived based on the generalized sizing laws. The principle of scalability is verified by designs with various power and speed ratings.

The performances of the novel dual-stator 6/4 FSPM machine are investigated by both 2-dimentional and 3-dimentional finite element analysis. Parametric studies are done to investigate the influence of key geometrical parameters, such as split ratio, stator tooth width, magnet thickness, and rotor pole width, to the output performances. Optimization is also performed for the proposed dual-stator 6/4 FSPM machine to maximum the torque density with acceptable torque ripple. Torque ripple minimization technique of tooth shaping and rotor step skew are implemented to reduce the torque ripple percentage of the proposed machine.

Design and performance comparison of the proposed dual-stator 6/4 FSPM machine are investigated with other FSPM machines. The dual-stator 6/4 FSPM machine has drastic reduction of harmonic distortion in the flux linkage and back-EMF, less cogging torque, and more average torque than the conventional 6/4 FSPM machine. The dual-stator 6/4 FSPM machine achieves reduction of high-frequency losses and improved efficiency than the 12/10 FSPM machine.

Mechanical tolerances of airgap region caused by offset angle deviation of rotor poles, rotor static and dynamic eccentricities are investigated for performance variation. The rationale to maintain tight mechanical tolerance in the airgap region is emphasised. The rotor dynamics including natural frequency, critical speeds, and vibrational modes of the high-speed dual-stator

6/4 FSPM machine are investigated. Mechanical stress on the rotor during operation is also estimated for structural safety purpose.

A proof-of-concept prototype of dual-stator 6/4 FSPM machine is designed and manufactured to validate the theoretical design. Dynamometer test setup of the prototype machine is built. Open circuit and loaded tests of the prototype machine are performed. Various losses of the prototype are characterized. The experimental results show good agreement with the analytical studies.

Organization of Chapters

This thesis is organized as follows:

- Chapter 1 reviews the state-of-the-art literature of flux-switching machines on the topics including modeling and analysis, developed flux-switching machine topologies, and design aspects on high-speed operations.
- Chapter 2 presents the unbalanced back-EMF challenge of conventional 6/4 FSPM machine, and proposes the novel dual-stator 6/4 FSPM machine to address this challenge. The even order harmonic cancellation principle is explained for the novel dual-stator 6/4 FSPM machine. Multiple alternative topologies of the dual-stator 6/4 FSPM machine are also introduced.
- Chapter 3 presents the harmonic analysis for the novel dual-stator 6/4 FSPM machine, including winding magnetomotive forces, airgap flux density harmonic contents, and torque production principles. The sizing equations for the dual-stator 6/4 FSPM machine are also derived based on the generalized sizing principles of electric machine.

- Chapter 4 presents the analysis and comparison studies of proposed novel dual-stator 6/4 FSPM machines. The performances of proposed novel dual-stator 6/4 FSPM machine are compared with the conventional 6/4 FSPM machine. Three alternative topologies of the dual-stator 6/4 FSPM machines are also compared for the design and electromagnetic performances including torque density.
- Chapter 5 presents the parametric analysis and optimization studies of the proposed dual-stator 6/4 FSPM machine. The influence of several key machine parameters to the performances such as flux linkage and torque are investigated. Torque density of the dual-stator 6/4 FSPM machine is calculated. Optimizations are performed to maximize average torque and minimize the torque ripple. A design for traction application is presented. The principle of scalability of the proposed machine is verified.
- Chapter 6 presents the performance comparison studies of the proposed dual-stator 6/4 FSPM machine with the 12/10 FSPM machine for high-speed operations. The design and optimization for 12/10 FSPM machine are discussed. Torque density, weight and loss distribution, and efficiency of these two machines are compared. Performance tradeoffs of 12/10 and proposed 6/4 FSPM machines are discussed.
- Chapter 7 presents the torque ripple reduction study and mechanical analysis of the proposed machine. The rotor dynamics including natural frequency, critical speeds, and vibrational modes are investigated. Mechanical stress on the rotor is also calculated to ensure safety operation.

- Chapter 8 presents the fabrication and test of the proof-of-concept prototype machine. Experimental results are done at open circuit and various loaded conditions in the dynamometer test stand to validate the analytical studies.
- Chapter 9 presents the conclusions, contributions, and the future work for this research program.

Chapter 1

State-of-the-Art Literature Review

The purpose of this literature review is to summarize the state-of-the-art research relating to FSPM machines and identify the potential opportunities for this research study, with a focus on the designs for medium and high-speed operations. An introduction is first provided to define high-speed electric machines and the potential candidate machine topologies. Then, the stator-mounted permanent magnet machines are introduced and compared. The basic operating principle of flux-switching permanent magnet machine is explained. To provide a solid foundation for this research study, a comprehensive literature review is given on the flux-switching machines. To have a better organization, the literature is divided into the following subsections: modeling and analysis of flux-switching machines, existing flux-switching machine topologies, and high-speed design aspects of flux-switching machines.

1.1 Introduction

The design of high-torque density and high-efficiency electric machines has been the research focus for the past few decades. Electric machines play an important role in a broad spectrum of applications such as the appliance, industrial drives, transportation vehicles, etc. The electric machine technology is becoming the enabling technology in every aspect of life, and its advancement has a huge influence on the modern society. The development of electric machines is always accompanied by the improvement of materials involved such as better steels, permanent

magnets, and conductors. With the emerging high energy density rare-earth permanent magnets available in the market, the permanent magnet machines are becoming increasingly popular over the past decade due to the advantages of high torque density and efficiency compared to electric machines without permanent magnet materials such as induction machine, synchronous reluctance machine, and switched reluctance machine, etc [1], [2], [3], [4], [5], [6], [7], [8], [9], [10].

The most widely investigated and implemented permanent magnet machines nowadays are surface permanent magnet (SPM) machines and interior permanent magnet (IPM) machines, whose permanent magnets are placed on the surface or embedded inside the rotor laminations. The IPM machines can be subcategorized into flux-weakening type or flux-intensifying types depending on the saliency property [11], [12], [13], [14], [15], [16], [17], [18], [19]. Although they have high torque density, the disadvantages are that the magnet are prone to great centrifugal forces at high-speed conditions and the rotor rigidity could be an issue. For SPM machines, the magnet containment problem can be solved by using sleeves on the surface of the rotor. The material for the sleeve is usually titanium steel, carbon fiber, or Inconel. However, an external sleeve adds extra airgap length and reduces the torque density. For IPM machines, the rotor bridges are the most vulnerable portion of the rotor lamination which has the highest risk of deformation under excessive centrifugal forces. As a result, IPM machines are not typically used for very high-speed operations [20], [21], [22], [23], [24], [25], [26].

1.1.1 High-Speed Electric Machines

High-speed electric machines are becoming increasingly important in various applications due to the high power density, reduced weight and volume benefits. When the torque density of

an electric machine is determined, the output power is proportional to the operating speed. However, the upper-speed limit of an electric machine is constrained by the machine structure integrity, acceptable losses produced at high-speed conditions, desirable efficiency, and available operating frequency of the drive electronics. The definition of the high-speed electric machine is that the rotor tip speed (or rotor surface speed), which refers to the velocity of the outer edge of a rotor, is very high which typically in the range of 200 m/s to 300 m/s or above. An illustration of the rotational speed *N* (rpm), rotor outer diameter *D* (mm), and tip speed V_{tip} (m/s) is shown in Figure 1.1. The table shown in Figure 1.1 states that high-speed electric machines can be designed for both large machines (large D) and small machines (small D), with appropriately designed operating speed. In other words, high power large electric machines with relatively low speed can still be categorized into high-speed machine if the tip speed falls into the high-speed range.

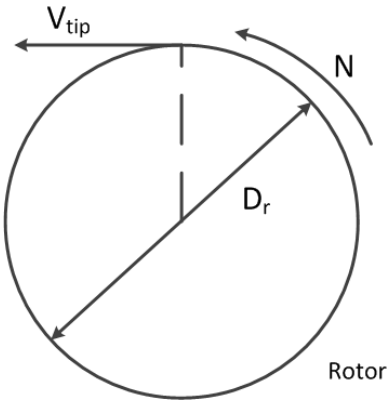

case	N (krpm)	D (mm)	V_{tip} (m/s)
1	10	500	261.8
2	100	50	261.8
3	500	10	261.8

Figure 1.1. Definition of high-speed machine, and examples of different speeds and rotor diameters for high-speed conditions.

High-speed electric machines have demanding requirements for the mechanical integrity of the machine, especially for the rotor part. Conventionally, there are three major electric machine types that are suitable for high-speed operation. These machines types are surface permanent

magnet machine, induction machine, and switched reluctance machine. There are less high-speed designs using interior permanent magnet machine or synchronous reluctance machine. [20], [21], [22], [23]. The surface permanent magnet machines have advantages of high power density and torque density, and their performance is relatively insensitive to small airgap length variations particularly at eccentric rotor conditions. The disadvantages of surface permanent magnet machines are that they need to have rotor sleeve to contain the permanent magnets from centrifugal forces, and the heat generated by permanent magnets and sleeves are difficult to dissipate which poses risks of thermal demagnetization of permanent magnets. The induction machines have advantages of mature manufacturing and design, and they are relatively easy to control, but the power factor and efficiency are comparably lower than that of permanent magnet machines. The switched reluctance machines have robust and simple rotor structure, but their performance is sensitive to airgap variations. In addition, the noise and vibrations of switched reluctance machines are usually unacceptably large for some applications [24], [25], [26]. There are many electric machine topologies that can be potentially considered for medium to high-speed operations as shown in Figure 1.2.

There are opportunities in developing new electric machine topologies that have the advantages of both using high energy permanent magnet materials to boost the torque density, and utilizing the rotor structural simplicity and robustness of the switched reluctance machine. This type of electric machines should have permanent magnets embedded in the stator structure. Thus, the stator-mounted permanent magnet machines are discussed in the next section.

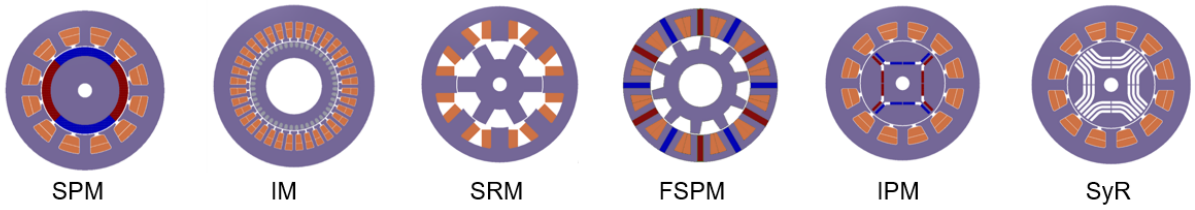

Machine Type	Advantages	Disadvantages
SPM - Surface PM Machine	1. High torque density 2. Easy control	1. Large equivalent airgap and low motor inductance 2. Magnets retention issue
IM - Induction Machine	1. Most widely used 2. Simple and robust structure	1. Relatively low efficiency because of closed rotor slots needed for containment
SRM - Switched Reluctance Machine	1. Robust rotor good for high speeds 2. Fault tolerant capability	1. Large torque ripple 2. High acoustic noise
FSPM - Flux-Switching PM machine	1. Robust rotor good for high speeds 2. PM is on the stator	1. Potential high fundamental frequency required
IPM - Interior PM Machine	1. High torque density 2. Good flux weakening or intensifying capabilities	1. Rotor bridge integrity 2. Not amenable to very high speeds
SyR - Synchronous Reluctance Machine	1. Salient machine without magnets 2. Simple control algorithm	1. Low power factor 2. Complicated rotor design 3. Not amenable to very high speeds

Figure 1.2. Comparison of various machine topologies for high-speed operation [20], [21], [22], [23], [24], [25], [26].

1.1.2 Stator-Mounted Permanent Magnet Machines

As discussed in the prior section, it would be desirable if the rotor of the high-speed electric machine has no magnets so that there would be no containment issue at high-speed conditions. This idea has given rise to a couple of new machine topologies where permanent magnets are moved from the rotor to the stator side. There are mainly three electric machine types that place the permanent magnets in the stator, i.e. Doubly Salient Permanent Magnet (DSPM) machine, Flux Reversal Permanent Magnet (FRPM) machine, and Flux-Switching Permanent Magnet (FSPM)

machine. In general, these class of new machines is called stator-mounted permanent magnet machines [27], [28], [29].

Depending on how the magnets are mounted to the stator, the operation principles of these three machines types are very different. The DSPM machines places permanent magnets in the stator yoke, and the magnets are magnetized circumferentially [30], [31], [32], [33], [34]. Concentrated winding is used, and the PM flux linkage induced in the winding is unidirectional when the rotor rotates. PM flux linkage is linear with rotor position so that the back-electromotive force (back-EMF) is a trapezoidal waveform. The single-phase 4 Slot/6 Pole configuration of DSPM generator was investigated in [35], and a three-phase 12 Slot/8 Pole DSPM motor was studied in [36] shown in Figure 1.3 below. There are other slot/pole combinations available for various applications. The key dimensions related to power equation was investigated in [37] describing that the power is proportional to the ratio of number of rotor poles over stator teeth.

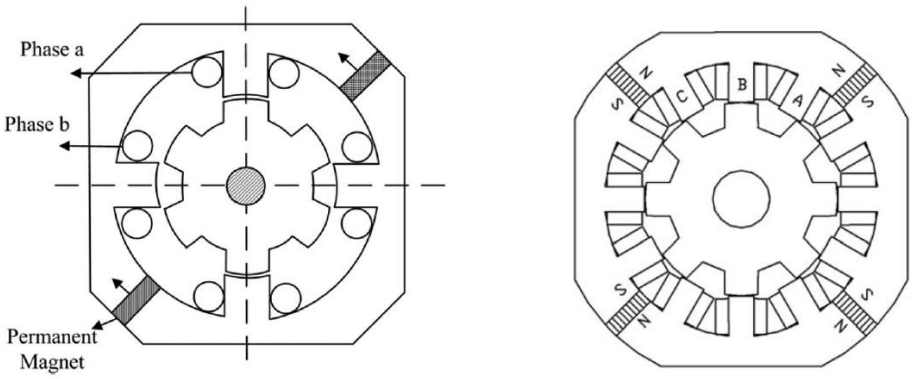

(a) (b)

Figure 1.3. Doubly salient PM machine example (a) 4 Slot/6 Pole single-phase DSPM generator [35] (b) 12 Slot/8 Pole three-phase DSPM machine [36].

When the permanent magnets are placed on the surface of stator teeth, the topology is named flux reversal permanent magnet machine. The PM flux linkage for each phase windings is bipolar as opposed to unipolar nature in the DSPM machine. The induced flux linkage also has a linear relation with the rotor position, so the back-EMF is again a trapezoidal waveform, which is designed for brushless DC (BLDC) operation [38], [39], [40]. The single-phase and three-phase versions of FRPM machine are both shown in Figure 1.4. It was found that FRPM machine exhibits good fault-tolerant operation capability because of magnetic isolation between phases. The reluctance torque is negligible due to the small saliency nature of this machine. The effective airgap length of the FRPM machine is large due to the factor that permanent magnets are in series with the flux path. The cogging torque is typically large and the power factor is not as high as conventional rotor-mounted PM machines [41], [42], [43]. There are research topics such as cogging torque minimization, high-speed FRPM machine design, and analytical studies for electromagnetic performances in the literature [44], [45], [46], [47], [48].

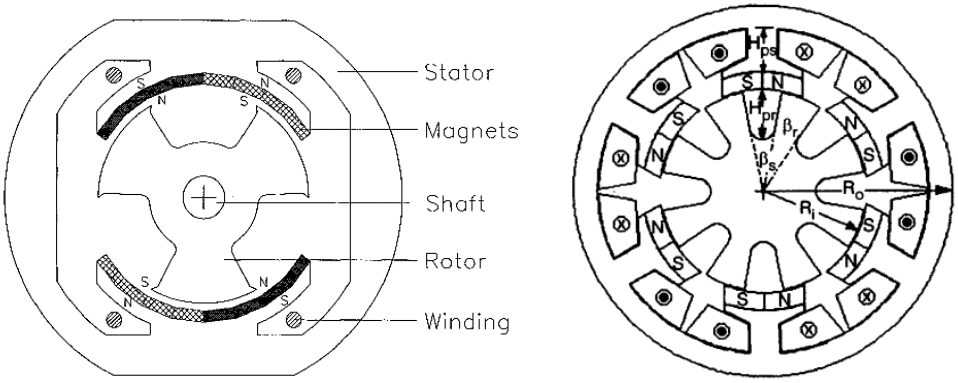

(a) (b)

Figure 1.4. (a) Single-phase flux reversal machine [39] (b) three-phase flux reversal machine [40].

One of the most promising candidates of stator-mounted PM machine is the flux-switching permanent magnet machine, whose magnets are sandwiched in-between the stator teeth and cores. Based on the bipolar PM flux linkage and sinusoidal back-EMF properties, the FSPM machine has higher torque density than that of the DSPM and FRPM machine [49], [50]. The first FSPM machine concept was proposed by Rauch and Johnson in 1955 [51] with a single-phase alternator topology. The rotor of FSPM machine is simple and robust as that of the switched reluctance machine, and the flux linkage in the windings are bi-directional as shown in Figure 1.5. The three-phase topology is proposed firstly by Hoang et.al. in 1997 [52] with two types of configurations shown in Figure 1.6.

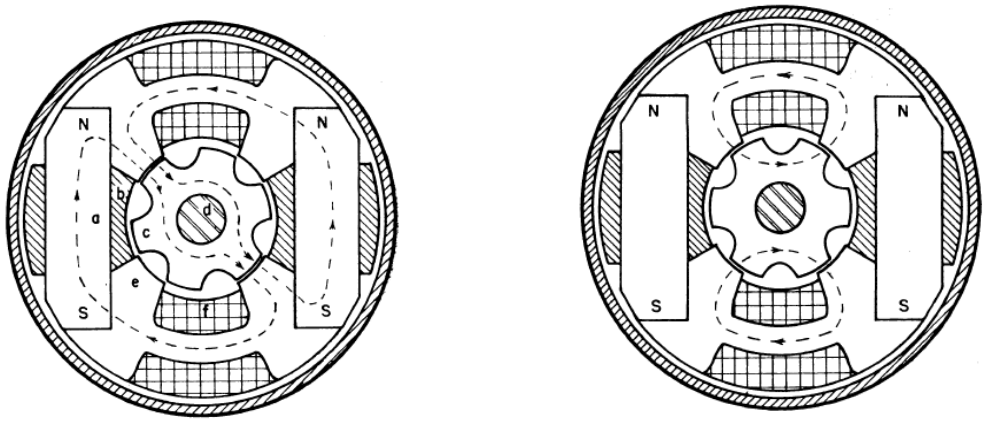

(a) (b)

Figure 1.5. Single-phase flux-switching alternator at (a) maximum flux linkage position machine and (b) zero flux linkage position [51].

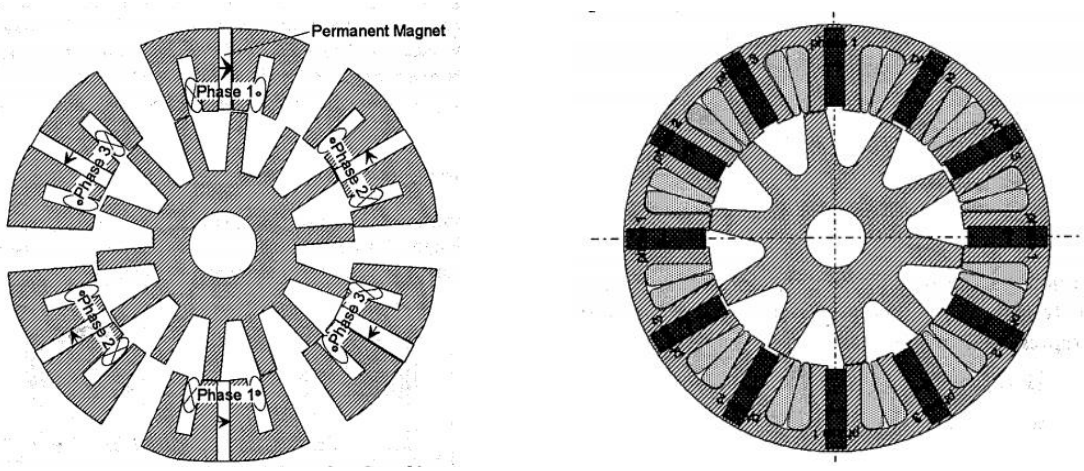

(a) (b)

Figure 1.6. Three phase flux-switching permanent magnet machine for (a) type A and (b) type B topologies [52].

The stator assembling of FSPM machine is more complex than conventional synchronous permanent magnet machines due to the integration of concentrated armature windings, permanent magnets, and segmented stator iron pieces into the stator structure. The magnets are circumferentially magnetized in alternative directions between segmented stator cores. The rotor is a passive steel lamination stack that has salient poles. The heat generated by all the active components is mostly in the stator, and there is less concern about the generated heat in the rotor since no permanent magnets are in the rotor. Thus, the applied cooling methods are more effective in regulating the thermal flow and preventing the overall machine being over-heated. This is especially advantageous for managing the temperature of the permanent magnets whose performance is highly dependent on the temperature variation. The conventional rotor-mounted PM synchronous machines do not have such an advantage because the magnets are from the cooling surface.

Since the invention of three-phase FSPM machine topology, researchers have been actively investigating various aspects of FSPM machine over the past decades. Flux-switching PM machines are applicable for a broad spectrum of ratings and applications ranging from low-power to high-power and low-speed to high-speed conditions. Although FSPM machines are not massively manufactured in the industry nowadays, the potential applications are abundant. Typically, examples are electric motors/generators in various applications such as appliances, industrial workforces, and vehicular applications such as in the (hybrid) electric vehicle, aerospace, marine, etc.

A comparison of the stator-mounted permanent magnet machines is summarized below in TABLE 1.1 to give a qualitative analysis of the three popular candidates. It is clear to see that the FSPM machines possess multiple beneficial properties such as bidirectional and sinusoidal flux linkage, symmetrical and balanced 3-phase EMF, and high torque density than the other two topologies. Thus, flux-switching PM machine is chosen for this research study.

TABLE 1.1. COMPARISON OF STATOR-MOUNTED PM MACHINES [27], [28]

Topologies	Doubly Salient	Flux Reversal	Flux-switching
Torque production	PM excitation torque rely on structural saliency and reluctance action, but negligible reluctance torque		
Windings	Non-overlapping concentrated windings		
PM placement	In stator yoke	On tooth face	In stator tooth
PM flux focusing	Not in general	None	Significant
Magnet volume	Low	Medium	High
Flux linkage	Unipolar	Bipolar	Bipolar
EMF	Non-sinusoidal, asymmetric and unbalanced 3 phase	Non-sinusoidal, symmetrical and balanced 3 phase	Sinusoidal, symmetrical and balanced 3 phase
Operation mode	Brushless DC	Brushless DC	Brushless AC
Torque density	Low	Low	High

1.1.3 Operation Principle of Flux-Switching Machine

Flux-switching PM machines have doubly salient structure because the number of stator teeth and rotor poles should be different. The stator cores are built by segmented steel stack pieces that are separated by the permanent magnets. The permanent magnets are circumferentially magnetized, and they are sandwiched by the stator segments. The rotor of FSPM machine is a passive laminated iron component with a salient structure in nature. An illustration of the FSPM machine with the most conventional three-phase topology (12 slot/10 poles) is shown in Figure 1.7. The selection of stator slot and rotor pole numbers is as important as the other synchronous machines which will be discussed in detail in the next sections. Concentrated windings are used to wrap around the stator teeth with enclosed permanent magnet in-between two stator segments. Since there are two coils residing inside a slot area, this concentrated winding has a double-layer configuration. The FSPM machine can also be configured to have a single-layer winding which has the benefits of electrically separated phase windings.

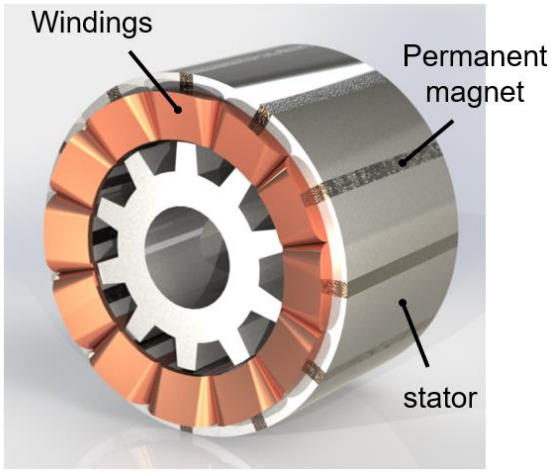

Figure 1.7. Rendering of a conventional FSPM machine with 12-slot and 10-pole.

Although the structure of FSPM machine is very complex and highly segmented, the flux linkage waveforms turn out to be very sinusoidal. To better explain the operation principle of the FSPM machine, flux linkage waveform of one phase coil is plotted in Figure 1.8 for an electric cycle. There are four corresponding rotor positions illustrated in Figure 1.9. For FSPM machine, one electric cycle is realized by $1/N_r$ of per rotor mechanical revolution when N_r is the number of rotor poles. So one electric cycle equals to 36° mechanically for the 12/10 topology, and the rotor moves counter-clockwise each time from Figure 1.9(a) to Figure 1.9(d). It is noticed that the flux is "switched" from one stator tooth to the other adjacent stator tooth by following the maximum permeance path when the rotor aligns with the corresponding stator tooth. The flux linkage in the studied coil achieves maximum positive and maximum negative values at Figure 1.9(a) and Figure 1.9(c) respectively. However, when the rotor pole aligns with the centerline of the permanent magnet, or the centerline between two rotor poles aligns with the centerline of the permanent magnet, the flux linkage in the corresponding windings is zero. This is due to the short circuit of magnet flux caused by the symmetry of the rotor permeance with respect to the corresponding stator teeth.

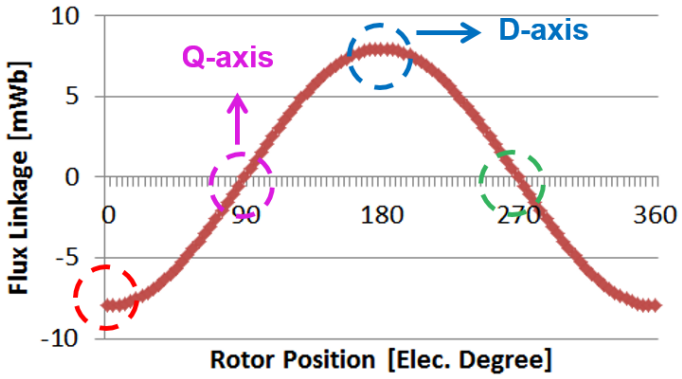

Figure 1.8. Sinusoidal flux linkage per phase winding in FSPM machine illustrating four key positions.

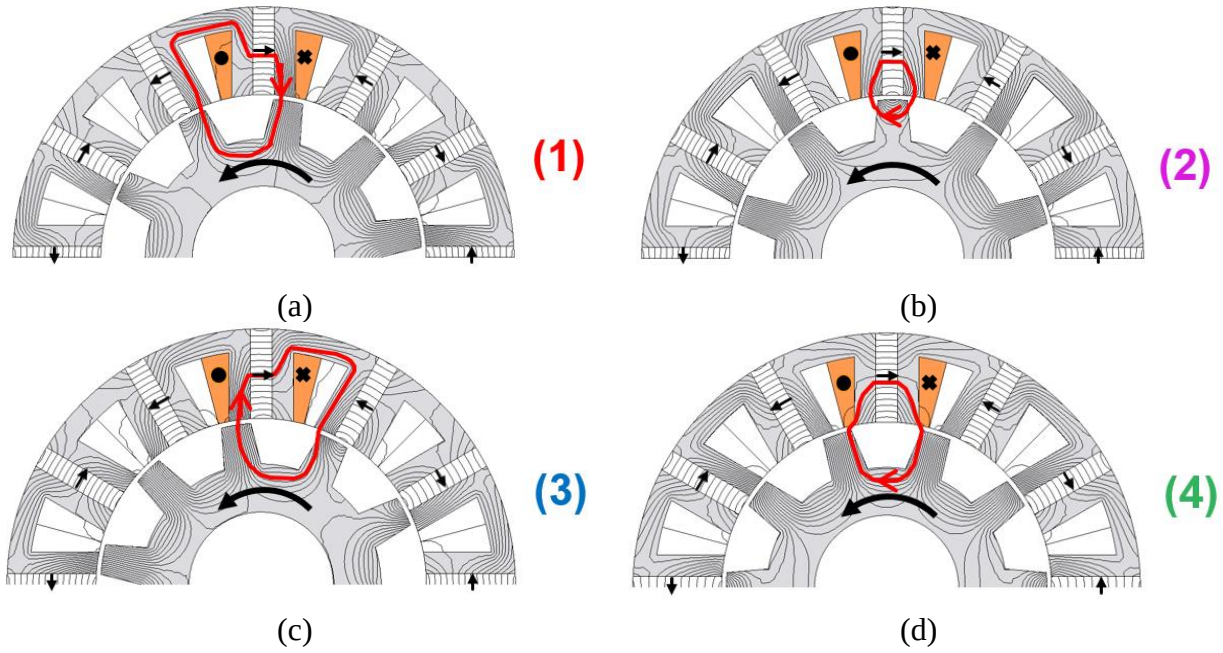

Figure 1.9. Different flux path produced by only the permanent magnets linking a coil at four key rotor positions. (a) position with maximum negative flux linkage in coil (b) position with zero flux linkage in coil showing q-axis (c) position with maximum positive flux linkage in coil showing d-axis (d) position with zero flux linkage.

The sinusoidal nature of the flux linkage justifies that the back-EMF is also sinusoidal, which is one of the most desirable properties for synchronous PM machine. Non-zero average torque is produced if applying sinusoidal three-phase currents with appropriate phase angle. It is shown that the FSPM machine operates on the flux modulation principle, which is a common ground for a wide range of electric machines. The permeance of the airgap is modulated by the stator teeth and rotor poles which operate like the Vernier permanent magnet machine. The airgap flux density has harmonic contents that have the same pole pair number and rotational speed with respect to the corresponding stator winding MMF harmonics. Thus, multiple harmonics from the

winding MMF and airgap flux density are coupled to produce the non-zero average torque, which will be discussed in detail in this research study.

Other important properties of FSPM machines include that the d, q-axis inductance are very close to each other so that the saliency is very limited. This indicates that the current control can be simplified by only applying q-axis current with zero d-axis current, which is identical to the surface permanent magnet machine. The permanent magnets are magnetized in the circumferential direction, whereas the flux from armature windings is in the radial direction. This property implies that the armature effect to the permanent magnets is much smaller compared to conventional synchronous permanent magnet machines.

1.2 Modeling and Analysis of Flux-Switching Machines

1.2.1 Analytical Modeling of Flux-Switching Machines

There are several review papers written by Zhu [53], [54] and Shen [55] about the latest FSPM machine research highlights. These review papers primarily summarized the development of novel FSPM machine concepts and topologies during the past decades. There are more papers focus on specific modeling and analytical studies of the FSPM machines. The dimensional parameters of FSPM machine for the conventional 12-slot 10-pole configuration is studied with the limit of the inverter and flux weakening capability by Hua [56]. The flux weakening capability is improved by adjusting the current density and slot copper fill factor. A simplified analytical model is derived for the sizing of FSPM machine by Somesan [57]. Zhang developed several key

magnetic parameters to quantify the characteristics of the proposed 12/10 FSPM machine, which they called “stator interior permanent magnet machine” [58].

The operation principles and torque production properties are investigated by several researchers. The airgap magnetic field modulation and magnetic gearing effects of FSPM machine are studied by Wu [59]. Results show that the airgap field has multiple harmonics with static component, forward and backward rotating components. The stator MMF produced by the three-phase windings are also modulated by the permeance from the stator teeth and rotor poles. The average torque produced by each of the harmonic order is calculated. McFarland also investigated the torque production mechanism of the FSPM machine and claimed that the airgap flux density is a heterodyning phenomenon of two different harmonic modulations from the magnet MMF harmonics and the rotor permeance harmonics [60]. The magnetic flux path of FSPM machine is also studied by McFarland to show that the winding MMF is always supporting the magnet MMF for both motoring and generating conditions, indicating an excellent capability of withstanding demagnetization from the perspective of permanent magnets. From a magnetic circuit point of view, the winding MMF is connected in series with magnet MMF [61]. It is identified that the lowest order of the spatial harmonic contributed to the non-zero average torque production is equal to the number of coils per phase (number of stator slots/number of phases). Gaussen also studied the analytical approach for the airgap field modeling of a field-excited FSPM machine at no-load conditions [62] by MMF and permeance theory. Close agreements are found between the analytical studies and the 2D FEA results.

The harmonic contents in the flux linkage of phase windings are studied by Hua to design the optimal back-EMF [63]. It is observed that each coil has odd and even harmonics in the flux

linkage, but the total phase winding has no even harmonics in the flux linkage at open circuit operation due to the diametrically placed coils in the 12/10 configuration as shown in Figure 1.10. Results show that the optimal geometry regarding reducing cogging torque and improving average torque is to design the rotor pole thickness as about 1.4 times the thickness of stator tooth. However, more analysis is needed to justify this value at different scaling conditions.

Design parameters including the magnet, teeth, and slot geometries to the output torque are parametrically studied by Zhu [64]. The study states that the maximum torque is achieved by designing equal stator tooth width, magnet thickness, and slot opening width. The study also suggests that torque can also be improved by designing the stator yoke thickness as ~70% of the tooth width to increase the slot area and increase the electrical loadings. The output torque is further increased by ~8% by increasing rotor pole thickness by 40%~60% of the original width when it equals to the stator tooth width. Inductance characteristics of FSPM machine are investigated by Hua, Ilhan, and Qi under various conditions accounting for the saturation effect [65], [66], [67]. The saliency of the FSPM machine is very limited as identified in the results, and the saliency relationship can be reversed under different operating conditions. The optimal split ratio of FSPM machine to achieve the maximum torque is near 0.65 which is shown by Li [68]. Nevertheless, more analysis should be done to generalize the optimal value of split ratio to achieve the maximum torque under different design requirement, such as the current density etc.

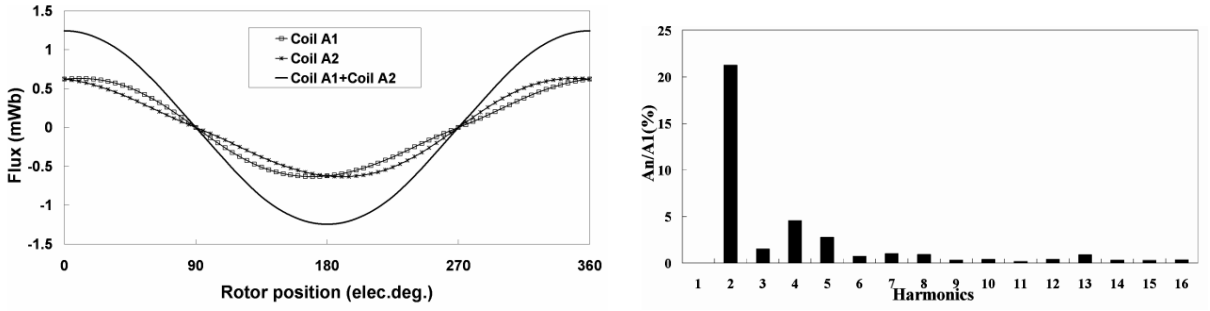

(a) (b)

Figure 1.10. Flux linkage harmonic analysis of 12/10 FSPM machine (a) flux linkage waveforms of two diametrically placed coils (A1 and A2) (b) normalized harmonic components of the flux linkage in coil A1 [63].

The FSPM machines have large blocks of permanent magnets facing the outsides, so the influence of end effects is non-negligible. The end effects of FSPM machine are investigated by Zhu in the aspects of modeling and output performance [69], [70], [71]. The magnetic circuit model is used to derive various leakage components and calculate the maximum flux linkage under the influence of end effects. The average torque in the 3D FEA is compared with the 2D results to show a reduction of torque due to the additional leakage and fringing effect that are captured by the 3D study. The cross-coupling effects on the d, q-axis inductances are also studied, and the results show a modest level of cross saturation effect in the FSPM machine.

A performance comparative study is conducted by Zhu for various alternative FSPM machine topologies, and the results show that wider speed range is achieved than the conventional 12/10 topology [72]. It is identified that the limited flux-weakening range of the conventional FSPM machine is caused by the low d-axis inductance value. The topologies proposed in the paper could have higher d-axis inductance to increase the high-speed power capability, but they may cause more saturation at smaller current conditions compared to the conventional 12/10 topology.

An axially laminated FSPM machine is developed by Xu to demonstrate the efficiency improvements of this topology because of iron loss reduction especially at high-speed conditions. The proposed axially laminated FSPM machine has slightly higher average torque than that of the conventional FSPM machine [73]. The thermal-electromagnetic analysis for FSPM machine during driving cycles is studied by Li, and the key contribution is to develop an accurate model that predicts the transient power losses and temperature variations with the specified driving cycle [74]. Multiple concentrated winding layouts are investigated for FSPM machine by Hwang to show that the single layer design is more suitable for high average torque requirement despite the torque ripple and efficiency [75].

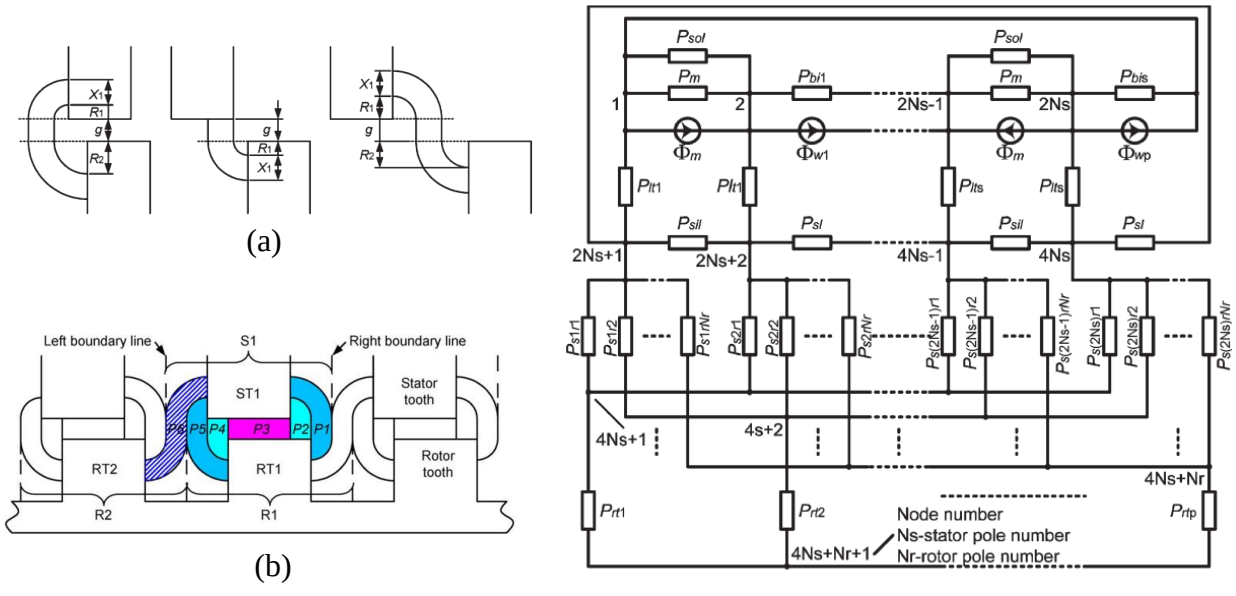

Figure 1.11. Lumped parameter magnetic circuit modeling of the flux-switching machine, (a) typical airgap permeance model, (b) magnetic permeance model between stator and rotor sides, (c) generalized lumped magnetic circuit model [81].

One of relatively fast and accurate method of modeling electric machines is by magnetic circuit analysis. A handful of researchers has been investigating the magnetic circuit modeling of FSPM machines for fast performance prediction for the machine design. Those pioneers include Zhu, Hua, Zhang, and Chen [76], [77], [78], [79], [80], [81], [82], [83]. The key technique of lumped parameter magnetic circuit analysis is to appropriately model various permeance or reluctance components in the network. This is especially challenging for different types of leakage flux permeance/reluctance components which rely upon complex geometrical shapes, fringing effects, and different rotor positions. The fundamental and repeatable segments of the studied FSPM machine should be identified and modeled in magnetic circuit first. Then, the components and connection mesh grid of the magnetic circuit model should be dynamically updated at different rotor positions to account for the alternation of the leakage flux patterns. The airgap flux is bidirectional so that modeling of permeance in airgap region and in areas that have swift changes in flux density and direction needs special caution and refinements.

The magnetic circuit model should also consider the non-linear and saturation effects in the material to offer an accurate prediction of flux linkage, back-EMF, and airgap flux density. This method is applicable for various FSPM machine types including conventional flux-switching structure, hybrid excitation structure, and linear machine [84], [85], [86]. Fourier analysis is used by Gysen for the modeling of FSPM machine to overcome the difficulties of relative complex adjustments of magnetic circuit model when rotor moves or parametric sweep [87]. The results show fairly good agreements with the FEA study. Based on the previous methods, some researchers also proposed a hybrid modeling technique that unites the magnetic circuit modeling with Fourier analysis to take advantages of both methods [88], [89].

Torque ripple is an undesirable property in electric machines especially for the applications where smooth torque is required such as servo motors. The flux-switching topology overall has non-negligible torque ripple that should be minimized in the design process. The reduction of torque ripple is a practical research area, and researchers have been developing multiple methods to address this challenges. Some of the common techniques of reducing the cogging torque/torque ripple is to use specific rotor design such as teeth notching, teeth chamfering, changing rotor pole arc width, rotor teeth axial pairing, rotor continuous or step skewing, and rotor pole shaping, which is shown in Figure 1.12 and Figure 1.13 [90], [91], [92], [93], [94], [95], [96], [97], [98], [99], [100], [101]. Other researchers use the harmonic current injection based control technique to compensate the torque ripple [102], [103], [104], [105]. It should be noted that the reduction of cogging torque usually is accompanied by the reduction of average torque. Optimization is needed to determine the most appropriate shape of the teeth that not only reduce the ripple percentage to an acceptable value but also maintain the average torque high enough. There might be occasions when multiple techniques are implemented simultaneously to achieve more effective torque ripple mitigation results. Multiple iterations of the machine design are expected to produce desirable torque properties.

Optimization is an effective analytical tool to maximize single or multiple performance objectives of flux-switching machines under certain design constraints. Optimization has been intensively implemented in other machine types, and there are research papers just dedicated to this subject. There is also some paper dedicated to discussing the optimization aspects of FSPM machine design using methods such as genetic algorithms, response surface methods, etc [106],

[107], [108], [109]. Optimization can be implemented in a variety of ways either from analytical-based or FEA-based techniques.

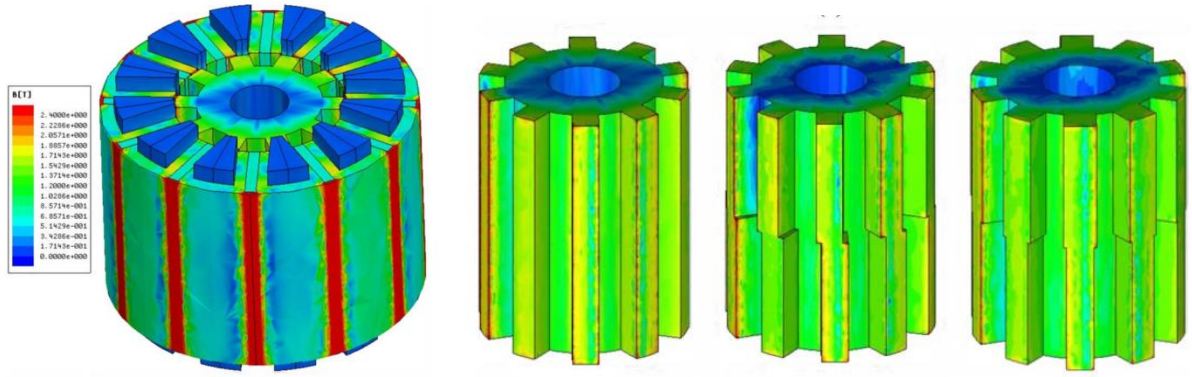

(a) (b) (c) (d)

Figure 1.12. Flux-switching permanent machine with three different rotor configurations for torque ripple minimization, (a) 12/10 FSPM machine topology, (b) rotor with uniform design, (c) rotor with step skew, (d) rotor with axial-pairing [92].

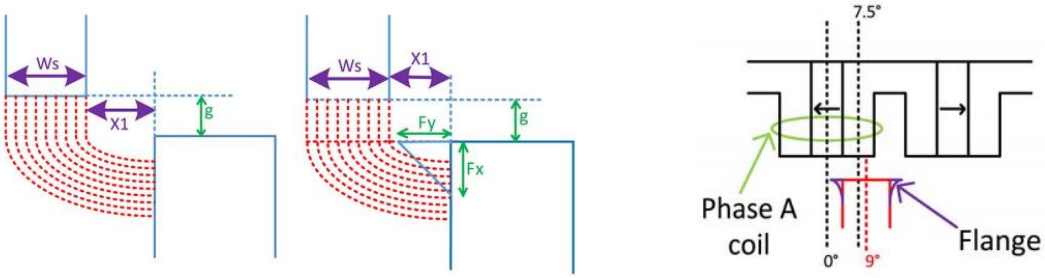

(a) (b) (c)

Figure 1.13. Flux-switching machine with flanged rotor design for torque ripple minimization, (a) simplified flux path without rotor flange, (b) simplified flux path with rotor flange, (c) rotor flange design for a 12/10 FSPM machine [101].

1.2.2 Stator Slot and Rotor Pole Combinations

The selection of appropriate stator slot/rotor pole combination of FSPM machine is critical to determining the output performance. Several researchers have reported investigations on this

aspect. The optimal stator slot/rotor pole combinations are systematically studied by Chen for both all poles wound and alternate poles wound FSPM machines [110], [111], [112], [113]. The feasible number of stator slots (N_s) and rotor poles (N_r) are determined based on the following two equations proposed in [111].

$$N_s = k_1 m, \qquad k_1 = 1,\ 2,\ \ldots \tag{1.1}$$

$$N_r = N_s \pm k_2, \qquad k_2 = 1,\ 2,\ \ldots \tag{1.2}$$

where m is the number of phases, k_1 and k_2 are integer numbers. It should be noted that k_1 is an integer number if m is an even number, and k_1 should be an even number if m is an odd number, because the number of stator slots should be an even number.

The number of stator slots and rotor poles should not be equal, and they can be different by multiple integer values. However, studies in [111] show that the number of stator slots and rotor poles should be close to each other to maximize the output torque, and this conclusion is similar to that of fractional-slot permanent magnet machines.

Different stator slot/rotor pole combinations for all poles wound (double layer) and alternate poles wound (single layer) configurations are studied. To include the basics, the winding factor (k_w) of a winding configuration is calculated by multiplication of distribution factor (k_d) and pitch factor (k_p). The distribution factor of the FSPM machine is calculated as,

$$k_d = \frac{\sin(qh\alpha/2)}{q\sin(h\alpha/2)} \tag{1.3}$$

where q is the number of least EMF vectors per phase winding, h is the harmonic order number, and α is the electric angle between two adjacent EMF vectors.

The pitch factor of the FSPM machine is calculated by first determining the electric angular difference between two adjacent EMF vectors, which is calculated as,

$$\theta_c = 2\pi h \left| \frac{N_r}{N_s} - 1 \right| \tag{1.4}$$

So the coil pitch factor of the h^{th} harmonic component is calculated as,

$$k_p = \cos\frac{\theta_c}{2} = \cos\left[\theta h \left(\frac{N_r}{N_s} - 1 \right) \right] \tag{1.5}$$

Therefore, the winding factor is calculated as,

$$k_w = k_d k_p \tag{1.6}$$

The different combinations are differentiated by the winding factors which are recorded in the tables. The investigated FSPM machine combinations of 2-phase, 3-phase, 4-phase, 5-phase, and 6-phase are shown in TABLE 1.2(A) to (E) respectively. Different combinations are also separately studied for all poles wound and alternate poles wound winding configurations. Since the number of stator slots and rotor poles should be similar, their difference is limited to 1 and 2.

It is observed in the table that if the number of stator slot and rotor pole is differed by 1, the all poles wound configuration applies to all the stator slot/rotor pole combinations, while the alternate poles wound configuration is only applicable to a few stator slot/rotor pole combinations. When the difference between the number of stator slot and rotor pole is 2, there are less feasible combinations for 2-phase, 4-phase, and 6-phase FSPM machines.

TABLE 1.2. WINDING FACTOR FOR KEY STATOR SLOT/ROTOR POLE COMBINATIONS IN MULTIPHASE FSPM MACHINES [111].

(A) 2-Phase

N_s=2km	$N_r = N_s \pm 1$							$N_r = N_s \pm 2$						
	N_r	All poles wound			Alternate poles wound			N_r	All poles wound			Alternate poles wound		
		k_d	k_p	k_w	k_d	k_p	k_w		k_d	k_p	k_w	k_d	k_p	k_w
4	3	1	0.71	0.71	--	--	--	--	--	--	--	--	--	--
	5	1	0.71	0.71	--	--	--	--	--	--	--	--	--	--
8	7	0.92	0.92	0.85	1	0.92	0.92	6	1	0.71	0.71	--	--	--
	9	0.92	0.92	0.85	1	0.92	0.92	10	1	0.71	0.71	--	--	--
12	11	0.91	0.97	0.88	--	--	--	--	--	--	--	--	--	--
	13	0.91	0.97	0.88	--	--	--	--	--	--	--	--	--	--
16	15	0.91	0.98	0.89	0.92	0.98	0.90	14	0.92	0.92	0.85	1	0.92	0.92
	17	0.91	0.98	0.89	0.92	0.98	0.90	18	0.92	0.92	0.85	1	0.92	0.92
20	19	0.90	0.99	0.89	--	--	--	--	--	--	--	--	--	--
	21	0.90	0.99	0.89	--	--	--	--	--	--	--	--	--	--
24	23	0.90	0.99	0.89	0.91	0.99	0.90	22	0.91	0.97	0.88	--	--	--
	25	0.90	0.99	0.89	0.91	0.99	0.90	26	0.91	0.97	0.88	--	--	--

(B) 3-Phase

N_s=2km	$N_r = N_s \pm 1$							$N_r = N_s \pm 2$						
	N_r	All poles wound			Alternate poles wound			N_r	All poles wound			Alternate poles wound		
		k_d	k_p	k_w	k_d	k_p	k_w		k_d	k_p	k_w	k_d	k_p	k_w
6	5	1	0.87	0.87	1	0.87	0.87	4	1	0.50	0.50	1	0.50	0.50
	7	1	0.87	0.87	1	0.87	0.87	8	1	0.50	0.50	1	0.50	0.50
12	11	0.97	0.97	0.94	1	0.97	0.97	10	1	0.87	0.87	1	0.87	0.87
	13	0.97	0.97	0.94	1	0.97	0.97	14	1	0.87	0.87	1	0.87	0.87
18	17	0.96	0.98	0.94	0.96	0.98	0.94	16	0.96	0.94	0.90	0.96	0.94	0.90
	19	0.96	0.98	0.94	0.96	0.98	0.94	20	0.96	0.94	0.90	0.96	0.94	0.90
24	23	0.96	0.99	0.95	0.97	0.99	0.96	22	0.97	0.97	0.94	1	0.97	0.97
	25	0.96	0.99	0.95	0.97	0.99	0.96	26	0.97	0.97	0.94	1	0.97	0.97

(C) 4-Phase

N_s=2km	$N_r = N_s \pm 1$							$N_r = N_s \pm 2$						
	N_r	All poles wound			Alternate poles wound			N_r	All poles wound			Alternate poles wound		
		k_d	k_p	k_w	k_d	k_p	k_w		k_d	k_p	k_w	k_d	k_p	k_w
4	3	1	0.71	0.71	--	--	--	--	--	--	--	--	--	--
	5	1	0.71	0.71	--	--	--	--	--	--	--	--	--	--
8	7	0.92	0.92	0.85	1	0.92	0.92	6	1	0.71	0.71	--	--	--
	9	0.92	0.92	0.85	1	0.92	0.92	10	1	0.71	0.71	--	--	--
12	11	0.91	0.97	0.88	--	--	--	--	--	--	--	--	--	--
	13	0.91	0.97	0.88	--	--	--	--	--	--	--	--	--	--
16	15	0.91	0.98	0.89	0.92	0.98	0.90	14	0.92	0.92	0.85	1	0.92	0.92
	17	0.91	0.98	0.89	0.92	0.98	0.90	18	0.92	0.92	0.85	1	0.92	0.92
20	19	0.90	0.99	0.89	--	--	--	--	--	--	--	--	--	--
	21	0.90	0.99	0.89	--	--	--	--	--	--	--	--	--	--
24	23	0.90	0.99	0.89	0.91	0.99	0.90	22	0.91	0.97	0.88	--	--	--
	25	0.90	0.99	0.89	0.91	0.99	0.90	26	0.91	0.97	0.88	--	--	--

(D) 5-Phase

N_s=2km	$N_r = N_s \pm 1$							$N_r = N_s \pm 2$						
	N_r	All poles wound			Alternate poles wound			N_r	All poles wound			Alternate poles wound		
		k_d	k_p	k_w	k_d	k_p	k_w		k_d	k_p	k_w	k_d	k_p	k_w
10	9	1	0.95	0.95	1	0.95	0.95	8	1	0.81	0.81	1	0.81	0.81
	11	1	0.95	0.95	1	0.95	0.95	12	1	0.81	0.81	1	0.81	0.81
20	19	0.99	0.99	0.98	1	0.99	0.99	18	1	0.95	0.95	1	0.95	0.95
	21	0.99	0.99	0.98	1	0.99	0.99	22	1	0.95	0.95	1	0.95	0.95
30	29	0.99	0.99	0.98	0.99	0.99	0.98	28	0.99	0.98	0.97	0.99	0.98	0.97
	31	0.99	0.99	0.98	0.99	0.99	0.98	32	0.99	0.98	0.97	0.99	0.98	0.97
40	39	0.98	1	0.98	0.99	1	0.99	38	0.99	0.99	0.98	1	0.99	0.99
	41	0.98	1	0.98	0.99	1	0.99	42	0.99	0.99	0.98	1	0.99	0.99

(E) 6-Phase

N_s=2km	$N_r = N_s \pm 1$							$N_r = N_s \pm 2$						
	N_r	All poles wound			Alternate poles wound			N_r	All poles wound			Alternate poles wound		
		k_d	k_p	k_w	k_d	k_p	k_w		k_d	k_p	k_w	k_d	k_p	k_w
6	5	1	0.87	0.87	--	--	--	4	1	0.50	0.50	--	--	--
	7	1	0.87	0.87	--	--	--	8	1	0.50	0.50	--	--	--
12	11	0.97	0.97	0.94	1	0.97	0.97	10	1	0.87	0.87	1	0.87	0.87
	13	0.97	0.97	0.94	1	0.97	0.97	14	1	0.87	0.87	1	0.87	0.87
18	17	0.96	0.98	0.94	--	--	--	16	0.96	0.94	0.90	--	--	--
	19	0.96	0.98	0.94	--	--	--	20	0.96	0.94	0.90	--	--	--
24	23	0.96	0.99	0.95	0.97	0.99	0.96	22	0.97	0.97	0.94	1	0.97	0.97
	25	0.96	0.99	0.95	0.97	0.99	0.96	26	0.97	0.97	0.94	1	0.97	0.97
30	29	0.96	0.99	0.95	--	--	--	28	0.96	0.98	0.94	--	--	--
	31	0.96	0.99	0.95	--	--	--	32	0.96	0.98	0.94	--	--	--
36	35	0.96	1	0.96	0.96	1	0.96	34	0.96	0.98	0.94	0.96	0.98	0.94
	37	0.96	1	0.96	0.96	1	0.96	38	0.96	0.98	0.94	0.96	0.98	0.94

It is easy to notice that when the number of stator slot increases, the winding factor has a trend to increase progressively close to 1. It is desirable to have a high value of winding factor to improve the torque production capability of the machine, but this means that FSPM machines with a large number of stator slot/rotor poles will be possibly selected. For high rotational speed operations, the fundamental frequency required by the high pole count FSPM machines are more challenging to be satisfied. Therefore, the feasible combinations with a small number of rotor poles are focused in this investigation.

One important feature of flux-switching machine identified in the literature [63] is that the flux linkage in each coil is asymmetric, with odd and even harmonics. However, the total phase open circuit flux linkage or back-EMF can still be symmetrical without even harmonics if the combination of slot/pole is appropriately chosen. This is because there are diametrically placed

coils in the same phase that cancel the even harmonics. The slot/pole combinations for symmetrical back-EMF without even harmonics are summarized in [111].

If the flux-switching machine has double-layer windings (all-poles-wound), the condition to yield symmetrical back-EMF is that the slot/pole combination satisfies the following equations. The HCF in the equation means the highest common factor.

When the number of phases (m) is an odd number or 2,

$$\frac{N_s}{HCF(N_s \ and \ N_r)} = 2jm, \qquad j = 1,\ 2,\ 3... \tag{1.7}$$

When the number of phases (m) is an even number excluding 2, both the number of stator slots (N_s) and the number of rotor poles (N_r) should be even numbers,

$$\frac{N_s/2}{HCF(N_s/2 \ and \ N_r/2)} = jm, \qquad j = 1,\ 2,\ 3... \tag{1.8}$$

If the flux-switching machine has single-layer winding (alternate-pole-wound), the relationship to achieve symmetrical and balanced back-EMF is modified as follows.

When the number of phases (m) is an odd number or 2,

$$\frac{N_s}{HCF(N_s \ and \ N_r)} = 4jm, \qquad j = 1,\ 2,\ 3... \tag{1.9}$$

When the number of phases (m) is an even number excluding 2,

$$\frac{N_s/2}{HCF(N_s/2 \ and \ N_r/2)} = 2jm, \qquad j = 1,\ 2,\ 3... \tag{1.10}$$

The asymmetrical back-EMF in the FSPM machines should be avoided in general to prevent large harmonic distortions in the voltage, current, and potential high torque ripple. The conventional 12/10 FSPM topology has symmetrical and balanced back-EMF.

The rotor poles of FSPM machines have salient structure, each of which produces electromagnetic forces by the interaction with stator teeth. It is desirable to have a rotor structure where all the radial forces on the rotor pole are compensated so that the net radial forces on the rotor is ideally zero. This is beneficial to reduce the stress of shaft and bearings, reduce the potential vibration and noise, and extend the life of the electric machine. However, there are certain stator slot/rotor pole combinations that have non-zero net radial forces on the rotor, which is named unbalanced magnetic forces (UMF).

The comparison of all- and alternate-poles-wound FSPM machines are discussed by Chen for various aspects including the torque properties and unbalanced magnetic forces [114], [115]. It is observed that the topologies with an odd number of rotor poles have UMF. The analytical calculation of the UMF components is derived based on the flux density distribution in the airgap as follows,

$$F_{mx} = \frac{rl_a}{2\mu_0}\int_0^{2\pi}[(B_c^2 - B_r^2)\cos\theta + 2B_r B_c \sin\theta]d\theta\,, \tag{1.11}$$

$$F_{my} = \frac{rl_a}{2\mu_0}\int_0^{2\pi}[(B_c^2 - B_r^2)\cos\theta - 2B_r B_c \sin\theta]d\theta \tag{1.12}$$

where F_{mx} and F_{my} are the two orthogonal components of the UMF, r is the radius of the airgap, l_a is the axial length of the machine, μ_0 is the permeability of free space, B_c and B_r are the circumferential and radial component of the airgap flux density.

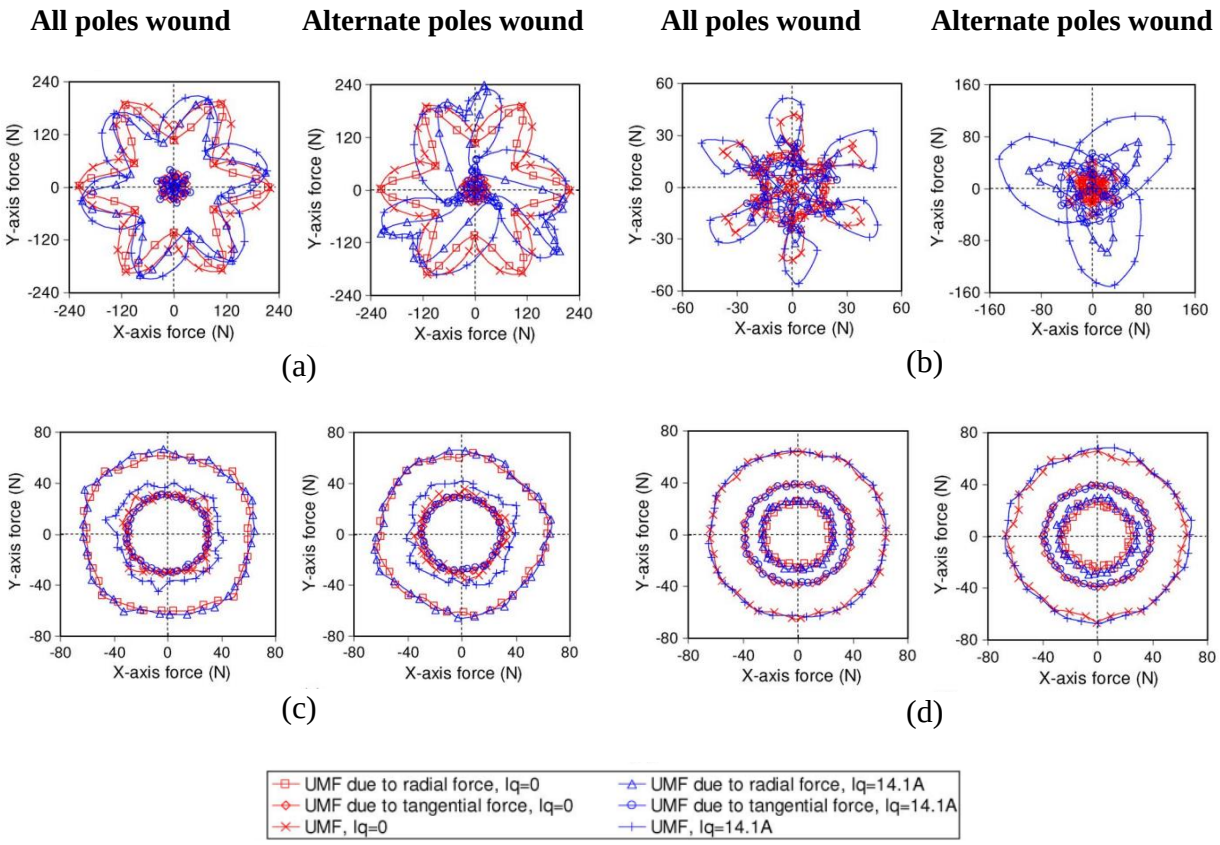

Figure 1.14. Unbalanced magnetic forces in FSPM machines (a) 6/5 FSPM machine, (b) 6/7 FSPM machine, (c) 12/11 FSPM machine, (d) 12/13 FSPM machine [115].

From the feasible stator slot/rotor pole combinations of three phase FSPM machines, the topologies with an odd number of rotor poles have UMF on the rotor. To quantify the UMF properties of the 6/5, 6/7, 12/11, and 12/13 combinations of FSPM machine, the UMF of both the all-pole-wound and alternate-pole-wound configurations are calculated and presented in a 2-dimentional diagram as shown in Figure 1.14. The UMFs due to radial force, tangential force, and both forces are studied at open circuit and loaded conditions. The pattern of the UMF in the 2-dimentional diagram depends on the actual design. The optimization of rotor pole number is

studied for the C-core FSPM machine by Chen, and the results show that the C-core 6/13 FSPM machine also has UMF on the rotor [116].

For the most commonly used stator slot/rotor pole combinations of the three phase FSPM machines, the unbalanced back-EMF (UBEMF) and unbalanced magnetic force (UMF) are evaluated for each of the combinations as shown in TABLE 1.3. It is seen that the 12/10, 12/14, 24/22, and 24/26 combinations with all poles wound have neither UBEMF nor UMF. These topologies are given higher priority to consider in the topology selection stage. However, for high rotational speed machine, topologies with a lower number of rotor poles need to be considered. If the number of stator slots was chosen as the minimum value of 6 for the three-phase topology, the rotor pole number could be chosen from either 4, 5, 7, or 8. Nevertheless, all these rotor pole options have either UBEMF or UMF or both. It should be noted that combinations with odd number of rotor poles are avoided due to the complication of UMF that increases mechanical stress and reduce the life of the FSPM machines.

TABLE 1.3. UNBALANCED BACK-EMF AND UNBALANCED MAGNETIC FORCES OF DIFFERENT STATOR SLOT/ROTOR POLE COMBINATIONS OF THREE PHASE FSPM MACHINES.

N_s=2km	$N_r = N_s \pm 1$					$N_r = N_s \pm 2$				
	N_r	All poles wound		Alternate poles wound		N_r	All poles wound		Alternate poles wound	
		UBEMF	UMF	UBEMF	UMF		UBEMF	UMF	UBEMF	UMF
6	5	No	Yes	Yes	Yes	4	Yes	No	Yes	No
	7	No	Yes	Yes	Yes	8	Yes	No	Yes	No
12	11	No	Yes	No	Yes	10	No	No	Yes	No
	13	No	Yes	No	Yes	14	No	No	Yes	No
18	17	No	Yes	Yes	Yes	16	Yes	No	Yes	No
	19	No	Yes	Yes	Yes	20	Yes	No	Yes	No
24	23	No	Yes	No	Yes	22	No	No	No	No
	25	No	Yes	No	Yes	26	No	No	No	No

UBEMF: Unbalanced back-EMF
UMF: Unbalanced magnetic force

In the literature, there are a few papers present the studies of the selection of slot/pole combinations and their performance comparisons. Study of 6/5 and 12/10 FSPM machine are conducted for the flux-weakening capability analysis by Wang and results shows 6/5 topology has higher flux-weakening capability [117]. Modular alternate poles-wound FSPM machines are studied and experimentally verified by Owen, and the 14-pole rotor can be used in conventional two alternate pole-wound topologies to increase output torque, reduce torque ripple, and back-EMF asymmetry without rotor skewing [118]. Alternative FSPM machine topologies with reduced stator slot number without UMF are investigated, and the low-pole topology with five rotor poles is studied [119]. The UMF issue still exists for the 6/5 topology. The torque-speed curves for various FSPM machines with 12 stator slots 10-pole, 13-pole, 14-poles are compared by Zhu with C-core, E-core, and multi-tooth topologies [120]. Infinite speed range is found for multi-tooth, E-core, and C-core machines. The E-core achieves the maximum torque per ampere while the multi-tooth is lowest.

1.3 Developed Flux-Switching Machine Topologies

One of the most active research areas of the FSPM machine is the invention of new topologies. Ever since the introduction of three-phase 12/10 FSPM machine, the flux-switching machine family has been growing very rapidly with emerging new topologies. Once the fundamental operation principle of the flux-switching machine is understood, multiple degrees of freedom in the geometry can be manipulated to create new topologies. Some novel flux-switching machine topologies are created by modifying the stator structure, while some are created by modifying the rotor structure, or both stator and rotor structures. The evolution and development

of new flux-switching machine topologies are the focus of this section. To simplify the discussion of this section, reviews are done by categorizing the novel flux-switching machine topologies into novel stator structure, novel rotor structure, and novel stator and rotor structures.

1.3.1 Topologies with Modified Stator Structures

A novel flux-switching PM machine with half the number of stator slots as the conventional 12/10 FSPM is proposed by Chen and Zhu, and the name is called C-core FSPM machine [53], [116]. By reducing the number of stator slots to half of the original design, the volume of the permanent magnets is decreased, and there is more slot area for additional windings to increase the electrical loading. One of the designs of C-core FSPM machine is shown in Figure 1.15. The configuration of 12/10, 12/11, 12/13, and 12/14 are feasible for C-core FSPM machine, but all of them have either unbalanced back-EMF or unbalanced magnetic forces.

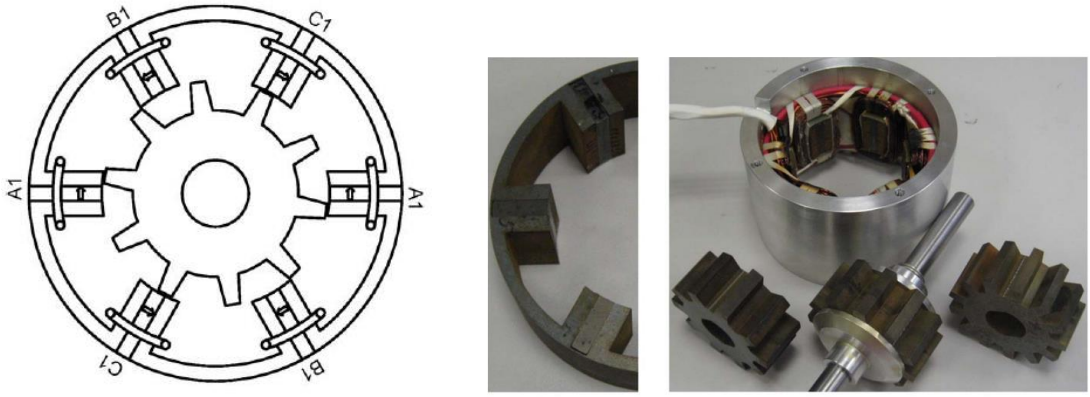

Figure 1.15. C-core flux-switching PM machine and one prototype [53], [116].

An E-core FSPM machine has been proposed by Chen for the benefits of reduced magnet volume and cost, and improved torque density as shown in Figure 1.16 [121]. An analytical method

is derived to identify the optimal stator slot/rotor pole combinations. When the stator slot number if fixed at 6, four topologies with different rotor pole numbers are compared. The results show that combinations with 11 and 13 rotor poles have symmetrical back-EMF, while combinations with 10 and 14 rotor poles do not. The optimized rotor-pole-width-to-rotor-pole-pitch ratio is approximately the same around 1/3. The combination with 11 rotor poles achieves the highest torque density. The E-core FSPM machine exhibits around 15% higher torque density but only requires half of the permanent magnets of conventional 12/10 FSPM machine.

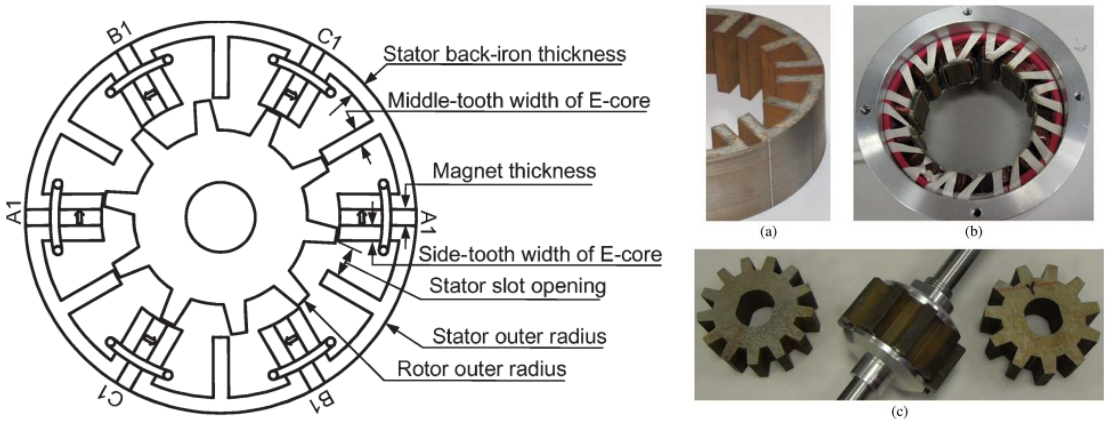

Figure 1.16. E-core flux-switching PM machine and one prototype [121].

The FSPM machine with multi-tooth topology was first proposed by Zhu and Chen for high-torque direct-drive applications [122], [123], [124]. The proposed multi-tooth topology has half the magnet volume as the conventional 12/10 FSPM machine topology, and one stator tooth is divided into two smaller teeth segments. To accommodate the change in stator tooth number, the number of rotor poles is increased to 19 as shown in Figure 1.17. Comparison results prove

that multi-tooth FSPM machine achieves about 40% increased magnitude in back-EMF than conventional 12/10 FSPM machine. The torque ripple is negligible compared to the 12/10 FSPM machine. This multi-tooth machine exhibits higher torque density with relatively low currents. One of the challenges for this topology is that the magnetic circuit saturates more easily as the current increases so that the armature reaction is higher than 12/10 FSPM machine.

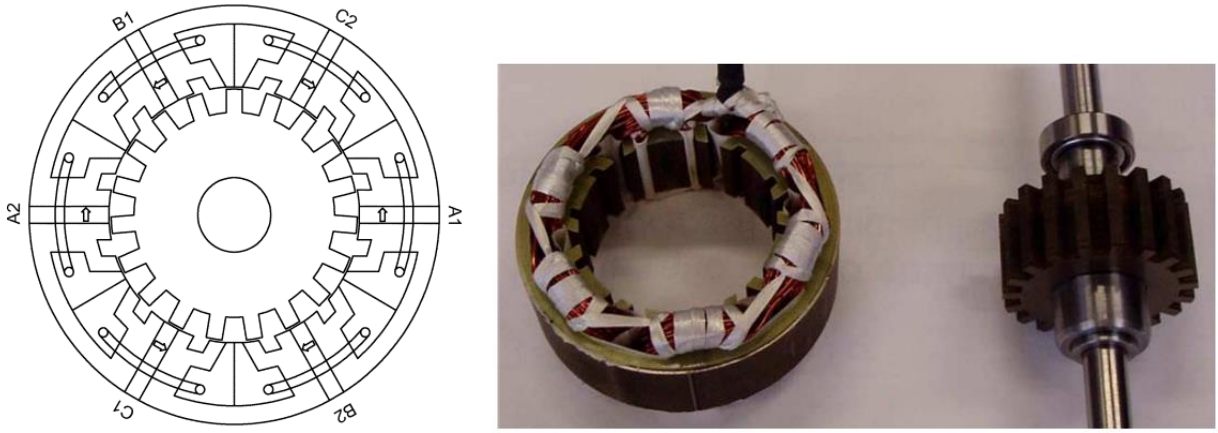

Figure 1.17. Multi-tooth flux-switching PM machine and one prototype [122].

One of the challenges of FSPM machine is that it requires a large volume of permanent magnets in the stator. Previous structures including C-core, E-core, and multi-tooth topologies reduce the magnet consumption by half to reduce the magnet cost. To eliminate the magnets and further reduce the material cost, DC excited flux-switching machines are proposed. Design considerations of using DC field windings are explored by Tang for torque production, scalability issue, and aspect ratios [125], [126]. A cross-sectional view of the proposed DC-excited flux-switching machine is illustrated in Figure 1.18. One of the prominent benefits of using DC field excitation is being able to control the flux density in the airgap by changing the excitation status of the DC field windings, thus to have better flux control especially for the flux weakening

operation. The operating temperature of DC excited machine can be higher than conventional FSPM machine because there are no permanent magnets, whose performance is much more sensitive to temperature variations than copper windings. One of the tradeoffs of DC excited flux-switching machine is relatively low efficiency due to the additional copper loss from excitation windings.

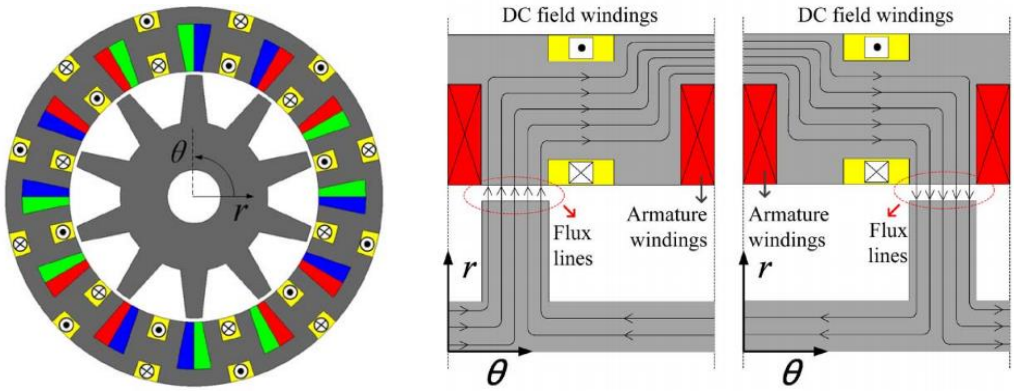

Figure 1.18. DC-excited flux-switching machine with 10 rotor poles [125].

Low-cost DC excited flux-switching machines with 12 stator slots are compared with FSPM machines using both NdFeB and ferrite magnets [127]. The results show that the DC excited machine has less torque density than NdFeB or even ferrite typed FSPM machine. The design of slot areas for field winding and armature windings should be carefully considered to increase the torque density. Zhou compared three types of low-cost wound-field flux-switching machines having the same coil-pitch of 1 slot-pitch (12/8), 2 slot-pitches (12/5, 12/7), and different coil-pitches (9/5) individually [128]. Choosing the slot/pole combination of 9/5 achieves the maximum torque density than conventional 12/8 segmented rotor pole machine and 12/5 machine. However, the 12/7 machine has even higher torque density and lower ripple than the 9/5 configuration.

Single-phase wound-field flux-switching machines with different coil-pitches and various rotor poles are studied by Zhou [129], [130]. One of the prototype machines is shown in Figure 1.19. The field winding topology with 6 poles has similar average torque but shorter end windings and better efficiency. The single-phase topology proposed in this paper with only 3 poles is beneficial to significant reduction of iron losses.

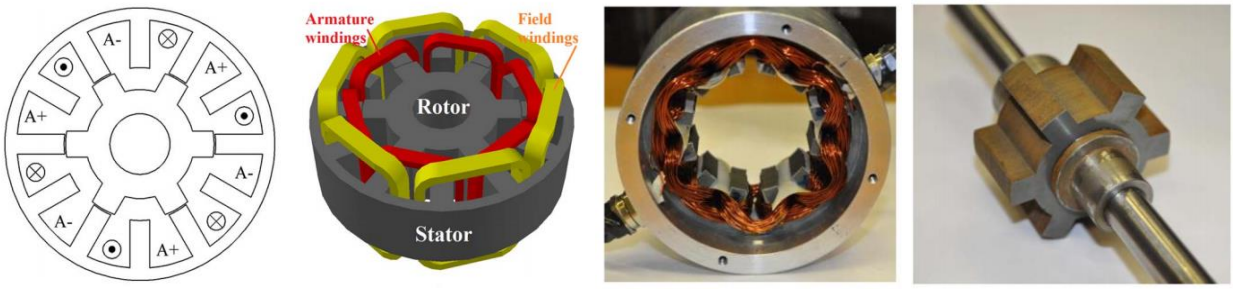

Figure 1.19. Single-phase 12-slot 6-pole wound-field flux-switching machine with prototype [129].

Both permanent magnets and DC field windings can be used to create hybrid excited flux-switching machines, which utilize the high torque density and high-efficiency benefits of PM materials but also has flux regulation capability enabled by the field windings. The hybrid excited design of flux-switching machines has been a popular area for the research study. Hoang proposed a hybrid excited poly-phase FSPM machine and experimentally verified the effects of lamination material on performance. A hybrid excited flux-switching machine designed for the hybrid (electric) vehicle is studied [131], [132], [133]. Hua investigated a novel hybrid excited flux-switching machine design for traction application whose topology is shown in Figure 1.20 [134]. He also analyzed the flux-regulation theory and capability of the hybrid-excited FSPM machine [135]. The effects of placing permanent magnets in different locations in the stator are studied

[136], [137], and the analytical model of the hybrid excitation principle is built [138]. An improved hybrid-excited flux-switching machine is proposed by Zhang to enhance the flux regulation capability and improve the output torque [139]. The over-saturation effect is studied and the stator-tooth-width coefficient is defined to evaluate the performance [140]. Several hybrid-excited flux-switching machine topologies are compared by Wang with a particular focus on a parallel hybrid excited topology [141], [142]. Owen, Chen, Sulaiman, and Gaussens proposed their own design of hybrid-excited topologies that are mainly targeted for HEV/EV application [143], [144], [145], [146], [147], [148], [149], [150], [151], [152]. An outer rotor hybrid-excited flux-switching machine is proposed for direct drive EV application with high torque density property [153].

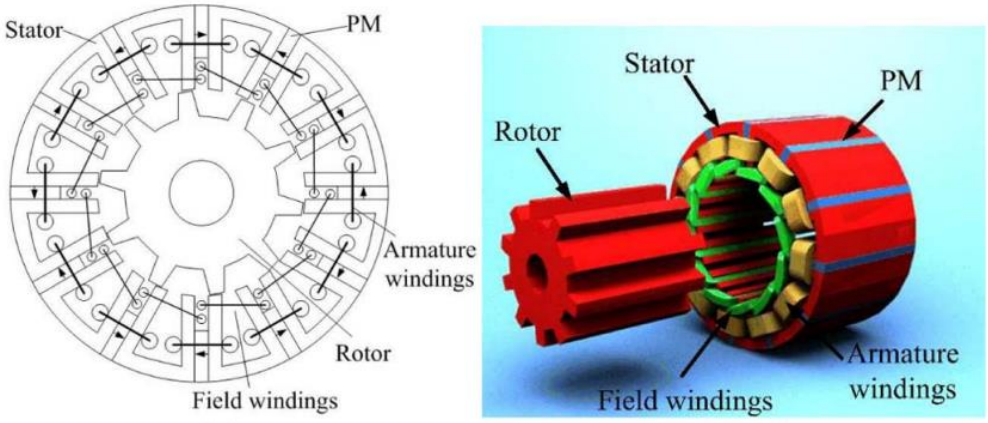

Figure 1.20. One topology of the hybrid-excited flux-switching machine [134].

One modification of FSPM machine is to use sandwiched permanent magnet topology as proposed by Mo [154]. The advantage of this topology is to greatly increase the flux linkage and back-EMF compared to the conventional 12/10 FSPM machine topology. The output torque and

PM usage efficiency are significantly enhanced. However, the torque ripple is higher than the conventional 12/10 topology, so it needs to be mitigated using various torque ripple minimization techniques. A novel sandwiched FSPM machine using V-shaped magnets shown in Figure 1.21 is studied by Zhou to show that average torque is increased by 13.8% under the same copper loss [155]. The PM volume is decreased by 4%, and the PM usage efficiency is increased by 18.5%. Stepped skewing is implemented to reduce the torque ripple. McFarland also investigated the V-shape sandwiched FSPM machine but using ferrite magnets instead of NdFeB magnets [241]. This machine is compared with the IPM machine using also ferrite magnets, and the results show the sandwiched FSPM machine has significant efficiency improvement over the IPM machine over a large operating range. The sandwiched FSPM machine topology is desirable if better rotor mechanical integrity justifies the increased cost due to more PM materials. Several reduced rare-earth or non-rare-earth flux-switching machines are investigated by Raminosoa for traction applications to meet the U.S DRIVE 2020 specifications [156], [157]. The prototype designs satisfy the requirements with slight margins. One of the challenges identified with the proposed FSPM machine topologies are the required high fundamental frequency for the high-pole-count machine, and aggressive methods should be used to minimize the loss to satisfy the efficiency requirement.

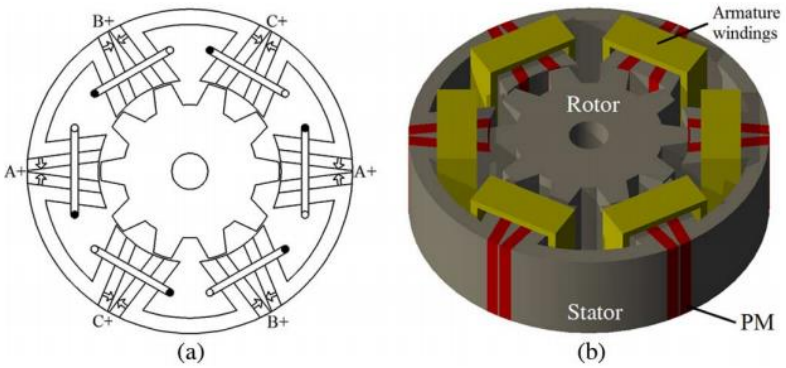

Figure 1.21. V-shaped sandwiched flux-switching PM machine [155].

The concept of memory electric machines is not entirely new. The application to the FSPM machine is a reasonable progression to utilize the advantages of this concept. A study on proposed two memory FSPM machines employing two types of permanent magnets (NdFeB and low coercive force magnets) was done by Yang [158], [159], [160]. The design has desirable magnet flux adjustability and high torque-density. There is also high armature demagnetization withstand capability shown in this topology. The memory FSPM machine is very suitable for applications in hybrid electric vehicles such as in the integrated-starter-generator, or for traction motors [161], [162]. The memory FSPM machine shown in Figure 1.22 is demonstrated to have better efficiency over IPM machine in the traction application [163]. An external rotor memory FSPM machine is proposed by Wu also using hybrid permanent magnets [164]. Another memory machine are also investigated by the same author [165], [166].

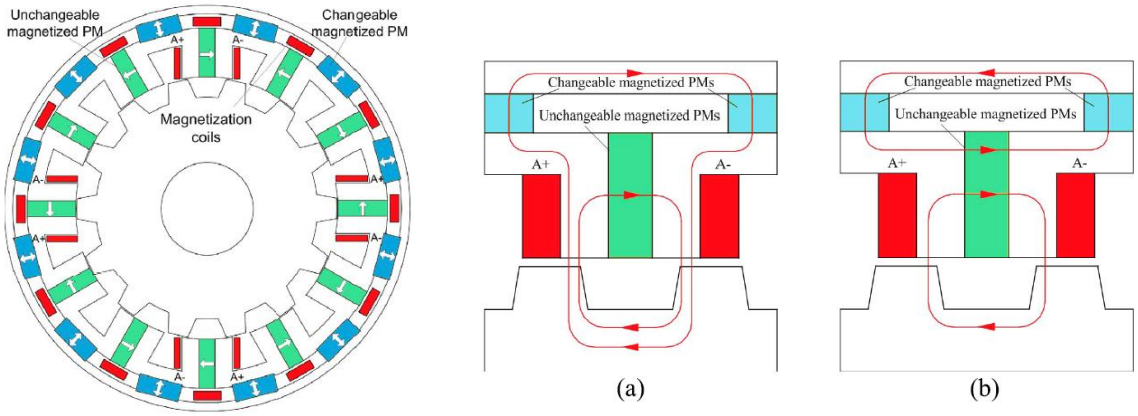

Figure 1.22. Flux-switching memory PM machine with illustration of flux regulation principle [163].

The FSPM machine has circumferentially magnetized permanent magnets that have leakage in the stator outer periphery. This property offers opportunities for variable flux control of FSPM machine by using external magnetic devices to guide the magnetic flux and change the flux linkage in the windings. Owen and Zhu proposed a novel method of using magnetic mechanical adjustors which are positioned on the stator outer surface to shunt the magnetic flux from the permanent magnets and reduce the main flux linkage [167], [168], [169], [170]. The magnetic mechanical flux adjusters can be placed in all the stator poles or alternate stator poles as shown in Figure 1.23. Alternative shapes of mechanical adjustors are compared to show that they all achieve better flux weakening performance. The improved flux regulation capability by using mechanical adjustors is beneficial to extending the constant power speed ratio of FSPM machine for applications that need flux weakening operation, on the condition that the mechanical devices are robust and reliable enough. However, the integrity of the mechanical devices deteriorates at

excessive friction during cycle operations. More investigation is necessary to justify the practicality of this method.

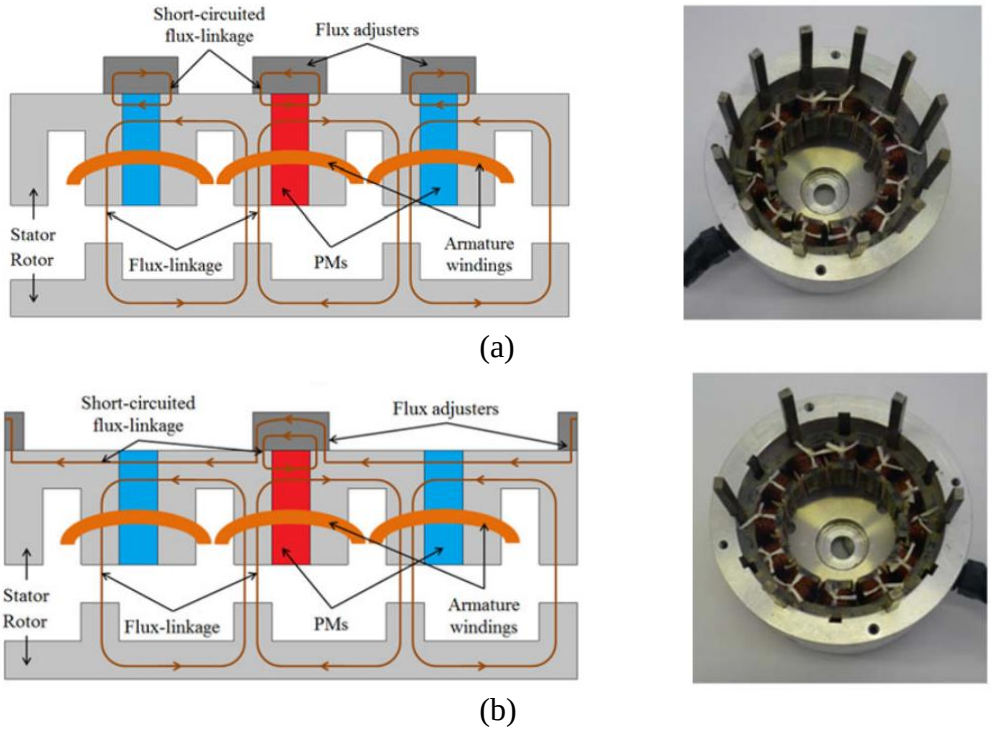

Figure 1.23. Flux-switching PM machine with adjustable mechanical adjustors for improved flux weakening capability, (a) flux adjustors are in all stator poles, (b) flux adjustors in alternate stator poles [170].

For flux-switching machines to operate reliably in critical applications, the fault tolerant aspects should be investigated to ensure that the machine would not fail under harsh environment. The multi-phase structure is commonly used in the fault-tolerant electric machines to introduce redundancy in the windings and provide backups when part of the phases fails. Various multi-phase FSPM machines designed for aerospace applications are studied to show the benefits of improved torque density [171], [172]. The design of five-phase FSPM machine is popular in the literature and couple of authors implemented the optimization to improve the performance [173],

[174], [175]. Other researchers focused on the fault diagnosis and redundant operation of the FSPM machine by using modular structure, stator-flux-oriented control, and second harmonic current injection control [176], [177], [178], [179], [180], [181], [182]. Linear fault-tolerant FSPM machine is also investigated [183], [184]. Fault diagnosis by measuring vibration is studied in [185]. A dual FSPM machine fault-tolerant control is proposed in [186]. Raminosoa systematically studied the fault-tolerant design aspects of FSPM machine, and compared its performance with the surface PM machine [187], [188]. Novel fault tolerant design and winding technology are studied for the FSPM machine [189], [190]. Li studied the double and single layers in the FSPM machine and the thermal-electromagnetic performances for critical applications [191], [192], [193].

1.3.2 Topologies with Modified Rotor Structures

The rotor of conventional FSPM machine has bi-directional magnetic flux, and the iron loss in the rotor can be comparable to the stator iron loss. To reduce the iron loss in the rotor, a segmented rotor structure was proposed by Thomas based on the 12/10 topology shown in Figure 1.24 [194]. The rotor is segmented into 5 pieces which is connected by non-magnetic materials. The flux path of the segmented rotor structure is shorter than conventional FSPM machine design and the iron loss can be reduced. The isolation of the flux path also provides fault tolerance in reducing the mutual flux coupling between phases. The study found that the iron loss is reduced by 13% for the same nominal torque. The rotor mass is also reduced by 11%.

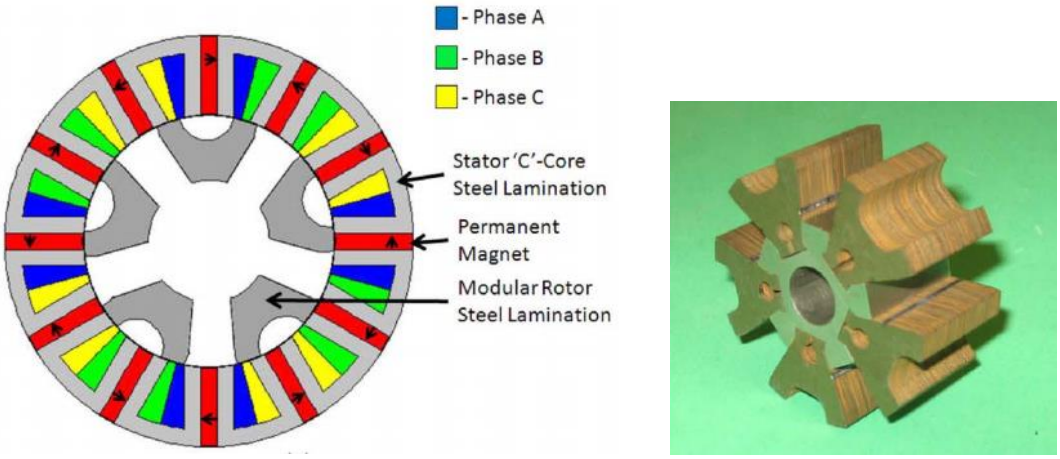

Figure 1.24. Flux-switching PM machine with modular rotor configuration [194].

Another interesting segmented rotor flux-switching machine was proposed by Zulu that has non-segmented stator structure [195]. The stator is not like a conventional FSPM machine, but is like a conventional synchronous PM machine, because the magnets are placed on the surface of the stator teeth. Several slot/pole combinations for this topology were investigated, and the 12/8 combination shows maximum torque density [196]. The proposed structure is applicable for flux-switching machines both using wound-field excitation as well as using PMs. The overall torque density is not as high as the conventional FSPM machine, but the consumption of PM is significantly less which reduces the cost by large amount [197], [198], [199], [200], [201]. A cross-sectional view and the operating principle to achieve bi-directional flux linkage is illustrated in Figure 1.25. One challenge for this segmented FSPM machine is the high torque ripple due to the interaction between segmented rotor pieces and the magnets on the surface of the stator teeth. More design and optimization effort is needed to reduce the high torque ripple for this topology as suggested by the author.

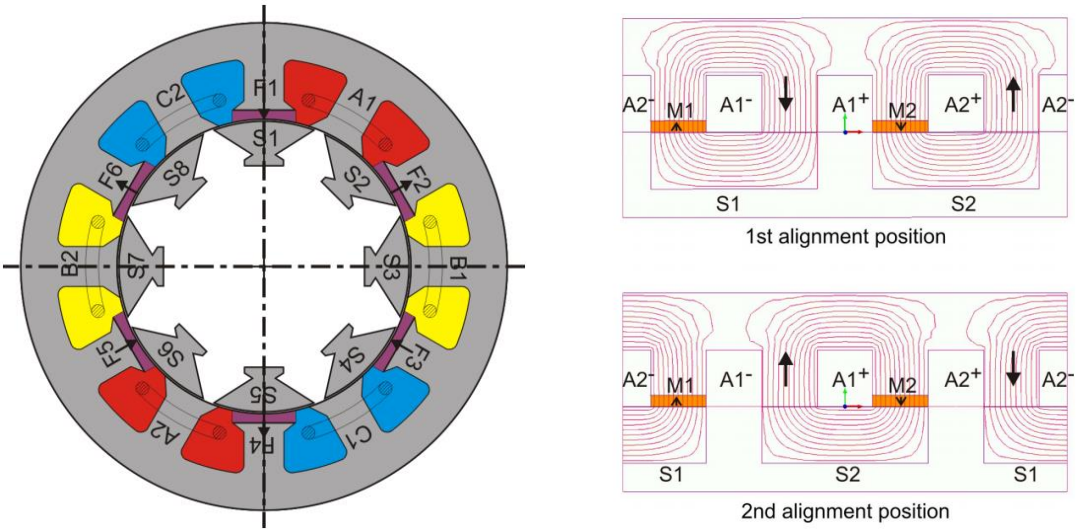

Figure 1.25. Segmented-rotor flux-switching PM machine with magnets on the surface of the tooth face, and illustration of operation principle for bi-directional flux linkage [200].

1.3.3 Topologies with Both Modified Stator and Rotor Structures

Typical FSPM machine has armature winding and permanent magnets both in the stator. One of the benefits of this structure is improved cooling for the magnets, but the downside is reduced slot area for the windings. To resolve the reduced slot area issue, a novel partitioned-stator FSPM machine is proposed by Evans such that the permanent magnets are removed from the stator teeth and placed on a secondary stator inside the rotor [202]. The concentrated coil windings are positioned in the outer stator part as shown in Figure 1.26. The operation principle of partitioned-stator FSPM machine is similar to the conventional FSPM machine.

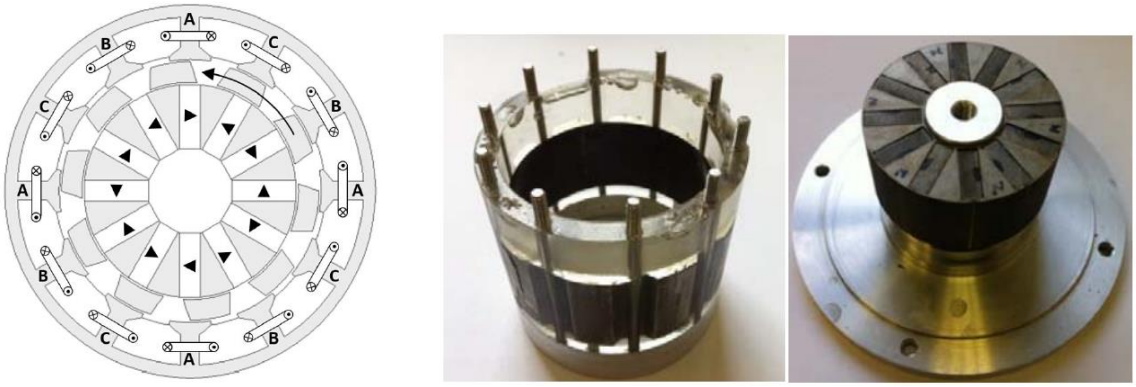

(a) (b) (c)

Figure 1.26. Partitioned-stator FSPM machine, (a) machine cross sectional view, (b) finished rotor after resin modeling, (c) inner side of the stator with permanent magnets [202].

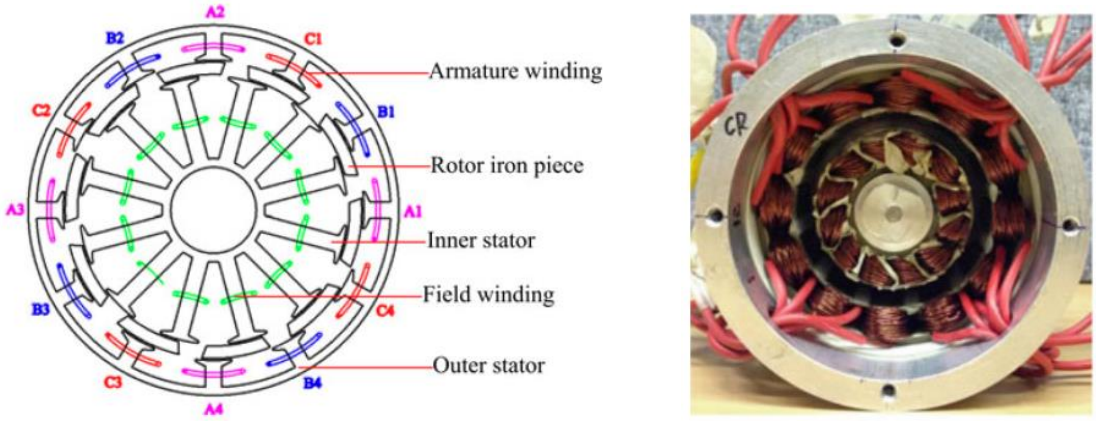

(a) (b)

Figure 1.27. Partitioned-stator flux-switching machine with field winding excitation, (a) machine cross sectional view, (b) one prototype [207].

The partitioned stator flux-switching machine can be applied to both single layer and double layer windings, which is analyzed by Awah to show they have higher torque density than the traditional structure. In addition, the single layer winding configuration has a better torque to PM volume ratio than the conventional structure [203], [204]. Wound field excitation concept is also applicable to the partitioned-stator flux-switching machine. The cross-sectional view of the

wound field partitioned-stator flux-switching machine and one of the prototype is presented in Figure 1.27. The hybrid excitation and axial flux version of the partitioned-stator flux-switching machines are also investigated by various researchers [205], [206], [207], [208]. The main advantages of the partitioned-stator flux-switching machines are the improved space utilization to accommodate more armature windings and to increase the average output torque. However, the rotor of the partitioned stator flux-switching machine is separated that non-magnetic materials such as resin should be used to connect the rotor pieces. The manufacturing of this structure is much more challenging not only due to the complex rotor assembling but also due to the difficulty to satisfy the tolerance requirement in both air gaps.

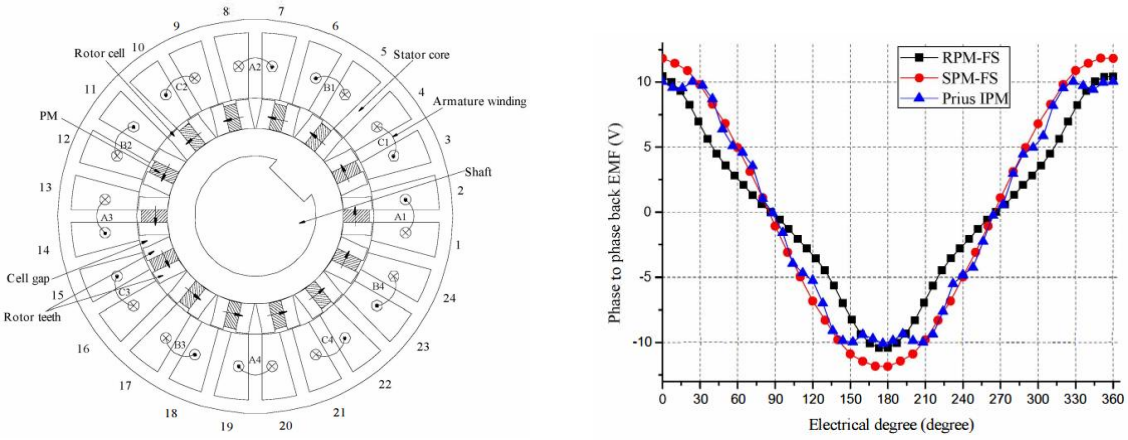

(a) (b)

Figure 1.28. Flux-switching machine with rotor-permanent magnet (RPM), (a) machine topology, (b) back-EMF comparison of RPM with stator-PM (SPM) flux-switching machine and Prius IPM machine [209].

Another new flux-switching machine with the permanent magnet in the rotor is proposed by Hua as shown in Figure 1.28 [209]. The magnets in the rotor are sandwiched by the steel pieces, and the magnetization directions for all the magnets are the same. The stator lamination is almost

the same as that of the conventional PM machine. There are more slot areas for the windings since the permanent magnets are in the rotor. However, this topology does not have the benefits of stationary PM as the conventional FSPM machines.

Flux-switching machine principle applies to linear machine configurations. The results studied in the rotational flux-switching machine can be readily applied to the linear machines [210], [211]. Wang studied a new method to reduce the detent force in the linear FSPM machine to improve the machine performance [212], [213], [214], [215]. Optimization and comparison of E-core and C-core linear FSPM machine are analyzed by Min [216]. A novel linear FSPM machine designed for wave energy extraction application is proposed by Huang [217]. Some of the new topologies such as double-sided linear FSPM machine, multi-tooth FSPM linear machine, modular linear FSPM machine for rail transit application, and hybrid excited linear FSPM machine are also proposed by the researchers [218], [219], [220], [221], [222], [223].

The axial flux FSPM machine can utilize the same principle developed from radial flux FSPM machines. Researchers have proposed multiple different topologies of axial field flux-switching machines including single-rotor-double-stator shown in Figure 1.29 and double-rotor-single-stator structures shown in Figure 1.30, [224], [225], [226], [227], [229], [230], [231]. One of the reasons to use double-sided stator or rotor structure in the axial field flux-switching machines is to balance the magnetic pull force generated on each side. Concepts such as hybrid excitation and others can be simply transferred to the axial flux machine design. The axial flux machine is suitable for low-speed high-torque applications such as the wind generator etc.

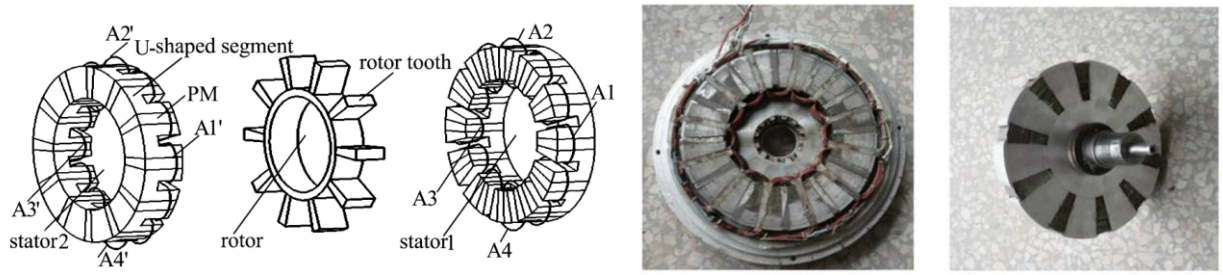

(a) (b)

Figure 1.29. Axial field flux-switching permanent magnet machine with two stators and one rotor, (a) topology illustration, (b) prototype stator and rotor [225].

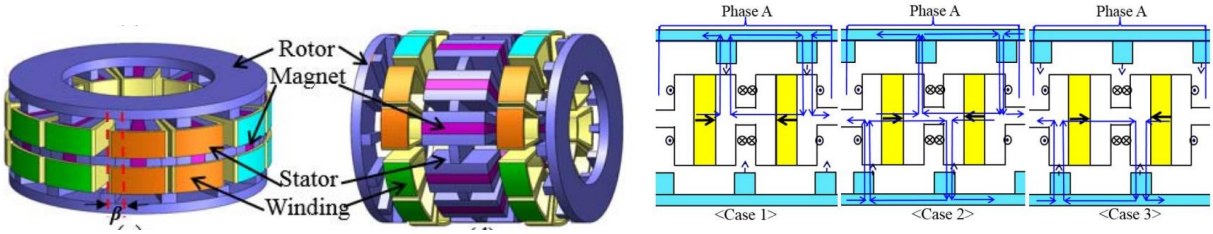

(a) (b)

Figure 1.30. Axial field flux-switching permanent magnet machine with one stator and two rotors, (a) topology illustration, (b) principle of operation [228].

The concept of transverse flux permanent magnet machine is integrated into an FSPM machine shown in [232]. A tubular FSPM machine is proposed for linear motion applications, and it achieved 10%-15% higher thrust force than a conventional winding FSPM machine [233]. Outer-rotor FSPM machines are designed for electric vehicle traction applications with an emphasis on the magnet design with iron bridges [234], [235].

A six-phase multi-tooth fault-tolerant FSPM machine designed with twisted rotor structure is shown in Figure 1.31. The rotor is divided into two parts which are offset by half electric cycle. The stator of the FSPM machine is also partitioned into two sections and the direction of the

magnets are opposite in the two stators [236]. The single layer winding configuration is used to create a physical separation between windings, but the asymmetrical back-EMF is introduced in the windings. The purpose to introduce twisted-rotor structure is to mitigate the asymmetrical back-EMF and improve the torque production capability without using skewing.

(a) (b) (c)

Figure 1.31. A six-phase multi-tooth fault-tolerant FSPM machine with twisted-rotor, (a) machine configuration, (b) prototype of the rotor, (c) prototype stator laminations [236].

1.4 Medium and High-Speed Design Aspects of Flux-Switching Machines

Upon the review of the recent developments of the flux-switching machine, it is demonstrated that flux-switching machine has desirable electromagnetic properties for high-power-density and high-efficiency operations. The simple and rugged rotor construction makes flux-switching machine a promising candidate for medium and high-speed applications. However, the design of the high-speed machine is a challenging task which needs to consider not only the electromagnetic properties, but also the multi-physics aspects such as the mechanical structure,

thermal regulation, and cooling methods. This section also presents the performance of the flux-switching machines compared with other types of electrical machines for medium and high-speed applications. The benefits and limitations of the existing flux-switching machines are discussed to show that more research should be done in the field of high-speed operations of flux-switching machines.

1.4.1 Comparison with Other Types of Electric Machines

This section presents the comparative studies of flux-switching machines with other types of electric machines, with an emphasis on medium and high-speed operations. It is mentioned in the previous section that the conventional electric machine types for medium and high-speed operation are induction machine, surface permanent magnet machine, and switched reluctance machine. To have a more comprehensive performance comparison of flux-switching machines, other electrical machines types such as interior permanent magnet machine, doubly salient permanent magnet machine, and flux reversal machines are also investigated. It should be noted that some of the designs are for applications such as electric vehicle, aerospace that are also considered as high-speed operations.

The interior permanent magnet machine is famous for its high torque density and high-efficiency properties especially appropriate for the applications where flux weakening operation is needed. The comparison of IPM with FSPM machines is done by Pang to show that FSPM machine has similar or even better performance than IPM machines in terms of flux weakening capability and torque density when the appropriate split ratio is designed [237]. Fasolo compared various IPM machines (radially magnetized PM, spoke-type PM, and V-shape PM) with the FSPM

machine by using both NdFeB and ferrite magnets to quantify the differences in torque production, active material cost, and demagnetization behavior [238], [239]. The radially magnetized IPM machine has the best demagnetization withstand capability. The spoke-type IPM machine is found to have the best torque per active material mass property, but its PMs are most vulnerable to demagnetization. V-shaped IPM machine has only partial demagnetization behavior at nominal load. If ferrite magnets are used, the spoke-type IPM machine and the FSPM machine have partial demagnetization behavior. For the FSPM machine, the risk of highest demagnetization happens at the tips of magnets near the airgap.

A quantitative comparison of FSPM machine with the Prius-IPM machine is researched by Cai. The key research findings are that the FSPM machine has benefits of sinusoidal back-EMF, smaller torque ripple, and excellent mechanical integrity for high-speed operation. However, the main challenges are the lower PM material utilization ratio and higher material cost [240]. A comparative study of IPM machine, conventional FSPM, and PM-sandwiched FSPM machines all with ferrite magnets are shown by McFarland in [241]. The torque density comparison shown in Figure 1.32 demonstrates that PM-Sandwiched FSPM machine achieves the maximum torque among the three machines for the same current excitation. In addition, the PM-sandwiched FSPM machine shows significant efficiency improvements over the IPM machine, but at the expense of increased magnet material cost and stator fabrication complexity. The adoption of either machine type depends on the application specification and performance preference.

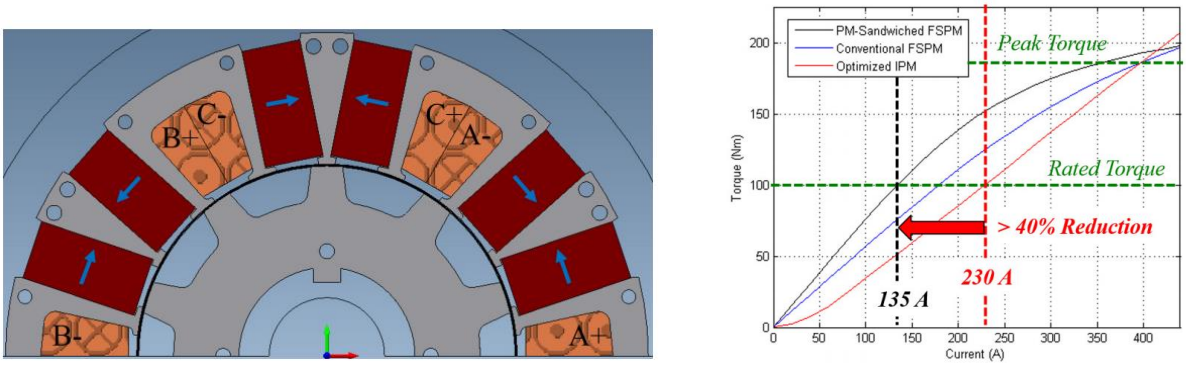

(a) (b)

Figure 1.32. PM-Sandwiched flux-switching machine with ferrite magnets (a) machine cross sectional view, (b) torque production capability comparison of PM-sandwiched FSPM, conventional FSPM machine, and optimized interior PM machine [241].

Multiple flux-switching machines with permanent magnets and field windings configurations are designed to meet the U.S. DRIVE specifications for traction applications [242]. The compared three designs and the prototype machine is shown in Figure 1.33. The analytical results show that all the designs achieve a large constant power speed ratio. The test results for the prototype demonstrate that the FSPM machine achieves high torque density and high efficiency across most the speed region. It can be noted that the iron loss and magnet eddy current loss are very large at the speed close to maximum speed, and the operating frequency is close to 2.5 kHz which is very challenging for the power electronics.

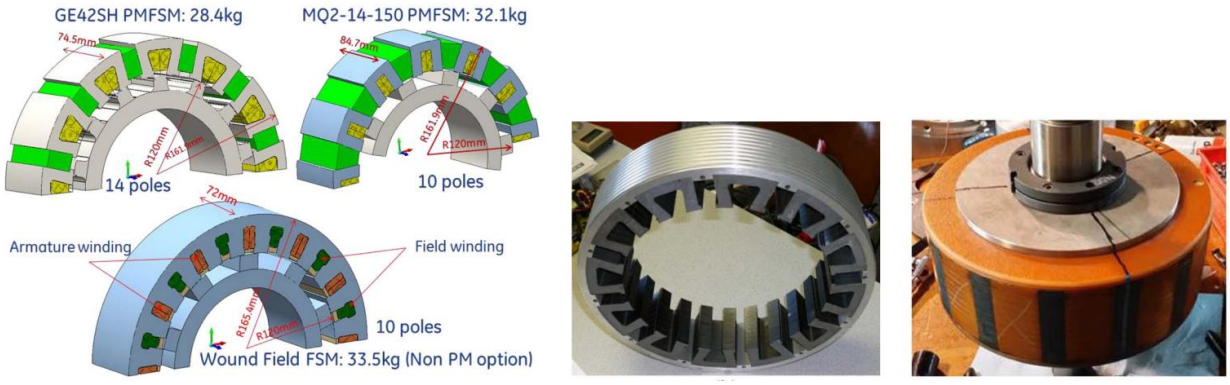

(a) (b) (c)

Figure 1.33. Flux-switching machines designed for traction application, (a) three flux-switching machines with and without PM, (b) prototype stator, (c) prototype rotor [242].

The comparison of FSPM machine with SPM machine (both NdFeB and ferrite magnets) is also investigated by Fasolo [238], [239]. The torque/active cost of using ferrite magnet FSPM machine is higher than ferrite SPM machine. The torque/active volume of NdFeB FSPM machine is comparable with SPM machine using same magnets. FSPM machine and SPM machine designed for high-speed generator application were compared by Thomas shown in Figure 1.34 [243], [244], [245]. The results show that SPM machine needs to apply a sleeve to increase the mechanical integrity of the rotor at the high-speed condition, and this increases the airgap length and decreases the flux linkage in the windings. The SPM machine has less torque and efficiency than FSPM machine.

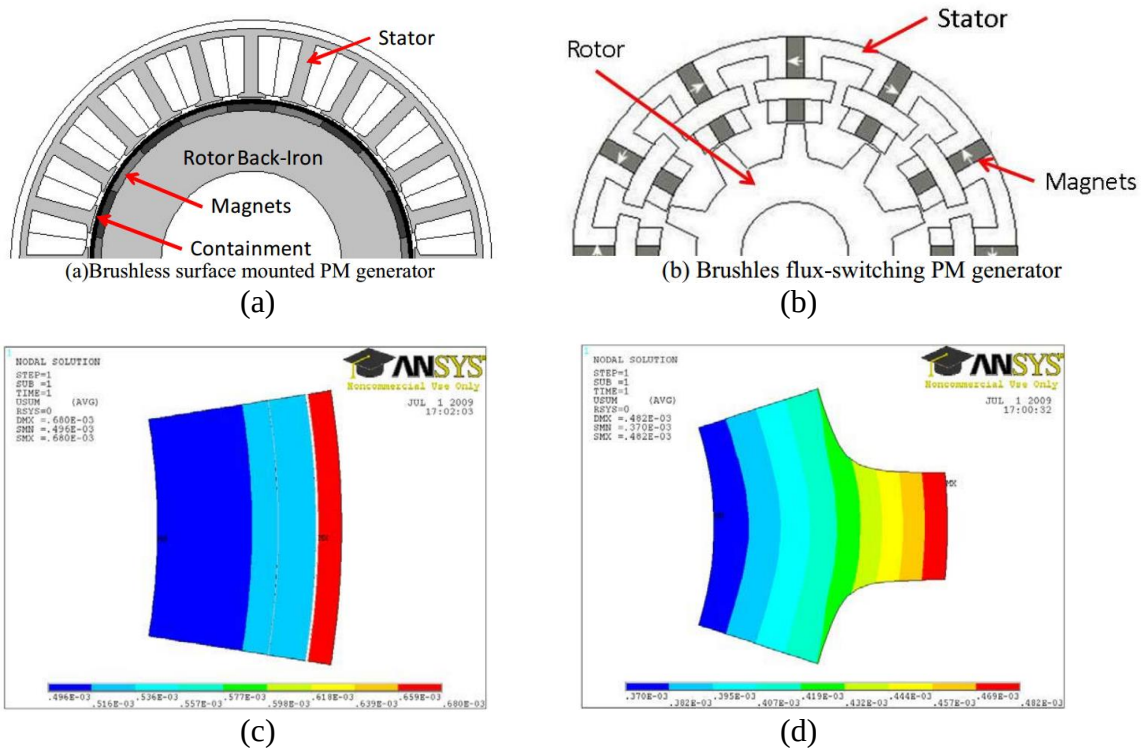

Figure 1.34. Comparison of surface mounted PM generator and flux-switching PM generator for aerospace applications, (a) SPM generator, (b) FSPM generator, (c) radial growth of SPM rotor at 12,7000 rpm 150˚C, (d) radial growth of FSPM rotor at 12,700 rpm and 150˚C [243], [244], [245].

The performance of FSPM and DSPM machines are provided by Hua for both 3-phase and 2-phase structures [246], [247], [248]. FSPM machine has some clear advantages over DSPM machine such as bipolar flux linkage, higher back-EMF per turn, more sinusoidal back-EMF waveform, and higher magnetic loading. The torque density of the FSPM machine is higher than that of the DSPM machine, but this advantage is achieved by consuming more magnet materials. The cogging torque is higher in FSPM machine. The general property comparison of FSPM and DSPM machine holds true for both 3-phase and 2-phase configurations.

A comprehensive comparison of FRPM and FSPM machine is also studied by Hua with the results as previously mentioned [249]. The FRPM machine has bidirectional flux linkage but with trapezoidal-shaped back-EMF which is suitable for brushless DC operation. The magnets are placed on the surface of stator tooth, and there are no obvious flux focusing effects as the FSPM machine. The PM consumption is lower than FSPM machine, but the torque density is also smaller. The structure complexity is not as much as FSPM machine, and assembling of the magnets is comparatively easier.

The FSPM machine is compared with an SRM machine by Pollock for the acoustic noise aspect. The experimental study shows that FSPM machine has fewer radial forces and less vibration and acoustic noise than SPM machine [250], [251]. For the same torque and speed of both machines, the FSPM machine has a lower peak-to-peak radial force, and the vibration acceleration of FSPM machine is 25% less than two-phase SRM. The magnetic flux transitioning from one set of stator poles is smoother to the next stator pole in the FSPM machine, and it has low-acoustic-noise. The electromagnetic properties of SRM and flux-switching machine (FSM) both using segmented rotor structure is compared including magnetic field, static torque, torque ripple, iron loss, and efficiency by Lian [252]. The results show that both machines have small rotor iron loss, but the SRM machine has higher torque ripple than the FSM.

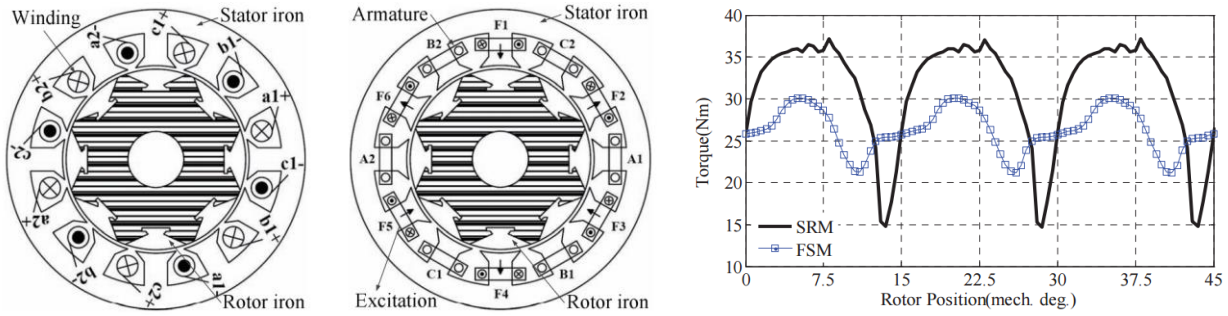

(a) (b) (c)

Figure 1.35. Performance comparison between switched-reluctance machine (SRM) and flux-switching machine (FSM) using segmented rotor structure (a) SRM design, (b) FSM design, (c) electromagnetic torque comparison [252].

A comparison between IM and FSPM machine for an axial fan application was done by Pollock [253]. Two machines were constructed by the same stator stack, shaft, end-caps, and bearings. The FSPM machine consumed 29% less power when driving the fan at the normal speed. The acoustic noise measurement test showed that the FSPM machine was only 1dB greater than the IM. With the same mechanical design, the FSPM machine has 8.5% efficiency improvement over IM and additional benefits of variable speed and controllability.

1.4.2 Studies of High-Frequency Losses

The study of various losses in the medium and high-speed flux-switching machines is necessary to justify the appropriate material selection and evaluate the operating efficiency. The high-frequency associated losses should be taken into serious consideration. In this section, latest research about various losses such as winding loss, iron loss, and magnet eddy current losses of

flux-switching machines are summarized. The methods to reduce the high-frequency associated losses are also presented.

The proximity loss in the stranded windings of high-frequency FSPM machine is studied in terms of developing an accurate 1-D model to quantify the loss values, and optimal number and diameter of the conductors are determined as shown in Figure 1.36 [254]. The proximity loss influenced by the PWM switching effects is studied by an FSPM machine designed for traction application. The effect of slot leakage field on the AC copper loss is also investigated [255]. The iron loss property for FSPM machine is studied to show that the flux density variation in the iron is very complicated including major and minor loop variations [256]. The different fundamental iron loss frequencies of FSPM machine are identified in [257], and the equations are shown below to demonstrate that the stator iron loss fundamental frequency is proportional to rotor pole number, while the rotor iron loss fundamental frequency is proportional to half the number of stator slots. The magnet eddy current loss in the FSPM machine is also an important subject since the magnet flux variations near the airgap is severe and prone to induce large magnet losses. An effective method proposed in [258] shows that cutting a small portion of the magnet at two radial ends reduces the generated magnet eddy current loss. In addition, segmentation of the magnets is also proven to be effective for loss reduction. Both the radial segmentation studied in [258], and the axial segmentation analyzed in [257] show good results in reducing the magnet eddy current loss.

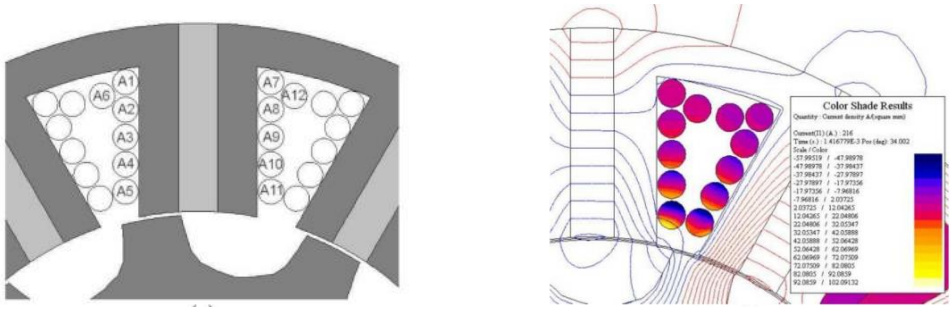

Figure 1.36. Winding schemes of a high-speed flux-switching machine and current density distribution due to proximity losses [254].

Fundamental frequency of stator iron loss is calculated below,

$$f_{e(s)} = \frac{n\ N_r}{60} \tag{1.13}$$

Fundamental frequency of rotor iron loss is determined below,

$$f_{e(r)} = \frac{n\ (N_s / 2)}{60} \tag{1.14}$$

Flux-switching PM machine is known for having large flux leakage at the outer periphery of the stator due to the spoke-positioned permanent magnets. There are pulsations of flux leakage in the frame when the FSPM machine rotates, so eddy current loss can be induced in the aluminum frame that touches the outside of the stator. A novel frame with holes facing the outside edge of the PM is proposed to reduce the generated eddy current loss as shown in Figure 1.37 [259]. A 3-D thermal model for the hybrid excited flux-switching machine and 2-D FEA method is shown in [260] which is especially important for high-speed machines. The losses and efficiencies of alternative FSPM machines are studied with focus on the winding loss and iron loss [261]. The flux-weakening high-speed operation capabilities of FSPM machine is studied for geometrical

variations in [262] to show that it has good potential for achieving high constant-power-speed-range.

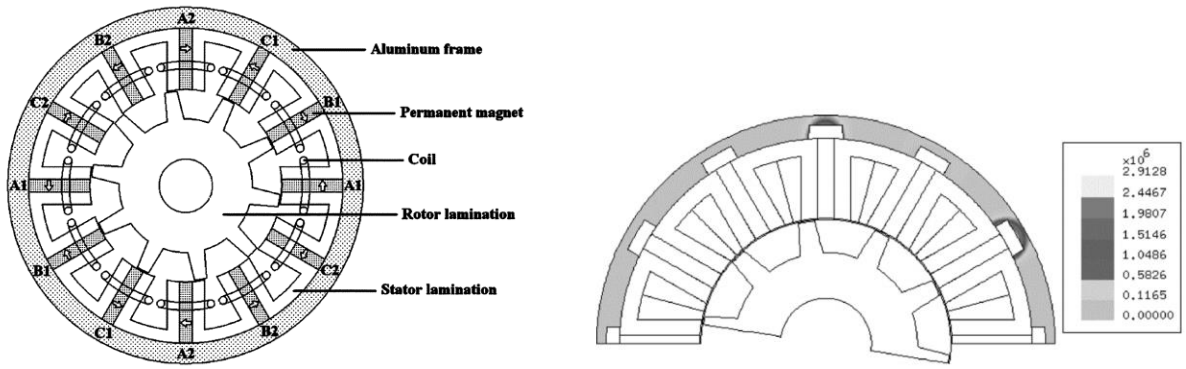

Figure 1.37. Cross-sectional view of the conventional 12-slot 10-pole flux-switching PM machine with aluminum frame, and eddy current density in the aluminum frame [259].

1.4.3 Low Pole Flux-Switching Machines

The flux-switching machine topologies with three or more phases usually have many rotor poles as can be observed in the previous literature review. Most the topology variations of flux-switching machines are based on the baseline 12/10 combination or combinations with a higher number of rotor poles. For the convenience of this research study, it is assumed that the flux-switching machine is regarded as high-pole topology if the number of rotor poles is equal or more than 10. On the contrary, the flux-switching machine is considered low-pole topology if the number of rotor poles is less than 10.

High-pole flux-switching machines are good candidates for the high-torque direct drive and relatively low-speed applications. One of the challenges associated with the high-pole flux-switching machine is the required high fundamental frequency especially when the machine

operates in high-speed regions. For example, if the conventional 12/10 flux-switching machine operates at 15,000 rpm, the fundamental frequency is 2.5 kHz. For Silicon-based power electronic converter, the required switching frequency limit is about 20 kHz which means only eight sampling points can be synthesized for a fundamental electric cycle. The current ripple of the machine as a result of low sampling rate is expected to be very high, and more losses are generated in both the electric machine and power converters. Even if the wide-band-gap devices such as Silicon Carbide (SiC) is used to provide the high switching frequency capability, the electric machine itself suffers from lower efficiency due to high-frequency associated losses if designed for high-speed operations.

The number of references on the low-pole flux-switching machines is much less than on the high-pole flux-switching machines. The topologies with 6 stator slots are compatible with various rotor poles such as 4, 5, 7, and 8 poles [111], [112]. The winding configurations can be either double layer or single layer. The challenges with the 6-slot low-pole flux-switching machines are that they have issues either in unbalanced back-EMF (for 6/4 and 6/8 topologies) or unbalanced magnetic forces on the rotor (for 6/5 and 6/7 topologies with an odd number of rotor poles). The unbalanced magnetic forces on the rotor increase the mechanical stress on the shaft and create vibrations and noises that reduce the life of bearing systems. There is still some literature reporting the low-pole flux-switching machines which are summarized here.

A 6/8 hybrid-excited flux-switching machine for the electric vehicle is studied by Sulaiman. Iron bridge is added in the topology to increase the DC-field regulation capability as shown in Figure 1.38. This topology only reduces the fundamental frequency by 20% compared with 12/10 configuration. However, this configuration further complicates the stator lamination design.

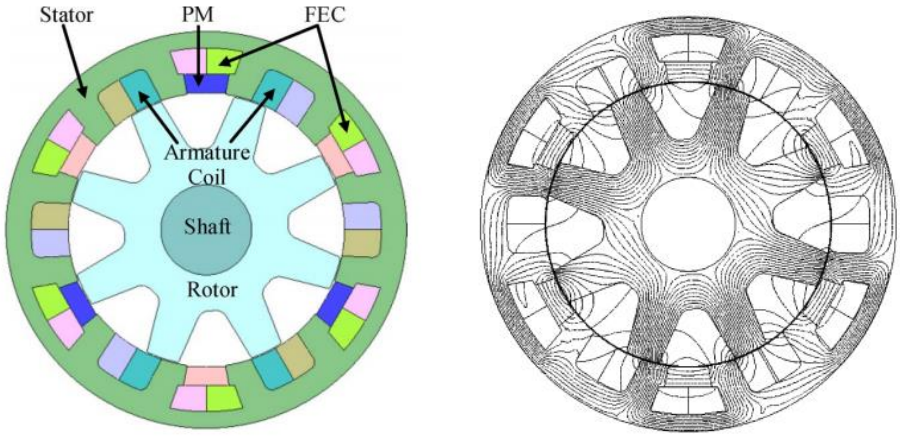

Figure 1.38. Topology of one hybrid-excited flux-switching machine with iron bridges for traction application [150].

A 6/7 FSPM machine with axially-laminated structure is studied by Xu as shown in Figure 1.39, and the results show better torque density, lower cogging torque, and higher efficiency than conventional topology [263], [264]. However, it should be noted that the axially-laminated structure is much more difficult to manufacture than the conventional laminated structure.

(a) (b) (c)

Figure 1.39. Structure of the axially laminated-structure flux-switching PM machine, (a) whole machine configuration, (b) prototype rotor, (c) prototype stator [263], [264].

A novel type of synchronous machines that have a doubly salient structure with permanent magnets in the stator yoke is proposed by Wu and Zhu [265]. The stator is constructed by T-shaped lamination segments sandwiched with circumferentially magnetized permanent magnets. The novel synchronous machines have sinusoidal back-EMF which is suitable for brushless AC operation. There are four configurations studied in the paper, which is 6/4, 6/5, 6/7, and 6/8 combinations as shown in Figure 1.40. The study shows that the machines with combinations of 6/5 and 6/7 have bipolar flux linkage and back-EMF, while the combinations of 6/4 and 6/8 have unipolar flux linkage and bipolar back-EMF shown in Figure 1.40(e), (f). Further finite element analysis reveals that the 6/5 and 6/7 topologies also have the unbalanced magnetic forces in the rotor.

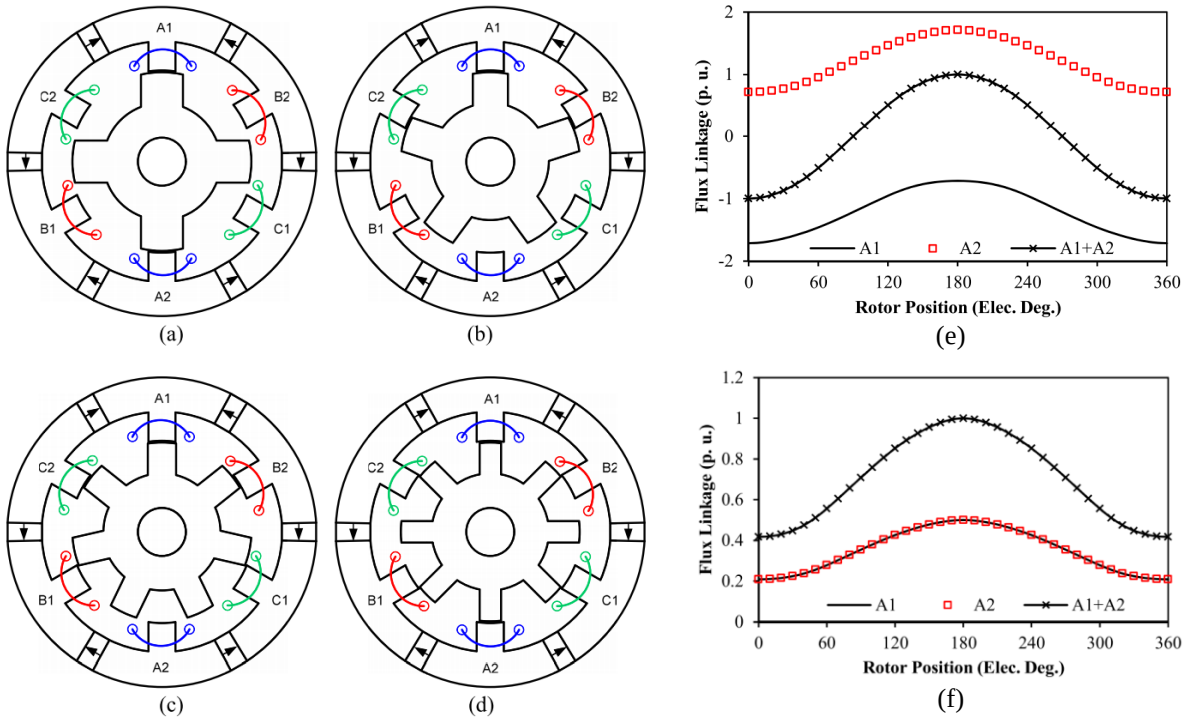

Figure 1.40. Stator-PM synchronous machines, (a) 6/4 configuration, (b) 6/5 configuration, (c) 6/7 configuration, (d) 6/8 configuration, (e) per-unit open circuit flux linkage for 6/5 and 6/7 configurations, (f) per-unit open circuit flux linkage for 6/4 and 6/8 configuration [265].

A twisted rotor concept for low-pole FSPM machine is introduced by Xie to study the cogging torque reduction capability as shown in Figure 1.41 [266], [267]. The twisted rotor structure can reduce the cogging torque up to 60% at the optimal twist angle as demonstrated by the author. The author investigated the combinations of 6/5, 6/7, 6/8, and 12/10, but the lowest possible pole combination of 6/4 is not studied. In addition, the author neglected the magnet flux leakage issue between two stators since the magnet orientations in the two stators are opposite, which creates axial magnetic flux leakage. The two stators should be somehow separated to prevent such magnet flux leakage, which is not addressed by the author.

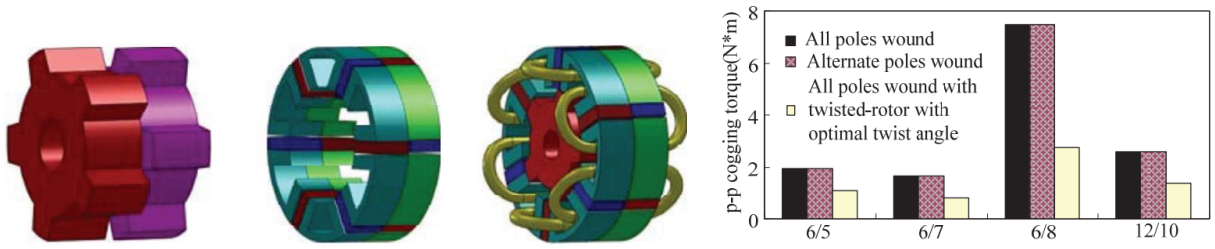

(a) (b) (c) (d)

Figure 1.41. Twisted rotor FSPM machine for cogging torque reduction, (a) rotor structure, (b) stator structure, (c) whole machine, (d) comparison of cogging torque for various slot/pole combinations [266], [267].

Low-pole wound-field flux-switching machines are studied by Zhou and Zhu for the combinations of 12/5, 12/7, 12/8, and 9/5 [268]. The combinations with 5 rotor poles are shown in Figure 1.42 with illustrations of winding distributions. The results show high torque density achieved by 9/5 configuration, but the rotor unbalanced magnetic forces are still present.

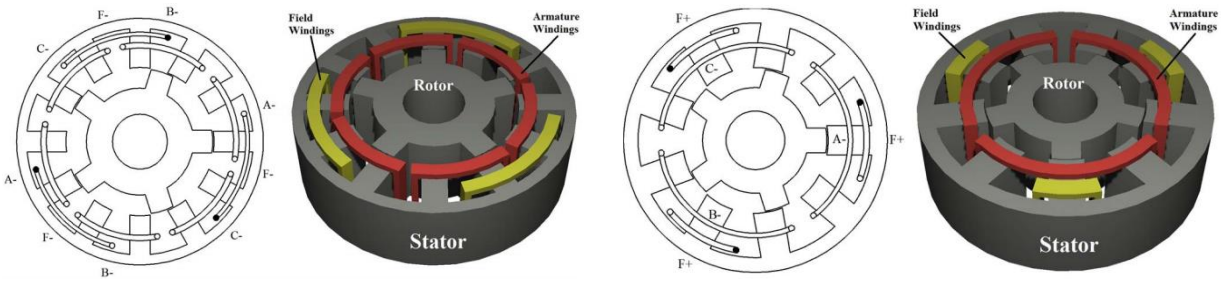

(a) (b)

Figure 1.42. Low-pole wound-field flux-switching machines, (a) 12/5 configuration, (b) 9/5 configuration [268].

There is a limited reference in the study of 6/4 FSPM machine. In reference [108], a 6/4 FSPM machine is analyzed for its flux linkage and back-EMF. It was revealed that the 6/4 topology has a large unbalanced back-EMF as shown in Figure 1.43. The author proposed a skewing method to reduce the harmonic distortion in the back-EMF, but this method has limitations that it cannot sufficiently reduce the harmonic distortion. Also, the skewing method reduces the average flux linkage and thus the torque production capability of the machine.

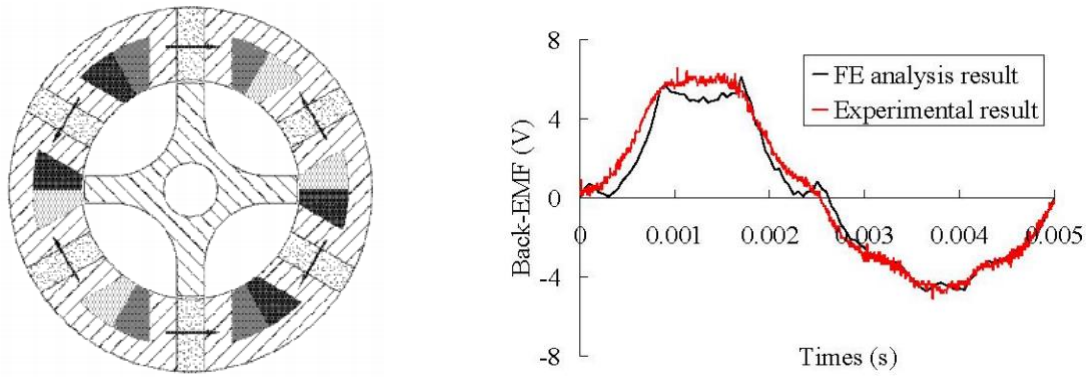

(a) (b)

Figure 1.43. A 6/4 FSPM machine studied (a) cross sectional view, (b) back-EMF waveform [108].

A concept of flux-switching hybrid magnet memory machine is proposed with the 6/4 topology in [165], [166]. The cross-sectional view of the machine with positions of hybrid permanent magnets is shown in Figure 1.44. However, this paper only proposed the topology without further analytical studies into the performance of the 6/4 machine. There is a knowledge gap in understanding what is the performance characterization of the 6/4 machine.

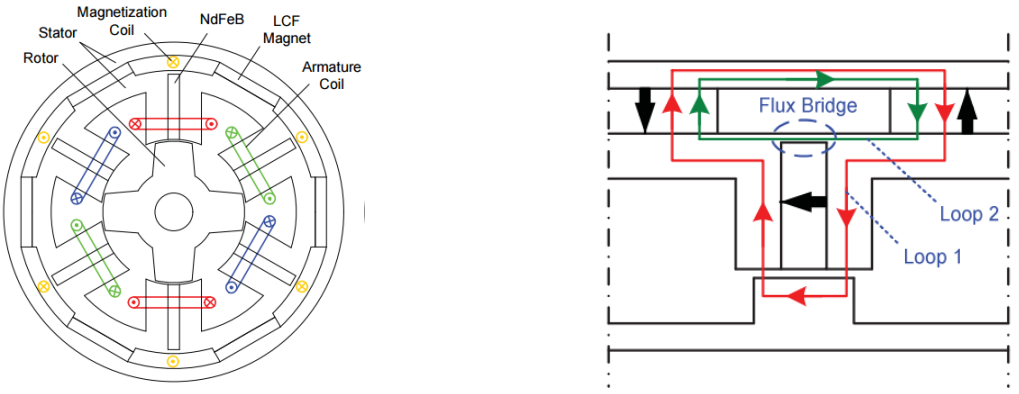

(a) (b)

Figure 1.44. A 6/4 flux-switching hybrid magnet memory machine (a) cross sectional view, (b) illustration of flux path [165], [166].

A summary of flux linkage and back-EMF waveforms for 6/4, 6/5, 6/7, and 6/8 FSPM machines are provided as shown in Figure 1.45 [257]. It was identified that the back-EMF waveform distortions are very severe in the 6/8, and especially in the 6/4 FSPM machine. Thus, the 6/4 FSPM machine should be redesigned to reduce such large harmonic distortion.

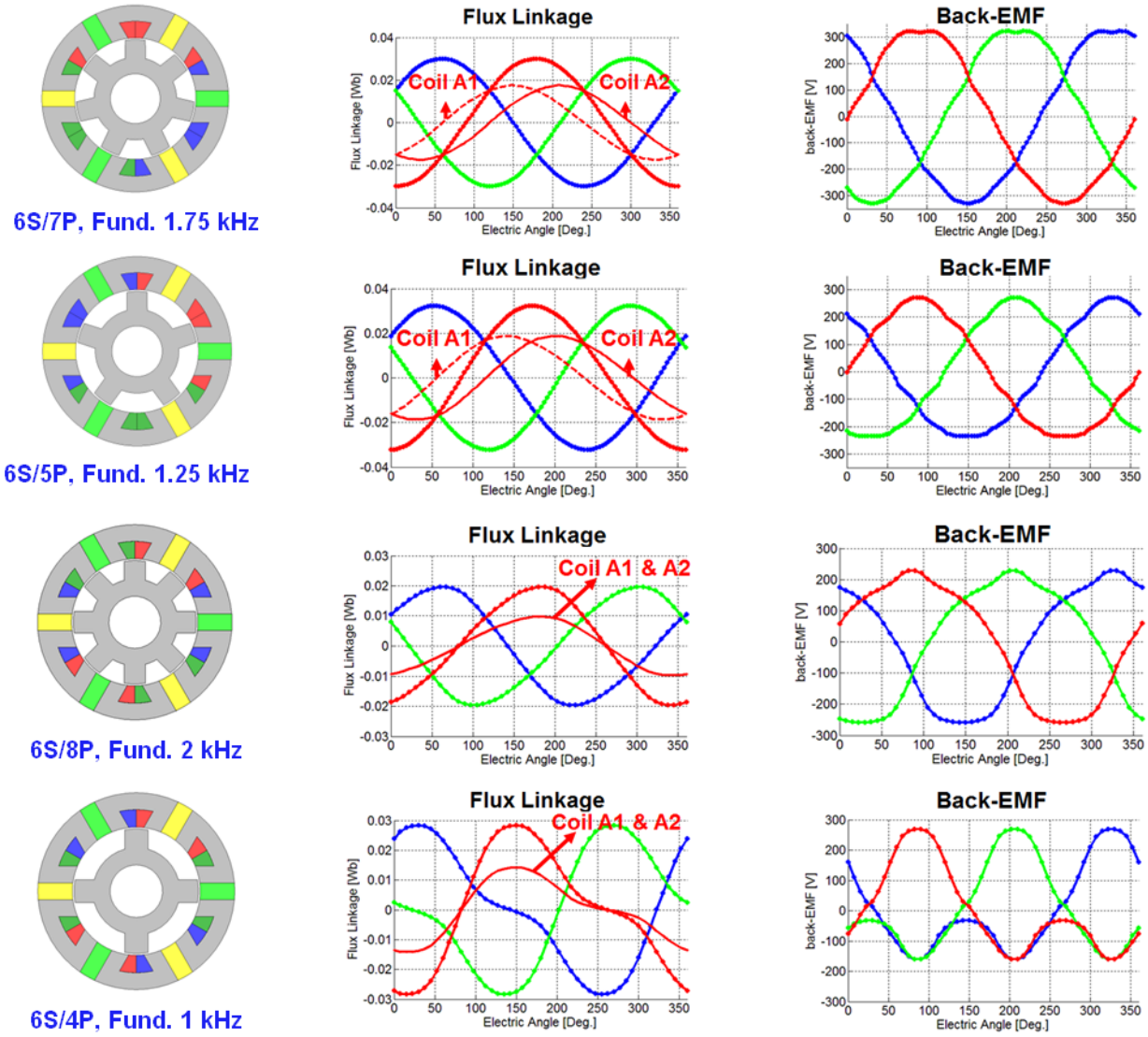

Figure 1.45. Flux linkage and back-EMF waveforms of multiple FSPM topologies with 6 stator slots, and fundamental frequencies of all the machines are calculated at 15,000 rpm condition [257].

For completeness, some of the research studies in the control aspects of FSPM machines are briefly summarized here. There are a limited number of papers discussing control methods of FSPM machine. One of the general properties of FSPM machine is its limited saliency at all

operating conditions. This implies that the control of FSPM machine can be approximated as the control method of surface PM machine where zero d-axis stator current method is used. A fault-tolerant control method considering the reluctance torque of the FSPM machine is discussed [269]. Stator flux orientated control method is also applicable to FSPM machines based on either voltage space-vector or current-hysteresis control [270], [271], [272]. Sensorless control methods is also studied for FSPM machine for position estimation and direct torque control [273], [274], [275].

From the above literature review, it is identified that the low-pole flux-switching machine topologies have not been fully investigated yet. The FSPM machine topology with the lowest number of rotor poles (6-slot/4-pole) has not been taken into serious consideration in the literature. There are research opportunities in investigating this topology and making it amenable for high-speed operations. The reason that the 6/4 FSPM machine is not considered in the literature should first be investigated. After the problem of 6/4 FSPM machine is identified, new methods should be implemented to redesign the machine and improve its performance for practical use. Design guidelines and equations will need to be developed for the machine, and performance will also need to be characterized. The rest of the chapters are dedicated to the analysis and design of this novel low-pole FSPM machine.

1.5 Summary

This chapter presents the state-of-the-art literature review on the flux-switching permanent magnet machines. The reason to choose flux-switching PM machine out of the three stator-mounted PM machine is explained. Modeling and analysis of the flux-switching machine, especially the selection of stator slot and rotor pole combinations are discussed. For convenience,

a diagram showing the most commonly investigated slot/pole combinations and whether they have unbalanced magnetic force or unbalanced back-EMF for both double layer and single layer winding configurations are shown in Figure 1.46. The 12/10 combination has no unbalanced magnetic force or unbalanced back-EMF at double layer configuration, which is considered the baseline machine in many literature studies. To avoid complications of unbalanced magnetic forces, the 6/5 and 6/7 topologies are not considered in the research. Therefore, the 6/4 FSPM machine topology is identified as the target slot/pole combination for further research study.

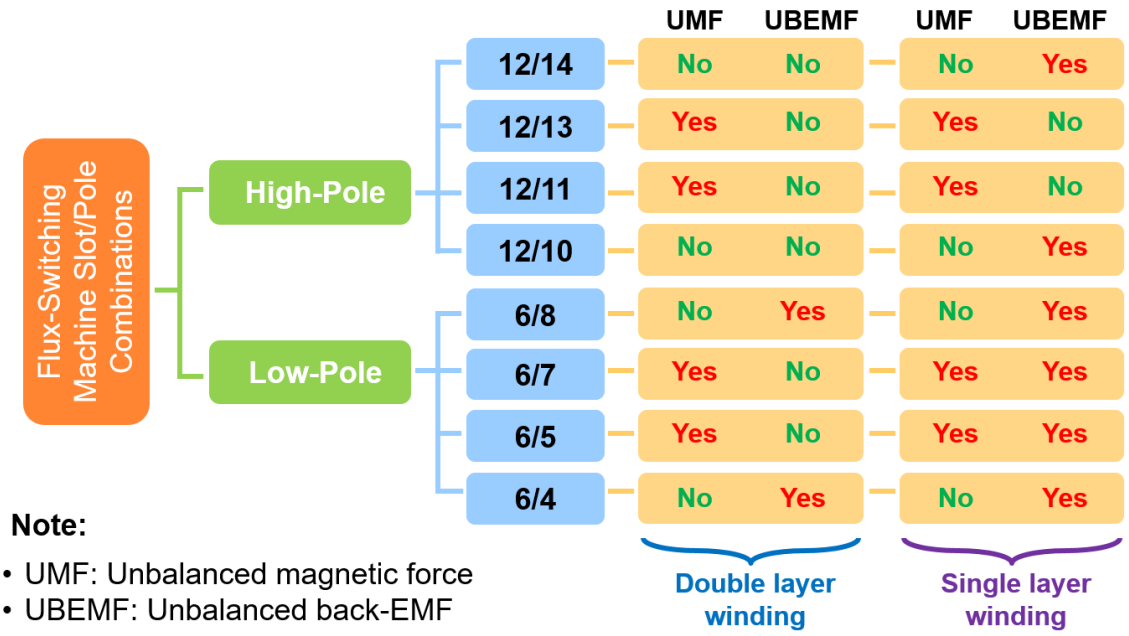

Figure 1.46. Commonly use slot/pole combinations of flux-switching machines showing UMF and UBEMF for double layer and single layer winding configurations.

The developed topologies for flux-switching machines are summarized in the diagram shown in Figure 1.47. Depending on the flux path, the flux-switching machines are categorized into radial flux, axial flux, and transverse flux machines. The radial flux type of flux-switching

machines is the focus of this research. The most important new topologies are subcategorized into structures by modified stator, modified rotor, or modified both stator and rotor. In the later research study of the 6/4 FSPM machine, a novel dual-stator concept is proposed that shares some of the features as in the twisted rotor topology.

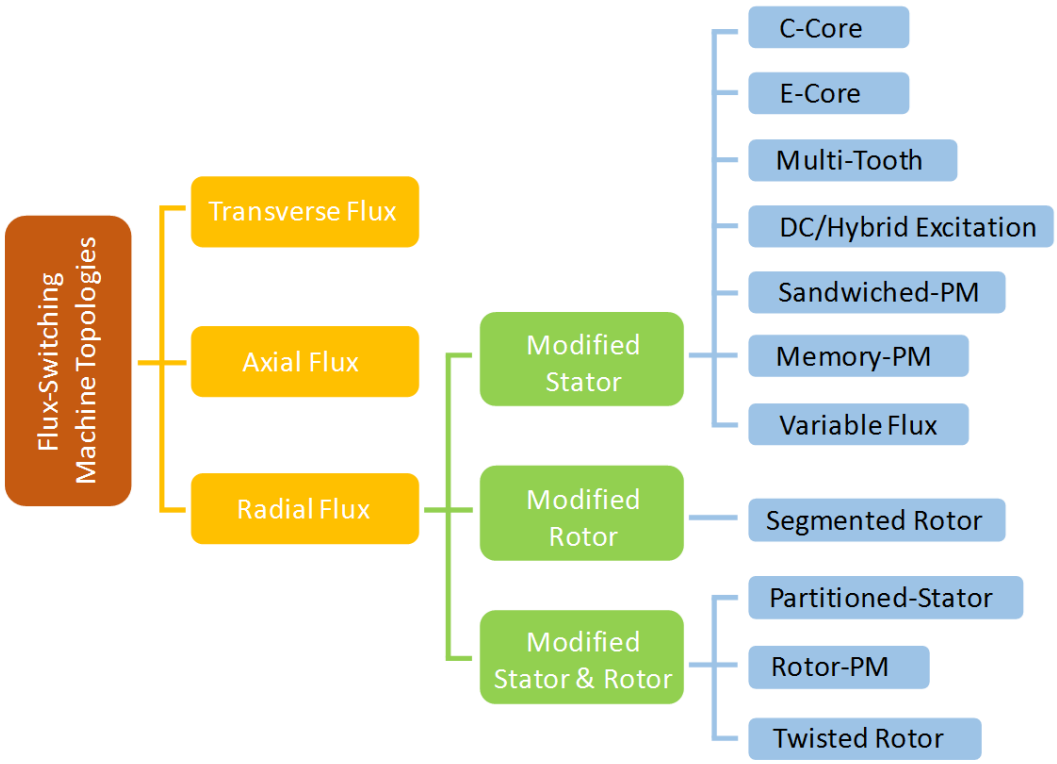

Figure 1.47. Flux-switching machine topology categorizations in literature review.

To summarize the studied slot/pole combinations in literature. Topologies with equal or greater than 10 rotor poles are considered high-pole flux-switching machines, whose references are concluded in TABLE 1.4. Similarly, topologies with lower than 10 rotor poles are considered as low-pole flux-switching machines, whose references are summarized in TABLE 1.5. It is seen that the literature primarily focuses on the high-pole topologies of flux-switching machines,

particularly for 12/10 topology. A percentage chart showing those slot/pole combinations in the investigated literature is presented in Figure 1.48. More than half of the literature investigates the 12/10 topology. There are few references that study the 6/4 topology. Therefore, there is a knowledge gap in understanding the operation and performance properties of 6/4 flux-switching machine.

TABLE 1.4. HIGH-POLE FLUX-SWITCHING MACHINES IN LITERATURE

Slot/Pole	References
6/19	[53], [55], [71], [72], [120], [122]-[124], [164], [169], [236]
12/14	[59], [72], [73], [81], [83], [84], [98], [100], [107], [110], [111]-[116], [118], [120], [145], [156], [157], [163], [167], [168]-[170], [172], [176], [190], [205]-[207], [228], [242], [261]
6/14	[116], [121]
12/13	[53], [59], [72], [81], [110], [111]-[116], [120], [145], [168]-[170], [172], [190], [205]-[207], [228], [261]
6/13	[101], [116], [120], [121], [159]-[161], [164], [169]
12/11	[53], [55], [59], [75], [81] ,[110], [111], [113]-[116], [145], [172], [203], [205]-[207], [261]
6/11	[101], [120], [121], [169], [172], [203]
12/10	[52]-[61], [63]-[70], [72], [74], [76]-[79], [81], [82], [84], [85], [87]-[93], [95]-[97], [100], [101], [103]-[105], [107], [110]-[121], [124]-[127], [131]-[149], [153], [156]-[158], [167]-[170], [172], [177]-[182], [185], [191], [192], [194]-[196], [202], [204]-[208], [225]-[228], [229]-[331], [236]-[244], [246], [248], [254]-[256], [258], [260]-[262]
6/10	[154], [155], [172], [241]

TABLE 1.5. LOW-POLE FLUX-SWITCHING MACHINES IN LITERATURE

Slot/Pole	References
6/8	[94], [119], [126], [150], [165], [166], [256], [266], [267]
6/7	[110], [164], [165], [166], [187]-[189], [263], [264], [256], [266], [267]
6/5	[94], [96], [108], [110], [117], [119], [126], [165], [166], [204], [256], [266], [267]
6/4	[108], [165], [166], [265]

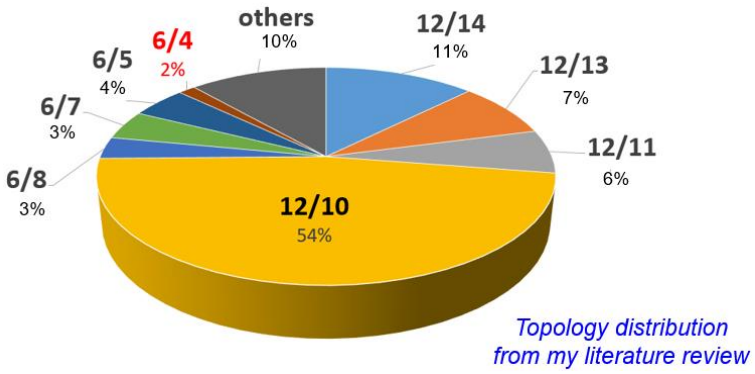

Figure 1.48. Topology distributions of different slot/pole combinations in literature.

Up till now, the research opportunities of designing low-pole FSPM machine are identified. The 6/4 FSPM machine is chosen as the primary topology for the research study. The conventional 6/4 FSPM machine will be evaluated for the performance challenges. Then, novel techniques of redesigning the 6/4 FSPM machine will be introduced and validated through analytical and finite element analysis. The performances of the proposed novel machine will be characterized compared to existing electric machines. The proposed concept machine will also be proved by a prototype machine with experimental studies. The following chapters are dedicated to address those research topics individually.

Chapter 2

Flux-Coupling Low-Pole FSPM Machine Topologies

The previous literature identified that the lowest possible stator slot/rotor pole combination of three phase FSPM machine is the 6/4 topology. This chapter presents the properties of conventional 6/4 FSPM machine. The challenges of the unbalanced back-EMF will be presented and the causes will be discussed. To address the issues in the conventional 6/4 FSPM machine, a novel concept of dual-stator topology will be proposed and explained in this chapter. The property of even harmonic cancellation in the proposed machine will be studied. Various topologies based on the dual-stator machine concept will also be introduced.

2.1 Conventional 6-Slot 4-Pole Flux-Switching PM Machine

2.1.1 Background Study

Flux-switching permanent magnet machines have a simple and robust rotor, and they have promising opportunities in the medium and high-speed application realm because the containment of the permanent magnet is no longer needed for high-speed operation. The FSPM machine is a viable alternative to the traditional switched reluctance machine (SRM) and the surface permanent magnet (SPM) machine [20]. Nevertheless, traditional designs of FSPM machines focused

primarily on topologies with a large number of rotor poles, which requires high fundamental frequency operation for medium and high-speed conditions. The associated high-frequency losses are expected to be very high, thus constraining the medium and high-speed application of the FSPM machine. In addition, the switching frequency of the power electronics converter can become a limitation to produce the very high fundamental voltage and current waveforms required by the FSPM machine.

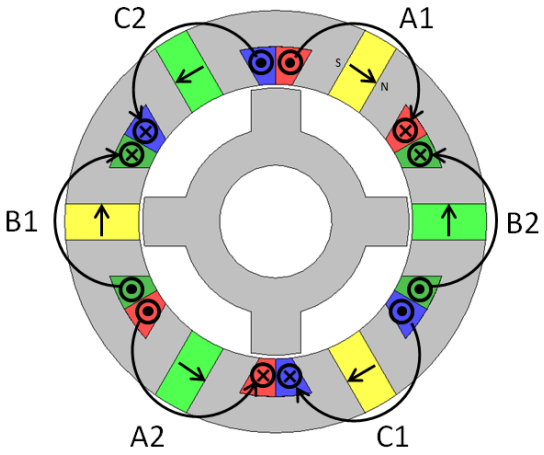

Figure 2.1. Cross sectional view of conventional 6/4 FSPM machine.

Medium or high-speed machines usually have a small number of poles to reduce the fundamental frequency for a given speed. It is a valid progression to investigate the three phase FSPM machine with the minimum number of rotor poles, which is the six stator slots four rotor poles (6/4) configuration shown in Figure 2.1. There are several researchers who study the low-pole number FSPM machines. Multiple FSPM topologies with all and alternate pole-wound types are studied, and 6/5 and 6/7 topologies are shown to have the unbalanced magnetic force (UMF) as mentioned earlier. However, the 6/4 topology does not have such UMF. As can be noted above,

the investigation of conventional 6/4 topology has not been done in the previous study because of its unfavorable characteristics.

2.1.2 Flux Linkage and Back-EMF Waveforms

The excitation frequency f (Hz) of FSPM machine is proportional to the number of rotor poles N_r and rotational speed n (rpm), shown in (2.1). The conventional 12/10 topology requires 2.5 kHz fundamental frequency at 15,000 rpm. This is a challenging requirement for Si-based power electronic drives. However, a 6/4 topology only needs 1 kHz at this speed. Utilizing a 6/4 topology instead of 12/10 topology achieves 60% reduction of fundamental frequency, which will further reduce high-frequency losses such as iron loss and magnet eddy current loss in the machine. Therefore, the study of 6/4 topology is of great importance for high-speed operation.

$$f = \frac{nN_r}{60} \tag{2.1}$$

Conventional 6/4 FSPM machine is presented as a baseline topology in this study. The basic requirement for an FSPM machine is that the back-EMF should be as close to the sinusoidal waveform as possible. The 12/10 topology has a back-EMF per phase with low total harmonic distortion, demonstrated in [63]. However, this is not the case for conventional 6/4 topology. The flux linkage in the baseline machine is represented in Figure 2.2. Fast Fourier Transformation (FFT) analysis shown in Figure 2.3 reveals that a significant amount of the 2nd order harmonic exists in the flux linkage, which mainly causes the distortion. There is also higher order even harmonics in the flux linkage, but their amplitudes diminish quickly as the order number increases.

The even order harmonics cause severely unbalanced back-EMF as shown in Figure 2.4. The negative half cycle has a large concave drop. This irregularity in the back-EMF renders it unfeasible to be used by a power electronics drive. The FFT analysis in Figure 2.5 again discloses that the low order even harmonics, especially the 2nd harmonic, are troublesome.

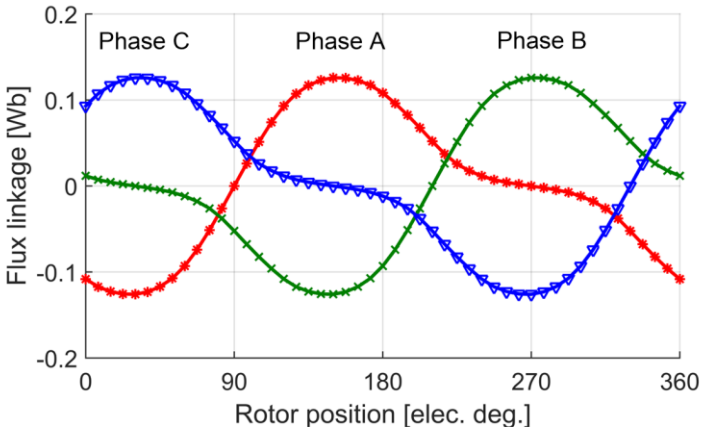

Figure 2.2. Flux linkage of conventional 6/4 FSPM machine.

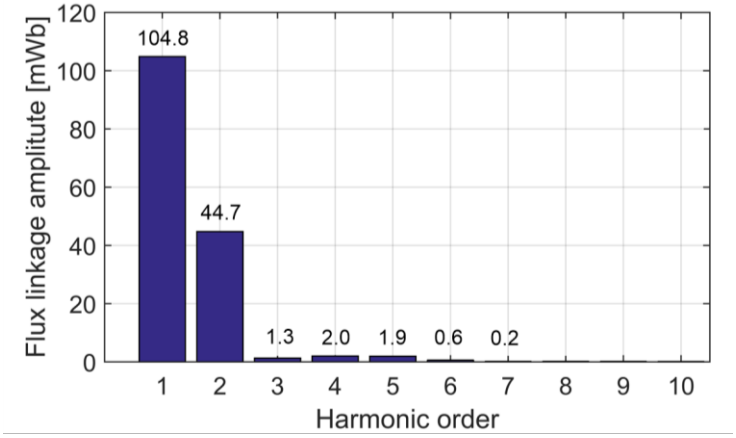

Figure 2.3. FFT of flux linkage of conventional 6/4 FSPM machine.

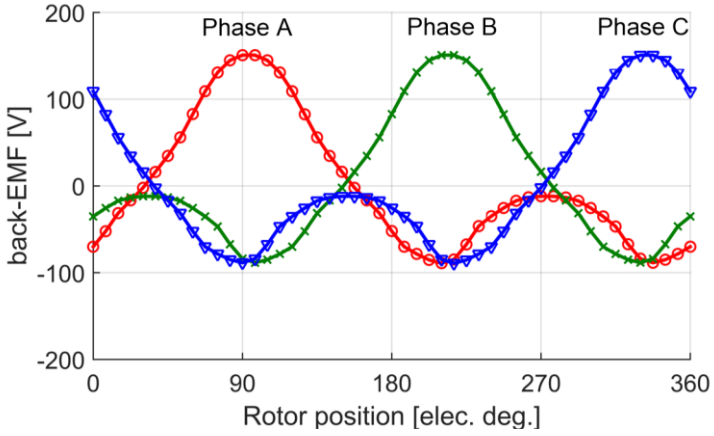

Figure 2.4. Back-EMF of conventional 6/4 FSPM machine.

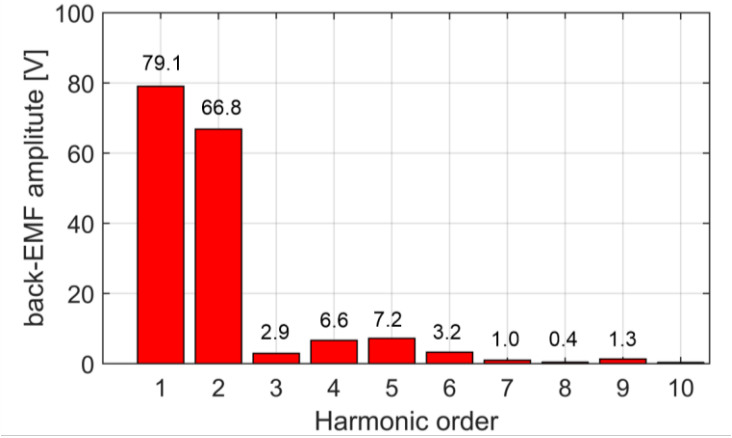

Figure 2.5. FFT of back-EMF of conventional 6/4 FSPM machine.

2.1.3 Second Order Harmonics Production Mechanism

The understanding of the cause of the 2nd order harmonic in the flux linkage provides valuable insights for the machine design. To simplify the explanation, the conventional 6/4 FSPM machine is shown in a linear structure in Figure 2.6, assuming the widths of stator tooth, magnet thickness, slot opening, and rotor tooth are all the same. As the rotor moves to the right, the flux

path that links phase A winding coils are illustrated at five key rotor positions, from Figure 2.7(a) to (e).

Total flux linkage is zero at both Figure 2.7(a) and (e) positions. The permanent magnet that is wound by phase A coil aligns either with one rotor pole, or with the center line between two rotor poles. The flux paths at these two positions have symmetric patterns so both the fundamental and the 2^{nd} order harmonics are zero.

The fundamental and the 2^{nd} order harmonics are shown in Figure 2.7 for each position. When the rotor moves to the position as shown in Figure 2.7(b), both fundamental and the 2^{nd} harmonics have positive flux linkage. As the rotor moves into position as shown in Figure 2.7(c), the fundamental component becomes the maximum while the 2^{nd} harmonic decreases to zero. At the position as shown in Figure 2.7(d), the 2^{nd} harmonic reaches the negative peak value. Total flux path for each position is illustrated in Figure 2.6.

From this analysis, it can be observed that the 2^{nd} order harmonic is caused by the permeance variation as the rotor pole sweeps across the stator tooth and magnet between phase A winding, with the magnet's permeability close to air. When the rotor rotates, its tooth is faced with high permeance stator tooth and low permeance magnet or air alternatively, causing the 2^{nd} order flux period in the flux linkage. In a similar way, higher order even harmonics are produced.

Due to the nature of the 2^{nd} order harmonic production mechanism, there is no way to eliminate the 2^{nd} order harmonic in each coil. As compared to the FSPM machine topologies such as 12/10, 12/14 where the total flux linkage is balanced, the even harmonics are canceled within the phase windings. Thus, the resultant total flux linkage has very small total harmonic distortion.

However, the 6/4 FSPM machine only has two coils per phase, and the two coils have the same flux linkage pattern that cannot cancel the even harmonics.

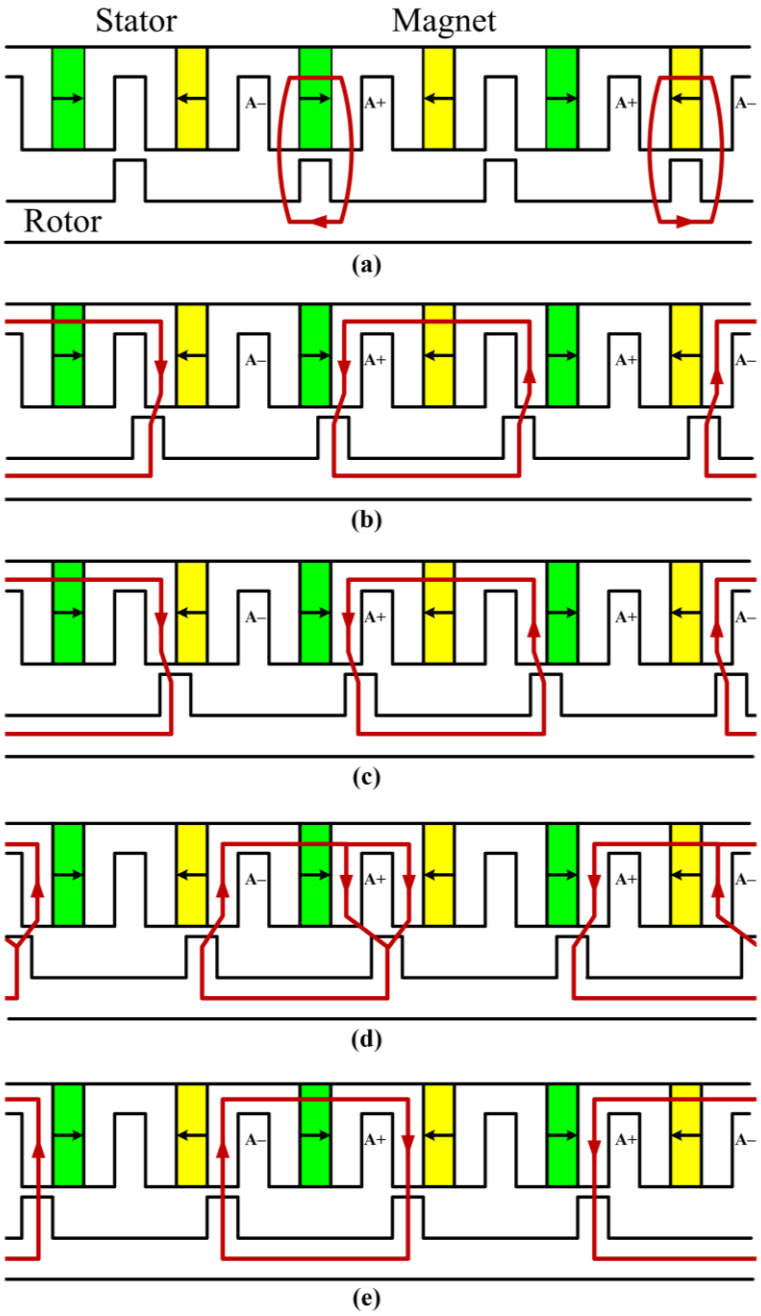

Figure 2.6. Flux path that links two phase A coils at five key rotor position as the rotor moves to the right side.

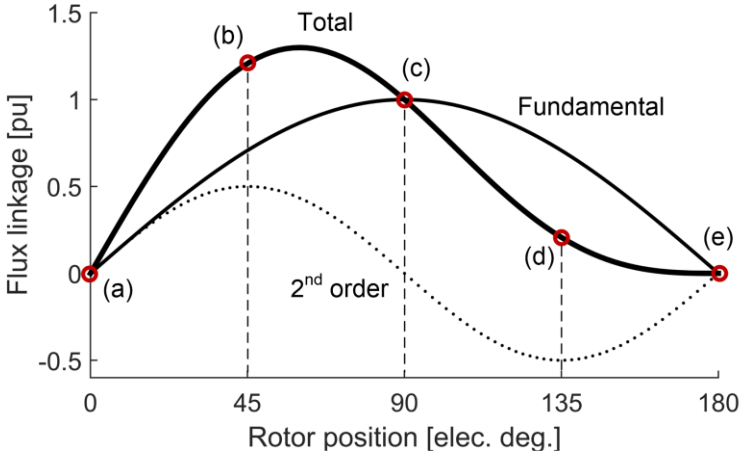

Figure 2.7. Flux linkage of phase-A windings at five key rotor positions, showing fundamental and the 2nd order components.

2.2 Proposed Dual-Stator 6-Slot 4-Pole Flux-Switching PM Machine

It is now clear that the even order harmonics in the flux linkage of conventional 6/4 FSPM machine need to be eliminated to produce back-EMF waveforms with low total harmonic distortion. The proposed solution is to implement a dual-stator structure and utilize a second set of windings to cancel the even order harmonics produced in the first set of windings. This section discusses the details of possible structure realization and the principle of cancellation of even order harmonics.

2.2.1 Realization of Flux-Coupling Dual-Stator Structure

One of the proposed structures of dual-stator 6/4 FSPM machine is shown in Figure 2.8. It is similar to the conventional 6/4 machine except that there are two stators and one modified rotor.

The winding connection schemes are illustrated in Figure 2.9 for both front and rear stators. Both stators have the same magnet flux orientations. However, the winding connection directions of all three phases in the rear stator are opposite to that in the front stator. The current directions in the windings are illustrated in Figure 2.9 using dot and cross symbols, which represent currents flowing out of and into the page. This winding design is used to provide phase shifts for the even order harmonics in the flux linkage. There is a total of four coils for each phase (e.g. A1 to A4) that are connected in series.

The rotor has four poles, but it is shifted into two parts that have a 45° mechanical angle offset. This offset ensures that the rear rotor is out of phase by 180° electrically with respect to the front rotor. Each side of the rotor is designed to interact only with the magnet flux and winding magnetomotive force (MMF) in the corresponding stator.

There is a mechanical gap between the two stators. The reason is to provide space to accommodate the end windings. Since the FSPM machine has concentrated winding configuration, the physical separation of the two stators is roughly about the width of one stator slot.

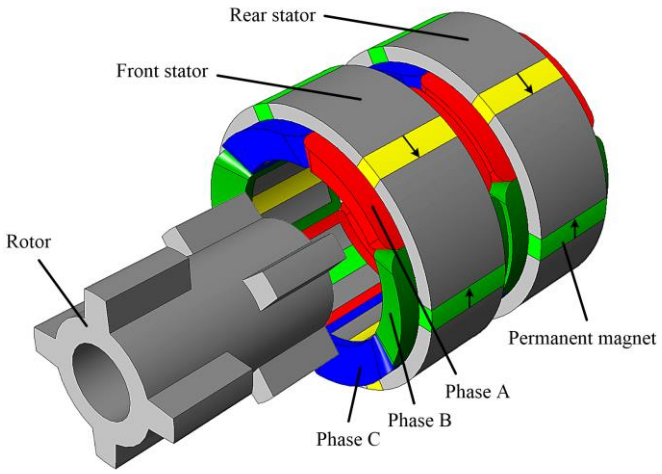

Figure 2.8. Proposed novel dual-stator 6/4 FSPM machine in exploded view.

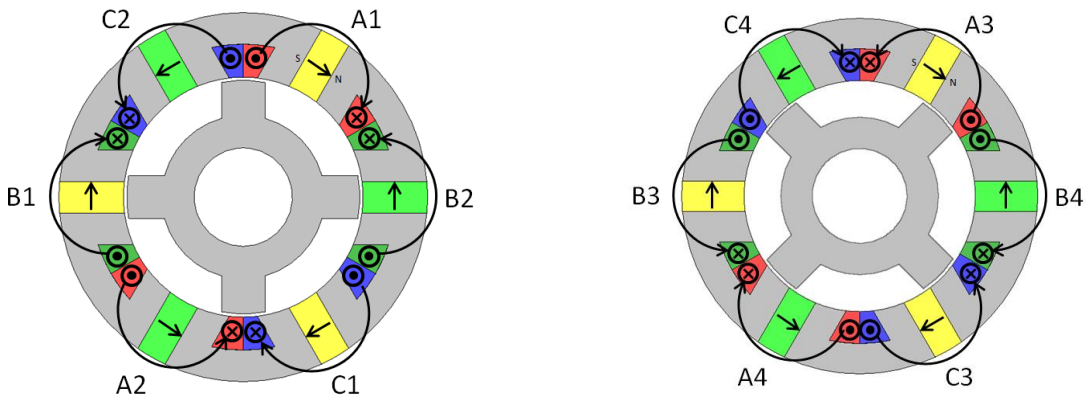

(a) (b)

Figure 2.9. Winding connection schemes and magnet directions of proposed dual-stator offset rotor machine (a) front stator (b) rear stator.

2.2.2 Cancellation of Even Order Harmonics in the Flux Linkage

The flux linkage in the proposed dual-stator FSPM machine has unique properties. Flux linkage waveforms of phase A winding coils (A1 + A2) in the front stator are shown in Figure 2.10 with different harmonic component, including fundamental, the 2nd order and harmonics that are higher than the 2nd order. The combined flux linkage of winding coils A1 + A2 is expressed in (2.2) as an infinite sum of odd and even harmonics, shown separately,

$$\lambda_{1,2} = \sum_{h=1,3,5...}^{\infty} A_h \cos(h\theta_e + \theta_h) + \sum_{h=2,4,6...}^{\infty} A_h \cos(h\theta_e + \theta_h) \tag{2.2}$$

where A_h is the amplitude of the h^{th} harmonic, θ_h is the initial phase angle of the h^{th} harmonic, and θ_e is the rotor position in electric degree.

Calculations show that initial phase angle θ_1 of fundamental component is 180°, and the initial phase angle of 2nd order harmonic is 90°. In fact, initial phase angle for odd harmonics will be either 180° or 0°, and initial phase angle for even harmonics will be either 90° or –90°. The amplitude of harmonics higher than the 2nd order is very small, but they still need to be included in the study.

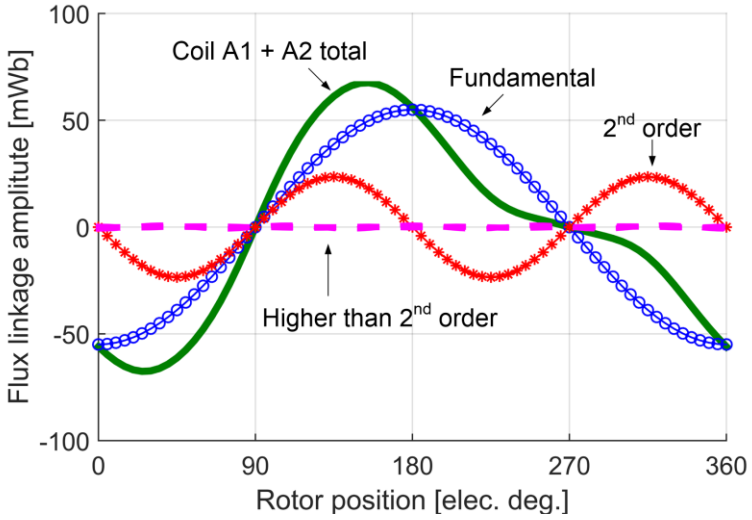

Figure 2.10. Harmonic decomposition of magnet flux linkage waveform of front stator phase A winding coil (A1 + A2).

The flux linkage of phase A winding coils (A3 + A4) in the rear stator is shown in Figure 2.11. The total flux linkage waveforms in the front and rear stator winding are symmetric about the y-axis. The flux linkage for rear stator winding is expressed in (2.3),

$$\lambda_{3,4} = \sum_{h=1,3,5...}^{\infty} A_h \cos(h\theta_e + \theta_h) - \sum_{h=2,4,6...}^{\infty} A_h \cos(h\theta_e + \theta_h) \qquad (2.3)$$

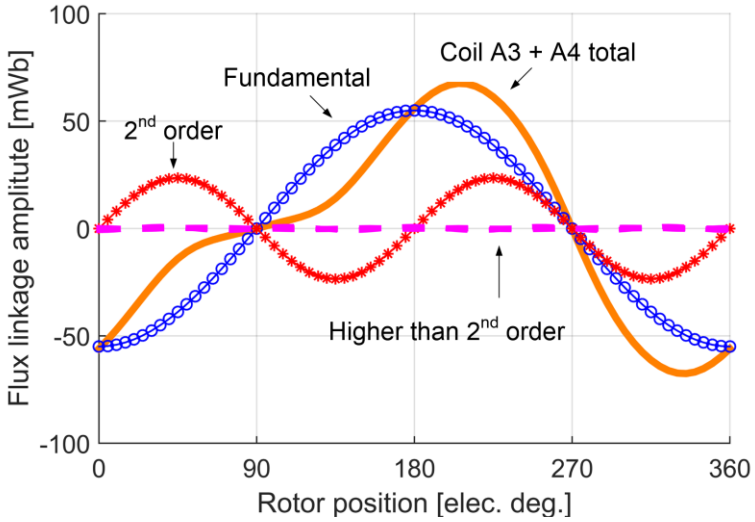

Figure 2.11. Harmonic decomposition of magnet flux linkage waveform of rear stator phase A winding coil (A3 + A4).

The odd-order harmonics have the same amplitude and phase to the front stator winding flux linkage, but all the even order harmonics are exactly 180° out of phase. When the front and rear stator windings are connected in series, the even order harmonics will completely cancel out, leaving only the odd order harmonics represented in (2.4),

$$\lambda_{total} = \sum_{h=1,3,5...}^{\infty} 2A_h \cos(h\theta_e + \theta_h) \tag{2.4}$$

The total phase winding flux linkage plotted in Figure 2.12 shows an almost sinusoidal waveform with small harmonic distortion. The back-EMF is also expected to be very close to sinusoidal waveforms, which will be shown later.

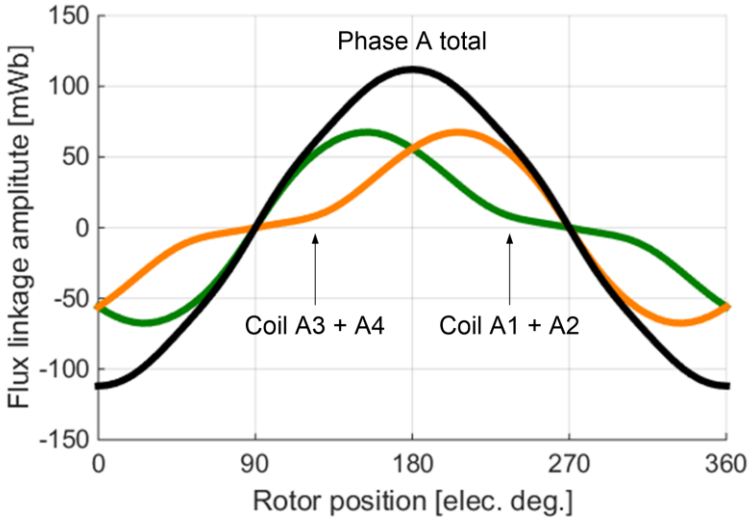

Figure 2.12. Resultant magnet flux linkage waveform for phase A windings total coils (A1 + A2 + A3 + A4).

2.3 Alternative Topologies of Dual-Stator 6/4 FSPM Machine

The idea of the canceling of even order harmonics can be realized by more than one topology. This section proposes more alternative topologies to achieve the same goal. To be general, either the rotor or the stator or both can be shifted to realize the 180° offset effect for the cancellation of the even harmonics. In fact, there could be an infinite number of possibilities in the angle shifts between the stator and rotor that achieves a total of 180-degree electrical phase shift for the even harmonics. All of these topologies are categorized by having two stators.

2.3.1 Rotor Shifted and Magnets in Opposite Direction

One viable topology is shown in Figure 2.13. It has the same offset-pole rotor as in Figure 2.8, but the stator configuration is different. In this topology, the magnets in the two stators have

opposite flux directions. Instead of having two separate windings for each stator, it requires only a single winding that wraps around both stators. One of the benefits of this winding configuration is to reduce the end windings between the two stators, thus to reduce the total phase resistance. However, it should be noted that there should be an appropriate physical clearance between the two stators as shown in the figure. The reason is to prevent short circuiting of the magnet flux through high permeable stator core in the axial direction if the two stators are too close to each other. If the distance between two stators is too close, most the flux generated by the permanent magnets will not link the windings but circulates within the machine itself, thus producing smaller torque. If the distance between two stators is too large, the magnetic reluctance of the air can sufficiently prevent the magnetic flux shunting effect, but the overall machine length is too large and this also degrades the torque density of the machine.

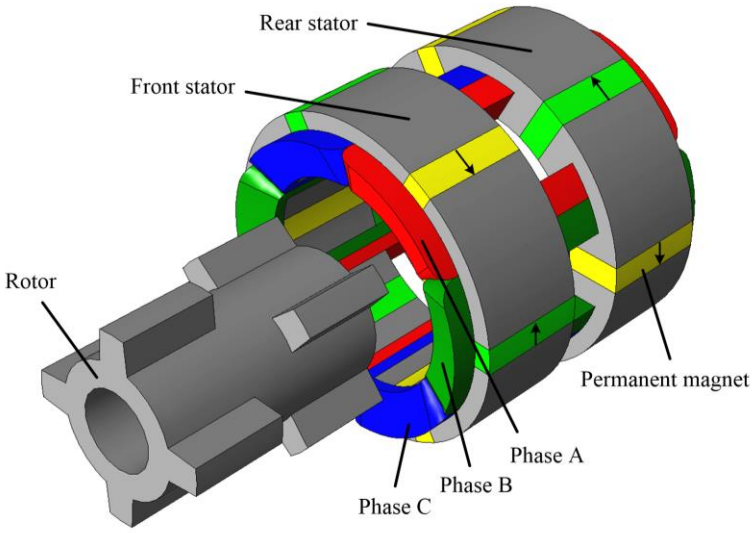

Figure 2.13. Alternative topology one- Rotor shifted and magnets in opposite direction.

2.3.2 Stator Shifted without Shifting Rotor

Another viable topology is shown in Figure 2.14. Starting from the first proposed topology, both rear stator and rotor are shifted mechanically by 45°, which could be in either the positive or negative directions. The resultant topology has a rotor without offset poles. Only the rear stator is shifted to create the even order harmonics cancellation effect. The rear stator and rear rotor can be shifted together by a common arbitrary angle. The 45° angle is one case shown here. It is also noted that there are multiple rotation angles (such as 135°, 225°, and 315°) that will result in a rotor without offset poles. The idea is to treat the dual-stator machine as two single machines that operate by only sharing the series-connected windings. The advantage of this configuration is that the rotor has only one kind of lamination piece, instead of three different pieces as in the first topology. Each of the stators can be manufactured and wound separately, whereas in the second topology, both stators should be in place and fixed before the winding process begins. This configuration simplifies the assembling process because it only needs to consider the correct offset angle between two stators when they are placed in the housing. The design of such machines obeys the same principle of operation as described in the previous section to cancel the even harmonics in the flux linkage and provide balanced and sinusoidal back-EMF.

The proposed three viable topologies of the dual-stator structure can be categorized into the same machine family. The performances and considerations of each of the topology will be discussed in more detail in the next chapter. Depending on the actual specification and application requirement, the most appropriate topology should be chosen to start with the design.

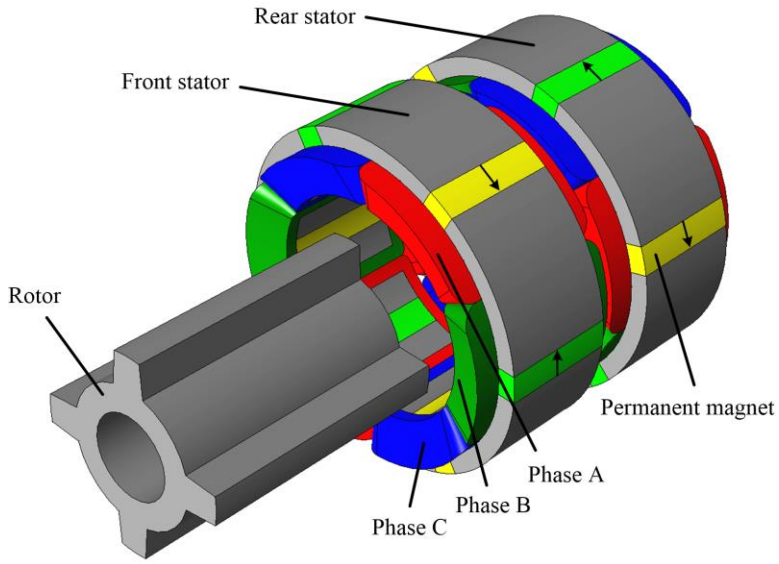

Figure 2.14. Alternative topology two- Stator shifted without shifting rotor.

2.4 Summary

This chapter presents the analysis of conventional 6/4 FSPM machine and proposes a novel dual-stator 6/4 FSPM machine concept. The unbalanced flux linkage and back-EMF properties of conventional 6/4 FSPM machine are explained by studying the 2^{nd} order harmonic production mechanism. The principle of even order harmonic cancellation of the proposed dual-stator 6/4 FSPM machine is explained by harmonic decomposition analysis. Several alternative topologies of the dual-stator 6/4 FSPM machine are introduced. The key research findings are summarized as below.

- The lowest possible three phase topology of FSPM machine is the 6-slot and 4-pole (6/4) topology, but the conventional 6/4 FSPM machine has unacceptably large

harmonic distortion in the flux linkage and back-EMF. Thus, the conventional 6/4 FSPM machine is not feasible to use.

- The large harmonic distortion in the flux linkage of conventional 6/4 FSPM machine is mainly attributed to the 2^{nd} order harmonic content, which is dominant among all the higher order harmonics. This 2^{nd} order harmonic component in the total flux linkage is caused by asymmetrical airgap harmonic permeance variation, and the lack of diametrically placed coil windings that compensates flux linkages and cancels the even harmonics.
- The proposed concept of dual-stator 6/4 FSPM machine can cancel all the even order harmonics in the magnet flux linkage and notably reduce the harmonic distortion in the phase winding flux linkage.
- There are multiple alternative topologies of the dual-stator 6/4 FSPM machines that achieve the same effect of even harmonic cancellation.

Chapter 3

Principles of Operation and Sizing Equations of Proposed Dual-Stator 6/4 FSPM Machine

To understand the operating principles of the proposed dual-stator 6/4 FSPM machine, harmonic analysis is performed to study the winding magnetomotive forces, magnet magnetomotive forces, airgap permeance variations, and airgap flux density harmonic components. The principle of torque production is also investigated by analyzing the harmonics interaction between winding magnetomotive forces with the airgap flux density harmonics. Sizing equation is a useful tool to determine the initial sizing for an electrical machine before performing more sophisticated and accurate finite element analysis. So, the sizing equations for the proposed dual-stator 6/4 FSPM machine are derived based on the generalized sizing laws for electrical machines.

3.1 Harmonic Analysis of Dual-Stator 6/4 FSPM Machine

3.1.1 Winding Magnetomotive Force

The stator structure is presented in a linear fashion in Figure 3.1 to better explain the winding theory. The winding function describes the spatial accumulation of the turns around the periphery of the airgap. Phase-A winding functions for both stators are illustrated in Figure 3.1(a)

and Figure 3.1(c). The value of the winding function has step changes when it crosses the positions where the coils are located. It is assumed that the winding function steps down when the position passes the cross sign of the winding direction (current flows perpendicular into the page), and vice versa as shown in Figure 3.1. The average value of the winding function is zero and its amplitude in this case is the number of turns per coil (N_c). Windings in the front and rear stator essentially have the same harmonic content, so only one stator winding function is investigated. The Fourier expansion of the front stator phase-A winding function $n_w(\theta_m)$ is provided in equation (3.1). Since $n_w(\theta_m)$ is an odd function that is symmetrical with respect to the origin as shown in Figure 3.1(a), only odd harmonics exist,

$$n_w(\theta_m) = \sum_{h=1,3,5}^{\infty} n_h \sin(h\theta_m) \tag{3.1}$$

where h is the harmonic order of the winding function, n_h is the h^{th} harmonic amplitude, and θ_m is the mechanical angle around the airgap.

The amplitude of h^{th} odd harmonic, n_h, is calculated using the Fourier series expansion method in equation (3.2),

$$\begin{aligned} n_h &= \frac{N_c}{\pi}\left\{\int_{-\frac{2\pi}{3}}^{\frac{\pi}{3}} (1)\sin(h\theta_m)d\theta_m + \int_{\frac{\pi}{3}}^{\frac{2\pi}{3}} (-1)\sin(h\theta_m)d\theta_m\right\} \\ &= -\frac{4N_c}{\pi h}\sin(\frac{\pi}{2}h)\sin(\frac{\pi}{6}h), \qquad h = 1,3,5,\ldots \end{aligned} \tag{3.2}$$

The winding function has all odd harmonics with the fundamental component having the largest amplitude. The rear stator winding is exactly electrically 180° out of phase. Again, only the front stator winding MMF is derived here.

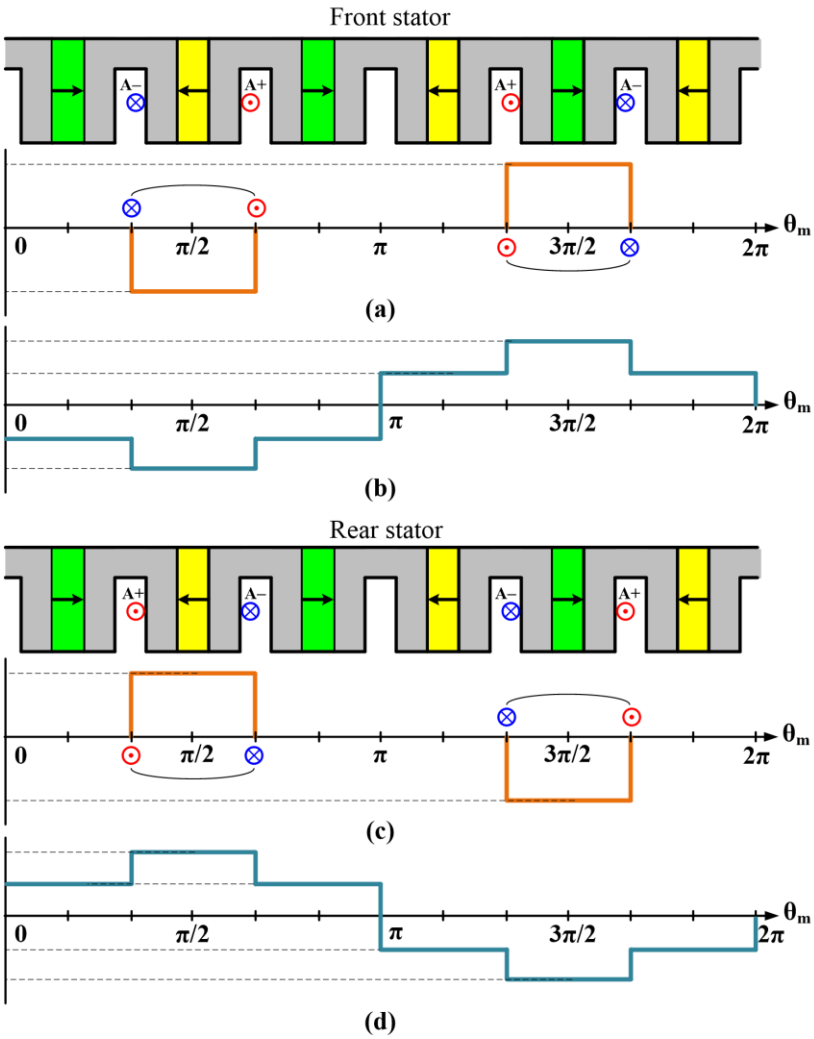

Figure 3.1. Winding function and three phase MMF for the dual-stator 6/4 FSPM machine (a) Front stator winding function (b) Front stator winding MMF (c) Rear stator winding function (d) Rear stator winding MMF.

The dual-stator 6/4 FSPM machine is assumed to be excited with balanced three phase currents. Then, the total MMF waveform at one time instant is shown in Figure 3.1(b) and Figure

3.1(d), when the phase-A current has an amplitude of I_m, and phase-B and C are both $-I_m/2$. If phase-A current is expressed as

$$i_a(t,\theta_{i0}) = I_m \cos(\omega_e t + \theta_{i0}) \tag{3.3}$$

where I_m is the current amplitude, ω_e is the electric angular frequency, θ_{i0} is the initial current phase angle. The total three phase MMF for the front stator winding is calculated below and the triplen harmonics are absent. When $h = 6k - 5$ and k is a positive integer, harmonic MMFs are positively rotating traveling waves shown as,

$$F_c(t,\theta_m) = 1.5 n_h I_m \sin(h\theta_m - \omega_e t - \theta_{i0}) \tag{3.4}$$

When $h = 6k - 1$ and k is a positive integer, harmonic MMFs are negatively rotating traveling waves expressed as

$$F_c(t,\theta_m) = 1.5 n_h I_m \sin(h\theta_m + \omega_e t + \theta_{i0}) \tag{3.5}$$

The above equations show that the fundamental MMF has one period around the airgap periphery that equals to one pole pair pattern, and it travels positively at a mechanical speed of ω_e. Generally speaking, the h^{th} MMF harmonic travels at a mechanical speed of ω_e / h with positive or negative rotational directions determined by either (3.4) or (3.5). Fourier decomposition of the total MMF is given in Figure 3.2 showing the 1^{st}, 5^{th}, and 7^{th} harmonic rotational directions and their speeds. The harmonic components of the winding MMFs are shown in Figure 3.3, and the magnitude diminishes as the order number increases. The winding MMFs in the rear stator have the same harmonic content and rotational speed but are out of phase by 180° electrically.

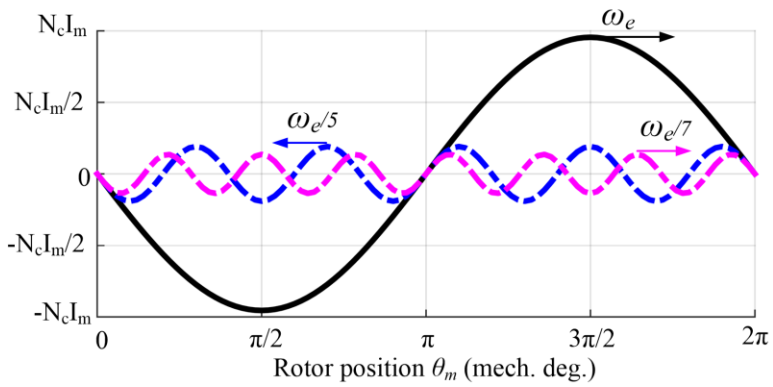

Figure 3.2. Three phase total winding MMF in the front stator winding decomposition into 1st, 5th, and 7th harmonics showing the rotational direction and mechanical speed.

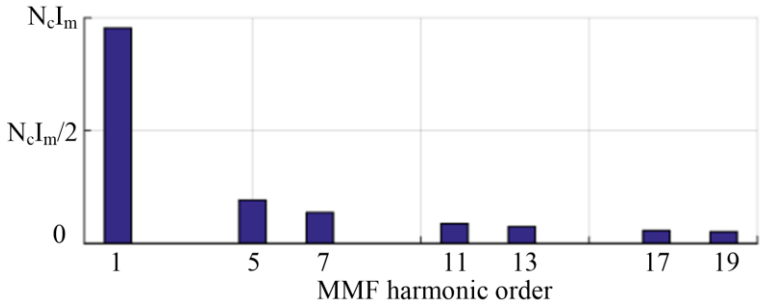

Figure 3.3. Total current MMF amplitude for different harmonic orders.

3.1.2 Magnetomotive Force from Permanent Magnets

The alternating permanent magnets produce stationary magnet MMF shown in Figure 3.4. The MMF has a positive amplitude of F_{pm} when the flux direction is from the rotor side to the stator side and vice versa. The harmonic expression derived based on Fourier expansion below shows that magnet MMF has orders that are odd multiples of $0.5N_m$ where N_m is the number of magnets.

$$
\begin{aligned}
F_{pm}(\theta_m) &= \sum_{n=1,2,3,\ldots}^{\infty} \left[F_{pm,n} \cos(n\theta_m) \right] \\
&= \frac{2}{\pi} \sum_{n=1,2,3,\ldots}^{\infty} [\int_0^{\frac{\pi}{6}} F_{pm} \cos(n\theta_m) d\theta_m - \int_{\frac{\pi}{6}}^{\frac{\pi}{2}} F_{pm} \cos(n\theta_m) d\theta_m \\
&\qquad + \int_{\frac{\pi}{2}}^{\frac{5\pi}{6}} F_{pm} \cos(n\theta_m) d\theta_m - \int_{\frac{5\pi}{6}}^{\pi} F_{pm} \cos(n\theta_m) d\theta_m] \cos(n\theta_m) \\
&= \frac{4F_{pm}}{\pi n} \sum_{\substack{n=3h \\ h=1,3,5,\ldots}}^{\infty} \left\{ \sin(\frac{\pi}{2} n)[2\cos(\frac{\pi}{3} n) - 1] \right\} \cos(n\theta_m) \\
&= \frac{4F_{pm}}{3\pi h} \sum_{h=1,3,5,\ldots}^{\infty} \left\{ \sin(\frac{3\pi h}{2})[2\cos(\pi h) - 1] \right\} \cos(3h\theta_m) \\
&= \sum_{h=1,3,5,\ldots}^{\infty} F_{pm,h} \cos(\frac{N_m}{2} h\theta_m)
\end{aligned}
\tag{3.6}
$$

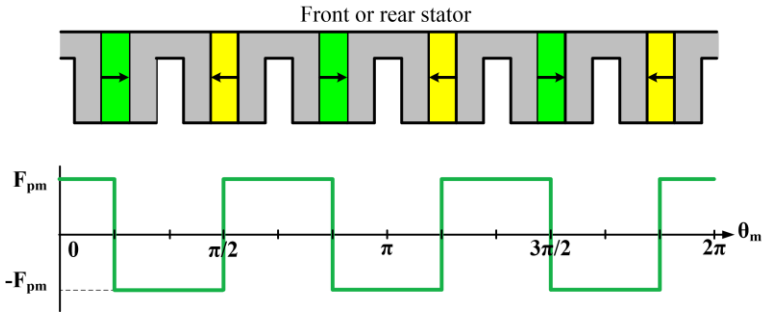

Figure 3.4. Magnet MMF for both front and rear stators.

3.1.3 Airgap Permeance from Rotor and Stator Sides

To make the study more general, the airgap flux permeance is assumed to be controlled by both the rotor side permeance and stator side permeance. The airgap permeance looking into the stator side is different than that looking into the rotor side. This doubly salient structure creates a

modulation effect similar to that in Vernier type of electric machines. The permeance function of rotor side is a traveling wave that is a function of both rotor position and time. The permeance function of stator side is stationary. To simplify the analysis and neglect the saturation effect and fringing effect, the permeance functions are approximated as step functions. The permeance is calculated for the rotor side first, and then for the stator side.

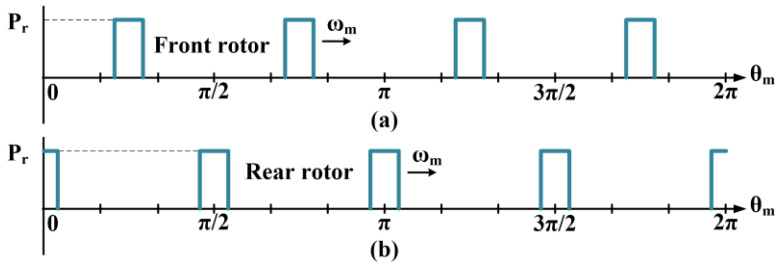

Figure 3.5. Permeance function for dual-stator 6/4 FSPM machine (a) front rotor rotational permeance function (b) rear rotor rotational permeance function.

The rotational rotor permeance is shown in Figure 3.5 at a particular rotor position for front and rear rotors respectively. When the front rotor is at the position shown in Figure 3.5(a), the harmonic expression for the rotor permeance is derived as,

$$P_{r,\,front}(\theta_m) = \frac{2P_r d}{\pi} + \frac{2}{\pi}\sum_{n=1,2,3\ldots}^{\infty}\left[\int_{\frac{\pi}{4}-\frac{d}{2}}^{\frac{\pi}{4}+\frac{d}{2}} P_r\cos(n\theta_m)d\theta_m + \int_{\frac{3\pi}{4}-\frac{d}{2}}^{\frac{3\pi}{4}+\frac{d}{2}} P_r\cos(n\theta_m)d\theta_m\right]$$

$$= \frac{2P_r d}{\pi} + \sum_{\substack{n=4h\\ h=1,2,3\ldots}}^{\infty}\frac{8P_r}{n\pi}\sin(\frac{nd}{2})\cos(\frac{n\pi}{2})\cos(\frac{n\pi}{4})$$

$$= \frac{2P_r d}{\pi} + \sum_{h=1,2,3\ldots}^{\infty}\frac{2P_r}{h\pi}\sin(2hd)\cos(h\pi)$$

$$= P_{r,0} + \sum_{h=1,2,3\ldots}^{\infty}(-1)^h P_{r,h} \qquad (3.7)$$

where P_r is the magnitude of rotor permeance, d is the angular width of rotor pole. When the rotor poles move to the right side, all the corresponding harmonics rotate at the same speed of ω_m. Therefore, the rotor permeance is also a function of time which is expressed as

$$P_{r,\,front}(\theta_m, t) = P_{r,0} + \sum_{h=1,2,3...}^{\infty} (-1)^h P_{r,h} \cos[N_r h(\theta_m - \omega_m t - \theta_{r0})] \tag{3.8}$$

where N_r is the number of rotor poles, ω_m is the rotor mechanical angular speed, and θ_{r0} is the initial rotor position.

It should be mentioned that $P_{r,front}(\theta_m,t)$ has non-negative values. The average value of the rotor permeance function is defined as $P_{r,0}$, and the amplitude of the h^{th} order rotor permeance is defined as $P_{r,h}$. Both $P_{r,0}$ and $P_{r,h}$ are functions of P_r and d. To simplify the analysis, $P_{r,front}(\theta_m,t)$ can be approximated as only considering the first harmonic content,

$$P_{r,\,front}(\theta_m, t) \approx P_{r,0} - P_{r,1} \cos[N_r(\theta_m - \omega_m t - \theta_{r0})] \tag{3.9}$$

The permeance function of the stator side of the dual-stator 6/4 FSPM machine is shown in Figure 3.6. It is assumed that the amplitude is approximated as P_s when the airgap faces the highly permeable stator teeth, and is zero when the airgap faces either the slot opening or the permanent magnet. The stator side permeance function has a period of two times the number of stator slots.

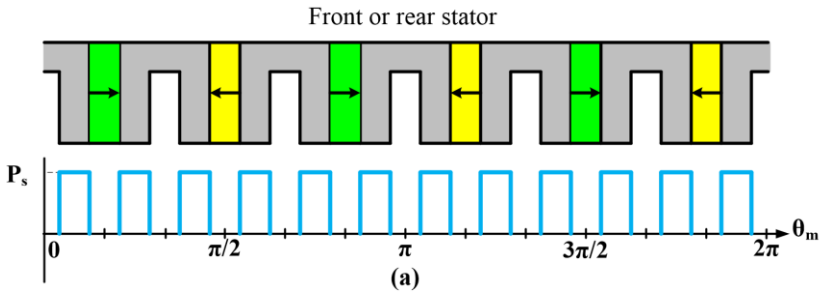

Figure 3.6. Permeance function of stator side of the dual-stator 6/4 FSPM machine.

The baseline design of the stator teeth width is chosen for this analysis, which assumes that the width of the stator teeth, magnet thickness, and slot opening are all the same. The stationary stator permeance as a function of mechanical angle θ_m in the airgap shown in Figure 3.6 is derived in the equation below,

$$
\begin{aligned}
P_s(\theta_m) &= \frac{P_s}{2} + \sum_{n=1,3,5...}^{\infty} P_{s,h}\cos(n\theta_m) \\
&= \frac{P_s}{2} + \sum_{n=1,3,5...}^{\infty} P_{s,h}\cos(n\theta_m) \\
&= \frac{P_s}{2} + \frac{2}{\pi}\sum_{n=1,2,3...}^{\infty}\Big[\int_{\frac{\pi}{24}}^{\frac{3\pi}{24}} P_s\cos(n\theta_m)d\theta_m + \int_{\frac{5\pi}{24}}^{\frac{7\pi}{24}} P_s\cos(n\theta_m)d\theta_m \\
&\qquad + \int_{\frac{9\pi}{24}}^{\frac{11\pi}{24}} P_s\cos(n\theta_m)d\theta_m + \int_{\frac{13\pi}{24}}^{\frac{15\pi}{24}} P_s\cos(n\theta_m)d\theta_m \\
&\qquad + \int_{\frac{17\pi}{24}}^{\frac{19\pi}{24}} P_s\cos(n\theta_m)d\theta_m + \int_{\frac{21\pi}{24}}^{\frac{23\pi}{24}} P_s\cos(n\theta_m)d\theta_m\Big]\cos(n\theta_m) \\
&= \frac{P_s}{2} + \frac{2}{\pi}\sum_{\substack{n=12h \\ h=1,3,5,...}}^{\infty}\left\{\frac{1}{n}\sum_{m=1,2,3}^{12}(-1)^m \sin\left[\frac{(2m-1)}{24}\pi n\right]\right\}\cos(n\theta_m) \\
&= P_{s,0} - \sum_{h=1,3,5...}^{\infty} P_{s,h}\cos(2N_s h\theta_m)
\end{aligned}
\tag{3.10}
$$

where $P_{s,0}$ is the average value of the permeance function, $P_{s,h}$ is the amplitude of the h^{th} permeance harmonic, and N_s is the number of stator slots which is six.

The stator side of the permeance can also be approximated by only considering the fundamental component of the harmonic, so that the stator permeance function is simplified as,

$$P_s(\theta_m) = P_{s,0} - P_{s,1}\cos(2N_s\theta_m) \tag{3.11}$$

A simplified model of airgap permeance can be obtained if only considering the rotor rotational permeance components. The airgap permeance in the front portion of the proposed dual-stator 6/4 FSPM machine is expressed as,

$$P_{g,front}(\theta_m, t) = P_{r,front}(\theta_m, t) \tag{3.12}$$

To take into consideration also the effect of stator side permeance variations, the airgap total permeance is obtained by the multiplication of normalized stationary stator permeance and rotational airgap permeance expressed in the equation below,

$$P_{g,front}(\theta_m, t) = P_s(\theta_m)P_{r,front}(\theta_m, t) / P_{s,0} \tag{3.13}$$

It should be mentioned that the total permeance in the airgap should maintain the same unit as permeance for physical meaning, and this is done by normalizing the stator side permeance with respect to its offset value ($P_{s,0}$). The rear airgap permeance is calculated in the same way such that the stator permeance is the same, but rotor rotational permeance is offset by electric 180° to the front rotor rotational permeance.

3.1.4 Airgap Flux Density due to Permanent Magnets

The airgap flux density in the front portion of the dual-stator 6/4 FSPM machine due to the permanent magnets is calculated by the multiplication of magnet MMF and airgap permeance.

$$\begin{aligned} B_{g,front}(\theta_m,t) &= F_{pm}(\theta_m)P_{g,front}(\theta_m,t) \\ &= \left[\sum_{h=1,3,5,\ldots}^{\infty} F_{pm,h}\cos(\frac{N_m}{2}h\theta_m)\right]\left[1-\sum_{h=1,3,5\ldots}^{\infty}(P_{s,h}/P_{s,0})\cos(2N_s h\theta_m)\right] \\ &\quad \cdot\left\{P_{r,0}+\sum_{h=1,2,3\ldots}^{\infty}(-1)^h P_{r,h}\cos[N_r h(\theta_m-\omega_m t-\theta_{r0})]\right\} \\ &= B_{g,sta}(\theta_m)+B_{g,rot}(\theta_m,t)+B_{g,\mathrm{mod}}(\theta_m,t) \end{aligned} \quad (3.14)$$

Based on the interactions of permanent magnet MMF harmonics and permeance harmonics, the resultant airgap harmonic components are categorized into three types defined as the stationary component $B_{g,sta}(\theta_m)$, the rotor permeance component $B_{g,rot}(\theta_m,t)$, and the modulation component $B_{g,mod}(\theta_m,t)$.

The stationary component of the airgap flux density $B_{g,sta}(\theta_m)$ comes from the interaction between magnet MMF harmonics and merely the stationary components of permeance variation shown as

$$\begin{aligned} B_{g,sta}(\theta_m) &= \left[\sum_{h=1,3,5,\ldots}^{\infty} F_{pm,h}\cos(\frac{N_m}{2}h\theta_m)\right]P_{r,0}[1-\sum_{h=1,3,5\ldots}^{\infty}(P_{s,h}/P_{s,0})\cos(2N_s h\theta_m)] \\ &\approx \left[F_{pm,1}\cos(\frac{N_m}{2}\theta_m)\right]P_{r,0}[1-(P_{s,1}/P_{s,0})\cos(2N_s\theta_m)] \\ &= P_{r,0}F_{pm,1}\left\{\cos(\frac{N_m}{2}\theta_m)-\frac{P_{s,1}}{2P_{s,0}}[\cos(\frac{N_m}{2}\theta_m+2N_s\theta_m)+\cos(\frac{N_m}{2}\theta_m-2N_s\theta_m)]\right\} \end{aligned} \quad (3.15)$$

The rotational component of airgap flux density is attributed from the interaction between magnet MMF harmonics and the harmonic components of rotor rotational permeance as

$$B_{g,rot}(\theta_m,t)=\left[\sum_{h=1,3,5,\ldots}^{\infty}F_{pm,h}\cos(\frac{N_m}{2}h\theta_m)\right]\left\{\sum_{h=1,2,3\ldots}^{\infty}(-1)^h P_{r,h}\cos[N_r h(\theta_m-\omega_m t-\theta_{r0})]\right\}$$

$$\approx-\left[F_{pm,1}\cos(\frac{N_m}{2}\theta_m)\right]P_{r,1}\cos[N_r(\theta_m-\omega_m t-\theta_{r0})]$$

$$=-\frac{1}{2}F_{pm,1}P_{r,1}\{\cos[(\frac{N_m}{2}-N_r)\theta_m+N_r(\theta_{r0}+\omega_m t)]$$

$$+\cos[(\frac{N_m}{2}+N_r)\theta_m-N_r(\theta_{r0}+\omega_m t)]\} \qquad (3.16)$$

The modulational component of airgap flux density is due to the interaction between magnet MMF and both stator and rotor teeth alternating permeance components as shown,

$$B_{g,\mathrm{mod}}(\theta_m,t)=\left[\sum_{h=1,3,5,\ldots}^{\infty}F_{pm,h}\cos(\frac{N_m}{2}h\theta_m)\right]\left\{\sum_{h=1,2,3\ldots}^{\infty}(-1)^h P_{r,h}\cos[N_r h(\theta_m-\omega_m t-\theta_{r0})]\right\}$$

$$\cdot\left[-\sum_{h=1,3,5\ldots}^{\infty}(P_{s,h}/P_{s,0})\cos(2N_s h\theta_m)\right]$$

$$=\left[F_{pm,1}\cos(\frac{N_m}{2}\theta_m)\right]\left\{-P_{r,1}\cos[N_r(\theta_m-\omega_m t-\theta_{r0})]\right\}\cdot\left[-(P_{s,1}/P_{s,0})\cos(2N_s h\theta_m)\right]$$

$$=\frac{1}{4}F_{pm,1}\frac{P_{s,1}P_{r,1}}{P_{s,0}}\{\cos[(\frac{N_m}{2}-2N_s+N_r)\theta_m-N_r(\theta_{r0}+\omega_m t)]$$

$$+\cos[(\frac{N_m}{2}+2N_s-N_r)\theta_m+N_r(\theta_{r0}+\omega_m t)]$$

$$+\cos[(\frac{N_m}{2}-2N_s-N_r)\theta_m+N_r(\theta_{r0}+\omega_m t)]$$

$$+\cos[(\frac{N_m}{2}+2N_s+N_r)\theta_m-N_r(\theta_{r0}+\omega_m t)]\} \qquad (3.17)$$

To simplify the study, only fundamental component of the stator permeance, rotor permeance, and magnet MMF are considered. By substituting the number of stator slots, rotor poles, and magnets into the equations, the stationary component is simplified as,

$$B_{g,sta}(\theta_m) = P_{r,0}F_{pm,1}\left\{\cos(3\theta_m) - \frac{P_{s,1}}{2P_{s,0}}[\cos(15\theta_m) + \cos(9\theta_m)]\right\} \tag{3.18}$$

The rotational component is simplified also by only considering the fundamental harmonic content as,

$$B_{g,rot}(\theta_m, t) = -\frac{1}{2}F_{pm,1}P_{r,1}\{\cos[\theta_m - 4(\theta_{r0} + \omega_m t)] + \cos[7\theta_m - 4(\theta_{r0} + \omega_m t)]\} \tag{3.19}$$

The modulational component can also be simplified by accounting for the fundamental harmonic component as,

$$\begin{aligned} B_{g,\mathrm{mod}}(\theta_m, t) = \frac{1}{4}F_{pm,1}\frac{P_{s,1}P_{r,1}}{P_{s,0}}\{&\cos[5\theta_m + 4(\theta_{r0} + \omega_m t)] \\ &+ \cos[11\theta_m + 4(\theta_{r0} + \omega_m t)] \\ &+ \cos[13\theta_m - 4(\theta_{r0} + \omega_m t)] \\ &+ \cos[19\theta_m - 4(\theta_{r0} + \omega_m t)]\} \end{aligned} \tag{3.20}$$

To better understand the properties of airgap harmonic components, the rotational speed, rotational direction, and initial phase angle for each harmonic are carefully examined with results shown in TABLE 3.1, TABLE 3.2, and TABLE 3.3. It is not surprising to see that the airgap flux density harmonic components have the same harmonic content as the winding MMF.

Stationary airgap flux density $B_{g,sta}(\theta_m)$ shown in TABLE 3.1 has harmonics that are equivalent to pole pair numbers of 3, 9, and 15. Those stationary harmonics are produced due to the fundamental magnet MMF with average rotor permeance.

TABLE 3.1 HARMONIC CONTENTS OF STATIONARY AIRGAP FLUX DENSITY

Stationary airgap flux density $B_{g,sta}(\theta_m)$				
Magnet MMF order	**Amplitude**	**Pole pair**	**Speed**	**Phase angle**
1	$F_{pm,1}P_{r,0}$	3	0	0
	$0.5F_{pm,1}P_{r,0}P_{s,1}/P_{s,0}$	9	0	π
		15	0	

Rotor rotational airgap flux density $B_{g,rot}(\theta_m,t)$ shown in TABLE 3.2 is of primary interests here. The magnet MMF harmonics of fundamental, 3rd, and 5th ($F_{pm,1}$, $F_{pm,3}$, and $F_{pm,5}$) orders are studied with their interactions with rotor fundamental permeance ($P_{r,1}$). The resultant airgap flux density harmonic contents from fundamental magnet MMF harmonic with fundamental rotor permeance have harmonic orders of 1 and 7. The 3rd harmonic magnet MMF interacts with fundamental rotor permeance to produce 5th and 13th harmonics, and the 5th harmonic of magnet MMF interacts with fundamental rotor permeance to produce 11th and 19th harmonics. Those results demonstrate that the airgap flux density harmonics produced by the magnet MMF and rotor rotational permeance harmonics have the same pole pairs and rotational speeds as the harmonics of winding MMFs. The initial phase angle for the airgap flux density harmonics is π for the front portion of the machine and is 0 for the rear portion of the machine.

TABLE 3.2. HARMONIC CONTENTS OF ROTATIONAL AIRGAP FLUX DENSITY

Rotational airgap flux density harmonic contents				
Magnet MMF order	**Amplitude**	**Pole pair**	**Speed**	**Phase angle**
1	$0.5F_{pm,1}P_{r,1}$	1	$N_r\,\omega_m$	π (front stator), 0 (rear stator)
		7	$N_r\,\omega_m$ /7	
3	$0.5F_{pm,3}P_{r,1}$	5	$-N_r\,\omega_m$ /5	
		13	$N_r\,\omega_m$ /13	
5	$0.5F_{pm,5}P_{r,1}$	11	$-N_r\,\omega_m$ /11	
		19	$N_r\,\omega_m$ /19	

The modulation airgap flux density $B_{g,mod}(\theta_m,t)$ is produced by the interaction of magnet MMF harmonics and the rotor and stator alternating permeance harmonics. If the harmonics of 1st, 3rd, and 5th are investigated for the magnet MMF, and only fundamental harmonics of rotor and stator permeance are studied, the resultant airgap flux density harmonics are calculated and tabulated in TABLE 3.3. It should be noted that the amplitude of those harmonics is progressively reduced at higher orders.

TABLE 3.3. HARMONIC CONTENTS OF MODULATION AIRGAP FLUX DENSITY

Stator and rotor teeth modulational airgap flux density $B_{g,mod}(\theta_m,t)$				
Magnet MMF order	**Amplitude**	**Pole pair**	**Speed**	**Phase angle**
1	$0.25F_{pm,1}P_{r,1}P_{s,1}/P_{s,0}$	5	$-N_r\,\omega_m$ /5	0 (front stator), π (rear stator)
		11	$-N_r\,\omega_m$ /11	
		13	$N_r\,\omega_m$ /13	
		19	$N_r\,\omega_m$ /19	
3	$0.25F_{pm,3}P_{r,1}P_{s,1}/P_{s,0}$	1	$N_r\,\omega_m$	
		17	$-N_r\,\omega_m$ /17	
		7	$N_r\,\omega_m$ /7	
		25	$N_r\,\omega_m$ /25	
5	$0.25F_{pm,5}P_{r,1}P_{s,1}/P_{s,0}$	*7*	$N_r\,\omega_m$ /7	
		23	$-N_r\,\omega_m$ /23	
		1	$N_r\,\omega_m$	
		31	$N_r\,\omega_m$ /31	

3.1.5 Torque Production Principle of Dual-Stator 6/4 FSPM Machine

It is known that the non-zero average torque of an electrical machine is produced by the interaction of winding MMF harmonic(s) with the corresponding airgap flux density harmonic(s). The torque production principle of the dual-stator 6/4 FSPM machine can be explained by analyzing the harmonic contents of the winding MMF and airgap flux density derived in previous sections.

Results show that the spatial pole pair numbers of the airgap flux density are the same as the winding MMF harmonics, i.e. 1^{st}, 5^{th}, 7^{th}, 11^{th}, 13^{th}, and 19^{th} etc. Further investigation also shows that each of these airgap flux density harmonics has the same rotational speed and rotational direction as the corresponding winding MMF harmonic. In addition, the winding MMF harmonics and airgap flux density harmonics of the same order are orthogonal in phase simultaneously for all harmonics. Thus, all of these harmonics contribute to the produced non-zero average torque in ideal condition. However, the positively rotating harmonics produce positive torque, and the negatively rotating harmonics produce negative torque.

The average torque component produced by the fundamental winding MMF and fundamental airgap flux density harmonic is dominant because their magnitudes are the largest. The net contribution of non-zero average torque from higher order harmonic components are less prominent because their magnitudes are relatively small, and the positive torque components are cancelled by the negative torque components.

3.2 Sizing Equations of Dual-Stator 6/4 FSPM Machine

3.2.1 Calculation of Flux Linkage

The even harmonics are canceled in the total flux linkage, but they still exist in each coil with the 2nd order being the dominant component. The flux linkage in each coil of the proposed dual-stator machine can be reasonably approximated as the summation of the fundamental component and 2nd order harmonic component since the magnitudes of higher order harmonics are negligible. The flux linkage of one coil as a function of rotor position is shown in Figure 3.7 for half an electric cycle. Five key rotor positions are marked by blue circles separated by 45° electrically. The peak flux linkage in one phase-A coil is reached between 45° and 90° electrically represented by the red circle in Figure 3.7. The rotor position at this maximum flux linkage is defined as angle θ_{max}. If the ratio of 2nd order harmonic magnitude over fundamental component magnitude is defined as $k = \lambda_2/\lambda_1$, the rotor position angle θ_{max} is calculated as

$$\theta_{\max} = \cos^{-1}(-0.125/k + 0.125\sqrt{1/k^2 + 32}) \tag{3.21}$$

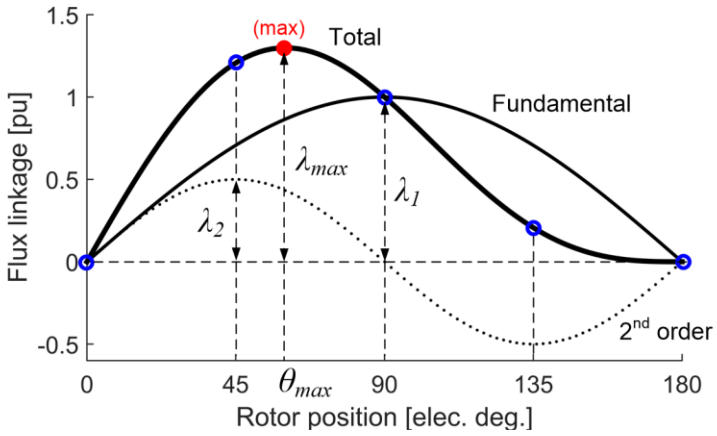

Figure 3.7. Flux linkage in the front stator winding approximated as the summation of fundamental and 2nd order harmonic components.

The maximum flux linkage for a coil winding is physically achieved when one of the rotor teeth faces exactly one stator tooth which is enclosed by that phase coil. For example, phase-A, the position shown in Figure 3.8, achieves maximum positive flux linkage corresponding to the rotor angle θ_{max}. The flux that links the phase-A coil is marked by solid red lines, and it has two paths. The first path is the main flux and it follows a path via the stator core directly. The second path is the leakage flux that circles in the air around the outer periphery of the magnets and then returns to the stator core to join the main flux path, as shown in Figure 3.8. The leakage flux that does not link phase-A coils is marked by dotted blue lines.

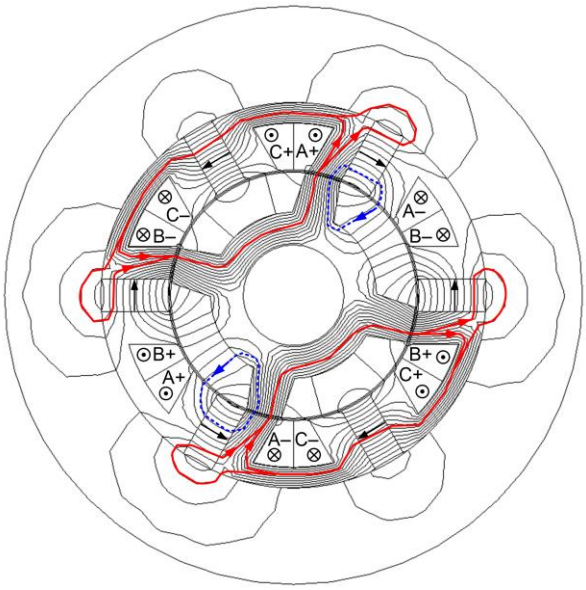

Figure 3.8. Main flux and leakage flux path at the rotor position where maximum phase-A flux linkage is achieved.

Given the flux path illustration for a single-phase winding, it is now reasonable to calculate the maximum flux per phase winding per stator at rotor position θ_{max} as

$$\lambda_{\max} = N_t B_{g,pk} K_m K_t (\frac{D_{is}\pi}{N_s}) L_{e,1/2} \cos(P_r \omega_m t) \tag{3.22}$$

where N_t is the number of turns connected in series per phase per stator, $B_{g,pk}$ is the peak airgap flux density in between the aligned stator tooth and rotor tooth, K_m is the ratio of linkage flux over the summation of main flux and leakage flux, K_t is the stator tooth width ratio defined by the ratio of stator tooth width over stator pole pitch width, D_{is} is the stator inner diameter, N_s is the number of stator slots, $L_{e,1/2}$ is the effective stack length for one stator only.

The fundamental flux linkage λ_1 is calculated by scaling the maximum flux linkage λ_{max} by K_{fund} as

$$\lambda_1 = K_{fund} \lambda_{\max} = N_t B_{g,pk} K_m K_{fund} K_t (\frac{D_{is}\pi}{N_s}) L_{e,1/2} \cos(P_r \omega_m t) \tag{3.23}$$

where K_{fund} is the fundamental coefficient defined by the ratio of fundamental flux linkage over the maximum flux linkage. It is calculated as

$$K_{fund} = \lambda_1 / \lambda_{\max} = 1/(\sin(\theta_{\max}) + k\sin(2\theta_{\max})) \tag{3.24}$$

Substituting (3.24) into (3.23), the fundamental component of the flux linkage in a single stator winding can be calculated. The total fundamental flux linkage per phase of the dual-stator machine is obtained by doubling the value of λ_1 as

$$\lambda_{1,tot}(t) = 2\lambda_1 = N_t B_{g,pk} K_m K_{fund} K_t (\frac{D_{is}\pi}{N_s}) L_e \cos(N_r \omega_m t) \tag{3.25}$$

where L_e is the summation of two effective stator stack lengths that is equal to $2L_{e,1/2}$. It is important to notice that L_e does not include the length of the physical gap between two stators.

3.2.2 Calculation of Back-EMF

The fundamental component of the flux linkage is calculated previously, so the peak value of the fundamental back-EMF is derived as

$$E_{pk1} = |d\lambda_{1,tot}(t)/dt| = 2\pi^2 N_t B_{g,pk} K_m K_{fund} K_t (\frac{f_e}{N_s}) D_{is} L_e \quad (3.26)$$

The even order harmonics are canceled in the back-EMF, but there will be some remaining low order odd harmonics of small magnitudes. However, their effects in power production are essentially negligible compared to the fundamental component. Therefore, the output power can be reasonably approximated as only considering the fundamental back-EMF.

3.2.3 Calculation of Output Power and Torque

The generalized sizing equation for synchronous machines states that the output power is calculated as the multiplication of peak EMF E_{pk1}, peak current I_{pk}, power waveform factor K_p, the number of phases m, and the efficiency η as below [276].

$$P_{out} = \eta \frac{m}{T} \int_0^T e(t)i(t)dt = \eta m K_p E_{pk1} I_{pk} = 0.5\eta m E_{pk1} I_{pk} \quad (3.27)$$

The dual-stator 6/4 FSPM machine has negligible saliency so that it is assumed that all torque is produced by magnet torque and there is negligible reluctance torque. The back-EMF space vector is in-phase with phase current vector, so the power waveform coefficient becomes 0.5 in the equation. When the electrical loading $A_{s,rms}$ is given, peak phase current magnitude is calculated as

$$I_{pk} = \frac{\sqrt{2} D_{is} \pi}{2 m N_t} A_{s,rms} \tag{3.28}$$

Substitution of the peak back-EMF value and peak current value into (3.27) yields the output power equation of the dual-stator 6/4 FSPM machine

$$P_{out} = \frac{\sqrt{2}\pi^3}{2} K_m K_{fund} K_t \eta (\frac{f_e}{N_s}) B_{g,pk} A_{s,rms} D_{is}^2 L_e \tag{3.29}$$

The output torque is calculated as

$$T_{out} = \frac{\sqrt{2}\pi^2}{4} K_m K_{fund} K_t \eta (\frac{N_r}{N_s}) B_{g,pk} A_{s,rms} D_{is}^2 L_e \tag{3.30}$$

The above equation shows that to increase the output torque, not only should the magnetic loading ($B_{g,pk}$) and electrical loading ($A_{s,rms}$) be increased, but the magnetizing coefficient (K_m) and fundamental coefficient (K_{fund}) should also be increased.

The ratio of 2nd order harmonic over fundamental component (k) is related to the torque production. The normalized per-unit torque as a function of k is plotted in Figure 3.9. It shows that the lower the value of k, the higher the output torque. The torque is maximized when there is no 2nd order component in each coil, which is an ideal case. From the machine design perspective, the 2nd order harmonic needs to be reduced to increase the average torque. Meanwhile, the leakage flux shown in dotted blue lines in Figure 3.8 should be minimized if possible.

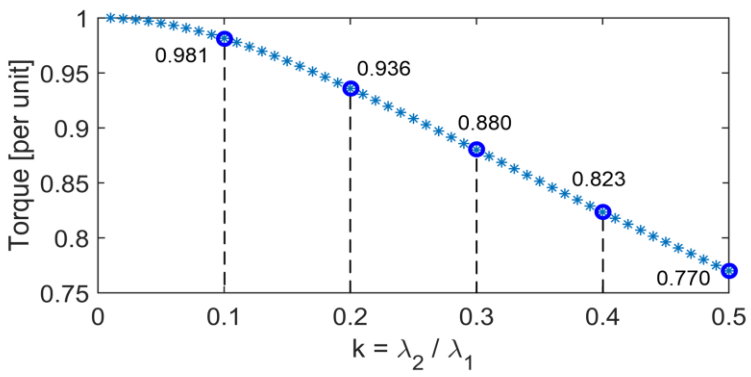

Figure 3.9. Per unit output torque as a function of the ratio *(k)* of 2nd order flux linkage λ_2 over fundamental flux linkage λ_1.

3.3 Summary

This chapter presents a comprehensive discussion on the fundamental principles of the dual-stator 6/4 FSPM machine. Harmonic analysis is performed to study the harmonic contents of the winding magnetomotive forces, magnet magnetomotive forces, airgap permeance harmonics, and airgap flux density harmonics. The torque production principle is explained based on analyzing the harmonic interactions between winding magnetomotive forces and airgap flux density harmonics. The sizing equations are derived to provide initial design guidelines for a given specification. The key research conclusions are summarized as follows.

- The proposed dual-stator 6/4 FSPM machine has odd harmonic orders of the winding MMF. The lowest winding MMF order is the fundamental component, which means that the MMF has one pole pair pattern. There are positively and negatively rotating MMF harmonics of higher orders.

- The proposed dual-stator 6/4 FSPM machine operates on the principle of flux modulation from the interaction between the magnet MMF harmonics and airgap permeance harmonics. When both the stator and rotor sides of the permeance variations are taken into consideration, the airgap flux density harmonic contents can be divided into three categories, which are the stationary components, rotor rotational components, and modulation components.
- The harmonic contents of the winding MMF have the same harmonic order, rotational speed, rotational direction, and are always orthogonal to the corresponding airgap flux density components. Those harmonics interact to produce both positive and negative non-zero average torque.
- The sizing equation of the proposed dual-stator 6/4 FSPM machine demonstrates that to increase the output power/torque the machine, the 2^{nd} order harmonic content should be reduced, the leakage flux linkage should be minimized, and the magnetic and electrical loading should be increased.

Chapter 4

Analysis and Comparison of Dual-Stator 6/4 FSPM Machines

This chapter presents first the characterization of a proof-of-concept design of dual-stator 6/4 FSPM machine. Then, the proposed novel dual-stator 6/4 FSPM machine is compared with the conventional 6/4 FSPM machine to quantitatively demonstrate the performance improvements such as the total harmonic distortion reduction in flux linkage, back-EMF harmonic, and reduction in cogging torque. Also, a more detailed comparison of the proposed three viable dual-stator 6/4 FSPM machine topologies in the previous chapter is studied to show the design considerations for each topology. The basic electromagnetic performance and the torque density of three topologies are compared. The manufacturing, assembling simplicity and overall performances are also evaluated for the three topologies.

4.1 Analysis and Performance Characterization of Proof-of-Concept Dual-Stator 6/4 FSPM Machine

4.1.1 Design for a Proof-of-Concept Dual-Stator 6/4 FSPM Machine

To demonstrate the concept of total harmonic reduction in the flux linkage and back-EMF in the novel dual-stator 6/4 FSPM machine, it is reasonable to start with designing a low-power-

low-speed machine in the beginning. The initial design utilizes the sizing equations derived in the previous chapter to quantify the key dimensions of the dual-stator 6/4 FSPM machine. Typical values of the parameters in the sizing equations are tabulated in TABLE 4.1 for a 1.5 kW 1,800 rpm dual-stator 6/4 FSPM machine design using the first topology. It should be noted that this design is a baseline design that is not optimized yet. The FEA study in the later section utilizes those design values to evaluate the machine performance.

TABLE 4.1. PARAMETERS FOR A 1.5 KW PROOF-OF-CONCEPT MACHINE

Magnetizing coefficient, K_m	0.92
Fundamental coefficient, K_{fund}	0.78
Stator tooth width ratio, K_t	0.25
Peak airgap flux density, $B_{g,pk}$ [T]	1.6
Electrical loading, $A_{s,rms}$ [kA$_{rms}$/m]	21.15
Number of stator slots, P_s	6
Number of phases, m	3
Efficiency, η	95 %
Output power, P_{out} [kW]	1.5
Rated speed, n_r [rpm]	1800
Fundamental frequency, f_e [Hz]	120
Stator outer diameter, D_{os} [mm]	130
Stator inner diameter, D_{is} [mm]	84.5
Airgap length, g [mm]	1
Magnet remnant flux density, B_r [T]	1.2
Magnet width, d_m [mm]	11
Single stator stack length, $L_{e.1/2}$, [mm]	42.5
Total effective stack length, L_e [mm]	85
Number of turns per phase per stator, N_t	120
Phase current, I_s [A$_{rms}$]	7.8
Current density, J_s [A$_{rms}$/mm^2]	7.5
Slot fill factor, K_{cu}	50 %

4.1.2 No Load Analysis of Proof-of-Concept Machine

4.1.2.1 Flux Linkage and Back-EMF at No Load Condition

The proposed dual-stator 6/4 FSPM machine is studied by FEA to validate the concept of even harmonic elimination in the flux linkage and back-EMF. To accurately calculate the complex nature of the proposed machine, a 3D FEA full machine model including the end winding is built for analysis. The permanent magnets used are NdFeB type with a remnant flux density of 1.2 T and a coercivity of 900 kA/m. The width of the magnet, stator tooth, and stator slot opening are all made equal as is the conventional design practice proposed by previous researchers [56]. The thickness of stator yoke is slightly reduced to increase the slot area provided so that the stator yoke saturation level is well-controlled.

The simulation result at open circuit condition for flux linkage is shown in Figure 4.1. Decomposition of phase A winding flux linkage in each coil matches the analyzed waveforms. FFT study for the flux linkage in Figure 4.2 shows that the fundamental component is dominant with minor 3^{rd}, 5^{th}, and 7^{th} harmonics. These low order odd harmonics typically exist in any FSPM machines. The even order harmonics in the flux linkage are completely canceled at the no-load condition, as expected.

The back-EMF waveforms are given in Figure 4.3. FFT analysis in Figure 4.4 shows the fundamental component plus several low order odd harmonics. The harmonics in the back-EMF are more prominent than that in the flux linkage. This is because the higher order harmonics are amplified by the harmonic order through differentiation. Due to the nature of the concentrated winding configuration, these odd order harmonics cannot be eliminated. The 3^{rd}, 5^{th}, and 7^{th}

harmonics in the back-EMF have 2.64%, 7.78%, and 4.19% of the amplitude of fundamental component respectively. Further work can be done to minimize those harmonics and make the back-EMF with less harmonic distortion, which will be discussed in later chapters. Compared with the conventional 6/4 FSPM machine whose flux linkage and back-EMF are shown in Figure 2.2 and Figure 2.4, the proposed machine has the workable back-EMF waveform that is suitable for a normal inverter drive.

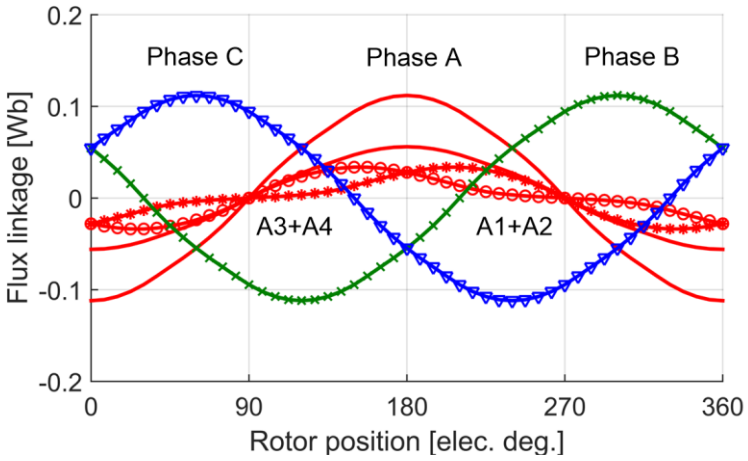

Figure 4.1. Flux linkage of the 1.5 kW dual-stator 6/4 FSPM machine.

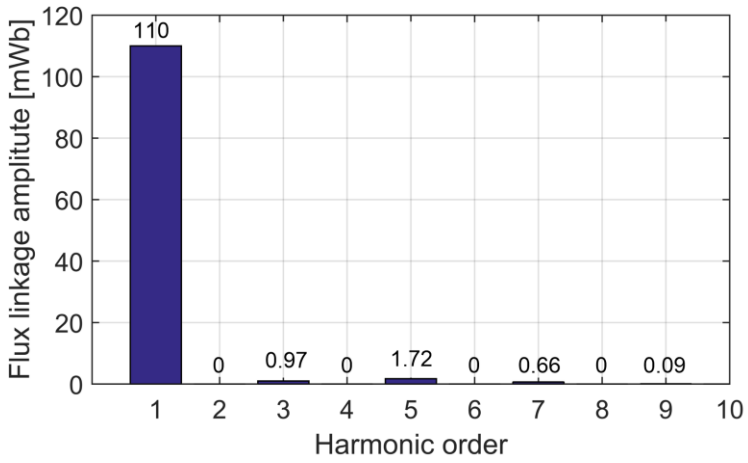

Figure 4.2. FFT of flux linkage of the 1.5 kW dual-stator 6/4 FSPM machine.

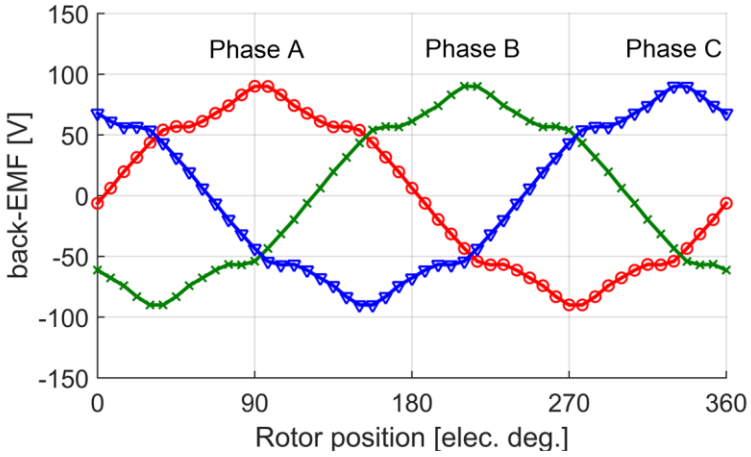

Figure 4.3. Back-EMF of the 1.5 kW dual-stator 6/4 FSPM machine.

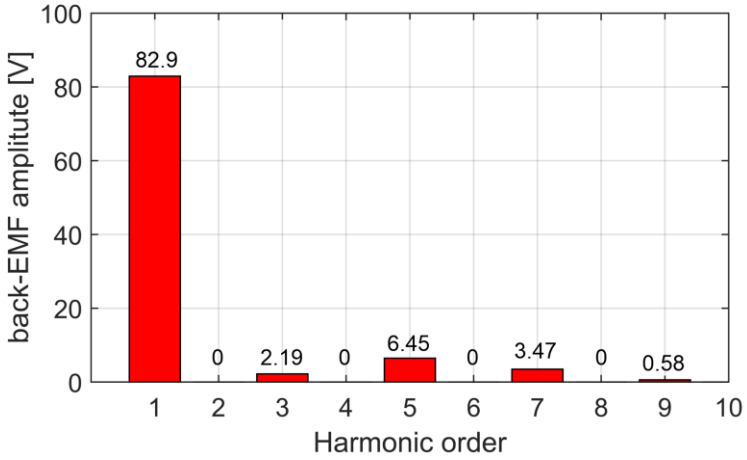

Figure 4.4. FFT of back-EMF of the 1.5 kW dual-stator 6/4 FSPM machine.

4.1.2.2 Magnetic Field Distribution at No Load Condition

The proposed dual-stator 6/4 FSPM machine has a 3D flux distribution pattern that is different than the conventional 6/4 FSPM machine. The magnetic field distributions at four key rotor positions are plotted in Figure 4.5 from an isometric view point. When the rotor rotates

counter-clockwise, the flux linkage in phase A winding changes by 90° electrically. The four positions (a) to (d) shown in Figure 4.5 correspond to 0°, 90°, 180°, and 270° in Figure 4.1.

The dual-stator structure introduces symmetry for the flux density distribution in the machine. Flux linkage for phase A winding reaches peak values at position (a) and (c) with negative and positive polarities. Flux linkage becomes zero at (b) and (d) positions. The front stator and rear stator are magnetized alternatively by 180° phase shift shown in the figure. The magnets in the dual-stator machine are shown to have higher average flux density than the conventional 12/10 topology. This is due to the much thicker magnets used in the 6/4 topology.

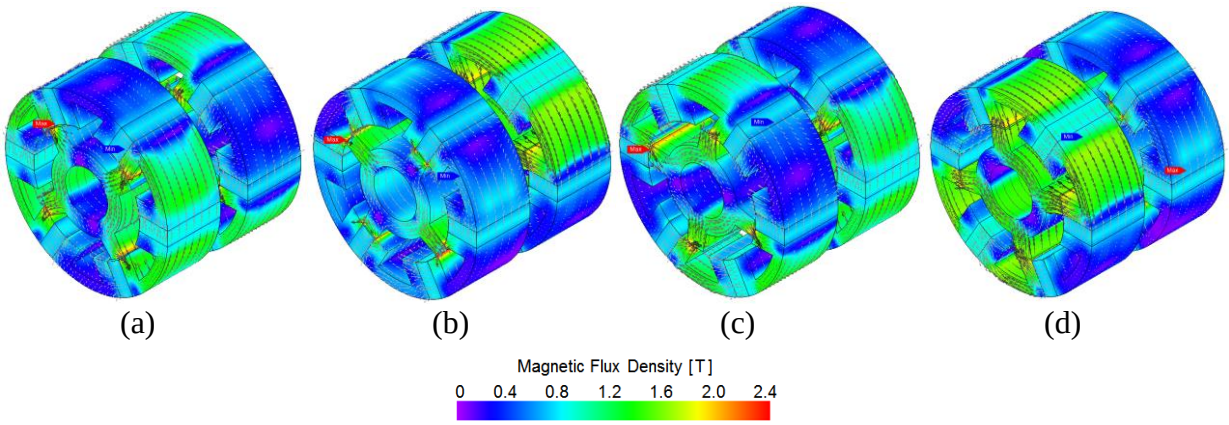

Figure 4.5. Open circuit magnetic flux density distribution in 3D view, with corresponding rotor position and flux linkage for phase A windings (a) rotor position at 0° elec., negative flux linkage (b) rotor position at 90° elec., zero flux linkage (c) rotor position at 180° elec., positive flux linkage (d) rotor position at 270° elec., zero flux linkage.

4.1.2.3 Influence of Stator Teeth and Rotor Pole Width to Low Order Harmonics

The performance of flux-switching permanent magnet machine is sensitive to the geometrical variations of the stator tooth width, magnet thickness, and rotor tooth width. This is

due to the airgap flux density modulation effects from the highly permeable steel in the stator teeth and rotor tooth. The baseline design for the machine is to assume that the width of stator tooth, magnet thickness, and slot opening width are the same. However, it is interesting to investigate how the fundamental magnetic properties change with respect to the variations of the width of stator tooth and rotor tooth.

To provide a better understanding of the influence of rotor tooth width to the multiple harmonics in the 6/4 FSPM machine, the low order odd harmonics (1^{st}, 3^{rd}, 5^{th}, and 7^{th}) as well as the 2^{nd} order harmonic in the flux linkage and back-EMF waveforms are shown as a function of rotor tooth width ratio in Figure 4.6 and Figure 4.7 respectively. It should be noted that the 2^{nd} harmonic does not exist in the total phase flux linkage or back-EMF, but each coil still has 2^{nd} harmonic. So, the red dotted line shows the total 2^{nd} order harmonic that would otherwise exist in the total phase windings. The rotor tooth width ratio is defined as the ratio of actual rotor tooth width over the baseline rotor tooth width which is equal to the baseline stator tooth width.

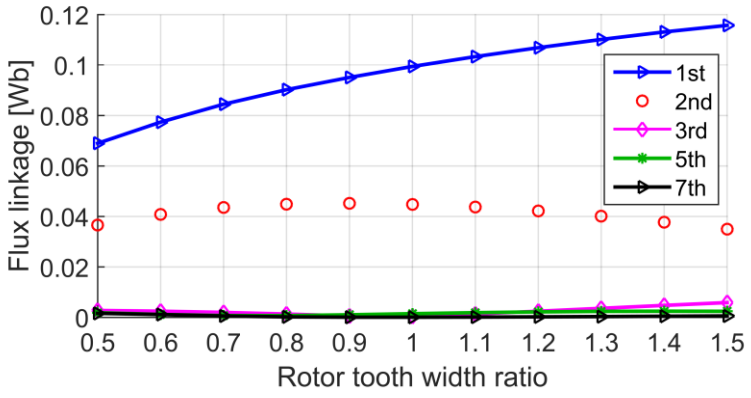

Figure 4.6. Flux linkage harmonic components variation as a function of different rotor tooth width ratio.

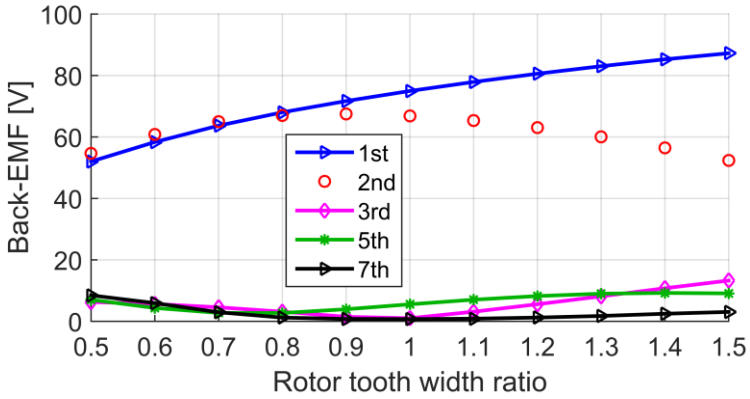

Figure 4.7. Back-EMF harmonic components variation as a function of different rotor tooth width ratio.

The results show that the fundamental flux linkage and back-EMF always increase because of wider rotor tooth. The reason for this is that more steel is available to conduct the magnetic flux that is linked to the windings, and there is less saturation in the rotor tooth. However, it is seen that the 2nd order harmonic does not change monotonically as the width of rotor tooth changes. There is a rotor tooth width that generates the maximum 2nd order harmonic. Also, higher order odd harmonics also have a non-monotonic relationship with the change of rotor tooth width.

The low order harmonic variations in flux linkage and back-EMF as functions of stator tooth width ratio are shown in Figure 4.8 and Figure 4.9. The stator tooth width ratio is defined as the ratio of actual stator tooth width over the baseline stator tooth width which is equal to the slot opening width and magnet thickness. The trend for each harmonic order is very close to the figures of rotor tooth width ratio. It can be observed that thicker stator tooth also increases the fundamental flux linkage and back-EMF. In terms of increasing the fundamental flux linkage and reducing the 2nd order harmonic, the width of the stator tooth and rotor tooth should be increased, given the

condition that higher order odd harmonics are negligible. However, designs that increase only the fundamental flux linkage are prone to increase cogging torque that are not desirable for operation.

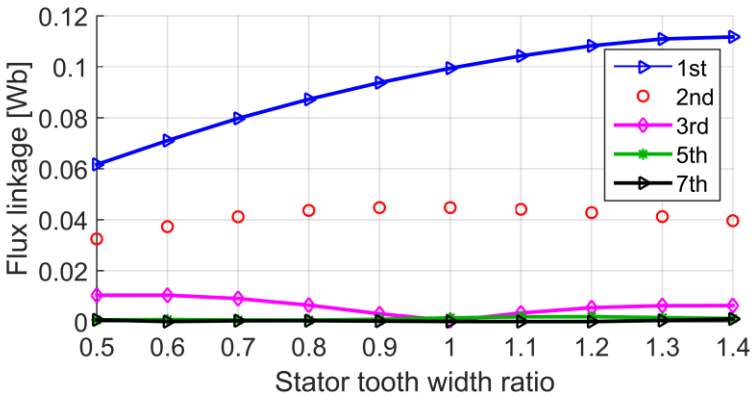

Figure 4.8. Flux linkage harmonic components variation as a function of different stator tooth width ratio.

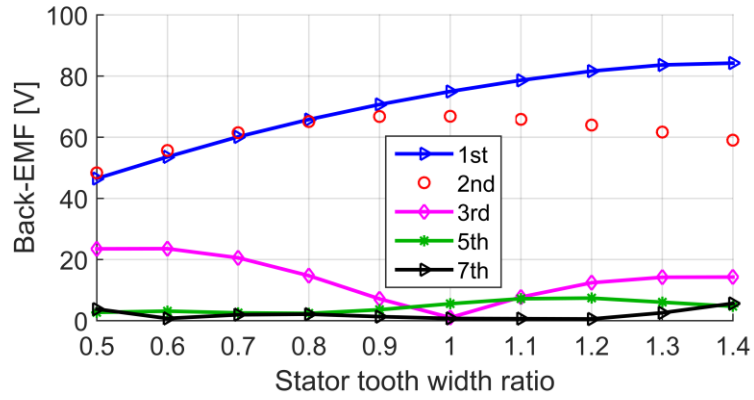

Figure 4.9. Back-EMF harmonic components variation as a function of different stator tooth width ratio.

The cogging torque for the dual-stator 6/4 FSPM machine should be evaluated at different rotor tooth width and stator tooth width conditions. It is recognized that there are six cogging periods per electric cycle for the dual-stator 6/4 FSPM machine. The cogging torque variation as

a function of both rotor tooth width ratio and stator tooth width ratio are plotted in Figure 4.10 and Figure 4.11 correspondingly. As the width of either rotor tooth or stator tooth increases from 0.9 to 1.3 by a step of 0.1, the cogging torque magnitude reduces to a minimum value and then increases again. More importantly, the phase angle for the cogging torque is also shifted by 180° electrically. Thus, the baseline design achieves a good compromise in increasing the fundamental flux linkage, reducing the 2nd harmonic, and reducing the cogging torque.

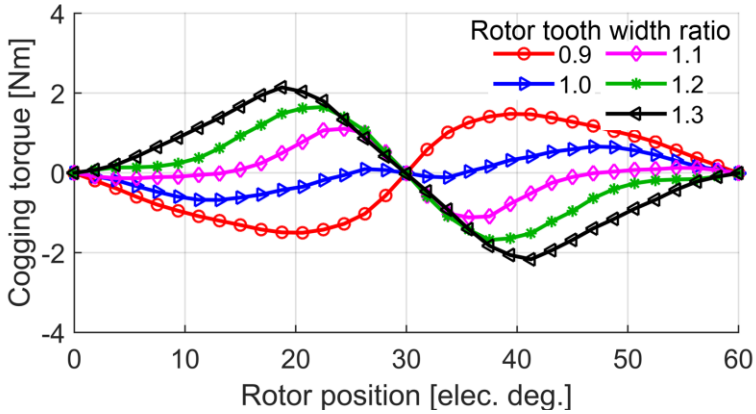

Figure 4.10. Cogging torque variation for different rotor tooth width ratios.

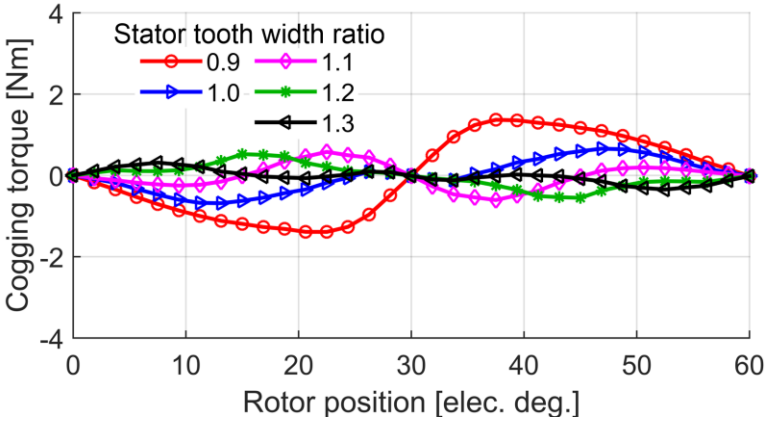

Figure 4.11. Cogging torque variation for different stator tooth width ratios.

4.1.3 Loaded Analysis of Proof-of-Concept Machine

4.1.3.1 Flux Linkage and Terminal Voltage at Loaded Condition

The proposed machine is designed with the dimensions shown in TABLE 4.1. At open circuit condition, the flux linkage is calculated to be almost a sinusoidal waveform as expected. The rated condition is reached by applying a phase current of 7.8 A_{rms} at an electrical loading of 21.15 A_{rms}/m, and the current space vector is in-phase with the back-EMF vector. The resulting flux linkage is plotted in Figure 4.12 to compare with the open circuit flux linkage. The FFT decompositions in Figure 4.13 show that the fundamental component dominates while there are low order odd harmonics of small magnitudes. The total harmonic distortion (THD) of flux linkage at open circuit and rated condition is 1.86% and 2.32%, respectively.

The back-EMF and rated terminal voltage are compared in Figure 4.14. The voltage waveform at rated condition has a phase advance angle of 21° electrically, so the calculated power factor is 0.934. By using FFT analysis, the harmonic spectrum of the voltage in Figure 4.15 shows that the fundamental component is increased, and the low order odd harmonics are amplified by the frequency. The calculated THD for the back-EMF and the rated terminal voltage is 9.2% and 9.8%, respectively. It is observed that the harmonic distribution at rated condition matches closely with the open circuit condition. To further reduce the THD of the terminal voltage, the low order harmonics need to be minimized in the back-EMF waveform.

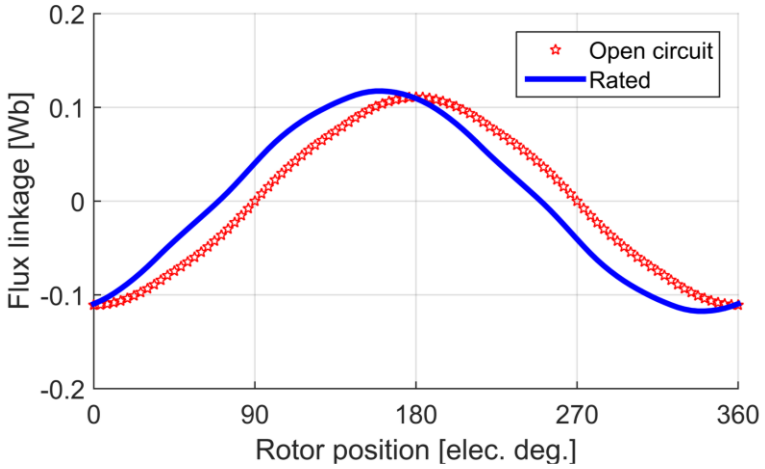

Figure 4.12. Flux linkage per phase winding of 1.5 kW machine at open circuit and rated conditions.

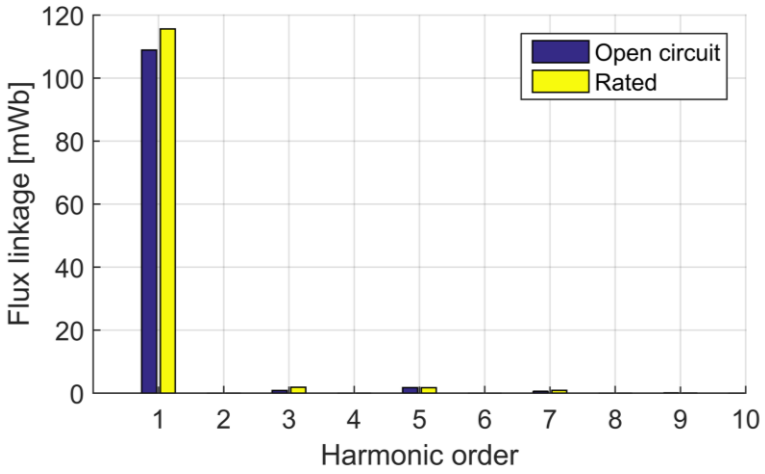

Figure 4.13. FFT of flux linkage per phase winding of 1.5 kW machine at open circuit and rated conditions.

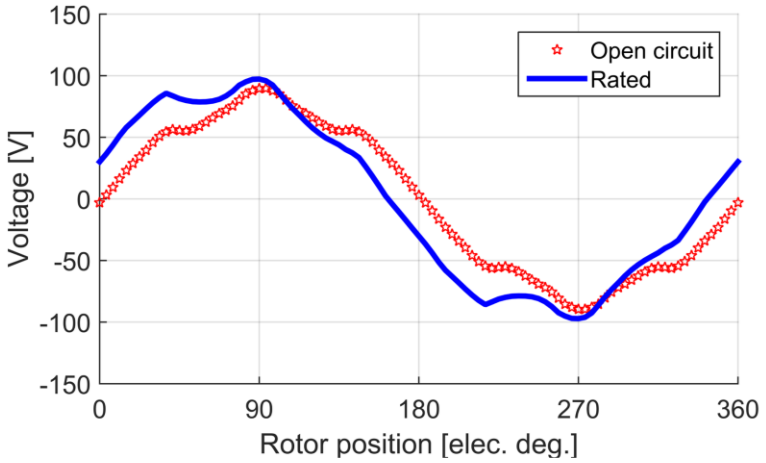

Figure 4.14. Voltage per phase winding at open circuit (back-EMF) and rated conditions.

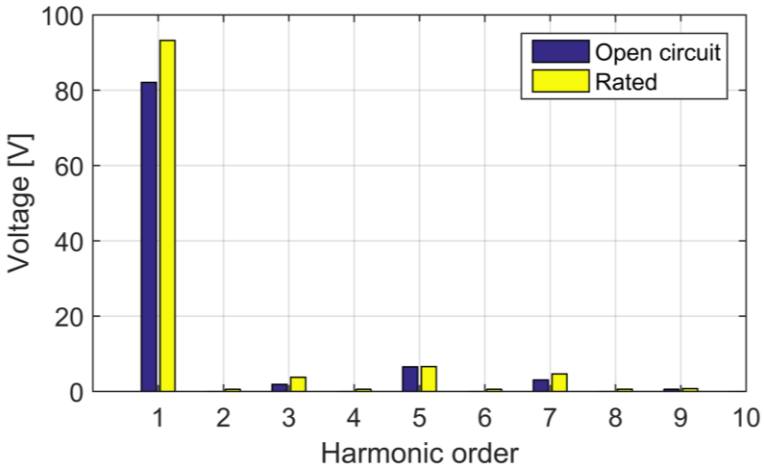

Figure 4.15. FFT of voltage per phase winding at open circuit (back-EMF) and rated conditions.

4.1.3.2 Electromagnetic Torque

The conventional 6/4 FSPM machine has a very large cogging torque. This is because the least common multiplier (LCM) of stator slots and rotor poles is 12, which is not a large number. There are 12 cogging periods per revolution. The four rotor poles will be aligned with four stator teeth at certain positions. The maximum and minimum cogging torque occur when the four rotor

poles rotate into and out of the alignment position, and the forces exerted on all four poles have the same direction which creates large cogging torque.

The dual-stator machine doubles the number of rotor poles and increases the cogging period per revolution to 24. If the conventional and proposed machine both have same effective stack length, FEA study reveals that the amplitude of cogging torque is reduced from 10.4 Nm (2D result) to only 1.2 Nm (3D result) shown in Figure 4.16. The cogging torque periods for conventional 6/4 FSPM machine is three and for dual-stator 6/4 FSPM machine is six during one electric cycle. The new machine has only about 11.5% of the cogging torque amplitude as the conventional machine.

When the machine is loaded with rated and 50% rated current, the electromagnetic torque is calculated to have an average value of 7.23 Nm and 3.63 Nm with torque ripple amplitude of 1.5 Nm and 1.2 Nm, respectively, as plotted in Figure 4.17. Low-pole PM machines generally produce higher cogging torque and ripple torque due to the small common multiplier of the number of rotor poles and stator slots. The produced average torque has a linear relation with the applied current shown in Figure 4.18.

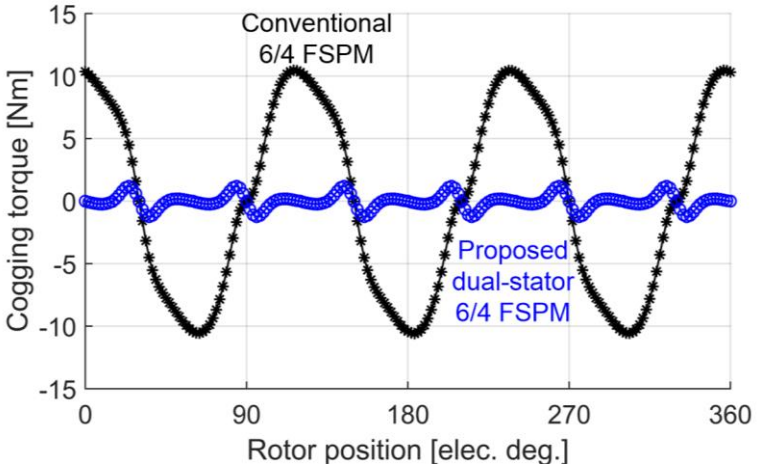

Figure 4.16. Cogging torque comparison of conventional 6/4 FSPM and proposed dual-stator 6/4 FSPM machine.

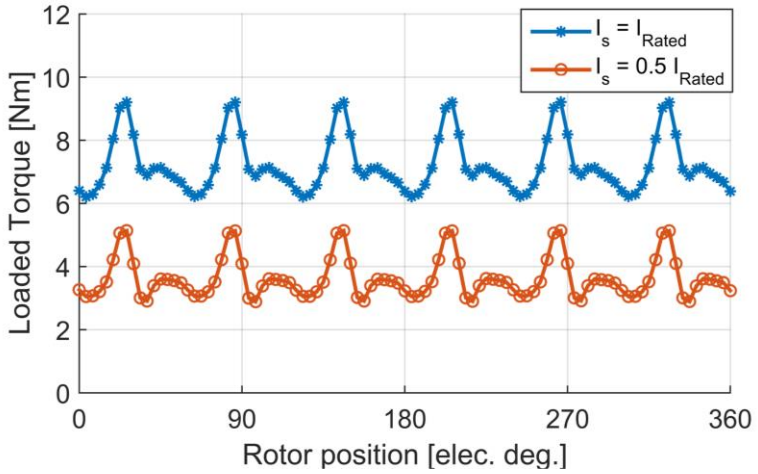

Figure 4.17. Loaded torque of the designed 1.5 kW machine at rated and 50% rated current conditions.

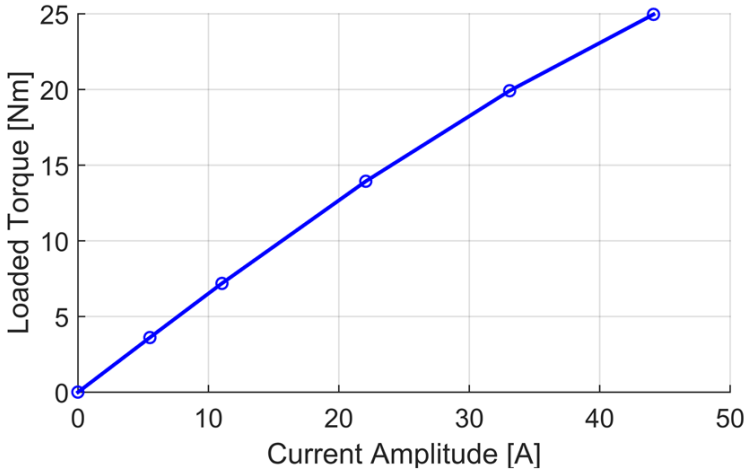

Figure 4.18. Average torque as a function of phase current amplitudes.

4.1.3.3 Airgap Flux Density

The magnetic loading of the electric machine is represented by the radial component of the airgap flux density. It is interesting to study the influence of end effects to the airgap flux density. Therefore, three planes in the front stator marked by A, B, and C that are perpendicular to the rotational axis are chosen as shown in Figure 4.19. The radial component of airgap flux density at no load and rated condition is plotted in Figure 4.20 and Figure 4.21. It is noted that the peak airgap flux density is reduced due to the end effect. Magnetic loading in a single stator is calculated from plane A to plane C in Figure 4.22, and it drops from 1.5 T in plane B to 1.0 T at plane A and C. The magnetic loading is not very high due to the 1 mm airgap length chosen in this design, but it can be increased by having a smaller airgap length.

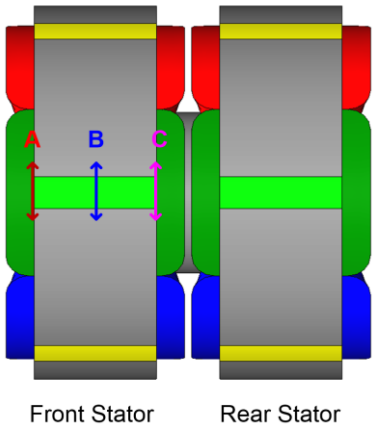

Figure 4.19. Side view of the proposed machine showing three planes (A, B, and C) that are perpendicular to the rotational axis.

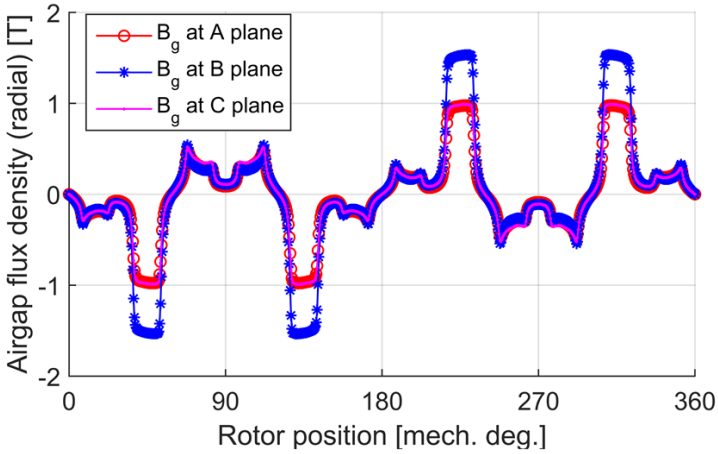

Figure 4.20. Radial component of airgap flux density at open circuit condition in three different planes.

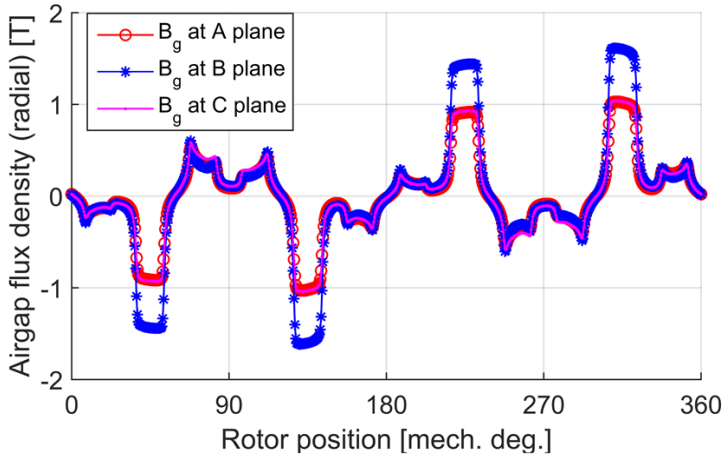

Figure 4.21. Radial component of airgap flux density at rated condition in three different planes.

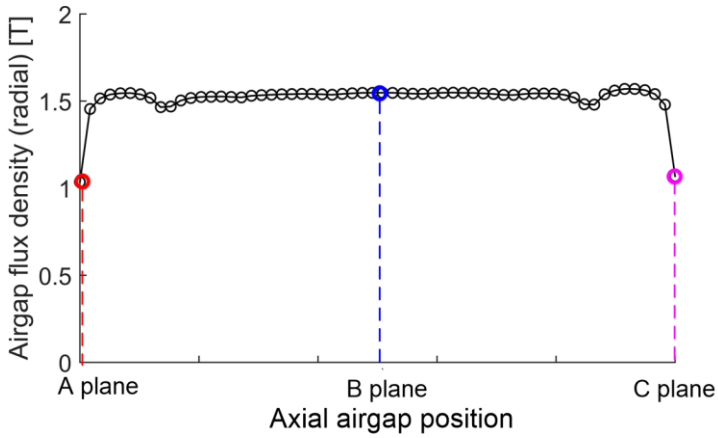

Figure 4.22. Peak radial airgap flux density inside a single stator from plane A to plane C to show the influence of end effect.

4.1.3.4 L_d and L_q Inductances

The calculated *d, q* instantaneous inductances for the designed machine are shown in Figure 4.23 for one electric cycle. It is noted that there is a limited saliency for the designed machine, which is consistent with the other FSPM machine designs. The calculated average L_d is 4.3 mH and L_q is 3.9 mH. When the base voltage and current are chosen as rated values of 66 V_{rms}

and 7.8 A_{rms}, the base impedance is calculated as 8.46 Ω. Thus, the per unit value of L_d and L_q is 0.383 and 0.348 respectively, which confirms the assumption that there is negligible saliency.

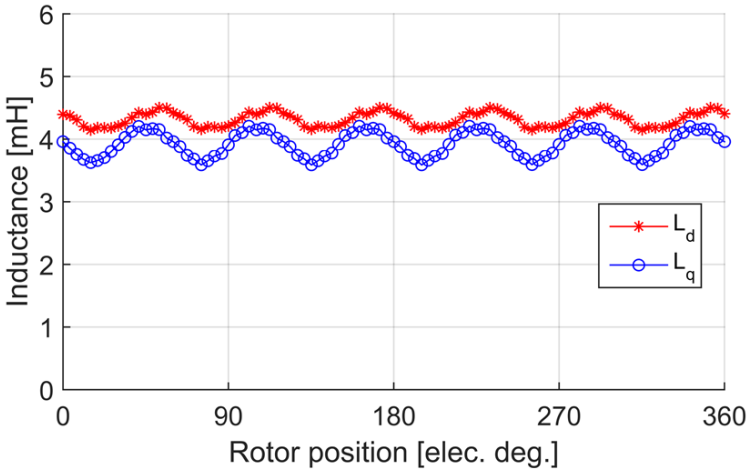

Figure 4.23. Calculated L_d and L_q for the designed 1.5 kW machine.

4.1.3.5 Rotor Magnetic Force

The radial force of the rotor needs to be evaluated since it may result in vibration and noise if the amplitude is too large. The proposed dual-stator structure has an even number of rotor poles in both parts, so the radial force produced in each rotor pole is compensated by the opposing rotor pole. The FEA results show that the net force on the whole rotor is below 1 N in all directions both under no load and rated conditions shown in Figure 4.24. This small net force on the rotor is beneficial for reducing the mechanical stress on the shaft and extending the life of the bearings.

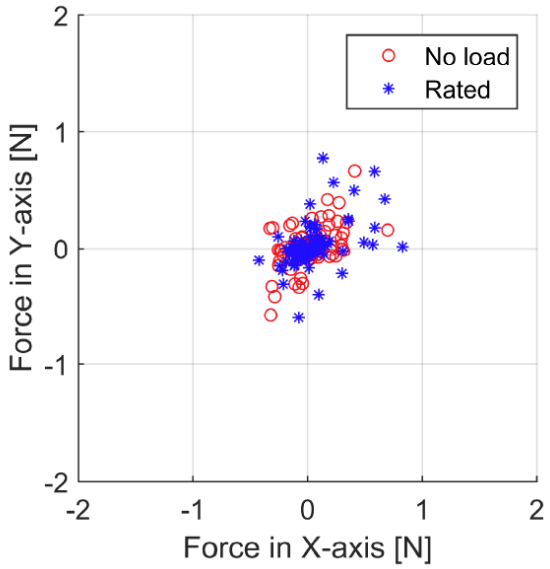

Figure 4.24. Rotor total magnetic force map for one electric cycle at no load and rated conditions.

4.1.4 Losses and Efficiency Analysis

4.1.4.1 Copper and Iron Loss Study

The designed dual-stator 6/4 FSPM machine has separated stators where two sets of end windings exist. The effect of additional resistance increase from the end winding between the two stators to the influence of machine losses needs to be evaluated. A single slot area of the designed machine is 302 mm^2. If the slot fill factor is about 50%, wire gauge #17 can be used when the number of turns per coil is designed as 60.

The total effective resistance per phase winding that does not consider the end winding resistance is calculated as 0.33 Ω. The total end winding resistance per phase alone is calculated as 0.41 Ω. Thus, the total phase winding resistance is 0.74 Ω. The additional end winding resistance

between two stators is 0.21 Ω. This amount of resistance contributes to 38 W of copper loss increase at rated condition. The total copper loss for the dual-stator machine is calculated to be 135 W.

Iron loss is proportional to the operating frequency and frequency squared for hysteresis and eddy current losses, respectively. The proposed machine has 60% reduction of the fundamental frequency compared to a 10-pole design. The calculated iron loss density at rated condition is shown in Figure 4.25 for rotor and stator separately. The iron loss in the stator and rotor is calculated as 16 W and 15 W respectively. It is noted that the total iron loss is evenly distributed between stator and rotor. The maximum iron loss density is achieved at the tips of the rotor poles where high-density bidirectional magnetic flux occurs. The lamination thickness used in the design is 0.35 mm. Iron loss can be reduced by employing thinner laminations, especially for high-speed designs.

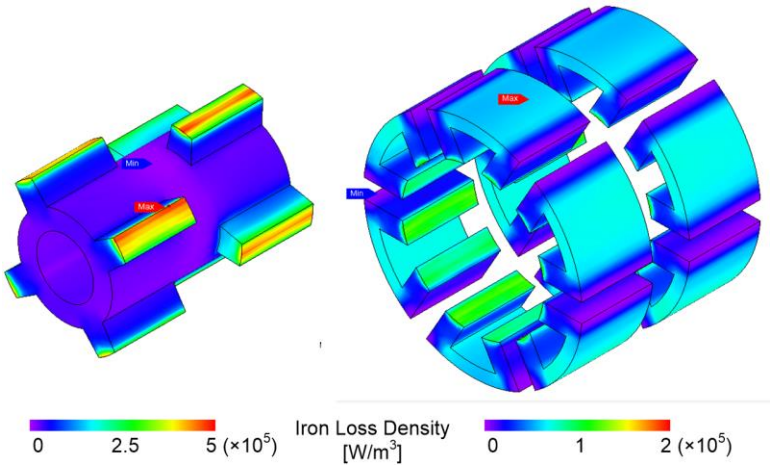

Figure 4.25. Total iron loss density distribution at rated condition for proof-of-concept machine.

4.1.4.2 Magnet Eddy Current Loss Study

The permanent magnets used in the design are NdFeB magnets with a remnant flux density of 1.2 T. The permanent magnets are not segmented in either direction in each stator. To evaluate the permanent magnet operating points at the rated condition, five key positions in the magnets are probed to show the magnetic flux pulsations during one electric cycle, which is plotted in Figure 4.26. It is observed that due to the thick magnets required in this design compared to higher pole options, the whole magnet operates well above the demagnetization knee point. Thus, the demagnetization risk for the design is much lower compared with higher pole designs where magnets are much thinner. The magnet eddy current loss density distribution at one particular time instant is drawn in Figure 4.27. The maximum loss density focuses on the two ends of the permanent magnets. The calculated total magnet eddy current loss is 10.4 W. Results for various losses are shown together in TABLE 4.2. Axial segmentations can be implemented to reduce the magnet loss, if needed.

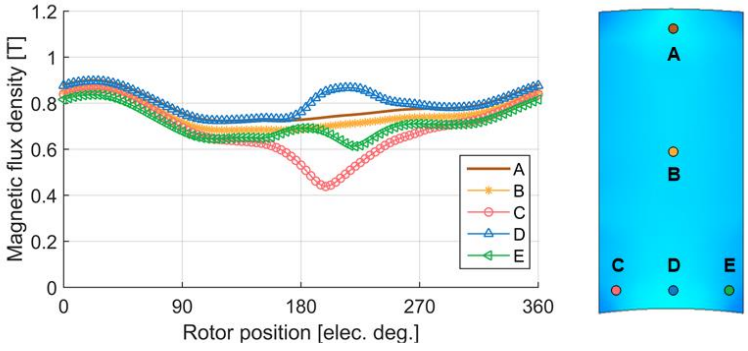

Figure 4.26. Flux density in permanent magnet at several key positions.

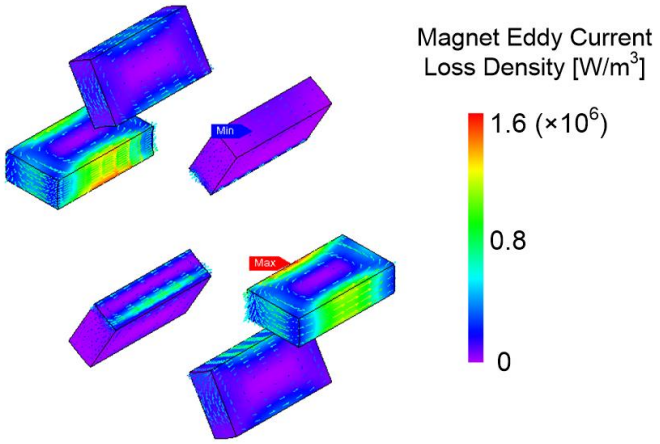

Figure 4.27. Permanent magnet eddy current loss distribution at one time instant for rated condition.

TABLE 4.2. LOSS ANALYSIS FOR THE PROOF-OF-CONCEPT MACHINE

Phase resistance without end winding, R_{s0} [Ω]	0.33
Phase resistance of end winding, $R_{s,end}$ [Ω]	0.41
Total phase winding resistance, R_s [Ω]	0.74
Copper loss, P_c [W]	135
Stator iron loss, $P_{fe,s}$ [W]	16
Rotor iron loss, $P_{fe,r}$ [W]	15
Total iron loss, P_{fe} [W]	31
Magnet eddy current loss, P_{mag} [W]	10.4
Total loss, P_{loss} [W]	176.4
Efficiency	89.5%

The proposed dual-stator 6/4 FSPM machine has superior performance characteristics to the conventional 6/4 FSPM machine. The conventional topology is studied to show that even order harmonics exist in the flux linkage, especially the large 2nd order component, which is caused by the permeance variations as the rotor rotates. The resulting back-EMF waveforms for conventional 6/4 FSPM machine have severe distortion that is not feasible for practical use.

Torque density of the dual-stator machine depends on the fundamental back-EMF amplitude, which is attributed to the fundamental flux linkage. The 2nd order harmonics of the flux linkage in the dual-stator FSPM machine are negated. Any designs that increase the fundamental component and decrease the 2nd order component in the flux linkage will essentially improve the torque density of the machine.

4.2 Comparison of Proposed Dual-Stator 6/4 FSPM Machine with Conventional 6/4 FSPM Machine.

The low-power-low-speed dual-stator 6/4 FSPM machine is characterized in the previous sections. This section focuses on the design and performance comparison of the proposed dual-stator 6/4 FSPM machine with the conventional 6/4 FSPM machine. In this comparative study, the proposed dual-stator 6/4 FSPM machine is designed with a rating of 5 kW and 15,000 rpm. To make a fair comparison, the conventional topology has the same dimensions with the dual-stator 6/4 FSPM machine showed in TABLE 4.3, and its stack length is equal to the total stack length of 65 mm in the dual-stator design (excluding gap length between stators). The gap distance between two stators in the dual-stator machine is 20 mm, which is the additional length than the conventional design. It should be noted that the phase winding resistance of conventional 6/4 FSPM machine is 22 mΩ, while that of the dual-stator 6/4 FSPM machine is 30 mΩ. It should also be pointed out that flanged rotor tooth design is implemented to reduce the cogging torque. The key dimensions of the proposed machine are already optimized to reduce the 2nd order harmonic

content in the flux linkage, improve the average torque, and reduce the cogging torque. Both machines are studied for no load and loaded conditions.

TABLE 4.3. COMPARISON OF PARAMETERS OF CONVENTIONAL 6/4 AND DUAL-STATOR 6/4 FSPM MACHINES

Key Performance Parameters	**Conventional 6/4**	**Dual-stator 6/4**
Expected output power, P_{out} [kW]	5	5
Rated speed, n_r [rpm]	15,000	15,000
Fundamental frequency, f_e [Hz]	1,000	1,000
Electrical loading, $A_{s,rms}$ [kA_{rms}/m]	15.2	15.2
Stator outer diameter, D_{os} [mm]	112.3	112.3
Stator inner diameter, D_{is} [mm]	73	73
Magnet width, d_m [mm]	9.6	9.6
Single stator stack length, $L_{e.1/2}$, [mm]	N/A	32.5
Total stack length, L_e [mm]	65	65
Gap between stators, d_{gap} [mm]	N/A	20
Airgap length, g [mm]	1	1
Magnet remnant flux density, B_r [T]	1.2	1.2
Turns per phase per stator, N_t	20	20
Phase current, I_s [A_{rms}]	29	29
Current density, J_s [A_{rms}/mm^2]	7.3	7.3
Slot fill factor, K_{cu}	60 %	60 %
Resistance per phase, R_s [mΩ]	22	30

4.2.1 Comparison of No Load Flux Linkage and Back-EMF

To provide a more accurate comparison, 3D FEA is used for both conventional 6/4 FSPM machine design and the dual-stator 6/4 FSPM machine design. The flux density distribution for both machines at no load condition is plotted in Figure 4.28. The open-circuit flux linkage of the conventional 6/4 FSPM machine has a total harmonic distortion (THD) of 32.53%, while the proposed dual-stator machine has only 2.65% as shown in Figure 4.29. The back-EMF of the

conventional machine has 65.24% THD, but this value is reduced to 10.26% in the dual-stator structure plotted in Figure 4.30. This significant reduction of harmonic distortion is realized mainly by the desirable even harmonic elimination effect. The back-EMF distortion in the conventional design using the optimized geometries is still unacceptably large, but this distortion is small enough and acceptable in the dual-stator design.

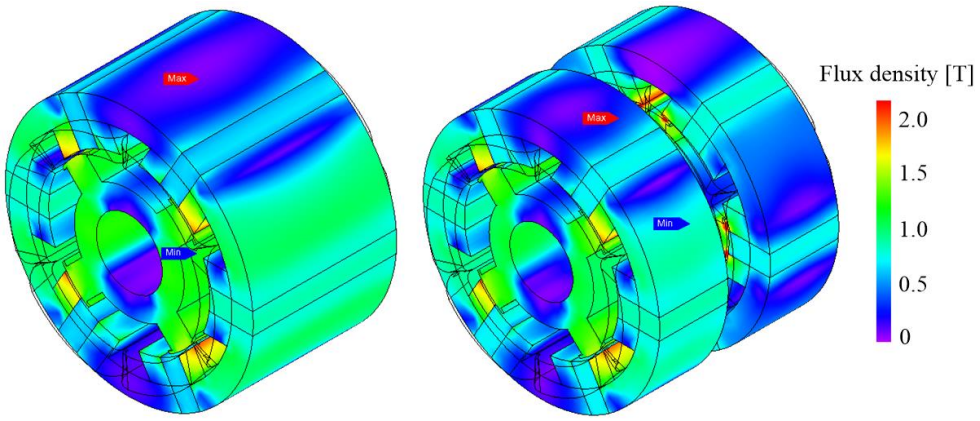

(a) (b)

Figure 4.28. Magnetic flux density distribution of (a) Conventional machine and (b) Dual-stator 6/4 FSPM machine at no load condition.

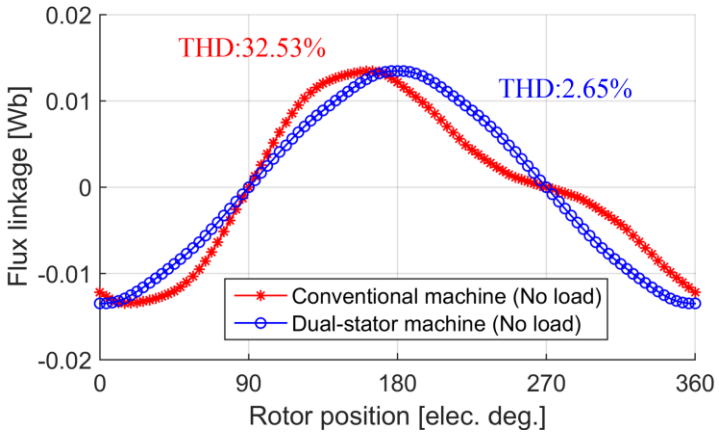

Figure 4.29. Flux linkage comparison of 5 kW machine at no load condition.

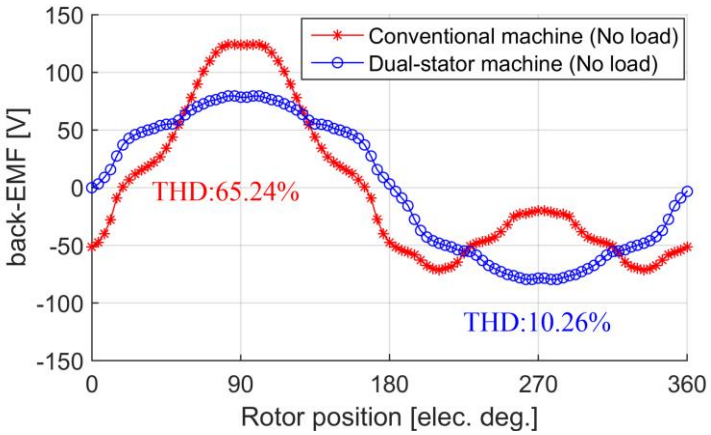

Figure 4.30. Back-EMF comparison of 5 kW machine at no load condition.

4.2.2 Comparison of Loaded Flux Linkage and Voltage

When both machines are loaded with the same rated current of 29 Arms, both the flux linkage and phase voltage waveforms in the proposed dual-stator machine maintain much lower THDs compared to the conventional design whose comparison is shown in Figure 4.31 and Figure 4.32. The Fourier harmonic decomposition of flux linkage and phase voltage (or back-EMF at no-load condition) waveforms for two machines under both no load and loaded conditions are compared in Figure 4.33 and Figure 4.34. There is no even order harmonics in the back-EMF for the proposed machine. Even at rated current condition, the even harmonics generated in the flux linkage is small enough to be neglected. These figures also show that the dual-stator machine has 10% more fundamental component of flux linkage compared to the conventional machine. The reason is that the dual-stator 6/4 FSPM machine has additional end windings that produce more end winding leakage flux than the conventional design. The higher fundamental flux linkage and

back-EMF in the dual-stator machine is beneficial to producing more torque at the same current excitation.

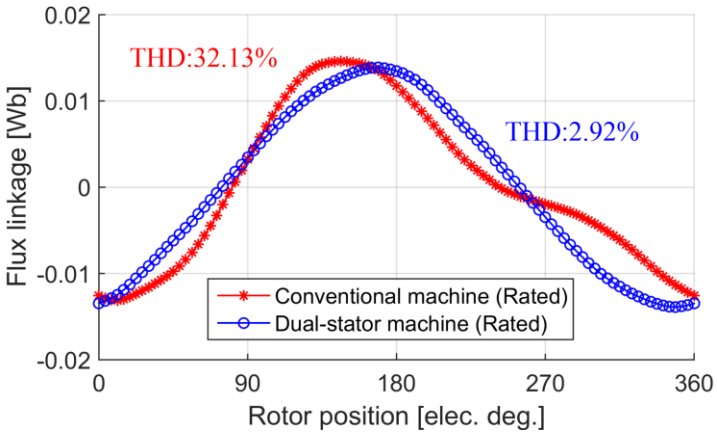

Figure 4.31. Flux linkage comparision of dual-stator 6/4 FSPM machine and conventional 6/4 FSPM machine at rated condition.

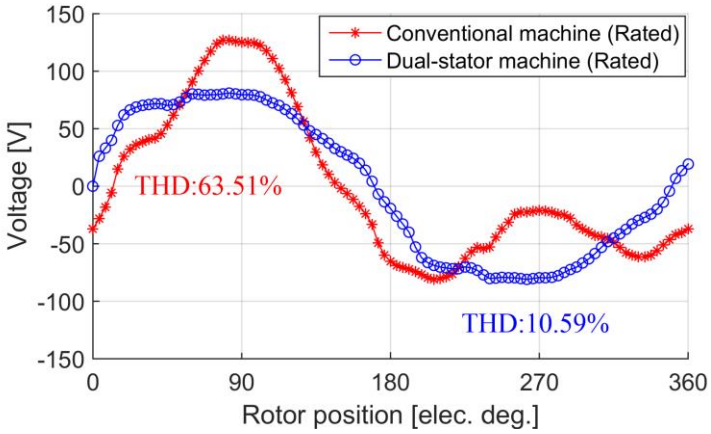

Figure 4.32. Phase voltage comparison of dual-stator 6/4 FSPM machine and conventional 6/4 FSPM machine at rated condition.

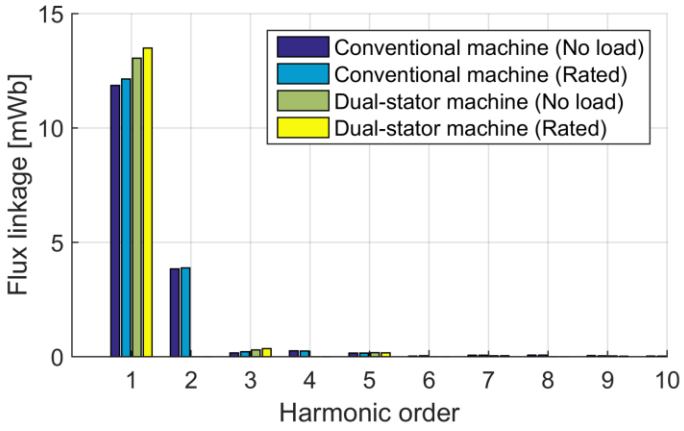

Figure 4.33. Flux linkage harmonic magnitudes comparison of dual-stator 6/4 FSPM machine and conventional 6/4 FSPM machine at no load/ rated conditions.

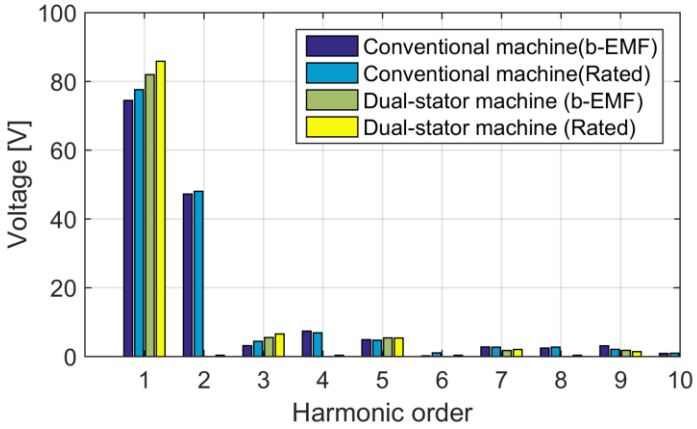

Figure 4.34. Back-EMF or terminal voltages comparison of dual-stator 6/4 FSPM machine and conventional 6/4 FSPM machine at no load/rated conditions.

4.2.3 Comparison of Cogging Torque and Torque Ripple

Cogging torque of the optimized conventional 6/4 FSPM machine has 5.21 Nm (peak-peak, pp) in the 3D FEA study, but the dual-stator machine can reduce the cogging torque down to 1.23 Nm (pp) shown in Figure 4.35. This equivalent amount of 76.4% reduction of cogging torque is a result of the offset-pole rotor structure where the cogging torque produced by the front part of the

rotor is compensated by the rear part, so the cogging period is doubled and the net torque is minimized. When the rated current is provided to the q-axis (assuming negligible saliency), the output torque calculated for the conventional machine has an average value of 2.906 Nm, but it severely oscillates with a ripple value of 7.55 Nm (pp) and a minimum negative value of –1.28 Nm which indicates generation operation shown in Figure 4.36. This large ripple torque makes conventional 6/4 topology inferior to use. In contrast, the proposed dual-stator machine has an average torque of 3.257 Nm with a torque ripple of 1.24 Nm (pp).

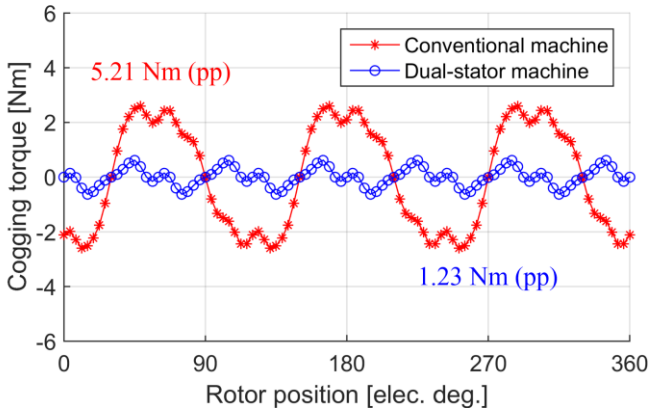

Figure 4.35. Cogging torque comparison for two machines.

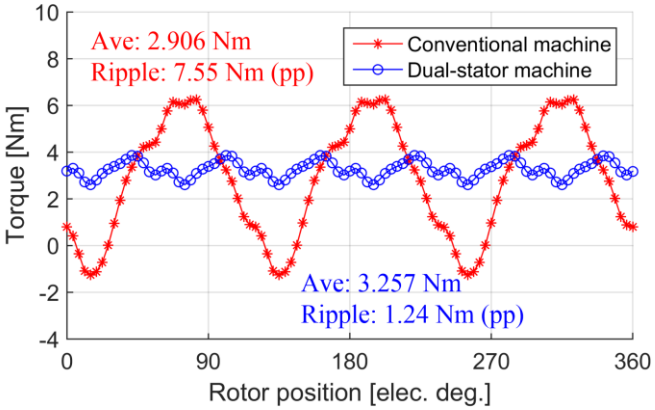

Figure 4.36. Rated torque comparison for two machines.

4.2.4 Comparison of Torque Density

It is necessary to evaluate the influence of introduced gap and additional end windings between stators to the overall machine torque density. A comparison of the mass distribution of the conventional and dual-stator machines is provided in TABLE 4.4. It is seen that due to the added lamination materials between two rotor parts, the dual-stator machine rotor has 21.1% more weight than the conventional rotor. Copper consumption is increased by 36.4% by the additional end windings in the gap space. The total weight increase of the dual-stator machine compared to the conventional machine is 11.5%. However, the dual-stator structure produces 12.1% more torque than the conventional design, so the actual specific torque density (defined by the ratio of produced torque over the total machine weight) is increased by 0.6%. The cogging torque is reduced by 76.4% and there is no negative torque at rated condition. These results show that the dual-stator machine achieves almost the same torque density with significant improvements in the performances.

TABLE 4.4. COMPARISON OF MASS DISTRIBUTION AND POWER DENSITY OF CONVENTIONAL AND DUAL-STATOR 6/4 FSPM MACHINES

Compared Parameters	**Conventional 6/4**	**Dual-stator 6/4**
Rotor mass [kg]	0.891	1.079 (+21.1%)
Stator mass [kg]	1.850	1.850
Copper mass [kg]	0.770	1.050 (+36.4%)
Magnet mass [kg]	0.553	0.553
Total weight [kg]	4.064	4.531 (+11.5%)
Total axial length [mm]	85	105 (+23.5%)
Cogging torque [Nm]	5.21	1.23 (–76.4%)
Average torque [Nm]	2.906	3.257 (+12.1%)
Specific torque density [Nm/kg]	0.715	0.719 (+0.6%)
Specific power density [kW/kg]	1.123	1.129 (+0.6%)

4.3 Comparison of Proposed Alternative Dual-Stator 6/4 FSPM Machine Topologies

The proposed dual-stator 6/4 FSPM machine concept applies to multiple topology variations mentioned in Chapter 2. This section discusses the design and performance comparisons of the three different topology variations in more detail. The properties of each alternative topology regarding manufacturing simplicity are also discussed. The electromagnetic output waveforms and torque density of these three designs are compared. It should be mentioned that the three proposed topologies are renamed as Topology I, II, and III in a way that the total material consumption is progressively increased.

4.3.1 Design Considerations of Topology-I (Rotor Shifted and Magnets in Opposite Direction)

In this configuration which is named Topology I, the rotor poles are offset and the orientation of the permanent magnets in two stators are of opposite polarity. The concentrated windings for each phase wrap across two stators, and there is a clearance distance between two stators to prevent magnetic flux shunting in the axial direction as shown in Figure 4.37. The cross-sectional view of this configuration with the connection of windings and orientation of the permanent magnets are also illustrated in the Figure 4.38. Since the permanent magnets change the orientation in two stators, the direction of the windings in the two stators stays the same.

This topology has the potential to be designed most compact out of the proposed three topologies of the dual-stator 6/4 FSPM machine because there are very few end windings in-between the two stators so that the gap distance can be reduced. However, due to the opposite

polarity of the magnets in two stators, this gap distance should not be too small as to increase the leakage flux through the gap in the axial direction and reduce the main flux passing through the airgap. To evaluate what is an appropriate distance between stators, the fundamental back-EMF in the windings as a function of the gap distance is simulated by 3D FEA to obtain the results in Figure 4.38. It should be mentioned that the inner diameter and outer diameter of the stator are 62 mm and 130 mm respectively. When the gap separation distance is 80 mm which is considered far enough, the magnet shunting leakage flux is close to minimum, and the fundamental back-EMF reaches a maximum value of 100 V_{pk}. The fundamental back-EMF stays almost unchanged when the gap distance is reduced to until 30 mm. When the gap distance is smaller than 30 mm, the fundamental back-EMF drops quickly when the gap distance becomes increasingly smaller. The fundamental back-EMF reduces to about 40 V_{pk} when the gap distance is only 1 mm as simulated in FEA program. This shows that about 60% of the fundamental back-EMF is reduced if there is no gap distance between two stators. Thus, the gap distance is chosen by the tradeoff of either having a compact design or having a slightly larger design but producing more back-EMF and torque.

It should be noted that the assembling process of Topology I is a little bit different than other topologies. The winding process of this topology cannot begin until the positions of two stators are fixed with a determined gap distance and good center alignment by the supporting housing structure.

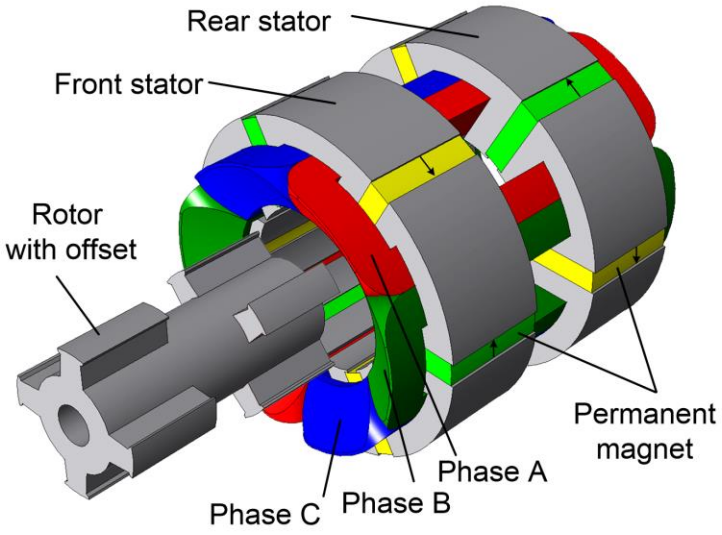

Figure 4.37. Exploded view of proposed Topology-I of the dual-stator 6/4 FSPM machine.

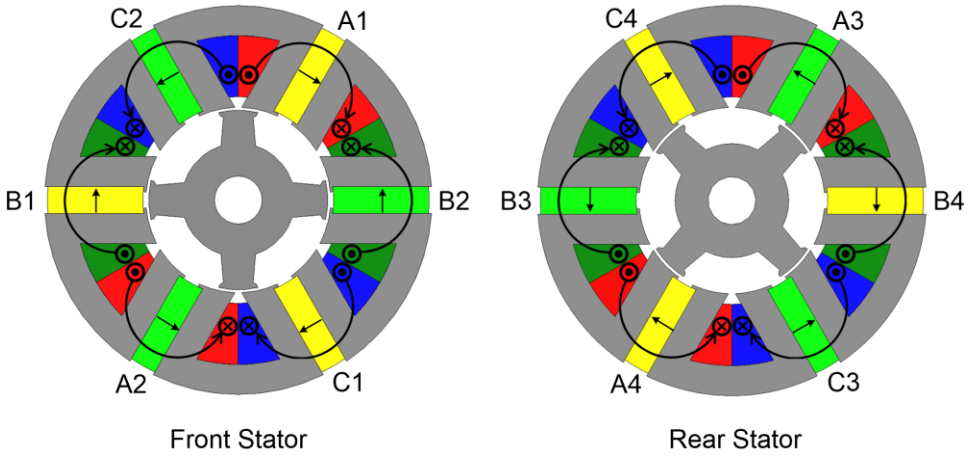

Figure 4.38. Cross section and winding configurations of the proposed Topology-I of the dual-stator 6/4 FSPM machine.

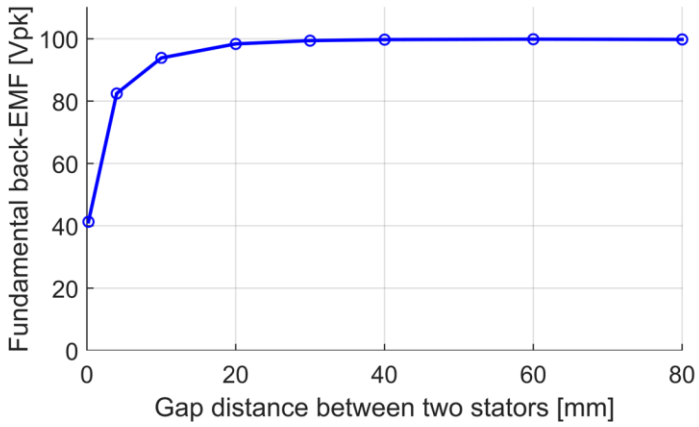

Figure 4.39. Fundamental back-EMF as a function of the gap distance between two stators for the proposed Topology-I.

4.3.2 Design Considerations of Topology-II (Rotor Shifted and Separate Winding)

In this embodiment of the proposed dual-stator 6/4 FSPM machine, the rotor poles are offset as that in Topology I. The permanent magnets in two stators are of the same orientation. However, the winding directions in two stators are opposite to provide the even order harmonic compensation effect as shown in the exploded view in Figure 4.40 and cross-sectional view in Figure 4.41. Different than the Topology I that the gap distance between stators can be chosen arbitrarily, the gap distance of this topology cannot be smaller than the axial length of two end windings between the stators. This minimum gap distance can vary depending on the actual end winding design and assembling, but usually this distance is more than the gap distance required in topology I. Therefore, Topology II has slightly bigger form factor than Topology I.

From a manufacturing viewpoint of this machine, the two stators can be laminated, stacked, and wound with each own winding separately before the final assembling and alignment process begins. This is unlike the assembling process of Topology I where two stators should be aligned before the winding process begins. Thus, Topology II is considered to have a better modular design capability than Topology I in terms of manufacturing.

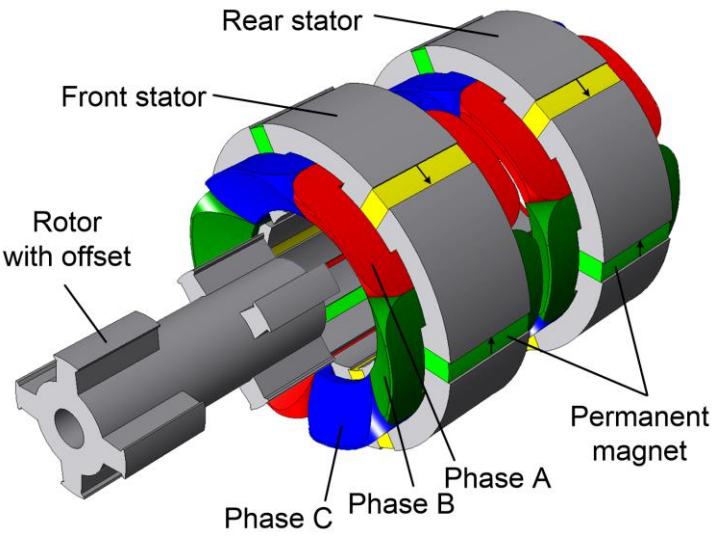

Figure 4.40. Exploded view of proposed Topology-II of the dual-stator 6/4 FSPM machine.

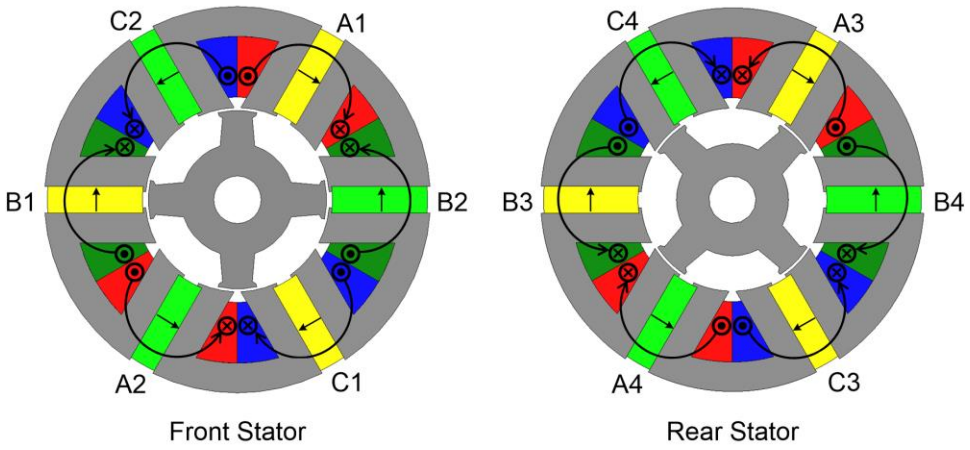

Figure 4.41. Cross section and winding configurations of the proposed Topology-II of the dual-stator 6/4 FSPM machine.

4.3.3 Design Considerations of Topology-III (Stator Shifted without Shifting Rotor)

In this embodiment of the proposed dual-stator 6/4 FSPM machine shown in Figure 4.42, the rotor is not offset as that in the previous two embodiments. The rotor has the same cross section across the whole axial length without distinguishing the front and rear part of the rotor. This aspect reduces the number of rotor lamination types and simplifies the design and manufacturing process. To realize the even order harmonic cancellation effect in the flux linkage, the rear stator along with the permanent magnets and the concentrated windings should rotate synchronously with the rear part of the rotor by 45° mechanically in either clockwise or counter-clockwise direction. From another perspective of this topology, this topology can be transformed from Topology II by rotating the rear stator part and rotor part simultaneously by 45° mechanically.

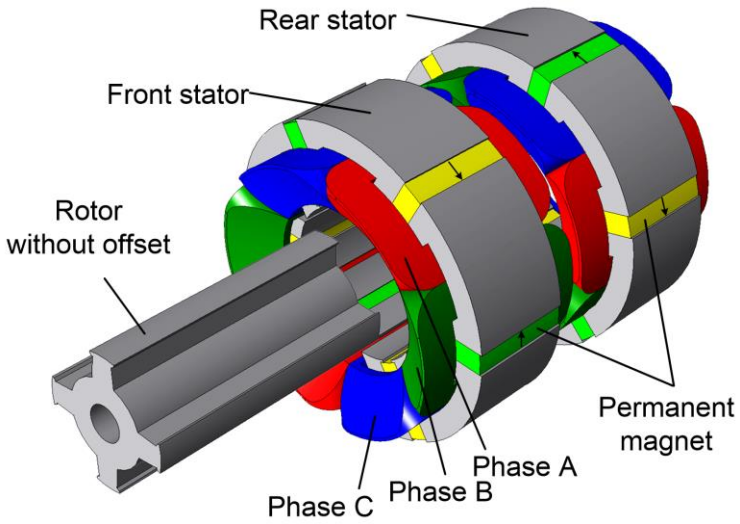

Figure 4.42. Exploded view of proposed Topology-III of the dual-stator 6/4 FSPM machine.

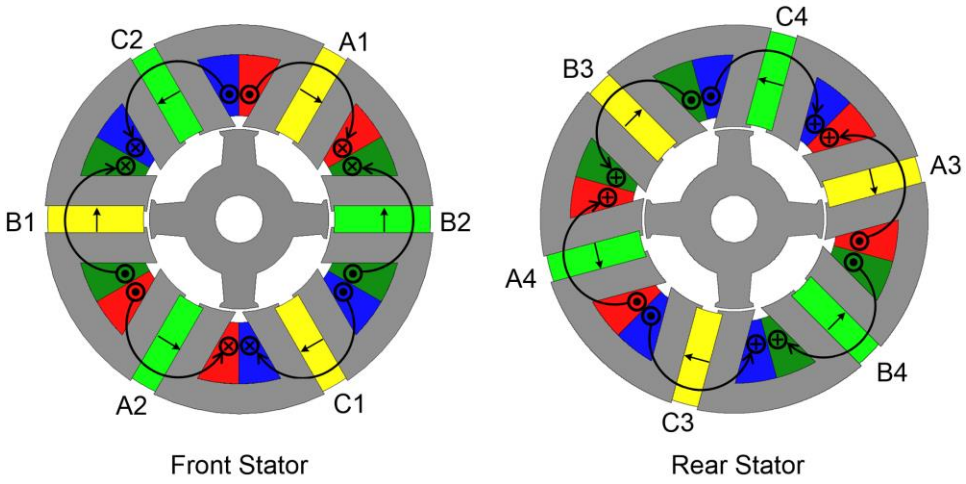

Figure 4.43. Cross section and winding configurations of the proposed Topology-III of the dual-stator 6/4 FSPM machine.

4.3.4 Comparison of Torque and Power Density

The proposed three alternative topologies are compared for the performance including flux linkage, back-EMF, and torque density in this section. The stator and rotor cross section geometries of three topologies and total stack length are all kept the same. It is noted that the gap distance of the stators in Topology I is chosen as 30 mm because the fundamental back-EMF is calculated to be 99.4 V_{pk}, whose value is 99.8% of the value of 99.8 V_{pk} when the gap distance is 80 mm. The gap distance of Topology II and III are selected the same of 40 mm to accommodate the end windings. The flux linkages and their harmonic components are shown in Figure 4.44 and Figure 4.45, and the back-EMFs and their harmonic components are plotted in Figure 4.46 and Figure 4.47. Fundamental back-EMF magnitudes for Topology I, II, and III are 99.4 V, 106.3 V, and 107.9 V correspondingly. Due to the absence of magnetic flux shunting and the additional end

winding flux leakage in Topology II and III, the fundamental back-EMF is higher than that of Topology I. Since Topology III has extended length of rotor pole between the regions of two stators, a slightly larger fundamental back-EMF is induced in the windings.

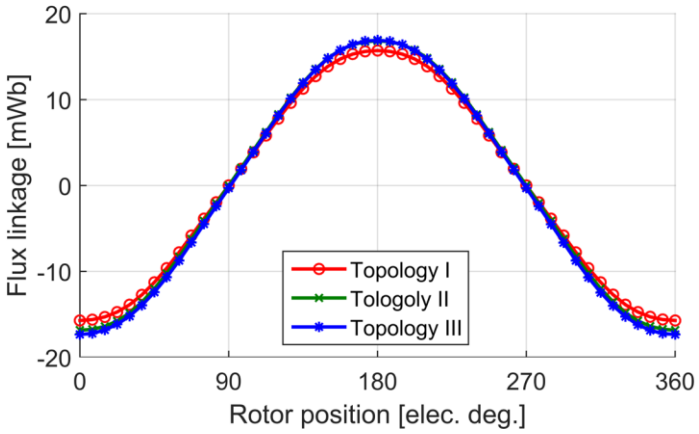

Figure 4.44. Comparison of flux linkage for three alternative topologies of dual-stator 6/4 FSPM machines.

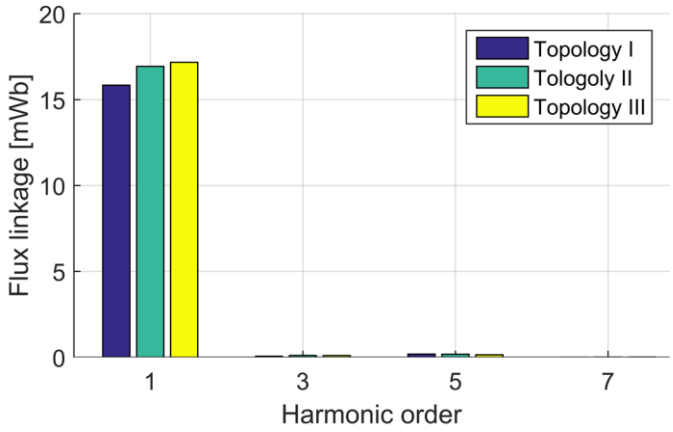

Figure 4.45. Comparison of harmonic components of flux linkage for three alternative topologies of dual-stator 6/4 FSPM machines.

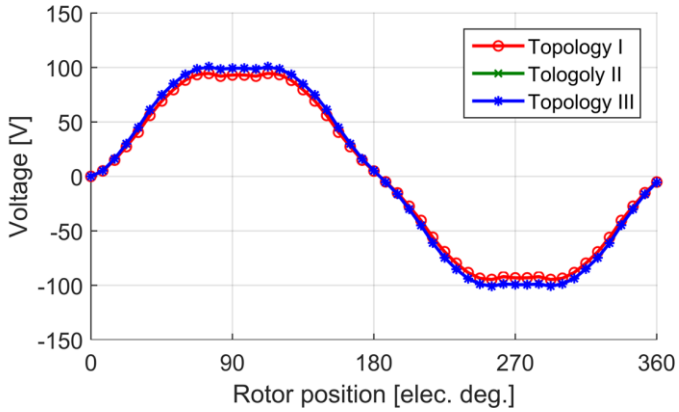

Figure 4.46. Comparison of back-EMF of three alternative topologies of dual-stator 6/4 FSPM machines at 15,000 rpm.

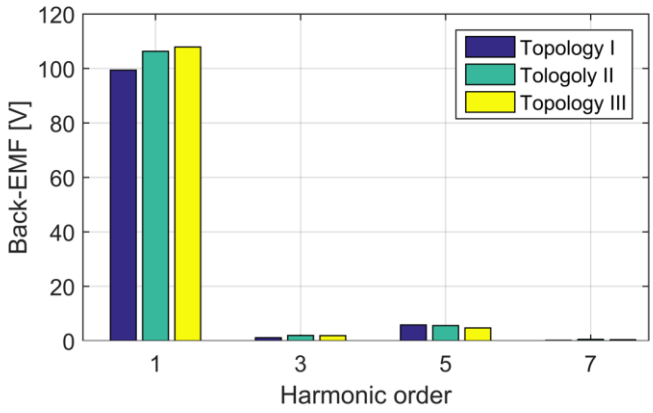

Figure 4.47. Comparison of harmonic components of three alternative topologies of dual-stator 6/4 FSPM machine at 15,000 rpm.

Magnetic flux density distribution of three alternative topologies are shown in Figure 4.48. The cogging torque for each of the topology is compared in Figure 4.49. Topology I has the smallest peak-to-peak cogging torque value of 1.39 Nm, while Topology II and III have 1.54 Nm and 1.84 Nm, respectively. The total phase winding resistance including the end winding resistance for Topology I is 17.9 mΩ, and for Topology II and III is both 20.9 mΩ. When all the topologies are fed by the same phase current of 48.1 Arms, the output torque for Topology I, II, and III are

6.439 Nm, 6.890 Nm, and 6.988 Nm respectively as shown in Figure 4.50. The mass distributions of the rotor, stator, permanent magnets, and windings for each of the topology are also calculated in TABLE 4.5. Topology-I, II, and III have a total mass of 7.453 kg, 7.735 kg, and 7.884 kg correspondingly. So, the calculated specific torque density for each of the topology is 0.8639 Nm/kg, 0.8908 Nm/kg, and 0.8864 Nm/kg. To compare the torque density easily, the total weight and torque density of Topology-I are assumed to be both 100%. Topology-II has 103.8% of the total weight and 103.1% of the torque density of Topology-I. Similarly, Topology-III has 105.8% of the total weight and 102.6% of the torque density of Topology-I.

The comparison results show that Topology-I is the most compact design out of the three topologies. Topology-II has slightly higher torque density than the other two topologies but at the expense of almost the same percentage of total mass increase. Topology-III has the highest mass among all the topologies, with a simpler rotor design.

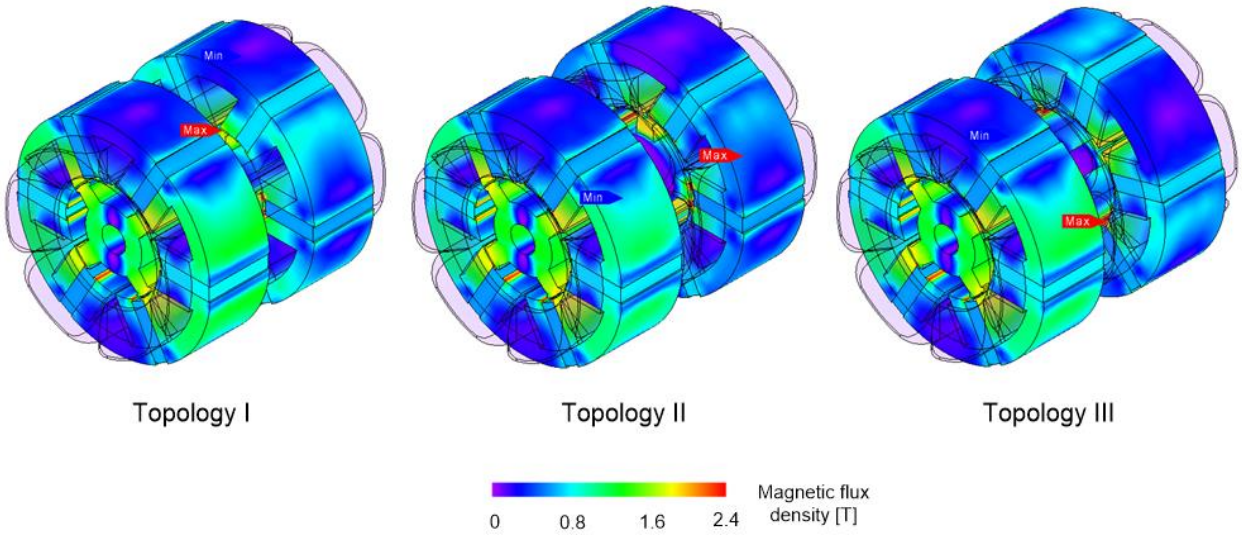

Figure 4.48. Magnetic flux density distribution for three alternative topologies of dual-stator 6/4 FSPM machine at no load condition.

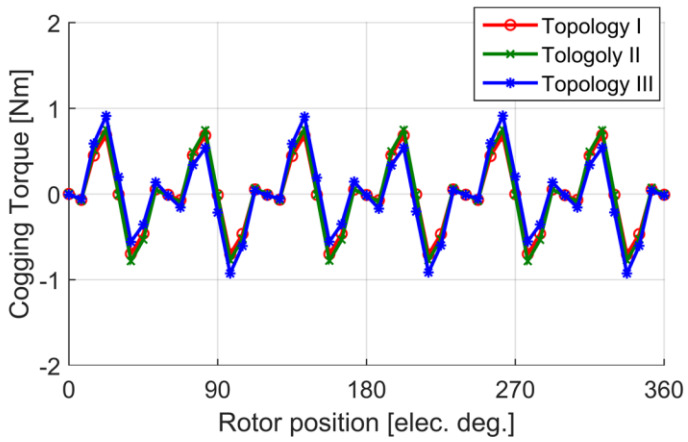

Figure 4.49. Cogging torque comparison of three alternative topologies of the dual-stator 6/4 FSPM machines.

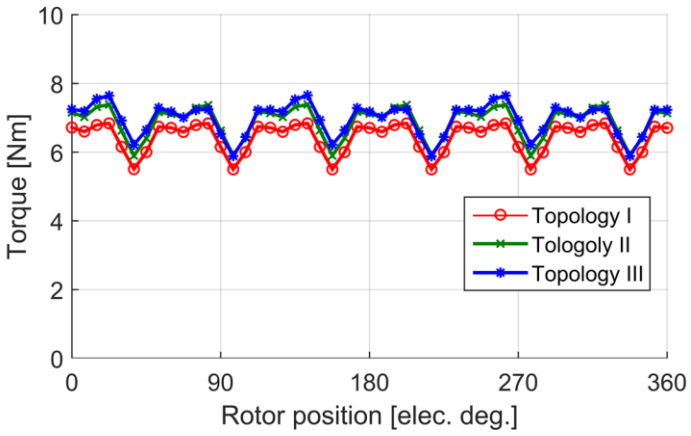

Figure 4.50. Loaded torque comparison of three alternative topologies of the dual-stator 6/4 FSPM machines.

TABLE 4.5. COMPARISON OF PARAMETERS OF THREE DUAL-STATOR 6/4 FSPM MACHINES

Key Performance Parameters	**Topology-I**	**Topology-II**	**Topology-III**
Fundamental frequency, f_e [Hz]	1,000		
Stator outer diameter, D_{os} [mm]	130		
Stator inner diameter, D_{is} [mm]	62		
Magnet width, d_m [mm]	9		
Airgap length, g [mm]	1		
Total steel stack length, L_e [mm]	80		
NdFeB remnant flux density [T]	1.2		
Gap between stators, d_{gap} [mm]	30	40	40
Resistance per phase, R_s [mΩ]	17.9	20.9	20.9
Stator mass [kg]	3.782	3.782	3.782
Rotor mass [kg]	1.077	1.148	1.297
Copper mass [kg]	1.556	1.767	1.767
Magnet mass [kg]	1.039	1.039	1.039
Total mass [kg]	7.453 (100.0%)	7.735 (103.8%)	7.884 (105.8%)
Torque [Nm]	6.439	6.890	6.988
Specific torque density [Nm/kg]	0.8639 (100.0%)	0.8908 (103.1%)	0.8864 (102.6%)

4.3.5 Comparison of Manufacturing and Performance Capability

The differences of design and performance of three alternative topologies are described in the prior sections. This section focuses on the comparison of the manufacturing, assembling simplicity, and overall performance of the three topologies. The purpose is to provide a comprehensive guideline for choosing the appropriate topology based on each of the advantages and disadvantages.

The manufacturing and assembling simplicity are important factors that determine the cost of the machine. The rotor design and assembling of Topology-III is simpler than I and II. The

winding assembling of Topology-I is simpler than II and III because only one set of winding is used to wrap around two stators, whereas the other two topologies need separated windings and series connection at the terminal. The alignment of two stators in Topology-I and II is simpler than III, because the two stators in Topology-III should maintain a 45˚ mechanically while the other two topologies maintain 0 degree. The modular design capability of Topology-II and III is better than I because the two stators can be manufactured and assembled separately before the final assembling process. The overall machine compactness and material consumption is best for Topology-I. Topology-II has the highest torque density, but the torque density percentage increase is almost proportional to the total mass percentage increase. To summarize the above comparison between the alternative topologies regarding manufacturing, assembling simplicity, and overall performance, TABLE 4.6 is provided with qualitative descriptions on each aspect. It is concluded that there is no one topology that is better in all aspects. The selection of the appropriate topology depends on the actual application requirements.

TABLE 4.6 COMPARISON OF MANUFACTURING, ASSEMBLING SIMPLICITY, AND OVERALL PERFORMANCES OF PROPOSED THREE ALTERNATIVE TOPOLOGIES OF DUAL-STATOR 6/4 FSPM MACHINE

Manufacturing and Performance	**Topology-I**	**Topology-II**	**Topology-III**
Rotor assembling simplicity	Simple	Simple	Most simple
Winding assembling simplicity	Less simple	Simple	Simple
Stator alignment simplicity	Simple	Simple	Less simple
Modular design capability	Good	Excellent	Excellent
Overall machine compactness	Most compact	Less compact	Less compact
Material consumption	Lowest	Higher	Highest
Torque density	High	Highest	Higher

(Note: the words used in the table only give qualitative descriptions on the “goodness” level on the aspects. Detailed comparison should refer to the actual designs.)

4.4 Summary

This chapter presents the analysis of the proposed dual-stator 6/4 FSPM machines. The performance characterization is done for a proof-of-concept machine under both no load and loaded conditions. The proposed dual-stator 6/4 FSPM machine is compared with the conventional 6/4 FSPM machine regarding harmonic distortion and torque density. The design, performance, and manufacturing properties of three alternative topologies of the dual-stator 6/4 FSPM machines are compared. Key research conclusions are summarized below,

- The proof-of-concept dual-stator 6/4 FSPM machine has balanced flux linkage, back-EMF that are amenable for sinusoidal excitation. There are almost no unbalanced magnetic forces on the rotor. The characterization shows the proposed machine achieves good power factor, and it operates similar to normal FSPM machines.
- The proposed dual-stator 6/4 FSPM machine achieves significant harmonic distortion reduction in the flux linkage and back-EMF compared to the conventional 6/4 FSPM machine. The cogging torque of the proposed 6/4 FSPM machine is also largely reduced than the conventional 6/4 FSPM machine.
- The total weight of the proposed dual-stator 6/4 FSPM machine is slightly higher than that of the conventional 6/4 FSPM machine, but the torque density is almost the same. The proposed dual-stator 6/4 FSPM machine has notably better performance than the conventional 6/4 FSPM machine.
- There are three alternative topologies of the dual-stator 6/4 FSPM machines. Topology-I with offset rotor and opposite magnet polarities has the most compact design and least

material consumption. Topology-II with offset rotor and separated winding has the highest torque density but with increased weight. Topology-III has the simplest rotor construction, but with the highest material consumption.

- The three proposed alternative topologies of the dual-stator machines have different material consumption, manufacturing and assembling simplicities. The selection of the appropriate topology depends on the actual design requirements.

Chapter 5

Design and Optimization of Dual-Stator 6/4 FSPM Machine

The dual-stator 6/4 FSPM machines have a complex geometry with many dimensional parameters that need to be appropriately designed. To give physical insights of varying the key machine parameters such as split ratio, stator teeth width, magnet thickness, and rotor pole width, the parametric analysis is performed to investigate the performance trending as a result of varying those parameters. The maximum torque density of the dual-stator 6/4 FSPM machine is characterized as a function of the current density. Optimization is used to maximize the average torque and minimize the torque ripple for the dual-stator 6/4 FSPM machine at a rating of 10 kW and 15,000 rpm. The output performances of the optimized machine are evaluated.

5.1 Parametric Analysis of Dual-Stator 6/4 FSPM Machine

The proposed dual-stator 6/4 FSPM machine has many parameters that need to be designed with the goal of producing maximum torque with minimum total weight and volume. No matter which one out of the three proposed topologies is chosen, the two stators of the dual-stator 6/4 FSPM machine has the same lamination dimensions. This section investigates the influence of key geometrical parameters to the performance of the dual-stator 6/4 FSPM machine. To perform large quantities of parametric studies on the geometry to characterize machine performances, 2D FEA

simulation is used to study one stator of the dual-stator machine. It is shown in previous chapters that the 2D FEA simulation gives a decent prediction of the fundamental flux linkage and back-EMF of the 3D-structured machine, with approximately 10% overestimation because the end effects are not considered.

To investigate the key machine parameters to the basic electromagnetic properties such as the flux linkage, back-EMF, average torque, etc., the design of the 6/4 FSPM machine is done by a progressive process. The split ratio, being one of the most important electric machine characteristics, is specifically studied in the following section for its influences on 6/4 FSPM machine performances. First, the baseline designs with different split ratios are compared for the flux linkage, current density, and average torque. Then, the influence of stator teeth width and magnet thickness are investigated for producing the maximum fundamental flux linkage. After that, the parametric studies are done for varying the rotor pole width. In the end, the weight distribution and torque density of the 6/4 FSPM machine are investigated.

This section of the design focuses on a higher power rating of the dual-stator 6/4 FSPM machine, and the target specification is chosen as 10 kW and 15,000 rpm. The constraints on the machine are that the stator outer diameter is fixed. The DC link voltage is fixed at about 200 V and the rated phase current is no more than 50 A_{rms}. The cooling of the machine is forced air cooling so that the current density for continuous operating should approximately below 10 A_{rms}/mm^2. Initial designs using the previously developed sizing equation predict that the stator outer diameter is approximately 130 mm, which is fixed in the later parametric analysis. Other geometrical parameters can change in the studies.

5.1.1 Analysis of Split Ratio of 6/4 FSPM Machine

It is known that to maximize the torque density of an electric machine, the design should aim to maximize both magnetic loading and electric loading simultaneously. The magnetic loading is maximized by having a design with a larger airgap flux density and more effective flux linkage (or back-EMF) in the windings. The electric loading is maximized by having more ampere-turns in the slot, and this typically means putting more turns in the winding and using larger currents. However, the number of turns chosen is also determined by the rated back-EMF requirement for the specified speed, and the inductance of the machine required. Using a larger current magnitude increases the current density in the windings that is limited by the available cooling capability. Typically, the design of maximizing both magnetic loading and electric loading are conflicting requirements that need to compromise one or another.

The split ratio is defined as the ratio of stator inner diameter over stator outer diameter, and the symbol used is λ. The choice of split ratio essentially dictates the design tradeoff between maximizing magnetic loading or electric loading or achieve an optimal compromise between both. It is obvious that the split ratio could have a wide range between zero and one, but not close to zero (this means the airgap periphery is too small to conduction magnetic flux from the stator to the rotor, so the magnetic loading in this case is close to zero) or one (this means that the stator inner diameter is almost the same as stator outer diameter, leaving no room for the slot to place the windings, and the electric loading in this case is close to zero).

$$\lambda_{split} = \frac{D_{is}}{D_{os}} \tag{5.1}$$

To investigate the effect of changing the split ratio to the electromagnetic properties of the 6/4 FSPM machine, baseline designs for each split ratio are compared. The baseline design assumes that stator tooth width, magnet thickness, and slot opening width are all the same. The width of rotor pole is 1.4 times the width of the stator tooth width as suggested in the previous literature [63]. There are a total number of 9 designs with different split ratios that are studied, and the calculated key parameters are shown in TABLE 5.1. The stator outer radius for all cases are kept the same as 65 mm, and the stack length is also kept the same as 80 mm, which is calculated by sizing equation. Airgap thickness for all designs are maintained at 1 mm.

TABLE 5.1 PARAMETERS OF THE 6/4 FSPM MACHINE FOR DESIGNS WITH DIFFERENT SPLIT RATIOS

Design No.	Split Ratio	Rotor Outer Radius [mm]	Rotor Pole Width [mm]	Stator Inner Radius [mm]	Stator Outer Radius [mm]	Stack Length [mm]	Magnet Thickness [mm]	Stator Tooth Width [mm]
1	0.45	28.25	10.72	29.25	65	80	7.66	7.66
2	0.477	30	11.36	31	65	80	8.12	8.12
3	0.50	31.5	11.92	32.5	65	80	8.51	8.51
4	0.523	33	12.46	34	65	80	8.90	8.90
5	0.55	34.75	13.1	35.75	65	80	9.36	9.36
6	0.585	37	13.92	38	65	80	9.95	9.95
7	0.60	38	14.3	39	65	80	10.21	10.21
8	0.631	40	15.02	41	65	80	10.73	10.73
9	0.65	41.25	15.48	42.25	65	80	11.06	11.06

The fundamental flux linkage in the winding as a function of the split ratio is shown in Figure 5.1. It shows that the fundamental flux linkage increases when the split ratio is changed from 0.45 to 0.6, and the fundamental flux linkage decreases when the split ratio increases further beyond from 0.6 to 0.65. The 2^{nd} order flux linkage in the winding as a function of the split ratio

is shown in Figure 5.2, which expresses that the 2nd order flux linkage increases monotonically as the split ratio becomes larger. Thus, the harmonic ratio (the ratio defined by the ratio of 2nd order flux linkage over fundamental flux linkage) becomes bigger as the split ratio increases, which is shown in Figure 5.3.

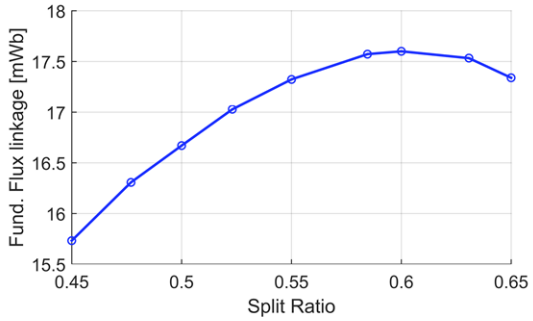

Figure 5.1. Fundamental flux linkage as a function of split ratio for 6/4 FSPM machine.

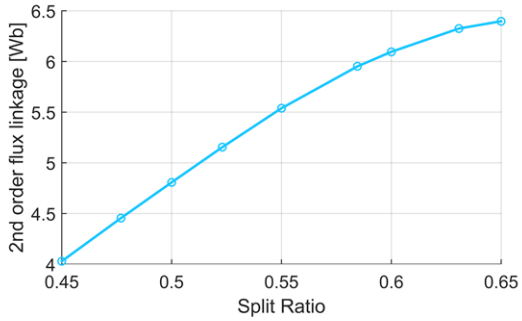

Figure 5.2. 2nd order flux linkage as a function of split ratio for 6/4 FSPM machine.

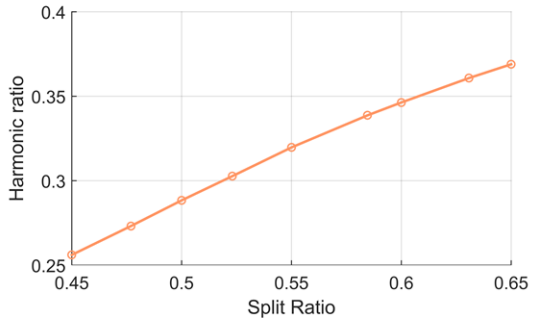

Figure 5.3. Harmonic ratio as a function of split ratio for 6/4 FSPM machine.

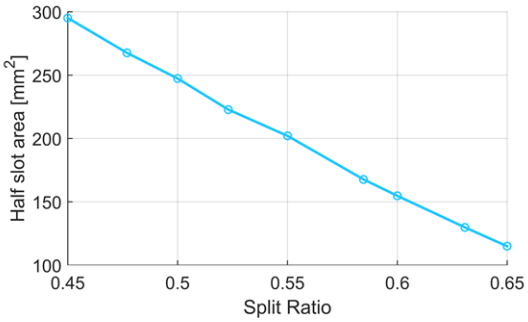

Figure 5.4. Half slot area as a function of split ratio for 6/4 FSPM machine.

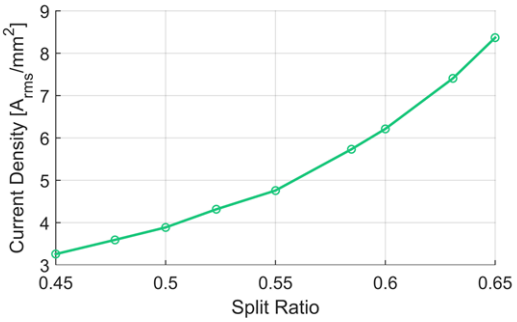

Figure 5.5. Current density as a function of split ratio for 6/4 FSPM machine.

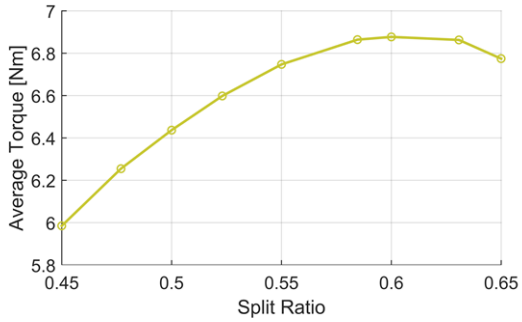

Figure 5.6. Average torque as a function of split ratio for 6/4 FSPM machine.

When the split ratio is increased, the area of half of the slot decreases as shown in Figure 5.4. If the phase back-EMF for the machine is designed at about 100 V_{pk} per phase, the rated current in the machine to produce 10 kW output is about 68 A_{pk}, which is 48.1 A_{rms}. Assume the same phase current of 48.1 A_{rms} is applied for all the cases, the current density in the windings increases from 3.2 A_{rms}/mm^2 at a split ratio of 0.45 to 8.4 A_{rms}/mm^2 at a split ratio of 0.65 shown in Figure 5.5. The average torque as a function of the split ratio is shown in Figure 5.6, which is similar to the variation of fundamental flux linkage curve in Figure 5.1. The torque is maximized at a split ratio of 0.6 in this design, while the current density is around 6.2 A_{rms}/mm^2.

5.1.2 Analysis of Stator Teeth Width and Magnet Thickness of 6/4 FSPM Machine

The flux-switching permanent magnet machines operate by airgap flux density modulation principles from the stator and rotor side permeance variations. Thus, the width of each of the flux modulation component is critical in determining the magnetic loading of the machine. In this parametric study, multiple combinations of different magnet thickness and stator teeth width values are evaluated for the fundamental flux linkage at various split ratio designs. For a given split ratio, the designs are varied such that the magnet thickness is increased from the minimum value (6 mm to 8 mm, depending on the split ratio) to the maximum value (12 mm to 15 mm, depending on the split ratio), and the stator teeth width is also increased from the minimum value (the same as the magnet thickness) to the maximum value (the value that cannot be further increased because the slot will be closed otherwise).

The analyzed split ratios are 0.45, 0.5, 0.523, 0.55, 0.585, 0.6, 0.631, and 0.65. When the split ratio is 0.45, the magnet thickness is changed from 6 mm to 12 mm, and the stator teeth width is changed from 6 mm to 10.5 mm. It needs to point out that to maintain the same minimum slot opening width, the maximum value of the stator teeth width plus half the thickness of the permanent magnet should be equal at a particular split ratio design. For example, when the magnet thickness is 6 mm, the maximum stator teeth width is 10.5 mm (6/2 mm + 10.5 mm = 13.5 mm), and when the magnet thickness is 7 mm, the maximum stator teeth width should be 10 mm (7/2 mm + 10 mm = 13.5 mm). The same rule is applied to other conditions.

The fundamental flux linkage variations at these different split ratio conditions are shown in Figure 5.7(a) to Figure 5.7(h). It is seen that wider stator teeth produce more fundamental flux linkage, given a specified magnet thickness. Similarly, thicker magnet also produces more fundamental flux linkage, given a specified stator teeth thickness. So both stator teeth width and magnet thickness should be maximized to increasing the fundamental flux linkage. However, due to the requirement that the slot should be open for inserting windings, the stator teeth width and magnet thickness should be appropriately allocated.

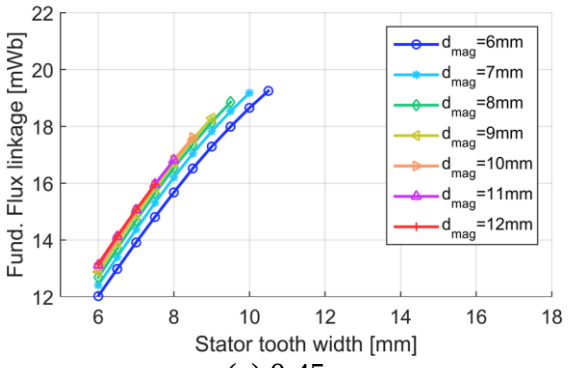

(a) 0.45

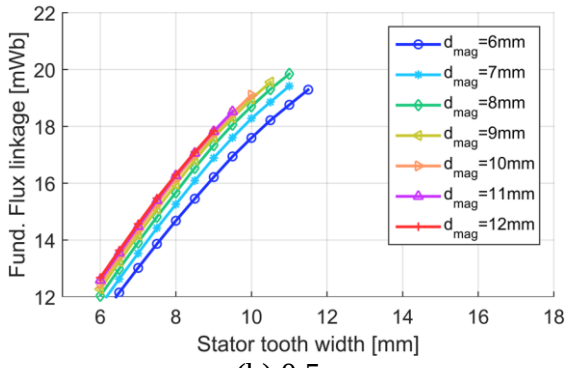

(b) 0.5

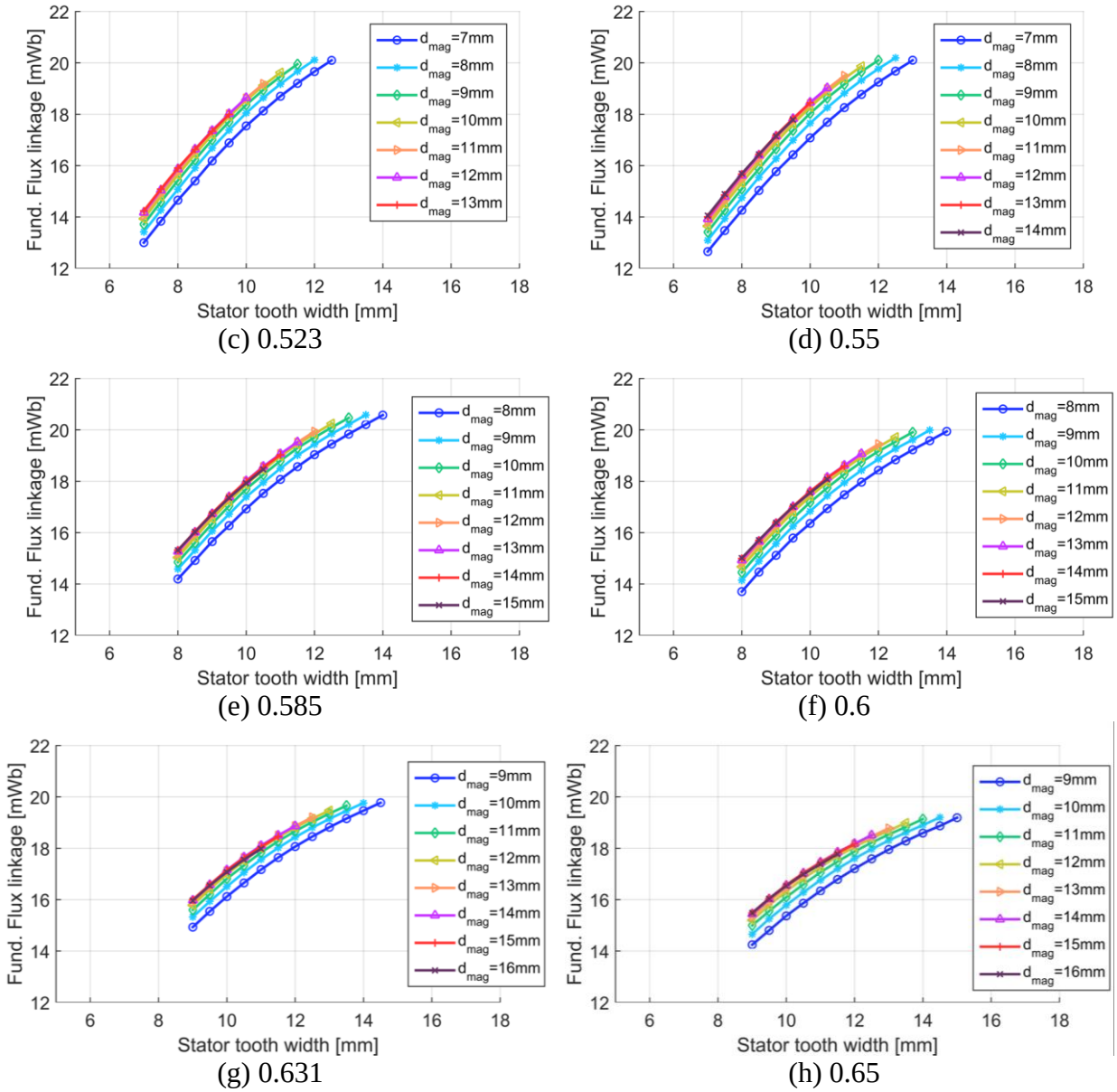

(c) 0.523 (d) 0.55

(e) 0.585 (f) 0.6

(g) 0.631 (h) 0.65

Figure 5.7. Fundamental flux linkage as a function of different stator teeth width and magnet thickness conditions under multiple split ratios λ (a) λ = 0.45 (b) λ= 0.5 (c) λ = 0.523 (d) λ = 0.5 (e) λ = 0.585 (f) λ = 0.6 (g) λ = 0.631 (h) λ = 0.65.

When the split ratio is 0.45, the maximum fundamental flux linkage is achieved at a magnet thickness of 6 mm and a stator teeth width of 10.5 mm. When the split ratio is 0.5, the maximum

fundamental flux linkage is reached at a magnetic thickness of 8 mm and stator teeth width of 11 mm. The same for other split ratio conditions, the maximum fundamental flux linkage at each condition is shown in TABLE 5.2. From the results, one can observe that the maximum flux linkage conditions are achieved when the stator teeth width is larger than the magnet thickness. The maximum fundamental flux linkage at each split ratio condition is also recorded in TABLE 5.2, and it shows that the maximum fundamental flux linkage is realized at a split ratio of 0.585.

TABLE 5.2 PARAMETERS OF THE 6/4 FSPM MACHINE AT DIFFERENT SPLIT RATIO DESIGNS THAT ACHIEVES THE MAXIMUM FLUX LINKAGE

Case No.	Split Ratio	Rotor Outer Radius [mm]	Rotor Pole Width [mm]	Stator Inner Radius [mm]	Stator Outer Radius [mm]	Stack Length [mm]	Magnet Thickness [mm]	Stator Tooth Width [mm]	Fund. Flux Linkage [mWb]
1	0.45	28.25	11	29.25	65	80	6	10.5	19.24
2	0.50	31.5	12	32.5	65	80	8	11	19.84
3	0.523	33	12	34	65	80	8	12	20.12
4	0.55	34.75	13	35.75	65	80	8	12.5	20.20
5	0.585	37	14	38	65	80	9	13.5	20.58
6	0.60	38	14	39	65	80	9	13.5	19.99
7	0.631	40	15	41	65	80	9	14.5	19.77
8	0.65	41.25	15	42.25	65	80	10	14.5	19.20

5.1.3 Analysis of Rotor Pole Width of 6/4 FSPM Machine

The width of the rotor pole also has a big influence on the airgap flux modulation effect. To characterize the effect of varying rotor pole width to the fundamental flux linkage, 2^{nd} order flux linkage, average torque, and ripple, parametric studies are studied and the results are shown for split ratio designs of 0.45, 0.5, 0.55, 0.6, and 0.65 as in Figure 5.8 to Figure 5.11. Increasing the rotor pole width is beneficial in improving the fundamental flux linkage because more steel

material and less saturated rotor poles are available to conduct the magnetic flux flow. The 2nd order flux linkage harmonic goes down as the rotor pole width is increased as shown in Figure 5.9. From the previous analysis, one knows that designs with high fundamental flux linkage and low 2nd order flux linkage produce more torque.

The average torque as a function of rotor pole width at different split ratio conditions is presented in Figure 5.10 which has similar trends as the fundamental flux linkage curves in Figure 5.8. The phase current for all the designs are kept the same at 48.1 A_{rms}. Wider rotor pole increases the torque production capability, but the torque ripple could be going up as a result. Figure 5.11 shows the torque ripple at loaded conditions as a function of rotor pole width. It is observed that when the split ratio is 0.5, the torque ripple goes down when the rotor pole width is changed from 11 mm to 12 mm, and goes up when rotor pole width is changed from 12 mm to 14 mm. In fact, the variation of the torque ripple is more complicated. Torque ripple is very sensitive to the flux modulation condition, which is influenced by both rotor and stator sides. More discussions about torque ripple will be discussed in the later chapters.

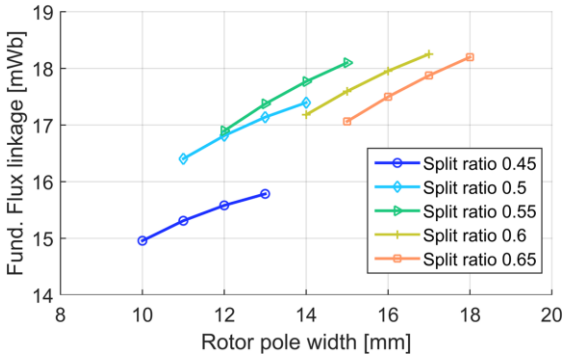

Figure 5.8. Fundamental flux linkage as a function rotor pole width for 6/4 FSPM machine.

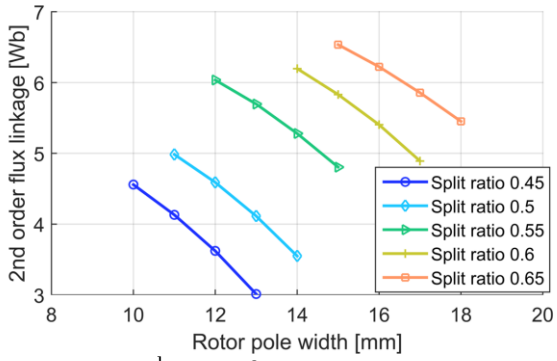

Figure 5.9. 2nd order flux linkage as a function of rotor pole width for 6/4 FSPM machine.

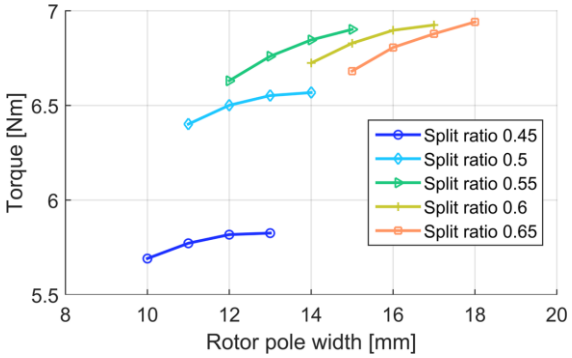

Figure 5.10. Average torque as a function of rotor pole width for 6/4 FSPM machine.

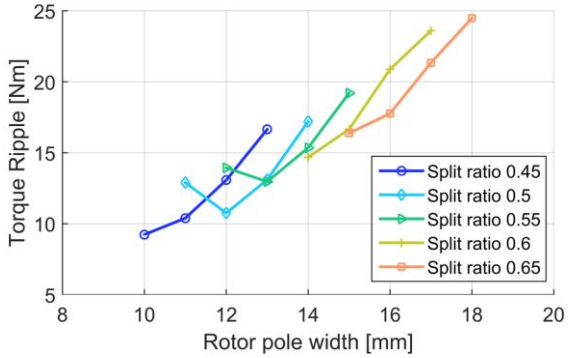

Figure 5.11. Torque ripple as a function of rotor pole width for 6/4 FSPM machine.

5.2 Torque Density of Dual-Stator 6/4 FSPM Machine

5.2.1 Torque Density Evaluated from 2D FEA Study

It is demonstrated that the split ratio, stator tooth width, magnet thickness, and rotor pole width have influences on the magnetic loading and electric loading. To better quantify the torque production capability of the dual-stator 6/4 FSPM machine, torque density needs to be investigated. This section studies the torque density of the dual-stator 6/4 FSPM machine by design of experiments (DOE). The weight distribution of all the designs is also compared.

In this design of experiments study, different combinations of the above four parameters (split ratio, stator tooth width, magnet thickness, and rotor pole width) are used for the 6/4 FSPM machine to explore a large design space. The outer diameter of the stator for all designs are kept at the same of 130 mm as before. It is required that all the designs need to produce almost the same back-EMF at the rated speed of 15,000 rpm, and the same phase current is used to produce almost the same power of 10 kW at this speed. The rated torque at 10 kW and 15,000 rpm condition is

6.366 Nm. Since this study uses 2D FEA to analyze the machine performance, and there is generally a 10% degradation from the more accurate 3D results to 2D results, the produced torque at 2D condition is improved to about 110% of the 6.366 Nm, which is chosen to be 7.04 Nm in this case.

To be more specific about how to set up the design of experiment studies, the designs are chosen such that the split ratio of the 6/4 FSPM machine is designed at 0.45, 0.477, 0.5, 0.523, 0.55, 0.585, 0.6, 0.631, and 0.65 respectively. At each of the split ratio condition, the magnet thickness and stator tooth thickness are chosen as combinations described in Figure 5.7, while each of these combinations is evaluated at four different rotor pole widths. The incremental change for the stator tooth width is 0.5 mm, for the magnet thickness is 1 mm, and for the rotor pole width is 1 mm. Thus, there is a total of 2417 design cases evaluated in this study. The number of individual design cases for each of the 9 different split ratio groups are 197, 181, 273, 253, 305, 305, 325, 273, and 305 individually. To ensure that all the designs produce almost the same torque, the stack length of each of the designs are not the same as 80 mm but adjusted accordingly to produce the same expected torque of 7.04 Nm.

The 2D FEA study is performed for all design cases at the rated condition, and Figure 5.12 shows the scatter plot of the average torque versus the torque ripple (peak to peak) for all the designs. It is noticed that the torque ripple for all the designs is spread across a large range, but the average torque almost stays the same so the output power is almost the same. The torque ripple in this design analysis is not the primary focus, and the final torque ripple for the dual-stator 6/4 FSPM machine can be largely reduced because a significant portion of the torque ripple will be canceled by the offset rotor structure. Additional torque ripple minimization techniques will also

be implemented later in the optimization stage. So, the actual designed dual-stator 6/4 FSPM machine will have much less torque ripple than that shown in Figure 5.12. All the designs use the same phase current value of 48.1 A_{rms}, and produce almost the same phase voltage.

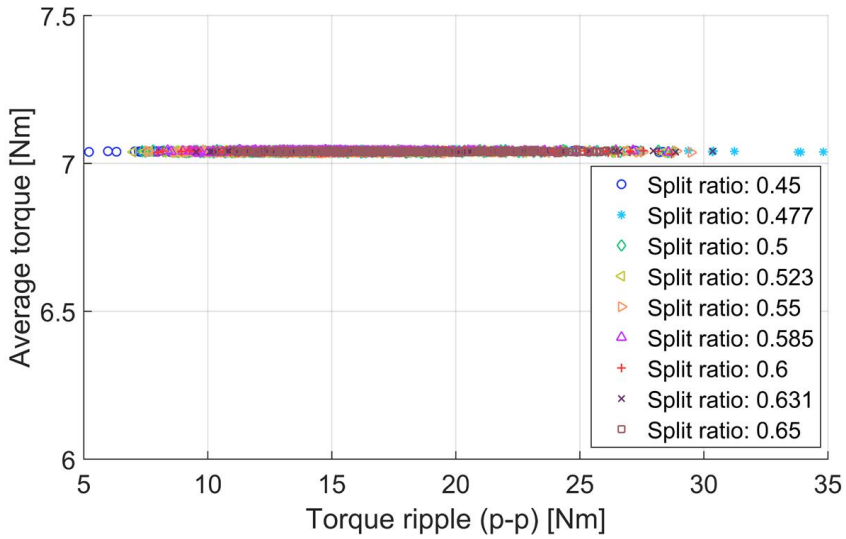

Figure 5.12. Average torque and torque ripple scatter plot for all the design variations of 6/4 FSPM machine.

To calculate the torque density of all the designs, the mass distribution for each design needs to be evaluated. The volume of each of the material, such as steel, permanent magnets, and copper, are determined once the design is finished. It is assumed that the mass density for each of the material is as follows: the steel is 7600 kg/m^3, NdFeB magnet is 7500 kg/m^3, and copper is 8960 kg/m^3. The copper fill factor for all the machines is assumed to be 50%. To have a more accurate prediction of total copper mass, the end winding copper mass is also included.

A scatter plot of the total mass versus rotor mass for all the designs is shown in Figure 5.13. For a given split ratio, the relationship between rotor mass and total mass for the evaluated designs

are almost linear. If designs with the same total mass are chosen to compare, the ones with a higher value of split ratio have larger rotor mass values. From another perspective, if the rotor mass is kept the same, the designs with a smaller total mass favor to have a high split ratio. The scatter plot of total mass with stator mass shown in Figure 5.14 has a more centralized cluster shape. The scatter plots of total mass with permanent magnet mass and total mass with winding mass are shown in Figure 5.15 and Figure 5.16 respectively. The general trend for the mass distribution figures is that the high split ratio designs tend to have smaller weights for the components, and the low split ratio designs tent to have larger weights for the components while the weight values are more spread around.

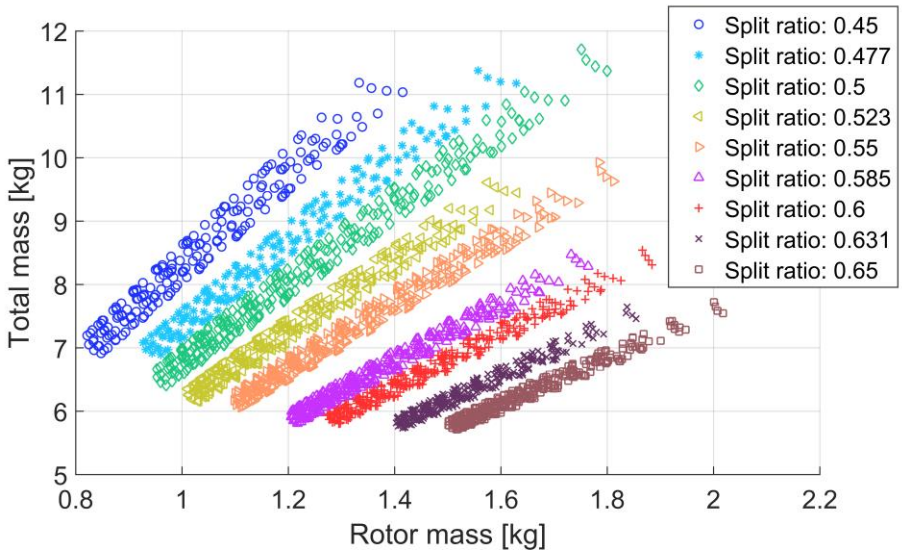

Figure 5.13. Total mass and rotor mass scatter plot for all the design variations of 6/4 FSPM machine.

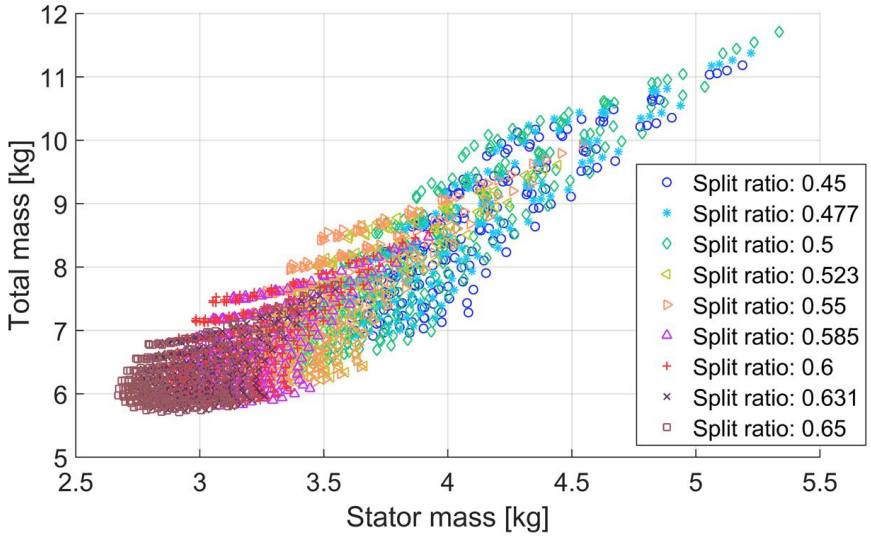

Figure 5.14. Total mass and stator mass scatter plot for all design variations of 6/4 FSPM machines.

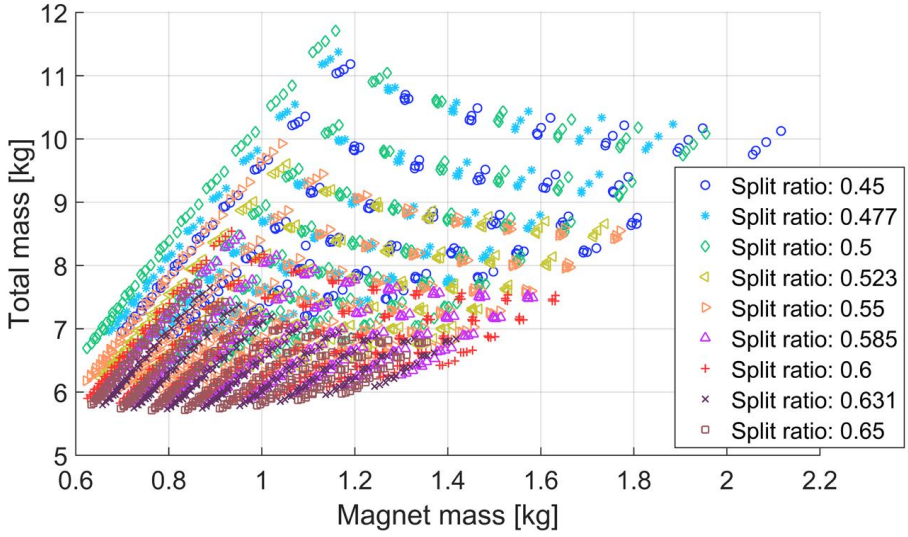

Figure 5.15. Total mass and magnet mass scatter plot for all design variations of 6/4 FSPM machine.

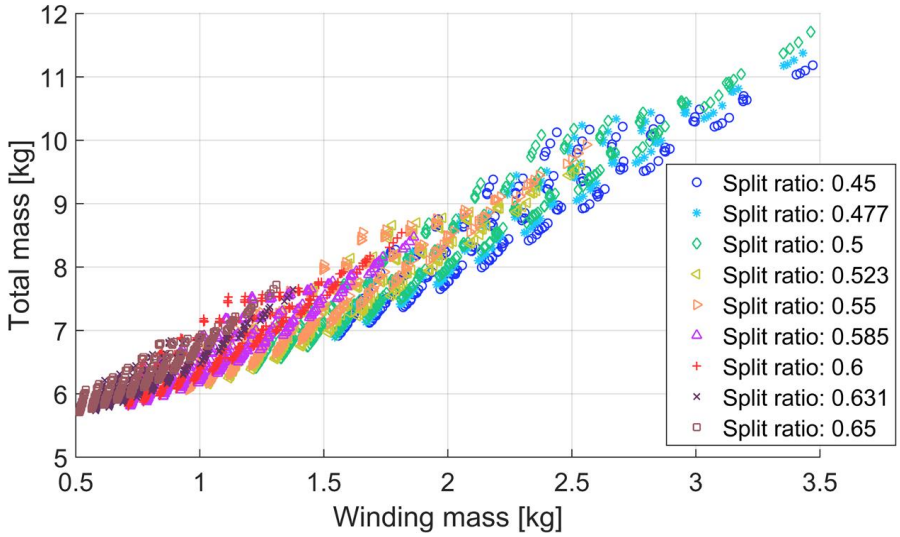

Figure 5.16. Total mass and winding mass scatter plot for all design variations of 6/4 FSPM machines.

Once the torque and mass distribution of all the designs are calculated, the torque densities regarding torque per kilograms are evaluated and compared for each of the designs. It should be emphasized that all the designs have almost the same output torque but may have different values of output weight. Since all the designs have the same phase current values and nearly the same phase voltage values, the comparison of torque density is based on the current density for each of the designs. Figure 5.17 shows the relationship of the torque density (Nm/kg) as a function of current density (A_{rms}/mm^2) for all the designs, which are distinguished by the different split ratios.

The relationship between the torque density and current density reveals design insights on the selection of appropriate geometries based on the cooling requirement that is surrogated by the allowable current density in the windings. Figure 5.17 shows that designs with higher current densities have more torque densities, but the maximum achievable torque density for a particular

current density does not have a linear relationship with the increase of current density. As reflected in the figure, the maximum torque density envelops "saturates" as the current density increases, and this phenomenon is attributable to the increased saturation conditions in the steel because of increased flux from the higher current loading. For example, the maximum torque density is 1.02 Nm/kg at a current density of 4 A_{rms}/mm^2, and 1.2 Nm/kg at a current density of 8 A_{rms}/mm^2. As the current density increases beyond 10 A_{rms}/mm^2, the cooling requirement becomes more challenging for continuous operation. In addition, the torque density improvement becomes very marginal even if the current density further increases.

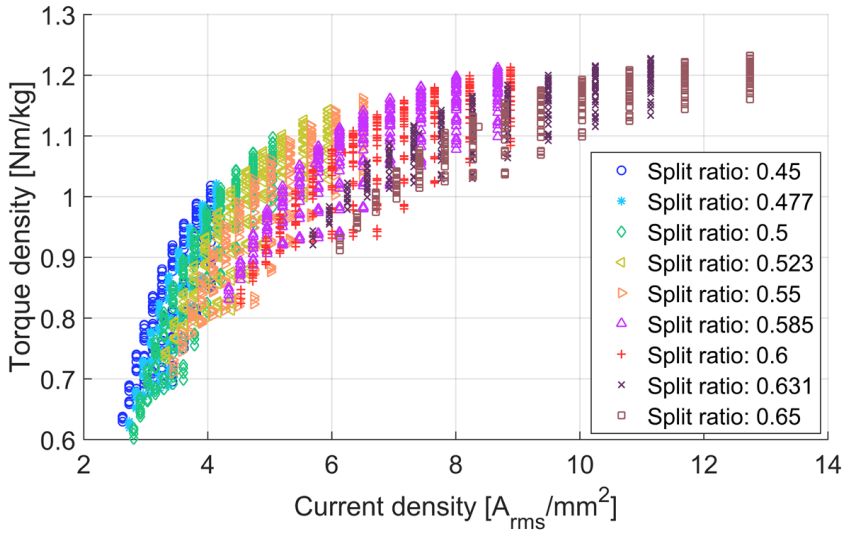

Figure 5.17. Torque density and current density scatter plots for all design variations of 6/4 FSPM machines.

It is also observed that designs with different split ratios across different torque density regions. For example, the torque density range for designs with a split ratio of 0.45 is from 0.62 to 1.03 Nm/kg, and the torque density range for designs with a split ratio of 0.65 is from 0.91 to 1.24

Nm/kg. In general, designs with a low split ratio have lower current density ranges than the designs with a higher split ratio, and this is due to the increased slot area in the low split ratio designs that reduces the current density. To understand the results in another way, it is concluded that selecting the appropriate geometry for maximizing the torque density depends on the current density requirement for that operating condition. When the current density can achieve a high value, designs that maximizing the torque density converge to high split ratio ones, and vice versa. The calculated maximum torque density trajectory with respect to the current density variations in Figure 5.17 is defined as the torque density profile for this 6/4 FSPM machine.

The scatter plot of total winding resistance including the end winding resistance as a function of the end winding resistance is shown in Figure 5.18. The overall relationship of total resistance with respect to the winding resistance is linear as represented in the figure. The designs with a higher split ratio tend to have larger total resistance than the designs with a smaller split ratio.

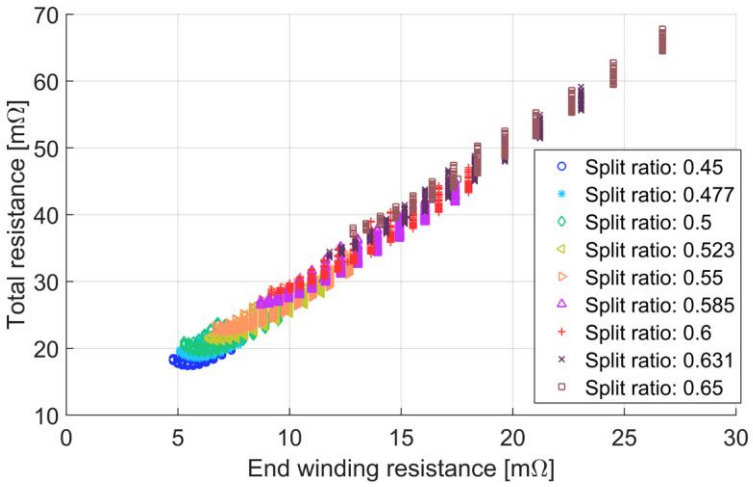

Figure 5.18. Total resistance and end winding resistance scatter plot for all design variations of 6/4 FSPM machines.

5.2.2 Torque Density Evaluated from 3D FEA Study

The previous analysis is done with only 2D finite element analysis for the 6/4 FSPM machine. To evaluate the torque density of the proposed dual-stator 6/4 FSPM machine, 3D finite element analysis should be used to capture the effects that are neglected in the 2D studies. Since the goal is to calculate the maximum torque density with respect to the current density, only the designs that are on the maximum torque density envelop shown in Figure 5.17 are recalculated in 3D FEA. It should be noted that the 3D topology chosen for this study is Topology-I with opposite oriented permanent magnets in the two stators and single winding wrapping around two stators.

There is a total of seven designs with the same rated conditions that are evaluated in the 3D FEA study. When the same current excitation of 48.1 Arms is applied to the phase winding, the output torque from the 3D FEA is reduced from the 2D results. It should also be mentioned that the total weight of the machine is slightly increased due to the addition of the middle rotor part and end windings between two stators. The calculated torque density at 3D FEA as a function of current density is also compared with the 2D FEA results in Figure 5.19 using curve fitting techniques. The comparison is shown to a current density value up to 10 A_{rms}/mm^2, and both curves become more flattened due to the saturation of the steel in the machines. The 2D FEA has approximately 11% more torque density than the 3D FEA results. For example, the calculated torque from 2D FEA is 1.144 Nm and from 3D FEA is 1.030 Nm, when the current density is 5.95 A_{rms}/mm^2.

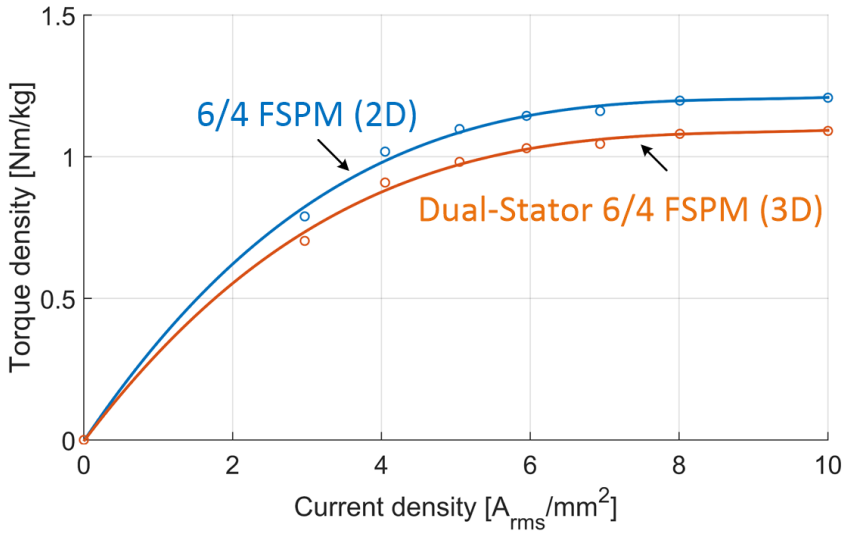

Figure 5.19. Comparison of torque density with respect to the current density of dual-stator 6/4 FSPM machines from both 2D and 3D results.

5.3 Optimization of Dual-Stator 6/4 FSPM Machine

5.3.1 Parametrized Model of Dual-Stator 6/4 FSPM Machine

The analysis shown in the previous sections demonstrate that the design of dual-stator 6/4 FSPM machine is challenging regarding meeting the conflicting performance requirements. To design a better dual-stator 6/4 FSPM machine, optimization is needed to maximize the torque density and minimize the torque ripple, with acceptable constraints such as current density.

The dual-stator 6/4 FSPM machine optimization problem can be simplified by using 2D FEA to optimize the cross section, and then the results should be verified by 3D FEA studies. It is noted that using 3D FEA for optimization is yet to be practical given the limitation of time and

computational resources. The optimization is performed by using the optimization tool in the JMAG-Designer.

The geometrical parameters of the 6/4 FSPM machines are chosen to represent the possible variations of the machine. The stator teeth and rotor poles are designed intentionally to include tips which are a more general condition than the designs without tips because the designs without tips are also included in the geometrical variations when the tips length are zero. The tips are used to adjust the airgap permeance modulation effect and change the torque ripple properties, without changing the width of the rotor pole or the stator teeth. The definition of those parameters in the optimization is illustrated in Figure 5.20. The outer radius of the stator is kept at 65 mm, and the airgap length is kept at 1 mm. The total stack length is also maintained at 80 mm. The parameters that allowed to vary are the stator inner radius R_{is}, magnet inner radius $R_{mag,in}$, magnet outer radius $R_{mag,out}$, stator slot bottom radius R_{slot}, stator teeth width d_{teeth}, half of the magnet thickness $d_{mag,half}$, stator teeth tip length $d_{s,tip}$, rotor shaft radius R_{shaft}, rotor inner radius R_{ir}, rotor pole tip bottom radius $R_{r,tip}$, rotor outer radius R_{or}, rotor pole half width $d_{pole,half}$, and rotor pole tip length $d_{r,tip}$.

The objectives of the optimization are to maximize the average torque and minimize the torque ripple, and both objectives are assigned with equal objective weight. There are also multiple constraints on the optimization that are described here. The continuous current density should be between 3 A_{rms}/mm^2 and 6 A_{rms}/mm^2 to ensure that the cooling capability can satisfy the rated operation. The slot opening width should be no less than 2.2 mm to guarantee that the windings can be inserted into the slots. The airgap length is kept at 1 mm. The copper fill factor is kept at 50%.

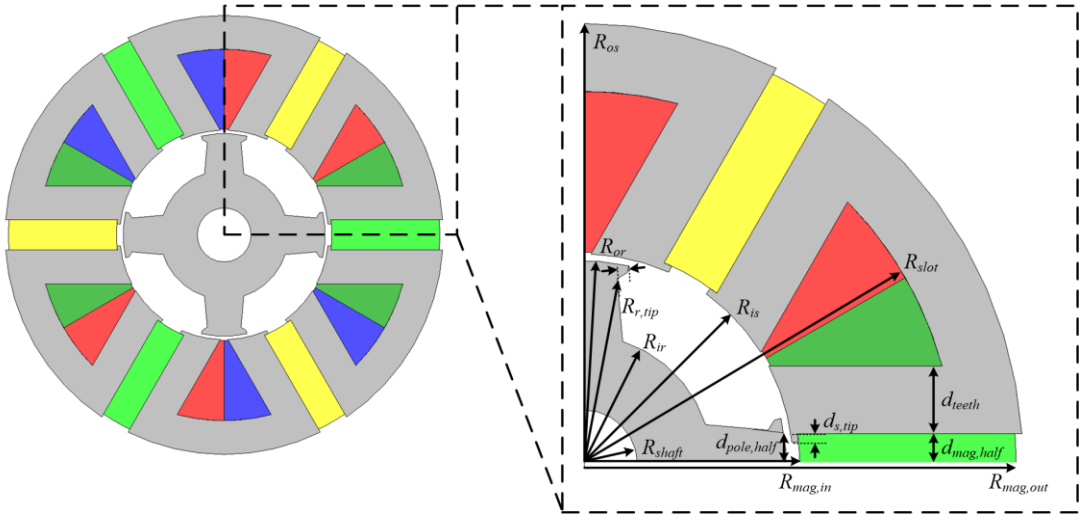

Figure 5.20. Definition of parameters of the 6/4 FSPM machine in the optimization.

5.3.2 Optimization Results of Dual-Stator 6/4 FSPM Machine

The optimization is performed with the above objectives and constraints and the results are shown in TABLE 5.3. It is noticed that the optimization converges on a design that has a stator inner diameter of 62 mm, which is equivalent to a split ratio of 0.4769. This result is consistent with the observations in the torque density profile study in the previous sections, which describes that a lower split ratio is preferred to maximize torque density when the current density is lower. The properties of the optimized dual-stator 6/4 FSPM machine is shown in TABLE 5.4. The optimized design has an average torque of 6.44 Nm with a torque ripple of 1.34 Nm at rated condition.

TABLE 5.3. OPTIMIZATION RESULTS OF THE 6/4 FSPM MACHINE FOR 10 KW AND 15,000 RPM.

	Geometrical Parameters	Symbol	Value
Fixed	Stator outer radius, [mm]	R_{os}	65
	Airgap length, [mm]	g	1
	Total stack length, [mm]	L_e	80
Stator Part	Stator inner radius, [mm]	R_{is}	31
	Magnet inner radius [mm]	$R_{mag,in}$	32
	Magnet outer radius [mm]	$R_{mag,out}$	64
	Stator slot bottom radius [mm]	R_{slot}	55
	Stator teeth width [mm]	d_{teeth}	10
	Magnet half thickness [mm]	$d_{mag,half}$	4.5
	Stator teeth tip length [m]	$d_{s,tip}$	1.8
Rotor Part	Rotor shaft radius [mm]	R_{shaft}	8
	Rotor inner radius [mm]	R_{ir}	19
	Rotor pole tip bottom radius [mm]	$R_{r,tip}$	29
	Rotor outer radius [mm]	R_{or}	30
	Rotor pole half width [mm]	$d_{pole,half}$	4.8
	Rotor pole tip length [mm]	$d_{r,tip}$	1.7

TABLE 5.4. ELECTROMAGNETIC PROPERTIES AND SOME GEOMETRIES IN THE OPTIMIZED Dual-Stator 6/4 FSPM MACHINE

Properties	Value
Average torque [Nm]	6.44
Cogging torque [Nm]	1.39
Torque ripple at rated condition, pp [Nm]	1.34
Current density [A_{rms}/mm^2]	4.97
Stator slot opening width [mm]	2.28
Stator mass [kg]	3.782
Rotor mass [kg]	1.077
Copper mass [kg]	1.556
Magnet mass [kg]	1.039
Total mass [kg]	7.453
Specific torque density [Nm/kg]	0.8639

All the constraints defined in the optimization are satisfied. The current density at rated condition is 4.97 A_{rms}/mm^2, the stator slot opening width is 2.28 mm. The total mass of the dual-stator 6/4 FSPM machine including the stator mass, rotor mass, magnet mass, and total winding mass is 7.453 kg. The calculated specific torque density is 0.8639 Nm/kg. This optimized dual-stator 6/4 FSPM machine is used for the performance comparison with 12/10 FSPM machine in the next chapter.

5.4 Design and Performance for Traction Application

5.4.1 Design Motivation

The proposed dual-stator 6/4 FSPM machine is suitable for designing for traction applications. The motivation of using such a low-pole topology is to reduce the associated high-frequency losses and increase the machine efficiency. The inverter only needs to provide 40% of the fundamental frequency as that of the 12/10 topology, so the reduction of switching frequency reduces the switching losses and increases the system efficiency.

An alternative topology of the dual-stator 6/4 FSPM machine described earlier is used in this traction application design. The key feature of this alternative topology is that it uses windings that wrap across two stators so that end windings between two stators are reduced, and the direction of the permanent magnets should be opposite in two stators. Since the traction machine has a large diameter over axial length ratio, this configuration can reduce the distance between two stators and yield a more compact machine. The two stators are designed with a 30 mm gap distance between

each other. This gap is to provide sufficient reluctance to the magnetic path and prevent permanent magnets shunting in the axial direction.

5.4.2 Performance Characterization

The final design is shown in Figure 5.21 with flux density distribution at the open-circuit condition. TABLE 5.5 summarizes the dimensions and key parameters of the designed machine. The total active mass of the machine is 34.6 kg. The designed machine demonstrates desirable flux weakening capability since the characteristic current (212 A_{rms}) is very close to the rated current (206 A_{rms}). The open-circuit phase back-EMF waveform at 3000 rpm shown in Figure 5.22 has a fundamental value of 67.8 V_{rms} with a total harmonic distortion of 10.5%. The relation of fundamental back-EMF to the rotor speed in Figure 5.23 demonstrates that the phase back-EMF at 100% maximum speed (15,000 rpm) will be 339 V_{rms}.

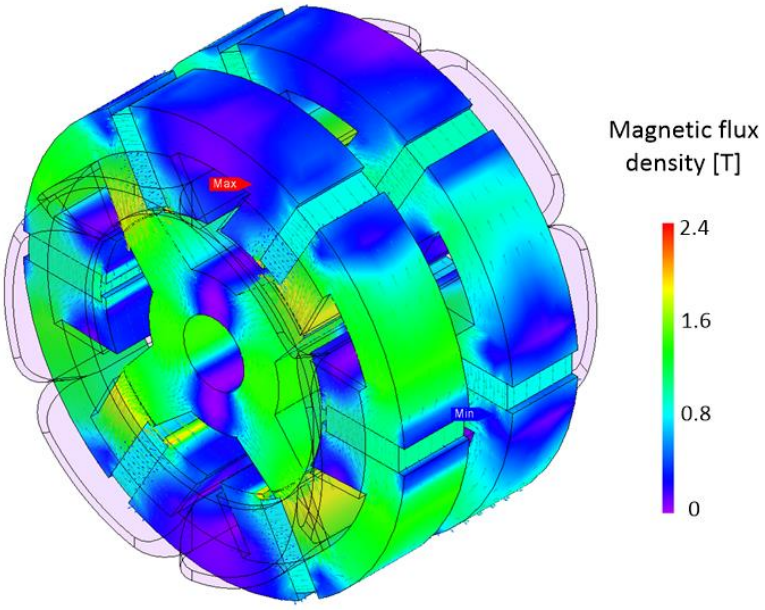

Figure 5.21. Magnetic flux density distribution at open-circuit condition for the dual-stator 6/4 FSPM traction machine.

TABLE 5.5. PARAMETERS FOR A 30 KW TRACTION MOTOR DESIGN

Continuous output power, P_{out} [kW]	30
Corner speed, n_r [rpm]	3000
Maximum speed, n_{max} [rpm]	15,000
Stator outer diameter, D_{os} [mm]	264
Stator inner diameter, D_{is} [mm]	150
Single stator stack length, $L_{e.1/2}$, [mm]	45
Total effective stack length, L_e [mm]	90
Gap distance between stators, L_{gap} [mm]	30
Airgap length, g [mm]	0.75
Phase resistance at 110°C [Ω]	0.017
Permanent magnet grade	N35SH
Stator and rotor lamination steel	20JNEH1200
Mass of copper with end windings [kg]	7.1
Mass of stator iron [kg]	16.8
Mass of rotor iron [kg]	7.4
Mass of NdFeB permanent magnets [kg]	3.2
Total active mass [kg]	34.6
Magnet flux linkage [Wb]	0.0779
Characteristic current [A_{rms}]	212
Rated current [A_{rms}]	206
Maximum phase current, $I_{s,max}$ [A_{rms}]	400
Phase back-EMF at maximum speed [V_{rms}]	339

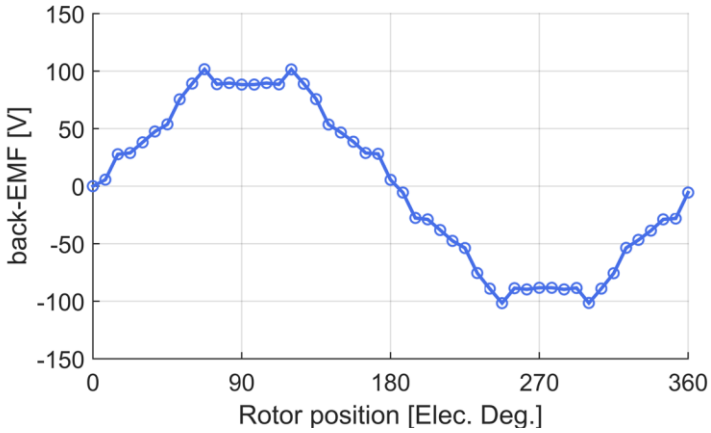

Figure 5.22. Open circuit phase voltage waveforms at a speed of 3000 rpm.

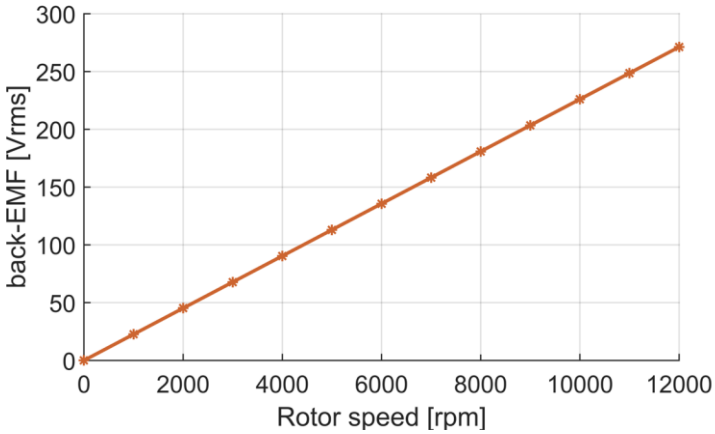

Figure 5.23. Variation of phase back-EMF as a function of rotor speed.

The output torque relation to the phase current is calculated in Figure 5.24. The torque-current relation remains linear for most of the operating regions. When the current is high enough, the lamination steels become more saturated especially in the tips of stator teeth.

The constant power operation capability of the proposed machine is studied and 30 kW continuous output power is maintained throughout the speed range as shown in Figure 5.25. This is to prove the excellent flux weakening capability predicted earlier. Figure 5.26 shows the current

and voltage relations to the rotor speed. The phase current angle of the machine is progressively advanced at higher speeds to increase the magnitude of I_d and counteract the field generated by the permanent magnet. Total phase current has a continuous current density of below 10 A_{rms}/mm^2 at the high-speed region. This modest current density is designed to ensure that cooling of the machine has sufficient margins to deal with the overload conditions.

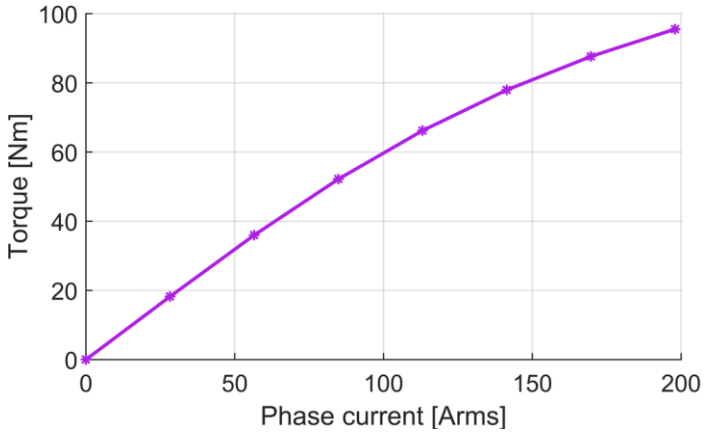

Figure 5.24. Relation of average torque to the phase current.

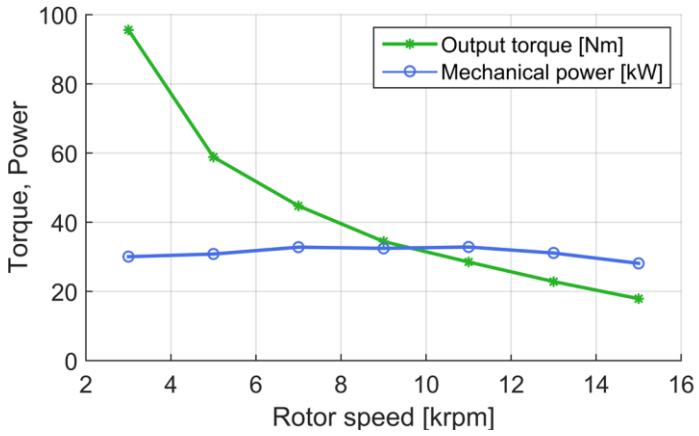

Figure 5.25. Output torque and mechanical power as functions of rotor speed.

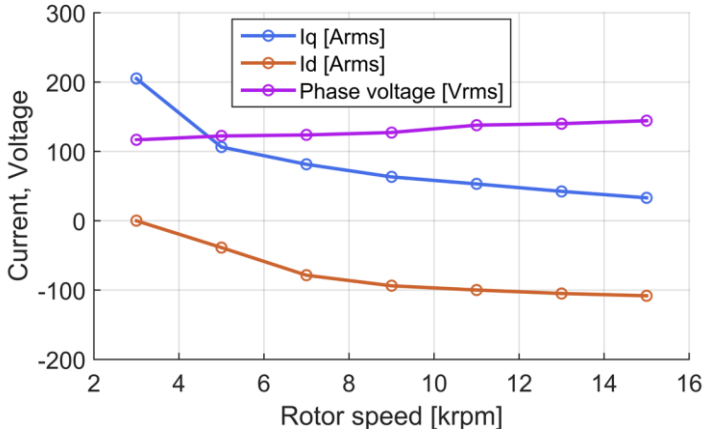

Figure 5.26. Phase current and voltage as functions of rotor speed.

The design of stator lamination structure went through an optimization process to maximize the average output torque for the given constraints. Stator tooth tips in the airgap side as shown in Figure 5.27 are introduced to suppress the cogging torque with only minor reduction of average torque. As identified in the loss study section, the permanent magnet eddy current loss concentrates on the two end parts in the radial direction. The shape of permanent magnets in this traction design is cut at the two ends to reduce the magnet loss. The grade of the permanent magnet used is N35SH. Both the stator and rotor steel laminations use 20JNEH1200 with a lamination thickness of 0.2 mm.

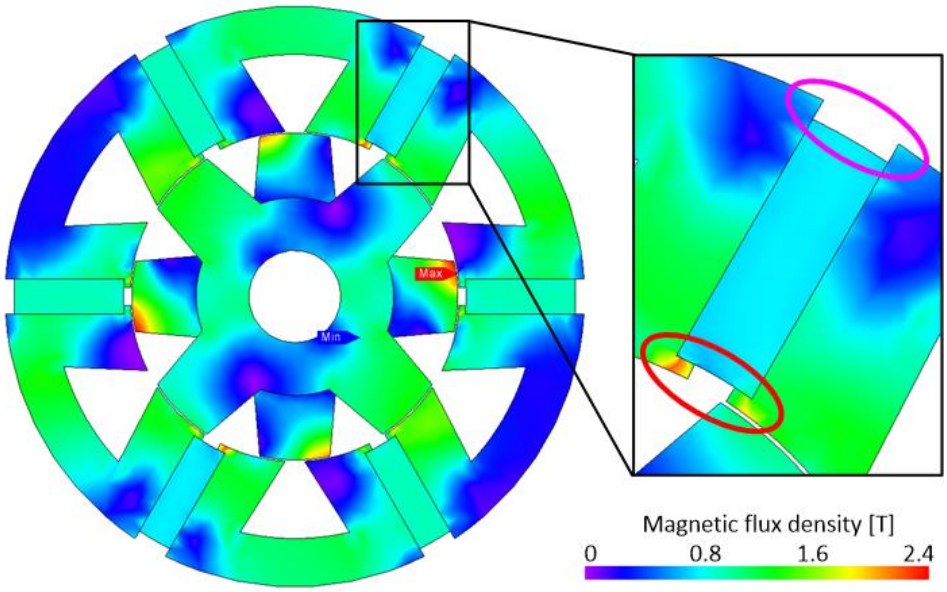

Figure 5.27. Design of stator lamination which shows the implementation of tooth tips in the airgap side, and the design of permanent magnets with cuts at two ends.

The segregation of various loss components at the constant power operating region is shown in Figure 5.28. It is observed that the copper loss accounts for a large percentage of total loss in the low and medium speed region. This is partly due to the increased phase winding resistances from the additional gap between the stators. The stator and rotor iron loss are relatively low across the whole speed range. This is mainly due to the low fundamental frequency benefits of the 6/4 topology. The maximum fundamental frequency is 1 kHz at 15,000 rpm, whereas it is 2.5 kHz for the 12/10 configuration at the same speed. The reduction of iron loss is also caused by the thin gauge lamination material used in the design.

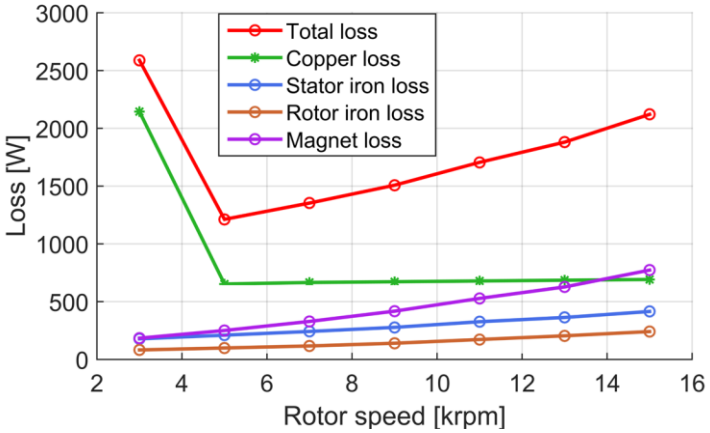

Figure 5.28. Loss segregation for the operating speed range.

The magnets are naturally segmented by two axial pieces as a direct outcome of the dual-stator structure. The magnet eddy current loss is further reduced by using axial segmentations in each stator. The reduced loss generated by the permanent magnets protects them from the risks of thermal demagnetization.

The total efficiency of the dual-stator 6/4 traction machine is higher than 95% for the medium speed range at 30 kW output power shown in Figure 5.29. High-pole FSPM machines have a large iron loss at high-speed conditions which penalize the efficiency. The high efficiency of the dual-stator 6/4 machine particularly at high-speed conditions is achieved mainly due to the reduction of iron losses.

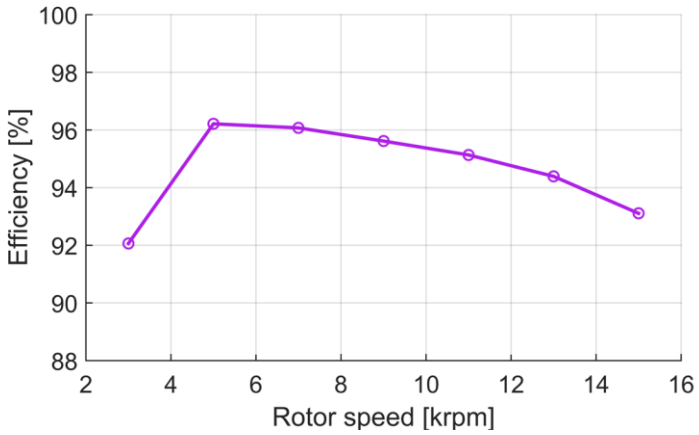

Figure 5.29. Machine efficiency across the operating speed range at 30 kW constant power condition.

Therefore, the dual-stator 6/4 FSPM machine is suitable for traction application. A design with a continuous power of 30 kW and wide constant power operation range up to 15,000 rpm is demonstrated. The iron loss of the dual-stator 6/4 traction machine is low under high-speed conditions. The design can offer above 95% efficiency in the medium speed range of the constant power operating region.

5.5 Design of a 100 kW, 15 000 rpm Machine

The machines presented in previous sections are focused on the designs that have low to medium power range up to 30 kW. To evaluate whether the proposed dual-stator 6/4 FSPM machine is suitable for higher power applications, a 100 kW, 15 000 rpm machine is designed and analyzed in this section to verify that the proposed topology is scalable to higher power and speed ratings. To design the geometrical dimensions of the 100 kW machine, sizing equations that

derived previously are used here to calculate the key machine parameters. In the prior section, the 10 kW 15 000 rpm dual-stator 6/4 FSPM machine is designed and optimized. To jumpstart the design of this higher power machine, the cross-sectional design of a 10 kW 15 000 rpm machine is utilized and scaled to the 100 kW 15 000 rpm machine. Based on the scalability relationship, the key parameters of the new design are shown in TABLE 5.6. This 100 kW design is again verified by 3-D FEA results shown in Figure 5.30. It should be noted that the high-power machine has a high stator diameter to axial length ratio, which is beneficial to increased torque density.

TABLE 5.6 PARAMETERS OF A 100 KW, 15 000 RPM DUAL-STATOR 6/4 FSPM MACHINE

Key Parameters	Symbol	Value
Rated power [kW]	P_r	100
Rated speed [rpm]	n_r	15 000
Stator outer radius, [mm]	R_{os}	135.6
Airgap length, [mm]	g	1
Total stack length, [mm]	L_e	89.5
Stator inner radius, [mm]	R_{is}	64.7
Stator slot bottom radius [mm]	R_{slot}	43.8
Stator teeth width [mm]	d_{teeth}	20.9
Gap between two stators [mm]	d_{gap}	40
Magnet half thickness [mm]	$d_{mag,half}$	9.4
Rotor shaft radius [mm]	R_{shaft}	17
Rotor inner radius [mm]	R_{ir}	40.5
Rotor outer radius [mm]	R_{or}	63.7
Rotor pole half width [mm]	$d_{pole,half}$	10.6
Number of turns per coil	N_c	6
Back-EMF [V_{pk}]	E_{pk}	147
Slot fill factor	k_{cu}	50%
Phase current [A_{rms}]	I_s	339
Current density [A_{rms}/mm^2]	$J_{s,rms}$	7.48
Rated torque [Nm]	T_r	63.7

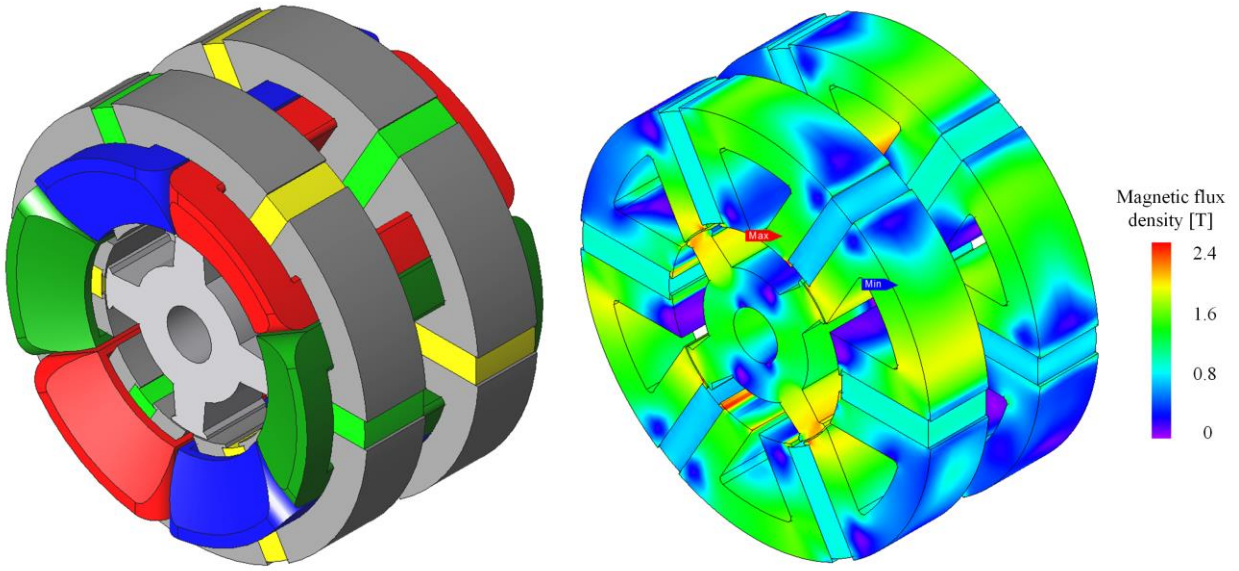

(a) (b)

Figure 5.30. Design of a 100 kW, 15 000 rpm dual-stator 6/4 FSPM machine (a) 3D configuration (b) magnetic flux density distribution at rated condition.

5.6 Principle of Scalability

5.6.1 Scaling Trends for Machine Parameters, Power, and Loss

The key parameters and performance index of the proposed dual-stator 6/4 FSPM machine are shown in TABLE 5.7. To capture the physical insights of the scaling trend of each of the key parameters with respect to the variation of size, the constants in the equations are neglected and only several important variables are remainted to be investigated such as the N_t, D_{is}, L_e, J_s, and g_e. To further simplify the analysis, it can be assumed that the scaling in all directions are proportional, i.e. the increase rate of D_{is}, L_e, and ge are all the same. Therefore, physical insights can be observed more clearly under these assumptions. For example, the winding resistance of the machine

decreases as the machine size increases. The per-unit inductance and time constant of the machine increase as the machine size increases, which means that larger machine tend to respond more slowly than small machines. The output power increases to the fourth order of scale, and the copper loss only increases to the third order of scale. Thus, the per-unit copper loss with respect to the apparent power decreases as the machine becomes larger.

The torque production capability of the proposed machine is determined by the shear stress. Given the condition that the current density of the machine stay unchanged, the shear stress or torque density increases proportional to the increase of scale, particularly of the increase of machine diameter. Therefore, larger machine has a higher torque density than small machine if the machine is designed more like “pancake” shape, when the current density is unchanged. However, the copper loss of the machine increases to the third order of scale, but the cooling surface increases to only the second order of scale. This means that the cooling issue for larger machines becomes more challenging. Therefore, the current density for larger machines are reduced to compensate for the decreased cooling capability.

The above discussed scaling trends are true not only for the proposed dual-stator 6/4 FSPM machine, but are generally true for all the electric machines. The benefits of increases torque density, reduced copper loss percentage, and presumably increased machine efficiency are the properties of larger machines. In the next section, the scaling trends of the axial airgap between two stators are discussed.

TABLE 5.7 SCALING TRENDS OF KEY PARAMETERS OF THE PROPOSED DUAL-STATOR 6/4 FSPM MACHINE

Parameters	Equation	Relation
Back-EMF	$E_{s,rms} = \sqrt{2}\pi^2 N_t B_{g,pk} K_m K_{fund} K_t (\frac{f_e}{N_s}) D_{is} L_e$	$N_t D_{is} L_e$
Current	$I_{s,rms} = \frac{J_s A_{slot} k_{cu}}{N_{coil}} = \frac{J_s K_{slot} D_{is}^2 k_{cu}}{N_t / 2}$	$\frac{J_s D_{is}^2}{N_t}$
Resistance	$R_s = N_t \frac{\rho_{cu}(1+K_{end})L_e}{A_{cond}} = N_t \frac{\rho_{cu}(1+K_{end})L_e}{K_{cond} D_{is}^2}$	$\frac{N_t L_e}{D_{is}^2}$
Inductance	$X_s = \omega_e L_s = (2\pi f_e)(\frac{3}{2})(\frac{8}{\pi})(\frac{k_1 N_t}{P})^2 \mu_0 \frac{D_{is} L_e}{g_e}$	$\frac{N_t^2 D_{is} L_e}{g_e}$
Inductance(p.u.)	$X_s^{p.u.} = \frac{X_s}{Z_B} = \frac{X_s}{V_B / I_B} = \frac{X_s}{E_{s,rms} / I_{s,rms}}$	$\frac{J_s D_{is}^2}{g_e}$
Time constant	$\tau = \frac{L_s}{R_s} = \frac{X_s / (2\pi f_e)}{R_s}$	$\frac{N_t D_{is}^3}{g_e}$
Output Power	$P_{out} = 3\eta K_p E_{s,pk} I_{s,pk}$	$J_s D_{is}^3 L_e$
Copper Loss	$P_{cu} = I_{s,rms}^2 R_s = K(\frac{J_s D_{is}^2}{N_t})^2 (\frac{N_t L_e}{D_{is}^2})$	$\frac{J_s^2 D_{is}^2 L_e}{N_t}$
Copper Loss(p.u.)	$P_{cu}^{p.u.} = \frac{P_{cu}}{VA} = \frac{P_{cu}}{3V_s I_s}$	$\frac{J_s}{N_t D_{is}}$
Shear Stress	$\sigma = B_{g,ave} A_{s,rms} = B_{g,ave} \frac{6N_t}{\pi D_{is}} \frac{J_s K_{slot} D_{is}^2 k_{cu}}{N_t / 2}$	$J_s D_{is}$
Output Torque	$T_{out} = K_{tot} \eta \sigma D_{is}^2 L_e$	$J_s D_{is}^3 L_e$
Torque Density	$\xi_T = T_{out} / V = \frac{\lambda^2 T_{out}}{(\pi / 4) D_{is}^2 L_e}$	$J_s D_{is}$

5.6.2 Scaling Trends for Axial Gap Length Between Two Stators

There is one alternative topology of the proposed dual-stator 6/4 FSPM machine where the magnetization directions of the permanent magnets in two stators are opposite, so that there needs to be an axial gap separation between two stators to prevent magnetic flux leakage in the axial direction. The additional gap between stators increases the overall machine volume and increases

the winding resistance. It is meaningful to understand how the axial gap length changes with respect to the different machine scalings.

To simplify the analysis, the magnetic circuit models are created for the main flux path and the axial leakage flux path as shown in Figure 5.31 and Figure 5.32, respectively. The assumptions made here are that the width of magnet, stator tooth, stator slot opening, and rotor pole are all the same. Fringing and saturation effects are neglected, and the reluctance of steel are neglected.

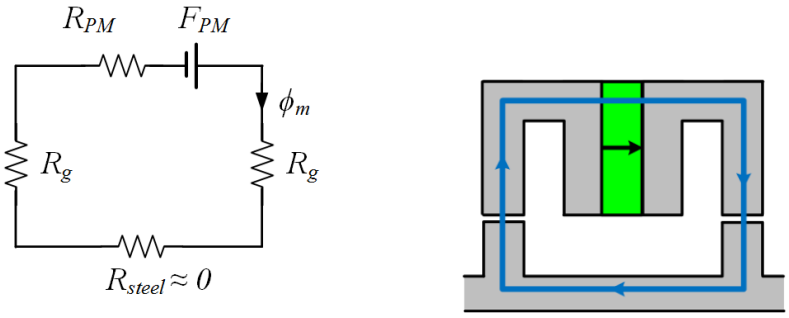

Figure 5.31. Magnetic circuit and illustration of the main flux path.

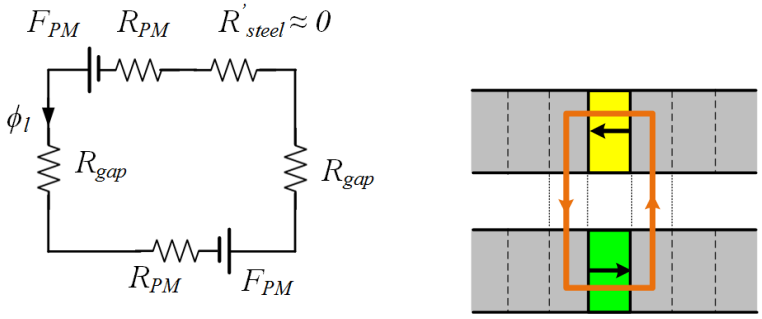

Figure 5.32. Magnetic circuit and illustration of the axial leakage flux path.

Therefore, the reluctance of the PM, the airgap, and the axial gap can be calculated as below where the split ratio (λ) is assumed to be 0.5,

$$R_{PM} = \frac{d_{pm}}{\mu_0 A_1} = \frac{\frac{1}{4}\frac{1}{6}\pi D_{is}}{\mu_0 (\frac{1}{2} L_e)(\frac{D_{os} - D_{is}}{2})} = \frac{\pi\lambda}{6\mu_0(1-\lambda)} \frac{1}{L_e} \tag{5.2}$$

$$R_g = \frac{g}{\mu_0 A_2} = \frac{g}{\mu_0 (\frac{1}{4}\frac{1}{6}\pi D_{is})(\frac{1}{2} L_e)} = (\frac{48}{\mu_0 \pi}) \frac{g}{D_{is} L_e} \tag{5.3}$$

$$R_{gap} = \frac{d_{gap}}{\mu_0 A_3} = \frac{d_{gap}}{\mu_0 (\frac{D_{os} - D_{is}}{2})(\frac{1}{4}\frac{1}{6}\pi D_{is})} = \frac{48\lambda}{\mu_0 \pi (1-\lambda)} \frac{d_{gap}}{D_{is}^2} \tag{5.4}$$

$$\lambda = D_{is} / D_{os} \tag{5.5}$$

To increase the torque production capability, the main flux needs to be maximized while the axial leakage flux needs to be minimized. Therefore, the ratio of main flux over axial leakage flux should be maximized as shown below,

$$\frac{\phi_m}{\phi_l} = \frac{R_{PM} + R_{gap}}{R_{PM} + 2R_g} = \frac{\pi^2 D_{is}^2 + 288 L_e d_{gap}}{\pi^2 D_{is}^2 + 576 D_{is} g} = \frac{\pi^2 + 288 K_L (\frac{d_{gap}}{D_{is}})}{\pi^2 + 576 (\frac{g}{D_{is}})} \tag{5.6}$$

After simplification, the requirement of maximizing the above ratio can be simplified as the equation below

$$d_{gap} >> \frac{2g}{K_L} \tag{5.7}$$

where the axial gap distance needs to be much larger than two times the airgap length over the aspect ration, which is defined by the ratio of effective machine length over inner diameter,

$$K_L = L_e / D_{is} \tag{5.8}$$

Rearrange the above equation to yield the following equation,

$$\frac{d_{gap}}{D_{is}} = \frac{[\pi^2 + 576(\frac{g}{D_{is}})](\frac{\phi_m}{\phi_l}) - \pi^2}{288K_L} \tag{5.9}$$

The above equation can be considered as the per-unit axial gap length over the machine inner diameter. It can be observed that if the ratio of main flux over leakage flux is unchanged and if the airgap length is unchanged, as the machine inner diameter increases, the per-unit value of axial gap length decreases. Also, as the effective length of the machine increases and the aspect ratio increases, the per-unit value of axial gap length decreases. This demonstrates that larger dual-stator 6/4 FSPM machine tends to minimize the impact from the introduction of axial gap length compared to small sizes.

5.6.3 Comparison of Different Scalable Designs

There is a total of four different dual-stator 6/4 FSPM machines designed for different power and speed combinations so far. This section is aimed to compare the key design parameters and performance of those four designs to validate that the proposed sizing principle is scalable for a wide range of power and speed ratings. The compared four designs are described as follows: Design-A is rated at 1.5 kW and 1800 rpm, which is the manufactured low-speed proof-of-concept prototype that will be discussed later in the thesis. Design-B is rated at 10 kW and 15 000 rpm. Design-C is rated at 30 kW and 3000 rpm (corner speed) for traction application designed in the prior section. Design-D is rated at 100 kW and 15 000 rpm, which is the design mentioned in the

prior section. All four designs are verified by 3D FEA, and their major design parameters are tabulated in TABLE 5.8. The 3D sizing comparison of the four designs are visualized in Figure 5.33.

TABLE 5.8 SCALABILITY COMPARISON AND VERIFICATION OF FOUR DESIGNED DUAL-STATOR 6/4 FSPM MACHINES UNDER DIFFERENT POWER AND SPEED CONDITIONS

Key Parameters	Symbol	Design-A	Design-B	Design-C	Design-D
Rated power [kW]	P_r	1.5	10	30	100
Rated speed [rpm]	n_r	1800	15 000	3000	15 000
Tip speed [m/s]	v_{tip}	7.8	47.1	23.3	100.0
Stator outer radius [mm]	R_{os}	65	65	132	135.6
Airgap length [mm]	g	1	1	0.75	1
Total stack length [mm]	L_e	83.1	80.0	90	89.5
Stator inner radius [mm]	R_{is}	42.25	31	75	64.7
Stator slot bottom radius [mm]	R_{slot}	58	55	110	43.8
Stator teeth width [mm]	d_{teeth}	11	10	24	20.9
Magnet half thickness [mm]	$d_{mag,half}$	5.5	4.5	8	9.4
Rotor shaft radius [mm]	R_{shaft}	12.7	8.5	21	17
Rotor inner radius [mm]	R_{ir}	28	19	45	40.5
Rotor outer radius [mm]	R_{or}	41.25	30	74.25	63.7
Rotor pole half width [mm]	$d_{pole,half}$	6	5	16	10.6
Number of turns per coil	N_c	60	10	16	6
Back-EMF [V_{pk}]	E_{pk}	100	100	96	147
Slot fill factor	k_{cu}	50%	50%	50%	50%
Phase current [A_{rms}]	I_s	7.8	48.1	206	339
Current density [A_{rms}/mm^2]	$J_{s,rms}$	7.5	7.7	9.1	7.48
Rated torque [Nm]	T_r	7.96	6.37	95.5	63.7
Peak airgap flux density [T]	B_g	1.6	1.7	1.6	1.7
Average magnetic loading [T]	$B_{g,ave}$	0.64	0.68	0.64	0.68
Electrical loading [kA_{rms}/m]	$A_{s,rms}$	21.15	29.6	84.8	60.0
Shear stress [kPa]	σ	13.5	20.1	54.3	40.8
K_{tot} from analytical	K_{tot}	1.12	1.14	0.99	1.14
$D_{is}^2 L_e$ [m^3]	$(D_{is}^2 L_e)$	5.66e-4	3.08e-4	20.3e-4	15.0e-4
Assumed efficiency	η	95%	95%	95%	95%
Calculated torque [T]	T_{cal}	8.17	6.71	103	66.3

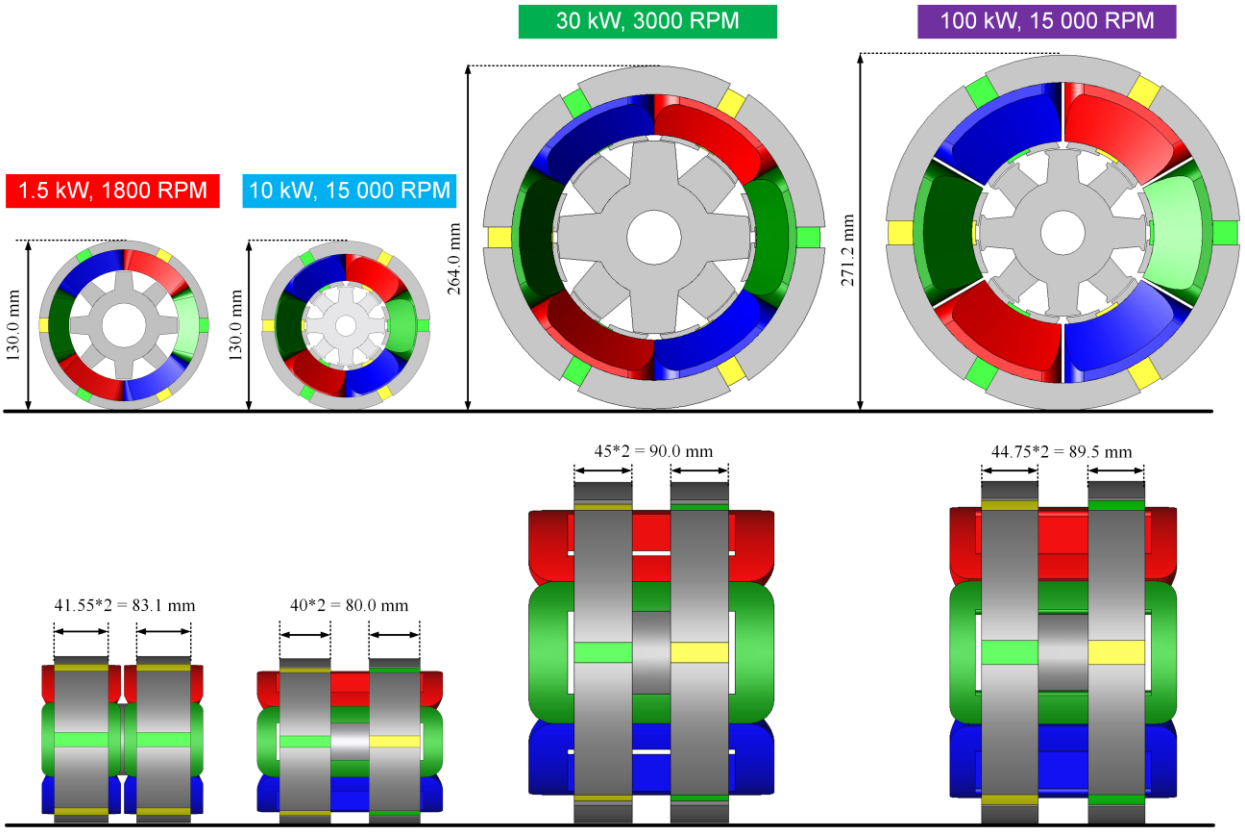

(a) (b) (c) (d)

Figure 5.33. 3D visual sizing comparison of the four designed dual-stator 6/4 FSPM machines. (a) 1.5 kW, 1800 RPM designed for low-speed prototype. (b) 10 kW, 15 000 RPM design (c) 30 kW, 3 000 RPM designed for traction application. (d) 100 kW, 15 000 RPM designed for higher power application.

The principle of scalability can be simply explained by the previously derived sizing equations. The torque equation of the proposed dual-stator 6/4 FSPM machine is shown below with rearrangements of various constants and parameters. The torque equation represents the essence of scalability as an electrical machine is sized by torque, not power. The rotational speed of an electrical machine is determined by the application requirement, loss and efficiency demand, and other related considerations. Once the torque and speed of the electrical machine are

determined, the power of the electrical machine thus can be calculated. Although there are many *K*-factors in the torque equation, they can be bundled into a congregated parameter of K_{tot} which lumps the constant ($2^{0.5}\pi^2/4$), the magnetizing coefficient K_m, fundamental coefficient K_{fund}, stator tooth width coefficient K_t, peak airgap flux density coefficient K_{pk} (defined by the ratio of peak airgap flux density over average flux density), and the ratio of number of rotor poles over stator slots N_r/N_s. The multiplication of magnetic loading (average airgap flux density in this case) and the electrical loading yields the shear stress σ, which is an important metric for an electric machine. Normal permanent magnet machines typically have a shear stress of 5-20 kPa. High-performance electrical machines with liquid cooling can achieve a shear stress value up to about 100 kPa.

$$T_{out} = \frac{\sqrt{2}\pi^2}{4} K_m K_{fund} K_t \eta (\frac{N_r}{N_s}) B_{g,pk} A_{s,rms} D_{is}^2 L_e$$

$$= (\frac{\sqrt{2}\pi^2}{4} K_m K_{fund} K_t K_{pk} \frac{N_r}{N_s}) \eta (B_{g,ave} A_{s,rms}) D_{is}^2 L_e$$

$$= K_{tot} \eta \sigma D_{is}^2 L_e \tag{5.10}$$

The above equation is a simplified expression of the torque equation. If the required torque for the electric machine is specified, the key dimensions of the machine $D_{is}^2 L$ can be calculated from scaling constant K_{tot}, the efficiency of the machine η, and shear stress in the airgap σ. It should be noted that the calculated $D_{is}^2 L$ defines the multiplication of square of airgap diameter and the active length of the machine. The actual values of D_{is} and L need to be calculated based on more information such as tip speed of the rotor, frame size requirement of the application, torque density,

etc. The outer diameter of the stator D_{os} needs to be also determined by factors including the frame size restriction, and the partition between magnetic and electrical loadings.

To verify whether the analytical torque equation holds true for the four compared designs, 3D FEA studies for all the four designs are shown in detail in TABLE 5.8 including the relevant design parameters of stator inner diameter, active length, magnetic and electrical loading, and the produced torque. The value of D_{is}^2L and σ can be calculated based on the designs from FEA. Therefore, by substituting the value of K_{tot}, D_{is}^2L, and σ into the previously simplified torque equation and assuming the efficiency η is 95%, the torque from analytical equation can be calculated for each design. The torque calculated from the FEA is compared with the torque calculated from the analytical torque equation, and excellent agreement is observed between these two calculations. Therefore, it can be summarized that the torque equation and other sizing equations can be scalable to a wide range of different power and speed ratings and maintain reasonably accurate predictions of the performance.

5.7 Summary

This chapter presents the parametric and optimization analysis of the proposed machine. Parametric analysis is used to study the influence of split ratio, stator teeth width, magnet thickness, and rotor pole width to the machine performance. Torque density of the dual-stator 6/4 FSPM machine is calculated. A design case for traction application with a rating of 30 kW and 15,000 rpm maximum speed is studied. In the end, the principle of scalability is discussed based on the comparison of four different designs. The key research conclusions in this chapter are summarized below.

- The design of dual-stator 6/4 FSPM machine needs to address the selection of appropriate split ratio, which is responsible for partitioning the electrical and magnetic loadings.
- Wider total width of stator teeth and magnet thickness is beneficial to increasing the output torque, but the width of stator teeth and magnet thickness is not usually equal. Typically, the width of stator teeth is larger than the magnet thickness when high energy NdFeB magnets are used.
- Rotor pole width has a big influence on the torque property. Wider rotor pole generally enables more average torque production, but it may also increase the torque ripple.
- The design objectives of maximizing average torque and minimizing torque ripple are conflicting requirements that are challenging to satisfy. The tips introduced in the stator teeth and rotor poles offers more degrees of freedom in the optimization design space of the machine. An optimized dual-stator 6/4 FSPM machine is obtained for a 10 kW and 15,000 rpm design.
- The proposed dual-stator 6/4 FSPM machine can be designed for traction application to meet the wide constant power speed range and high-efficiency requirement. Due to the low number of rotor poles, the high-frequency related losses of this machine are less.
- The proposed dual-stator 6/4 FSPM machine can be scaled to different power and speed ratings. The derived sizing equation can provide a reasonably accurate prediction of key machine dimensions including the multiplication of the square of airgap diameter and active length based on the information of shear stress and required torque.

Chapter 6

Performance Comparison of Dual-Stator 6/4 FSPM Machine and 12/10 FSPM Machine

One of the strongest motivations of designing low-pole FSPM machine is to reduce high-frequency losses at the high-speed condition, compared to the high-pole FSPM machines. The performance of proposed dual-stator 6/4 FSPM machine needs to be compared with the baseline high-pole FSPM machines to prove the loss reduction benefits. Therefore, the baseline 12/10 FSPM machine is investigated here for the basic design equations and loss properties. The sizing equations of 12/10 FSPM machine are also derived here for completeness. A design case study for 12/10 FSPM machine at high-speed condition is provided to studying various loss properties including iron loss, magnet eddy current loss, and windage loss. Parametric analysis and optimization similar to the 6/4 FSPM machine are done for 12/10 FSPM machine. The torque density of dual-stator 6/4 FSPM and 12/10 FSPM machines are compared. Design and performance including mass and loss distributions and efficiencies are evaluated.

6.1 Sizing Equation of 12/10 FSPM Machine

The sinusoidal nature of PM flux linkage and back-EMF of the 12/10 FSPM machine makes it easy to derive the sizing equations using generalized sizing laws for synchronous machines. If stator phase winding resistance and leakage inductance are neglected, the output power of the FSPM machine is expressed as,

$$P_{FSPM} = \eta m K_p E_{pk} I_{pk} \tag{6.1}$$

where η is the efficiency of the machine, m is the number of phases, K_p is the electrical power waveform factor. E_{pk} is the peak value of single phase winding back-EMF in V, I_{pk} is the peak value of the stator phase current in A. It is known that the reluctance torque of FSPM machine is negligible and PM torque is the main contributing torque component, so stator current vector is assumed to be in alignment with the back-EMF and there is no d-axis current. Thus, the value of K_p is determined as 0.5 according to [276].

The flux per pole as a function of rotor position is expressed as,

$$\Phi_p = B_{g,pk} K_{av} (\frac{D_{is}\pi}{N_s}) L_e K_t \cos(N_r \theta_m) \tag{6.2}$$

where $B_{g,pk}$ is the peak value of airgap flux density in T when the rotor tooth is aligned with the corresponding stator tooth. $B_{g,pk}$ is also defined as the magnetic loading of FSPM machine. The coefficient of K_{av} is introduced to convert the peak airgap flux density to the average flux density seem by the winding coil. D_{is} is the stator inner diameter in m, N_s is the number of stator poles, L_e is the effective length of the machine in m, K_t is the ratio of stator tooth width over stator pole pitch since the flux is assumed to pass via the stator tooth when flux links the coil winding. N_r is

the number of rotor poles. θ_m is rotor mechanical angle around the airgap. If N_t is defined as the number of series connected turns per phase, and ω_m is the mechanical angular speed of the rotor, the flux linkage per phase winding is expressed as,

$$\lambda_p = N_t B_{g,pk} K_{av} (\frac{D_{is}\pi}{N_s}) L_e K_t \cos(N_r \omega_m t) \tag{6.3}$$

Stator excitation frequency can be express as,

$$f_e = \frac{n\ N_r}{60} \tag{6.4}$$

This equation is different than the normal PM synchronous machine equation because in the numerator N_r is the number of rotor poles, not pole pairs. The rotational speed n is defined in rpm. Substitute the relationship of $\omega_m = n \cdot \pi/30$ into the above equation and get $\omega_m = 2f_e \cdot \pi/N_r$. The peak value of phase winding back-EMF can be derived by calculating the derivative of flux linkage with respect to time as expressed as,

$$E_{pk} = 2\pi^2 N_t B_{g,pk} K_{av} K_t (\frac{f_e}{N_s}) D_{is} L_e \tag{6.5}$$

The peak value of phase winding current is expressed as,

$$I_{pk} = \frac{\sqrt{2} D_{is}\pi}{2mN_t} A_{s,rms} \tag{6.6}$$

where A_s is the stator linear current density or electrical loading in A_{rms}/m. Substitute the above expressions into the output power equation and yields,

$$P_{FSPM} = \frac{\sqrt{2}\pi^3}{2} K_{av} K_t \eta (\frac{f_e}{N_s}) B_{g,pk} A_{s,rms} D_{is}^2 L_e \quad (6.7)$$

The output power of FSPM machine is proportional to the magnetic loading, electrical loading, and operating frequency. It should be observed that the magnetic loading of FSPM machine is much higher than SPM machine because of the flux concentrating effect. If the split ratio is defined as stator inner to outer diameter ratio as expressed in $\lambda = D_{is}/D_{os}$, and the aspect ratio is defined as $K_L = L_e/D_{is}$, then the power equation can also be expressed as,

$$P_{FSPM} = \frac{\sqrt{2}\pi^3}{2} K_{av} K_t \eta (\frac{f_e}{N_s}) B_{g,pk} A_{s,rms} K_L \lambda^3 D_{os}^3 \quad (6.8)$$

If the loss components are neglected, i.e. winding copper loss, stator and rotor iron loss, magnet eddy current loss, and friction and windage loss are not considered, the output torque can be expressed as,

$$T_{FSPM} = \frac{P_{FSPM}}{\omega_m} = \frac{\sqrt{2}\pi^2}{4} K_{av} K_t \eta (\frac{N_r}{N_s}) B_{g,pk} A_{s,rms} K_L \lambda^3 D_{os}^3 \quad (6.9)$$

The magnetic loading of the FSPM machine in low-speed application can be higher than 2 Tesla due to the flux concentrating effect. However, peak airgap flux density needs to be reduced for the high-speed operation to avoid excessive high-frequency losses.

6.2 Design Considerations of 12/10 FSPM Machine for High-Speed Operation

The 12/10 FSPM machine has been the most popular topology because it does not have issues of unbalanced back-EMF and unbalanced rotor force. In this section of the study, the design

considerations regarding the loss properties of the 12/10 FSPM machine are investigated. Key parameters of the machine, such as stator outer diameter, back-EMF, phase-current, are calculated using analytical equations for a specification of 10 kW and 15,000 rpm. One of the designs that has the maximum efficiency is chosen for the loss property studies. The parameters of the designed 12/10 FSPM machine are tabulated in TABLE 6.1. The machine has a split ratio of 0.6 and an aspect ratio of 0.9, and the stator outer diameter is 117 mm. Phase AC resistance is calculated by accounting for the ending winding resistance, and the skin and proximity effect also are included by assuming the total AC resistance is two times the DC resistance.

The analytical design yields a rated phase current of 25.9 Ampere peak with a current density of 4.4 A_{rms}/mm^2 (assuming slot fill factor is 50%). The number of turns per coil is designed as low as ten turns so that the amplitude of back-EMF is within the converter output limit at such high speeds. Rated torque is achieved at 6.4 Nm.

TABLE 6.1. PARAMETERS FOR THE HIGH-SPEED 12/10 FSPM MACHINE FOR LOSS PROPERTY ANALYSIS

Parameter	Values
Output power (kW)	10
Rated speed (rpm)	15,000
Stator outer diameter (mm)	117
Stator inner diameter (mm)	70.2
Airgap length (mm)	1
Magnet width (mm)	4.6
Effective length (mm)	63.2
Phase current (A pk)	25.9
Current density (A_{rms}/mm^2)	4.4
Phase AC resistance (mΩ)	68
Number of turns per coil	10
Number of coils per phase	4
Slot fill factor	50 %

6.2.1 Iron Loss Properties

One property of 12/10 FSPM machine for high-speed operation is that it requires high fundamental excitation frequency. For the speed of 15,000 rpm, the fundamental frequency is as high as 2.5 kHz, which creates a big challenge for the converter design. The associated high-frequency losses, such as copper loss (including eddy current loss and proximity loss) and iron loss, could be excessive. Proximity loss of the winding is studied in [254] and is not considered in this study.

To reduce the iron loss and maintain a reasonable efficiency for the machine, thin gauge lamination material 10JNEX900 with a lamination thickness of 0.1 mm is used for the stator and rotor steel. 10JNEX900 is a non-oriented electrical steel with 6.5% mass content of silicon. The iron loss for high-frequency applications of this steel is shown to be very low [277]. Saturation flux density of this steel is around 1.8 T. Since the peak airgap flux density of FSPM machines is designed to be around 1.7 T, the stator and rotor teeth are not heavily saturated at the rated condition. Another potential candidate for steel material for FSPM machines is Hiperco 50, which has a high saturation flux density of 2.4 Tesla. FSPM machines can take advantage of this high saturation flux density material made of cobalt-iron and increase the magnetic loading to a much higher level and further reduce the size and weight of the machine.

The total iron loss is separated into two components, which are eddy current loss and hysteresis loss in the finite element analysis study. Iron loss density contour plots are shown in Figure 6.1 for rated operating condition. Maximum iron loss density is in the rotor tips where the

change of magnetic flux is most dramatic. Eddy current loss dominates over the hysteresis loss at such high-frequency operating conditions.

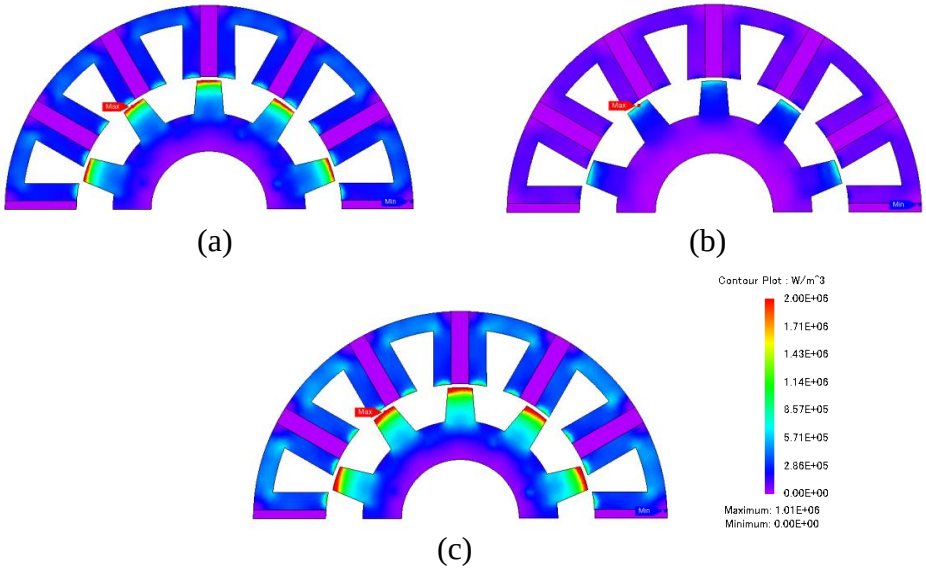

Figure 6.1. Iron loss density distribution of 12/10 FSPM machine at rated condition (a) eddy current loss density, (b) hysteresis loss density, (c) total iron loss density.

Magnetic flux waveforms in one of the stator tooth, stator yoke, and one rotor tooth are drawn in Figure 6.2. Harmonic components of eddy current losses in the stator and rotor are studied in detail by performing FFT analysis. Results show that, as expected, stator eddy current losses have a fundamental frequency of 2.5 kHz. Low-order harmonics of eddy current loss exist, including both odd and even order harmonic components, as shown in Figure 6.3. This is because the flux waveforms in the stator iron are quasi-sinusoidal, which is not symmetrical for the positive and negative half cycles as seen in Figure 6.2.

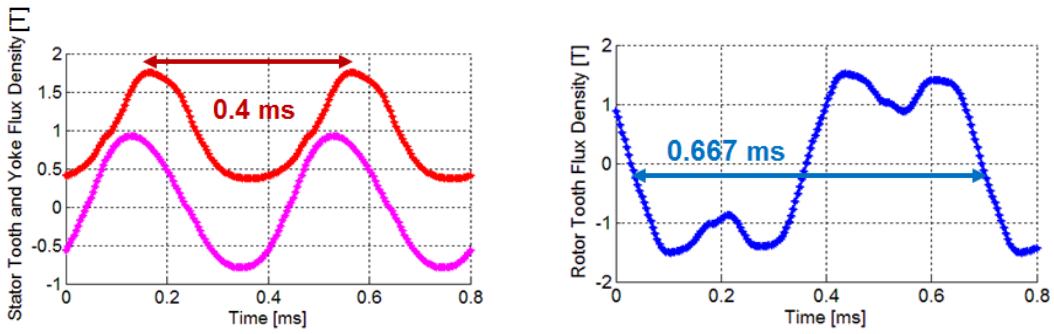

(a) (b)

Figure 6.2. Flux density in 12/10 FSPM machine (a) flux waveforms in stator tooth (radial component) and stator yoke (circumferential component), (b) flux waveform in rotor tooth (radial component).

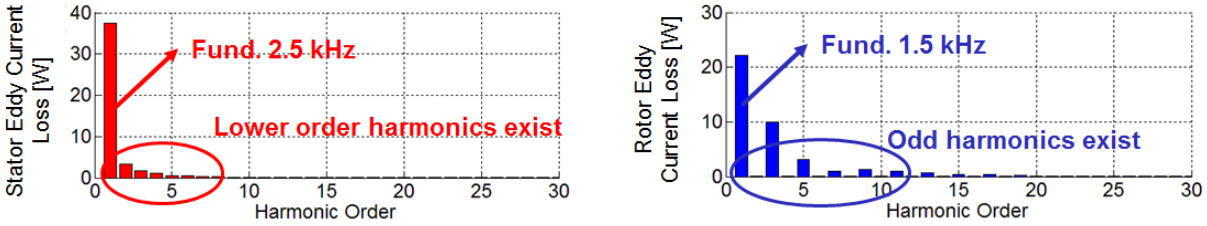

(a) (b)

Figure 6.3. Harmonic analysis of 12/10 FSPM machine eddy current losses (a) stator eddy current loss harmonic components, (b) rotor eddy current loss harmonic components.

However, the rotor eddy current loss has a fundamental frequency of only 1.5 kHz. This is because the magnetic flux in the rotor teeth only has six cycles per mechanical revolution when stator magnetic flux has ten electric cycles. Fundamental eddy current loss frequency is calculated. Flux waveforms in the rotor are symmetrical as shown in Figure 6.2 . The rotor eddy current loss only has odd order harmonics as shown in Figure 6.3. Distribution of iron loss is given in TABLE

6.2. Rotor iron loss accounts for about 45% of the total iron loss if same lamination materials are used for both stator and rotor.

It is possible to take advantage of this iron loss property in the design process to optimize the performance and material cost. For example, the rotor can use a different steel material than the stator since its fundamental frequency is much lower than the stator side. The geometrical optimization of the rotor can be investigated to mitigate those odd harmonic components and reduce rotor iron loss. Other methods to reduce iron loss are not discussed in detail here.

TABLE 6.2. IRON LOSS DISTRIBUTION FOR THE CASE STUDY HIGH-SPEED 12/10 FSPM MACHINE

Item	Values
Fundamental frequency of stator eddy current loss (kHz)	2.5
Stator eddy current loss (W)	60.3
Stator hysteresis loss (W)	24.5
Stator total iron loss (W)	84.8
Stator iron loss percentage	55 %
Fundamental frequency of rotor eddy current loss (kHz)	1.5
Rotor eddy current loss (W)	50.6
Rotor hysteresis loss (W)	18.9
Rotor total iron loss (W)	69.5
Rotor iron loss percentage	45 %

6.2.2 Magnet Eddy Current Loss Properties

Understanding the flux density distribution and variation in the magnets of FSPM machines is important for evaluating the loss property in the magnets. Flux waveforms in five representative points in the magnet at rated condition are shown in Figure 6.4. Note that the variation of flux density in point A is most dramatic due to the permeance variation caused by the different rotor

teeth alignments with respect to the stator. Waveforms in point A and C are not symmetrical due to the influence of stator armature flux. This design utilizes NdFeB magnets with a remnant flux density of 1.2 Tesla and a coercively of 900 kA/m. Resistivity is very small and assumed to be $1.4 \cdot 10^{-6}$ Ω m. Because there is a big pulsation in the portion of the magnets facing the airgap, large eddy current loss is induced. There is also a significant variation of permeance in the portion of the magnets at the other end that faces the stator outer diameter. This is also due to the "flux switching" effect that changes the flux path from one stator tooth to the other and varies the reluctance.

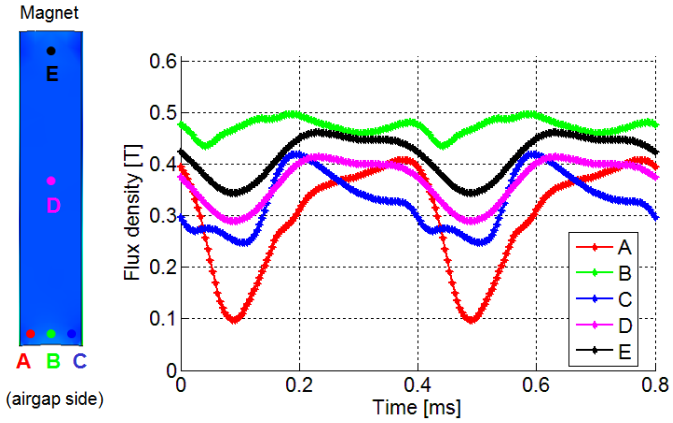

Figure 6.4. Flux waveforms of five representative points in the magnet at rated operating condition.

To capture the axial flow of magnet eddy currents during operation, 3D finite element analysis is used for the study. The first design is without magnet segmentation, and the induced magnet eddy current loss is calculated to be as high as 978 W. This much loss equals about 10% of the total power output which is not acceptable for practical design. Thus, methods should be taken to reduce the magnet eddy current loss. It is observed that the equivalent resistance of the

eddy current path will be significantly increased if the eddy current flow is reduced by magnet segmentation. In this machine, the axial segmentation is more effective in reducing the magnet eddy current loss than circumferential segmentation, so only the former technique is implemented.

Multiple designs with different numbers of magnet axial segmentations are simulated. If the number of segmentations is increased to 13 with a single magnet length of 6.3 mm, the total magnet loss is reduced to only 74.5 W from 978 W. An exponential reduction of magnet loss is observed in Figure 6.5. Magnetic flux density contour plots and magnet eddy current loss density contour plots are provided in Figure 6.6 and Figure 6.7. There is a diminishing effect in reducing the loss if the number of segmentations is further increased beyond 13 segments. The large number of segmentations can increase the cost and complexity of manufacturing. The final number of segmentations is determined by targeted efficiency requirements and manufacturing considerations. It is worth mentioning that FSPM machine designed with ferrite magnets do not suffer the magnet eddy current loss because of the very large resistivity of ferrite material. Magnet eddy current loss can result in a temperature rise and potentially lead to thermal demagnetization, so the use of ferrite magnet has compelling reasons for the investigation.

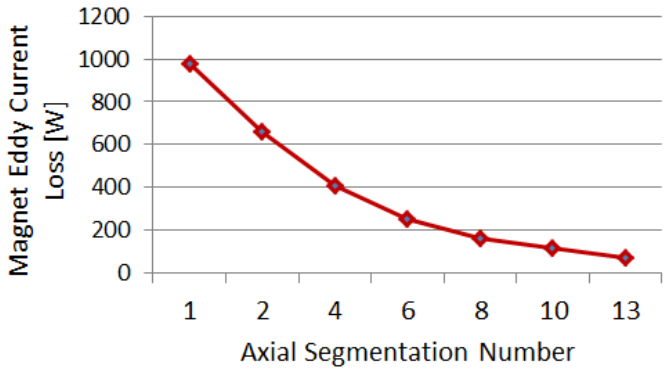

Figure 6.5. Total magnet eddy current loss as a function of different number of axial segmentations.

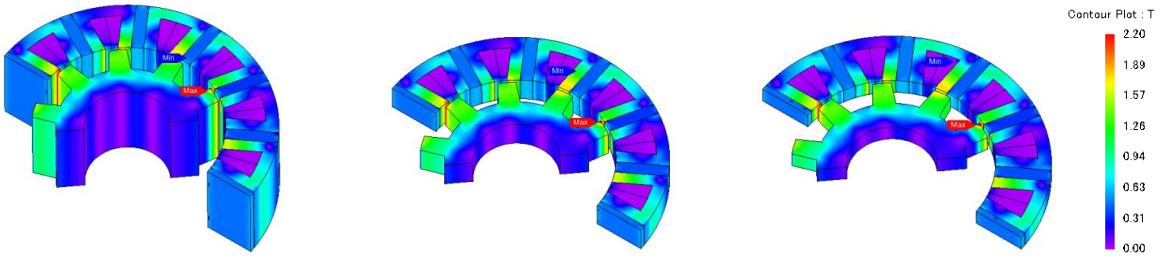

(a) 2 segments (b) 6 segments (c) 10 segments

Figure 6.6. Magnetic flux density distribution contour plot for three design cases with different number of axial segmentations.

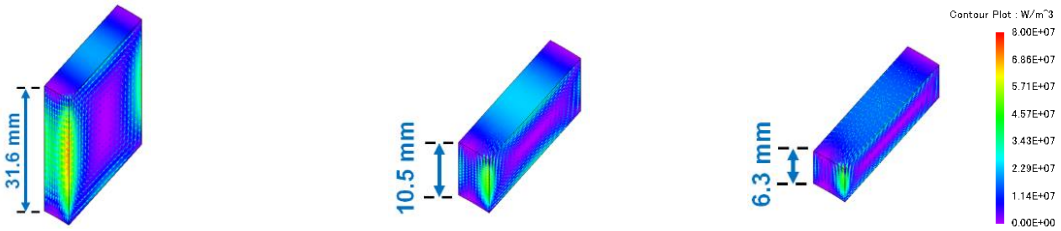

(a) 2 segments (b) 6 segments (c) 10 segments

Figure 6.7. Magnet eddy current loss density distribution contour plot for three design cases with different number of axial segmentations.

6.2.3 Windage Loss Properties

The windage loss is determined by many factors, such as temperature, the density of fluid surrounding the rotor, the length of rotor, and more importantly, radius and the rotational speed of the rotor. The windage loss of a smooth cylinder rotating within a concentric cylinder is defined in (6.10) from [278], [279]. For salient rotor pole FSPM machines, windage loss will be much greater because of the unsmooth rotor surface. Equation (6.11) from [278] is used to predict the windage loss of a rotor with salient poles rotating within a concentric cylinder. Windage loss is

very large at high-speed operating conditions and when the rotor outer diameter is increased to a large value.

$$W = \pi\, C_d\, \rho\, r^4\, \omega^3\, L \tag{6.10}$$

$$W = K\, \pi\, C_d\, \rho\, r^4\, \omega^3\, L \tag{6.11}$$

$$K = 8.5(H / r) + 2.2 \qquad \text{when, } H/r > 0.06 \tag{6.12}$$

where ρ is the density of the fluid in kg/m^3, r is the radius of rotor in m, ω is the angular velocity of rotor in rad/s, L is the rotor length in m, C_d is the skin friction coefficient which is calculated from (6.13) [279]. H is the rotor pole height.

$$\frac{1}{\sqrt{C_d}} = 2.04 + 1.768 \ln(\mathrm{Re}\sqrt{C_d}) \tag{6.13}$$

The above equations are theoretical derivations with the exception that the constant 2.04 is an empirical value. Based on this empirical constant, the error of calculated windage loss can be controlled within 10% of its actual value.

Reynolds is defined in (6.14).

$$\mathrm{Re} = \omega\, r\, \frac{\rho}{\mu} \varphi \tag{6.14}$$

The windage loss is plotted with respect to the rotor outer radius when the rotation speed is set at 15,000 rpm in Figure 6.8. Windage loss has a quadruple relationship with the radius of the rotor, and this signifies that windage loss is significantly larger in bigger machines. Windage loss also has a cubic relationship with the rotational speed. This explains why the windage loss for

small and low-speed machines can be neglected but should be considered for large and high-speed machines.

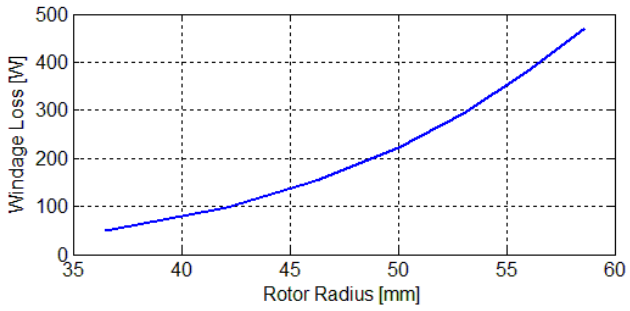

Figure 6.8. Estimated windage loss of 12/10 FSPM machine at a speed of 15,000 rpm as a function of rotor outer radius.

The loss distribution of this case study 12/10 FSPM machine at high-speed condition is plotted in Figure 6.9. The iron loss and magnet eddy current losses account for a large percentage of total loss. Thus the high-frequency losses could be excessive if the machine operates at higher speeds. The high-speed operation of high-pole 12/10 FSPM machine is challenging due to the large losses especially from steel and rare earth magnet materials.

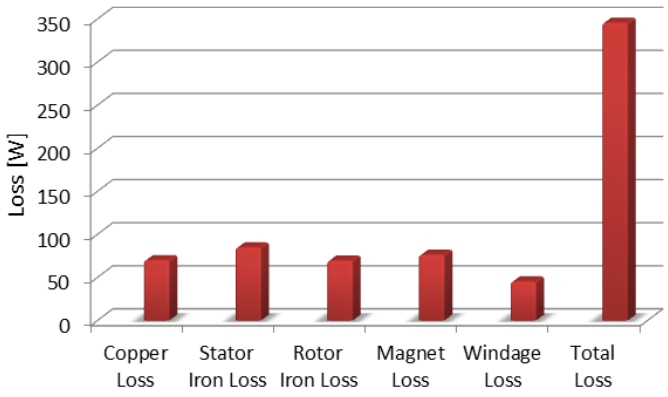

Figure 6.9. Loss distribution of 12/10 FSPM machine at 10 kW and 15,000 rpm.

6.3 Parametric Analysis of 12/10 FSPM Machine

6.3.1 Analysis of Split Ratio of 12/10 FSPM Machine

As identified in the previous studies of dual-stator 6/4 FSPM machine, the split ratio of the machine should be studied to evaluate its influence to the basic electromagnetic properties. The stator outer diameter of the 12/10 FSPM machine is maintained at 130 mm, while the split ratio is changed from 0.5 to 0.677. It is known that the dimensions of the stator teeth width, magnet width, and rotor pole with have the influence on the flux linkage, torque etc. Thus, to make cases at different split ratio comparable to each other, the baseline design for those geometries are chosen. The baseline design assumes that the width of the stator teeth width, magnet thickness, and stator slot opening width are all the same which equals to the baseline width. The rotor pole width is designed to be 1.4 times the baseline width. The stack length for all cases is the same as 80 mm. The detailed parameters for the eight cases are summarized in TABLE 6.3.

TABLE 6.3. PARAMETERS OF THE CONVENTIONAL 12/10 FSPM MACHINE AT DIFFERENT SPLIT RATIO CASES

Case No.	Split Ratio	Rotor Outer Radius [mm]	Rotor Pole Width [mm]	Stator Inner Radius [mm]	Stator Outer Radius [mm]	Stack Length [mm]	Magnet Thickness [mm]	Stator Tooth Width [mm]
1	0.50	31.25	5.956	32.5	65	80	4.254	4.254
2	0.523	33	6.230	34	65	80	4.450	4.451
3	0.55	34.75	6.552	35.75	65	80	4.680	4.680
4	0.569	36	6.780	37	65	80	4.843	4.843
5	0.60	38	7.140	39	65	80	5.105	5.105
6	0.631	40	7.514	41	65	80	5.367	5.367
7	0.65	41.25	7.742	42.25	65	80	5.531	5.531
8	0.677	43	8.064	44	65	80	5.760	5.760

The fundamental flux linkage per phase winding at no load condition as a function of the split ratio is shown in Figure 6.10. It is seen that higher split ratio results in a higher magnitude of fundamental flux linkage. The available half slot area to accommodate the windings as a function of the split ratio is shown in Figure 6.11. So, as the split ratio is increased, the available slot area for the windings are reduced. If all the machines in those eight cases are supplied with the same phase sinusoidal current of 48 A_{rms}, the calculated current density and the average torque both increase as the split ratio goes up which are shown in Figure 6.12 and Figure 6.13, respectively.

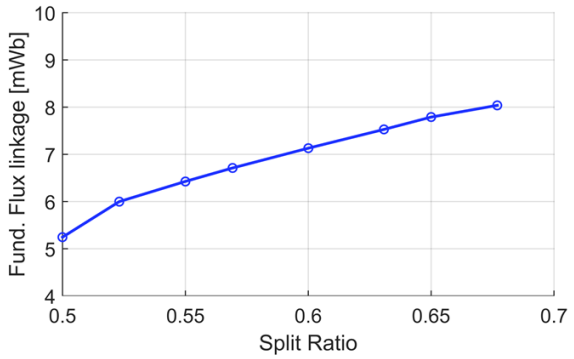

Figure 6.10. Fundamental flux linkage as a function of split ratio for 12/10 FSPM machine.

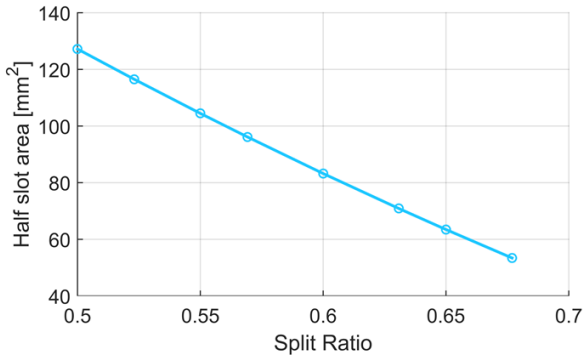

Figure 6.11. Half slot area as a function of split ratio for 12/10 FSPM machine.

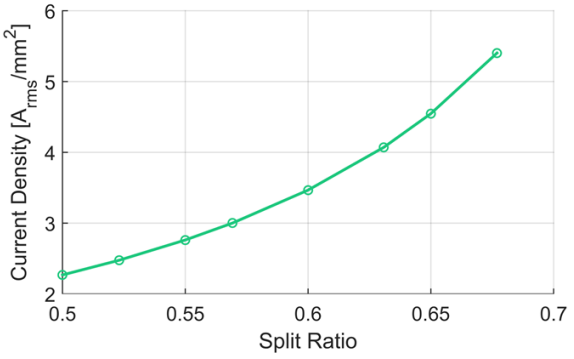

Figure 6.12. Current density as a function of split ratio for 12/10 FSPM machine.

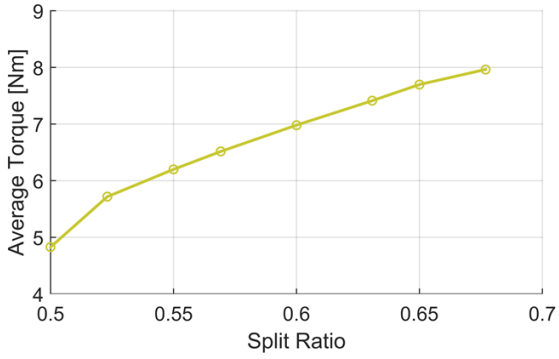

Figure 6.13. Average torque as a function of split ratio for 12/10 FSPM machine.

It is summarized that designs with a higher split ratio have a larger fundamental flux linkage and thus larger back-EMF magnitude, which is favored to increasing the torque production capability given a fixed current excitation. However, designs with higher split ratios also have less available slot area to accommodate the winding turns and thus result in increased current density, which is more difficult to cool the machine.

6.3.2 Analysis of Stator Teeth Width and Magnet Thickness of 12/10 FSPM Machine

The dimensions of the stator geometry have a big influence on the performance of FSPM machine. Of the most important stator geometries are the stator teeth width and magnet thickness. In this section, the influence of both stator teeth width and magnet thickness are evaluated for six different groups with different split ratio designs. At each group of designs, the magnet thickness is increased from 4 mm to 7 or 8 mm, depending on the available room for the stator teeth width. The stator teeth width is also increased from 4 mm by a step of 0.5 mm to a maximum value that is constrained by the geometry (the slot opening width should be larger than 1.2 mm). The fundamental flux linkage because of different stator teeth width and magnet thickness at split ratios of 0.5, 0.531, 0.55, 0.6, 0.65, and 0.677 are shown in Figure 6.14(a) to Figure 6.14(f).

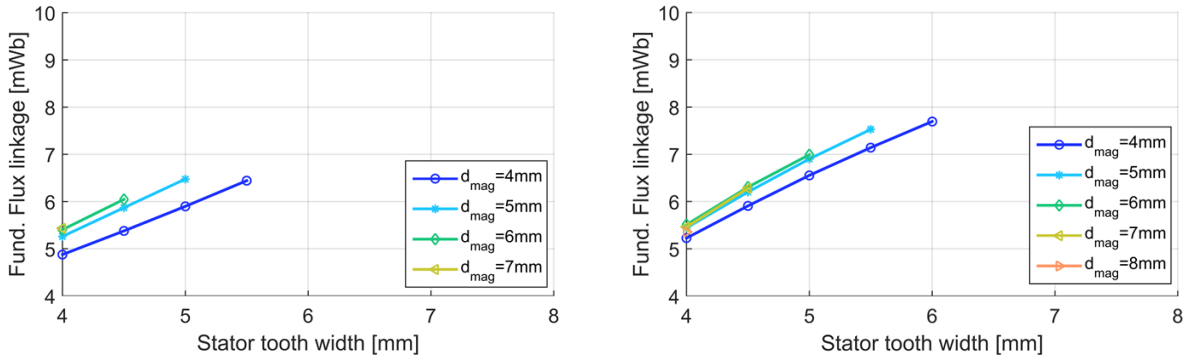

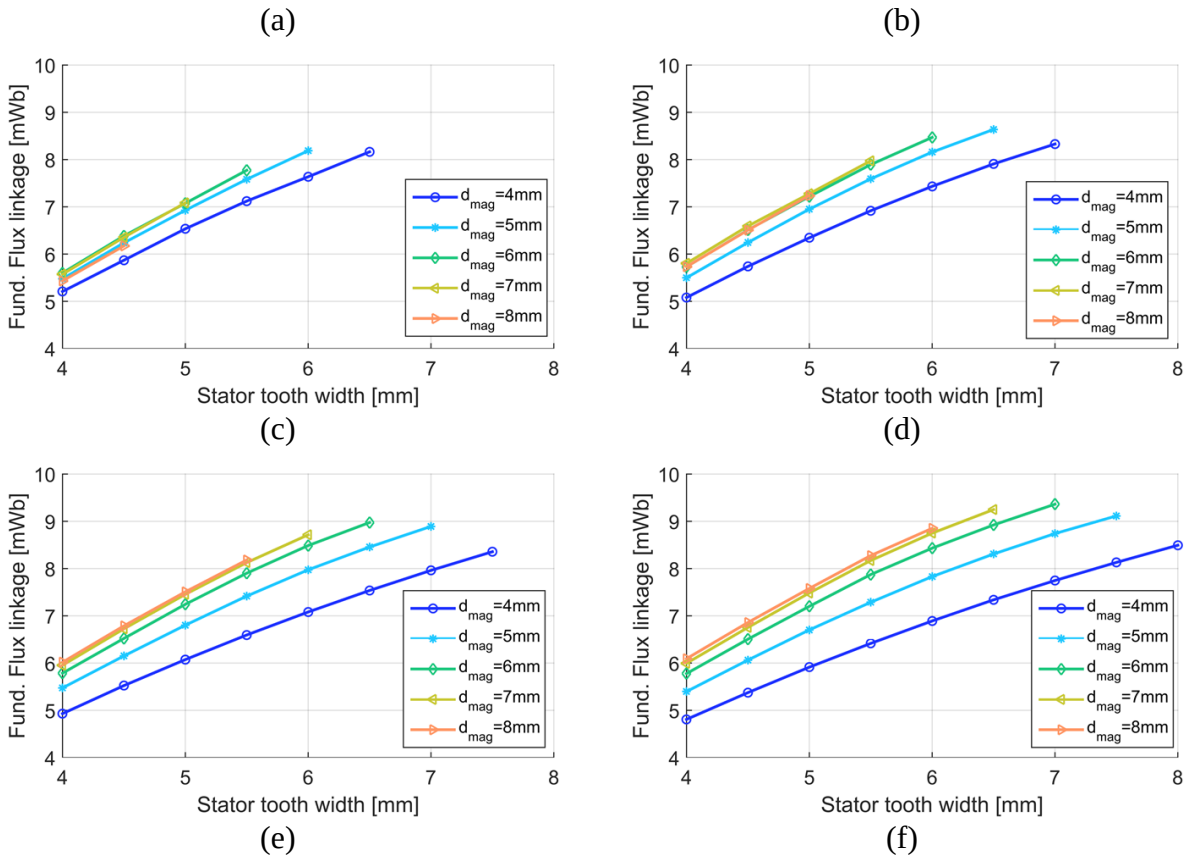

Figure 6.14. Fundamental flux linkage as a function of different stator teeth width and magnet thickness conditions under multiple split ratios λ (a) λ = 0.5 (b) λ= 0.531 (c) λ = 0.55 (d) λ = 0.6 (e) λ = 0.65 (f) λ = 0.677.

When the split ratio is as low as 0.5, there is limited airgap circumferential space to accommodate thicker permanent magnets and wider stator teeth to boost the fundamental flux linkage. The stator teeth width cannot be increased larger than 5.5 mm if the magnet thickness is 4 mm. However, there is larger airgap circumferential space in designs that have a higher split ratio, thus possible to use both thicker permanent magnets and wider stator teeth. When the split ratio is 0.677 as shown in Figure 6.14(f), the widest stator teeth width is 8 mm if the magnet thickness is 4 mm (half the width of magnet plus the width of stator teeth should be the same if the

slot opening width is kept at the same minimum value, i.e. 2 mm + 8 mm = 10 mm), or the widest stator teeth width is 6 mm if the magnet thickness is 8 mm (4 mm + 6 mm = 10 mm). It is seen that when the airgap circumferential space is fully utilized (the slot opening width is at its minimum value), different width distribution between the permanent magnet and the stator teeth results in different maximum fundamental flux linkage magnitudes. Parametric studies shown in Figure 6.14 present that the width of stator teeth should no less than the thickness of the permanent magnet. The parameters of these six designs in Figure 6.14 is shown in TABLE 6.4 below. This study chooses the discrete values for the magnet thickness and stator teeth width, and it is possible to further increase the produced fundamental flux linkage by choosing non-discrete values for them.

TABLE 6.4. DESIGNS THAT ACHIEVES MAXIMUM FUNDAMENTAL FLUX LINKAGE IN THE CONVENTIONAL 12/10 FSPM MACHINE AT DIFFERENT SPLIT RATIO CASES

Case No.	Split Ratio	Rotor Outer Radius [mm]	Rotor Pole Width [mm]	Stator Inner Radius [mm]	Stator Outer Radius [mm]	Stack Length [mm]	Magnet Thickness [mm]	Stator Teeth Width [mm]
1	0.50	31.25	6	32.5	65	80	5	5
2	0.523	33	6	34	65	80	4	6
3	0.55	34.75	6.5	35.75	65	80	5	6
4	0.60	38	7	39	65	80	5	6.5
5	0.65	41.25	7.52	42.25	65	80	6	6.5
6	0.677	43	8	44	65	80	6	7

The magnetic flux density distribution at loaded conditions for the analyzed six cases are shown in Figure 6.15(a) to Figure 6.15(f). Design with a higher split ratio and thicker stator teeth width has better utilization of the steel material because the magnetic flux is more evenly

distributed in the steel, not locally concentrated in the stator tip and highly saturates the material as the case with the design with a low split ratio.

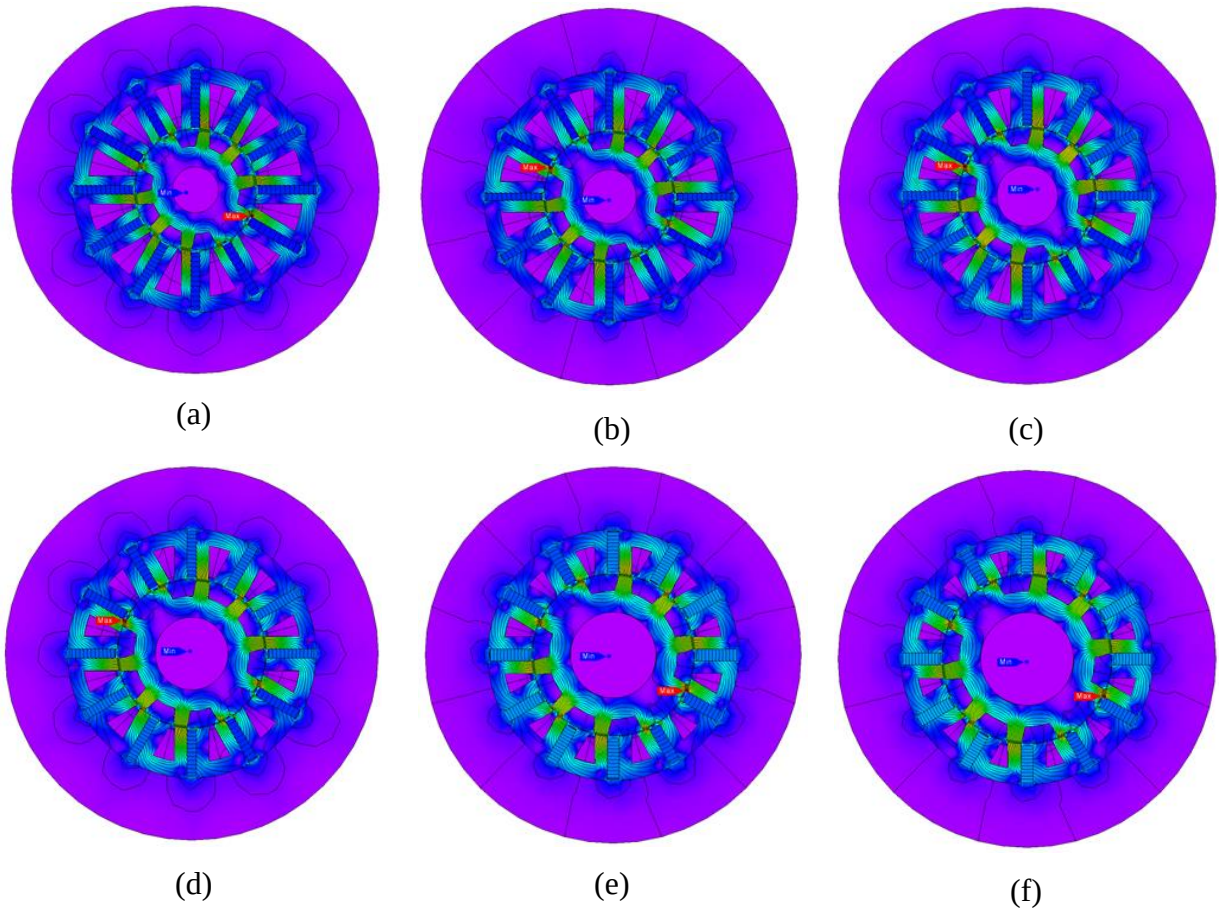

Figure 6.15. Magnetic flux density distribution of the design that has the maximum fundamental flux linkage under multiple split ratios λ (a) λ = 0.5 (b) λ= 0.531 (c) λ = 0.55 (d) λ = 0.6 (e) λ = 0.65 (f) λ = 0.677.

6.3.3 Analysis of Rotor Pole Width of 12/10 FSPM Machine

The design of rotor structure is also crucial for the electromagnetic performances. One of the most influential parameters is the width of the rotor pole, which has a big impact on the average torque and ripple torque. The fundamental flux linkage as a function of rotor width at six different

split ratio conditions is shown in Figure 6.16. Wider rotor pole improves the fundamental flux linkage, while the designs with higher split ratios also produce more fundamental flux linkage. The torque ripple at loaded condition has non-monotonically relation with the increase of rotor pole width as shown in Figure 6.17. The torque ripple is first reduced at an increase of rotor pole width, and then increases as the rotor pole width becomes larger. The average torque as a function of the change of rotor pole width is shown in Figure 6.18, which is similar to Figure 6.16.

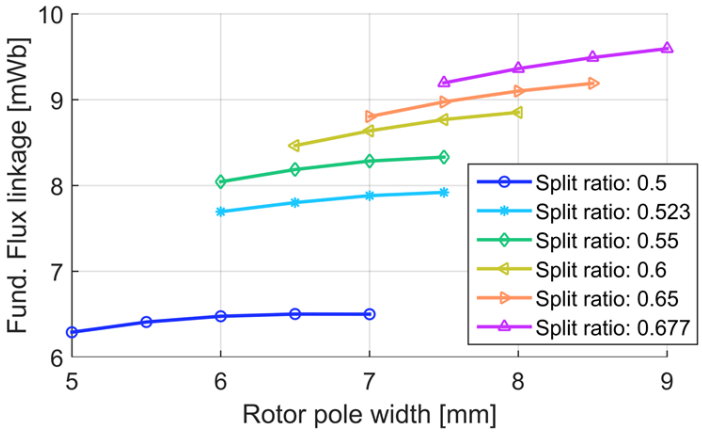

Figure 6.16. Fundamental flux linkage as a function of rotor pole width at six different split ratio conditions.

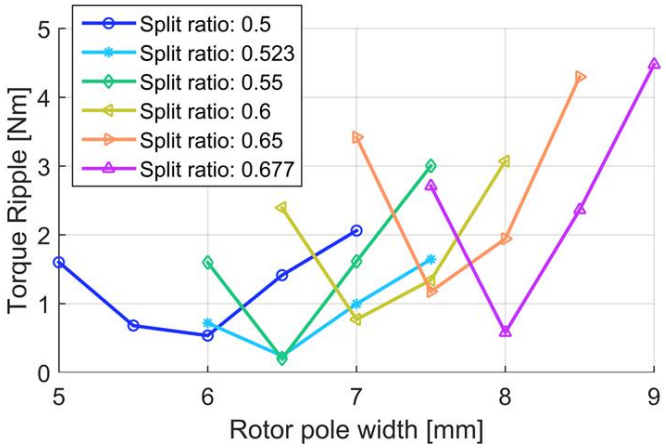

Figure 6.17. Torque ripple (peak to peak) as a function of rotor pole width at six different split ratio conditions.

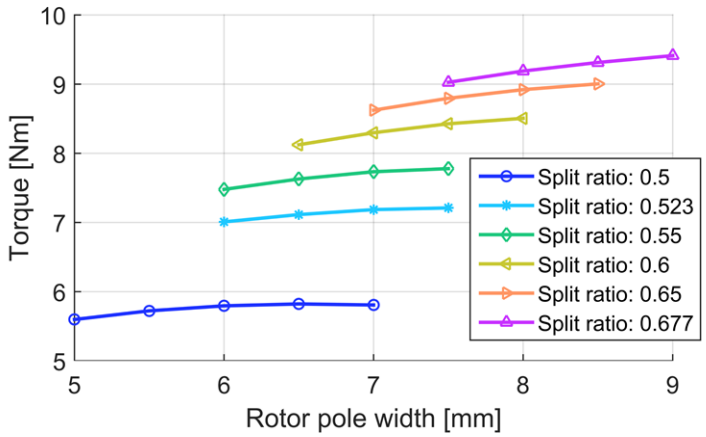

Figure 6.18. Average torque as a function of rotor pole width at six different split ratio conditions.

Therefore, the design of rotor pole width should consider the tradeoff of improving the average torque production capability as well as reducing the torque ripple magnitude. From the above analysis, one knows that the widths of the three dimensions (stator teeth width, magnet thickness, and rotor pole width) dictate the airgap flux harmonic modulation property and the torque characteristics.

6.4 Torque Density of 12/10 FSPM Machine

6.4.1 Torque Density Evaluated from 2D FEA Study

The torque density of the conventional 12/10 FSPM machine will also be evaluated using the same metric of torque per unit mass [Nm/kg]. To make a fair comparison with the proposed dual-stator 6/4 FSPM machine, the conventional 12/10 FSPM machine is designed for the same power of 10 kW and speed of 15,000 rpm. Due to the 2D FEA simulation of this study, the torque

is increased by a margin of 10% to 7.04 Nm to account for the reduction of torque because of the end effect in real conditions that is neglected in 2D FEA study. Similar to the analysis of 6/4 FSPM machine, the design of experiments studies of varying four important machine geometrical parameters (stator teeth width, magnet thickness, rotor pole width, and split ratio) are investigated simultaneously. The designs are grouped into six different split ratios, i.e. 0.5, 0.523, 0.55, 0.6, 0.65, and 0.677 with parametric combinations of different stator teeth width, magnet thickness, and rotor pole width. The incremental change for the stator teeth width is 0.5 mm, for the magnet is 1 mm, and for the rotor pole width is 0.5 mm. The total number of designs evaluated in the study is 734, and the number of designs for the split ratio of 0.5, 0.523, 0.55, 0.6, 0.65, and 0.677 are 51, 61, 81, 73, 101, 105, 121, and 141, respectively.

The outer diameters for all the parametric designs are maintained at the same 130 mm as previously done for the 6/4 FSPM machines. The axial lengths of each of the designs are adjusted to make sure that all design variations produce almost the same torque of 7.04 Nm as shown in Figure 6.19. It is noticed that the average torque stays almost the same at the designed value. In this design comparison, only analyzing the average torque is of interest, and the torque ripple is yet to be minimized in the later design procedure.

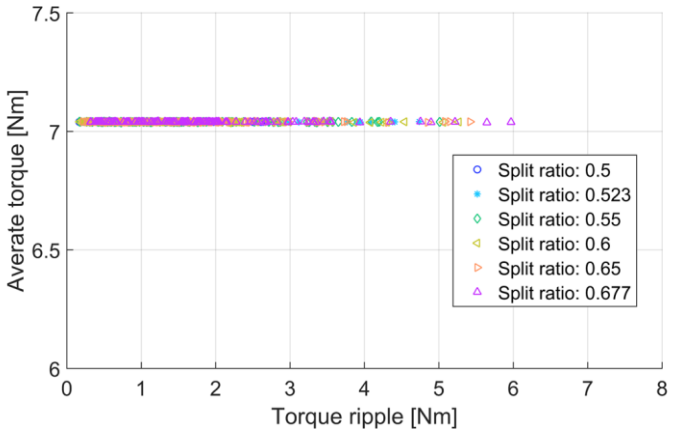

Figure 6.19. Average torque and torque ripple scatter plot for all the design variations of 12/10 FSPM machine.

The mass distributions of each of the active components are calculated by multiplying the volume by the density of each material, that is 7600 kg/m^{3}for the steel, 7500 kg/m^3 for NdFeB magnet, and 8960 kg/m^3 for the copper. The scatter plots of total mass as functions of rotor mass, stator mass, magnet mass, and winding mass are shown in Figure 6.20, Figure 6.21, Figure 6.22, and Figure 6.23 respectively. Similar to the previous results for the 6/4 FSPM machine, the designs with a higher split ratio tend to have less total weight than those with a smaller split ratio.

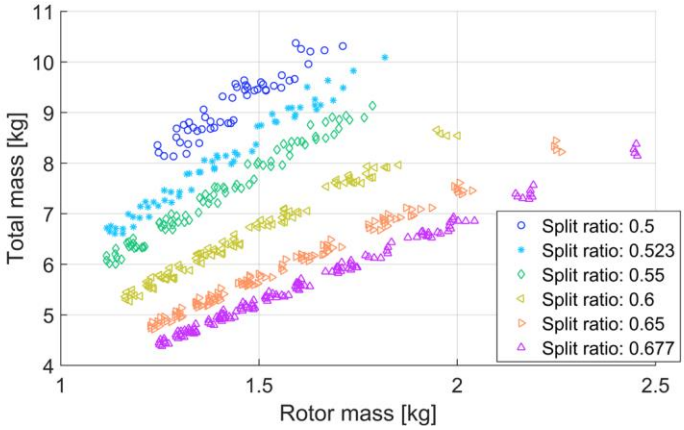

Figure 6.20. Total mass and rotor mass scatter plot for all the design variations of 12/10 FSPM machine.

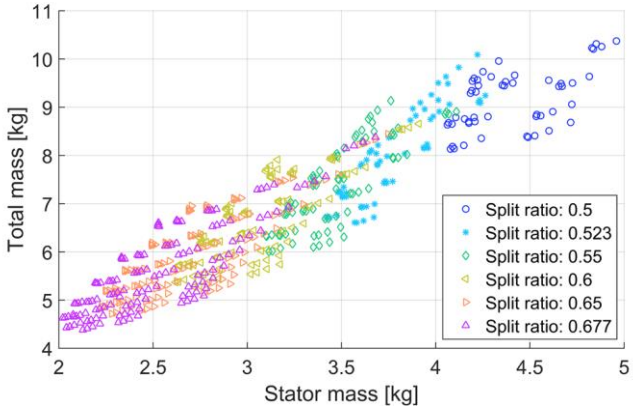

Figure 6.21. Total mass and stator mass scatter plot for all the design variations of 12/10 FSPM machine.

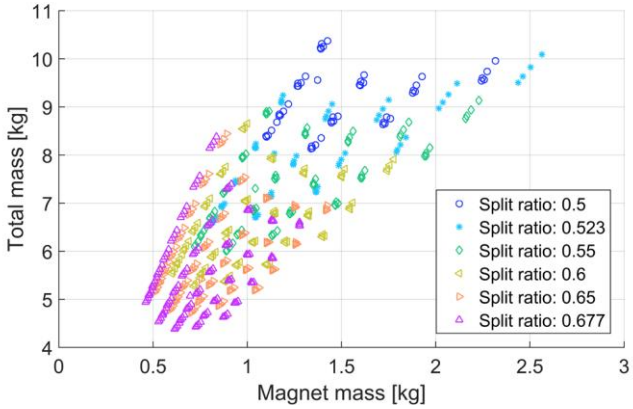

Figure 6.22. Total mass and magnet mass scatter plot for all the design variations of 12/10 FSPM machine.

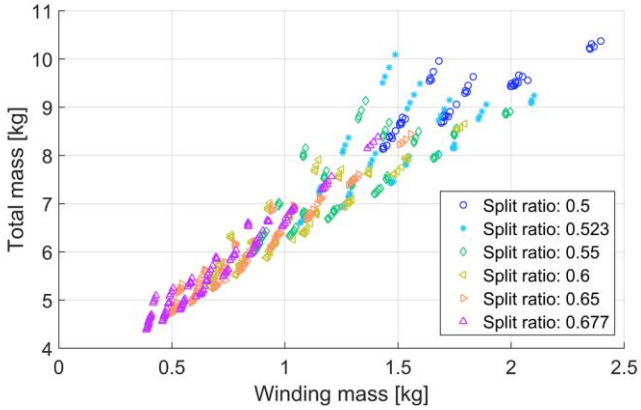

Figure 6.23. Total mass and winding mass scatter plot for all the design variations of 12/10 FSPM machine.

When the output torque and total mass for each of the design are determined, the torque densities for all these designs are calculated as shown in Figure 6.24 as functions of the current density variations. The maximum torque density trajectory with respect to the current density is calculated below. For the designs with the same phase current and voltage at the rated condition, aggressive designs with high current densities have a large split ratio, while designs with low current densities have a small split ratio. It is again demonstrated that torque density of the machine is highly dependent on the current density applied, and there is an optimal split ratio that maximizes the torque density at that current density condition. The total resistance as a function of the end winding resistance is shown in Figure 6.25.

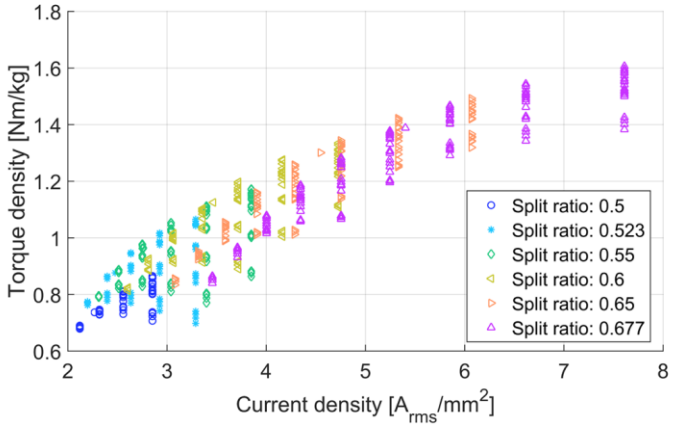

Figure 6.24. Torque density and current density scatter plots for all design variations of 12/10 FSPM machines.

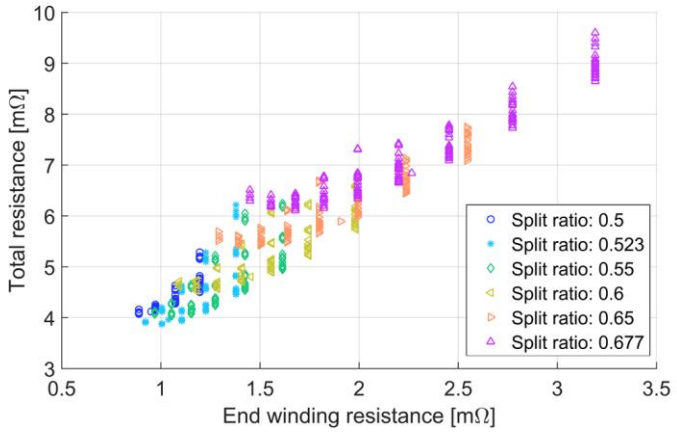

Figure 6.25. Total resistance and end winding resistance scatter plot for all design variations of 12/10 FSPM machines.

6.4.2 Torque Density Evaluated from 3D FEA Study

The torque density of the 12/10 FSPM machine is evaluated by 2D FEA study in the prior section. To calculate the torque density more accurately, 3D FEA study should be implemented to consider the 3D effects such as end effect. The approach used here is like that of the 6/4 FSPM machine. The maximum torque density enveloped with respect to the current density curve from 2D FEA results is shown in Figure 6.24. The designs on this maximum torque density lines are chosen to be reevaluated in 3D FEA studies including the modeling of the end windings. The calculated torque density from 2D and 3D results are compared in Figure 6.26, and the 3D results show about 5% discrepancy with the 2D results.

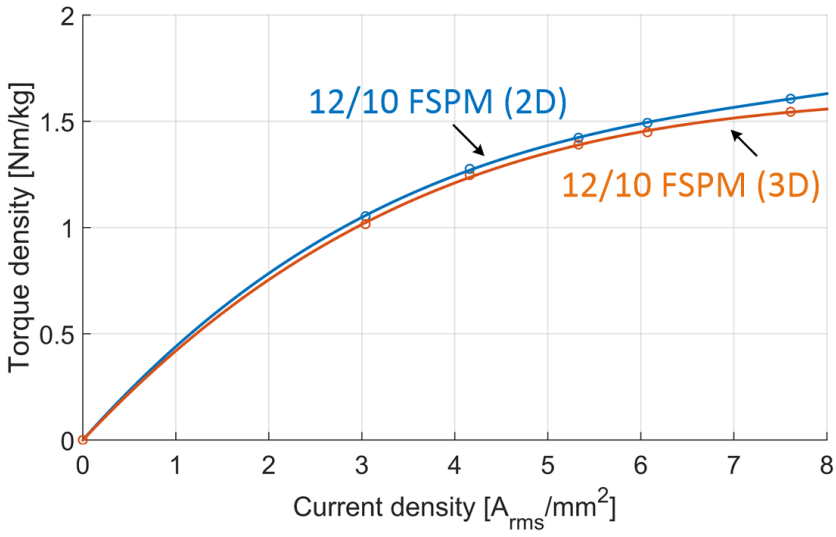

Figure 6.26. Comparison of torque density with respect to the current density of 12/10 FSPM machines from both 2D and 3D results.

6.5 Torque Density Comparison of Dual-Stator 6/4 FSPM and 12/10 FSPM Machines

The torque densities of the 12/10 FSPM machine and dual-stator 6/4 FSPM machine are separately analyzed in the previous chapters. This section compares the torque density of these two machines. The calculated torque density from 2D and 3D FEA results are shown in Figure 6.27. The 12/10 FSPM machine has approximately 1.3 to 1.5 times the torque density of the dual-stator 6/4 FSPM machine at a given current density. This result is consistent with the torque density comparison of other types of high-pole-count versus low-pole-count electric machines. The high-pole-count machines generally have a higher torque density (Nm/kg) than low-pole-count

machines due to the reduced stator yoke thickness and less iron mass, given the same current density in the windings.

Given the different torque density profiles of the dual-stator 6/4 FSPM machine and 12/10 FSPM machine, one can observe that the comparison of these two machines should have some common metric on the torque density curve to justify a more reasonable comparison. To compare various output performances, loss distribution, and efficiency of this two machine, either current density or torque density of two machines wound need to be kept the same in the studies. In the optimization study presented in the next section, the 12/10 FSPM machine is optimized based on the similar current density to that of the dual-stator 6/4 FSPM machine.

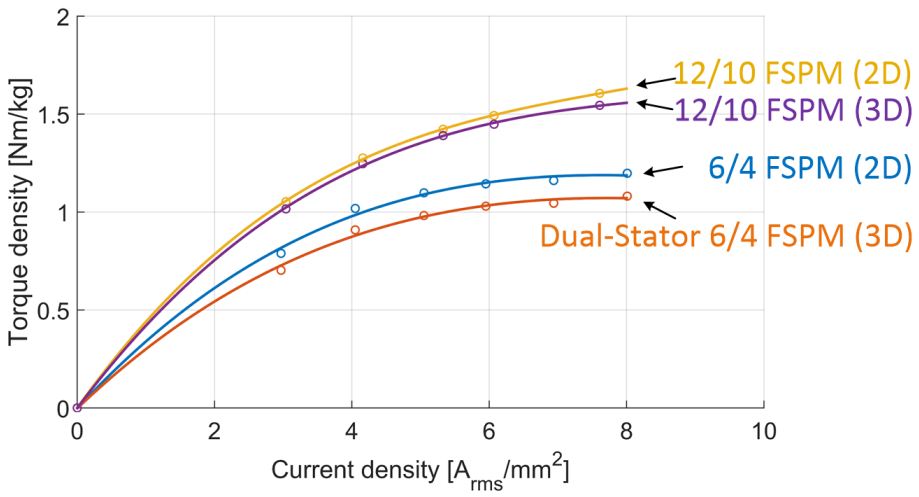

Figure 6.27. Torque density comparison of 12/10 FSPM and dual-stator 6/4 FSPM machine from 2D and 3D finite element analysis studies.

6.6 Optimization of 12/10 FSPM machine

The previous parametric analysis reveals that the conflicting objectives in the machine are challenging to satisfy. Thus, optimization of the 12/10 FSPM machine is investigated in this section to study the performance capabilities of this topology at the high-speed condition. To compare the performance of the 12/10 FSPM machine with the dual-stator 6/4 FSPM machine in the next chapter, same power and speed rating of 10 kW and 15,000 rpm is chosen for the 12/10 FSPM machine.

6.6.1 Parametrized Model of 12/10 FSPM Machine

The 12/10 FSPM machine are defined by various geometrical parameters that are allowed to change during the optimization process. An illustration of all the parameters is shown in Figure 6.28. Most the defined parameters are the same as that defined in the dual-stator 6/4 FSPM machine, but the stator and rotor tips are not included in this study for simplicity. The stator outer diameter of the 12/10 FSPM machine is again fixed at 130 mm, and the airgap length is chosen as 1 mm. The parameters that allowed to change are the stator inner radius R_{is}, magnet inner radius $R_{mag,in}$, magnet outer radius $R_{mag,out}$, stator slot bottom radius R_{slot}, stator teeth width d_{teeth}, half of the magnet thickness $d_{mag,half}$, rotor shaft radius R_{shaft}, rotor inner radius R_{ir}, rotor pole tip bottom radius $R_{r,tip}$, rotor outer radius R_{or}, and rotor pole half width $d_{pole,half}$.

To compare the optimized 12/10 FSPM machine with the previously optimized dual-stator 6/4 FSPM machine, the constraints of the 12/10 FSPM machine in the optimization should be designed carefully. Since the 12/10 FSPM machine has a different torque density profile than dual-stator 6/4 FSPM machine, the comparison of these two machines can be made more fairly if the

current density is kept the same. Thus, the 12/10 FSPM machine will be optimized to the similar current density as that of the optimized dual-stator 6/4 FSPM machine.

In the optimization process, the 12/10 FSPM machine has objectives of maximizing the average torque and minimizing the torque ripple, with equal weights on both objectives. The constraint during the optimization is to keep the same current density with the dual-stator 6/4 FSPM machine, which is 4.97 A_{rms}/mm^2.

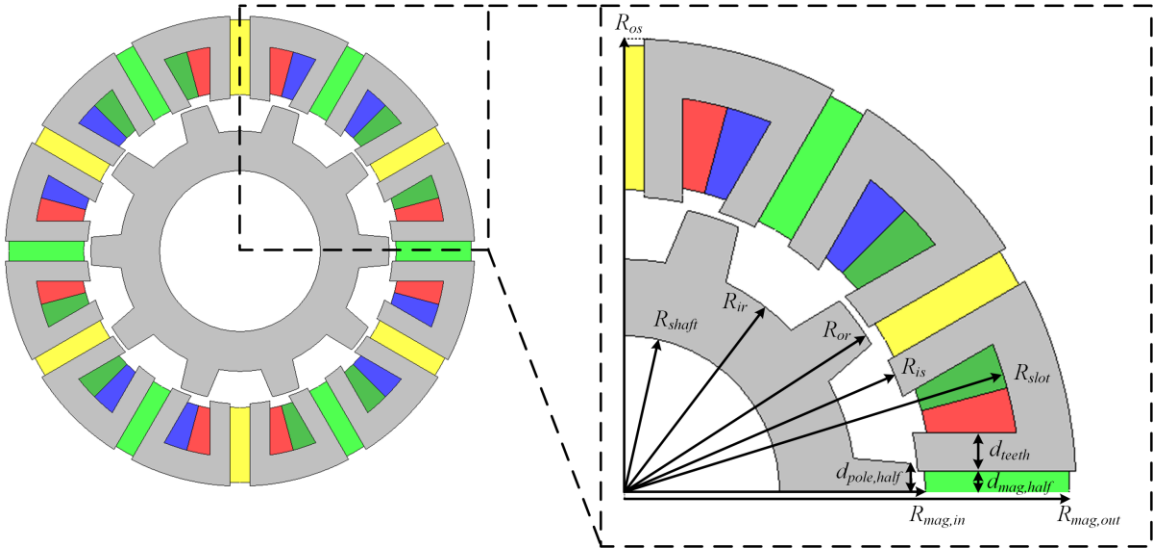

Figure 6.28. Definition of parameters of the 12/10 FSPM machine in the optimization.

6.6.2 Optimization Results

The optimization results from the given objectives and constraint for the 12/10 FSPM machine is shown in TABLE 6.5 with the stator and rotor dimensions. The optimized machine has a stack length of 65 mm and stator inner radius of 42.3 mm. The machine can produce 10 kW output power at the speed of 15,000 rpm. The detailed weight distribution and performance of the

optimized 12/10 FSPM machine is compared with the dual-stator 6/4 FSPM machine in the next section.

TABLE 6.5. PARAMETERS FOR THE OPTIMIZED 12/10 FSPM MACHINES AT A RATING OF 10 KW AND 15,000 RPM.

Geometrical Parameters		Symbol	12/10 FSPM
Fixed	Stator outer radius, [mm]	R_{os}	65.0
	Airgap length, [mm]	g	1.0
Stator Part	Total stack length, [mm]	L_e	65.0
	Stator inner radius, [mm]	R_{is}	42.3
	Magnet inner radius [mm]	$R_{mag,\,in}$	43.3
	Magnet outer radius [mm]	$R_{mag,out}$	64.0
	Stator slot bottom radius [mm]	R_{slot}	57.0
	Stator teeth width [mm]	d_{teeth}	6.5
	Magnet half thickness [mm]	$d_{mag,half}$	2.5
Rotor Part	Rotor shaft radius [mm]	R_{shaft}	22.0
	Rotor inner radius [mm]	R_{ir}	33.0
	Rotor pole tip bottom radius [mm]	$R_{r,tip}$	40.0
	Rotor outer radius [mm]	R_{or}	41.3
	Rotor pole half width [mm]	$d_{pole,half}$	4.0

6.7 Design and Performance Comparison of Dual-Stator 6/4 FSPM and 12/10 FSPM Machines

6.7.1 Comparison of Design and Mass Distribution

This section presents the comparison studies of the dual-stator 6/4 FSPM and 12/10 FSPM machines regarding geometrical designs, mass distribution, and torque density. The optimized parameters of the dual-stator 6/4 FSPM and 12/10 FSPM machines are shown in TABLE 6.6. For

the same stator outer diameter of 130 mm, the dual-stator 6/4 FSPM machine has a stack length of 80 mm, which is larger than the 65 mm in the 12/10 FSPM machine. The total weight of dual-stator 6/4 FSPM machine is 7.453 kg with a rotor weight of 1.077 kg. The total weight of 12/10 FPSM machine has a total weight of 4.966 kg with a rotor weight of 1.264 kg. The dual-stator machine has a smaller rotor and less inertia, which equals to have better dynamic performance capability. The stator iron mass of dual-stator 6/4 FSPM machine is higher than the 12/10 FSPM machine because the low-pole topology has thicker stator back iron and tooth to conduct the magnetic flux. Due to the smaller weight, the 12/10 FSPM machine has a higher specific torque density of 1.315 Nm/kg than the 0.864 Nm/kg of the dual-stator 6/4 FSPM machine.

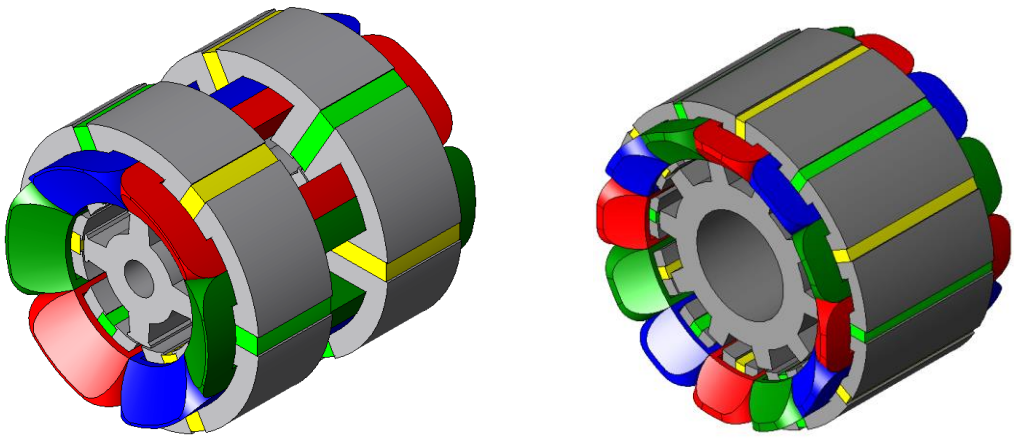

(a) (b)

Figure 6.29. Optimized two machines in 3D view, (a) dual-stator 6/4 FSPM machine, (b) 12/10 FSPM machine.

TABLE 6.6. COMPARISON OF OPTIMIZED DUAL-STATOR 6/4 FSPM AND 12/10 FSPM MACHINES AT 10 KW, 15,000 RPM SPECIFICATION.

Compared Parameters		Symbol	Dual-Stator 6/4 FSPM	12/10 FSPM
Fixed	Stator outer radius, [mm]	R_{os}	65.0	65.0
	Airgap length, [mm]	g	1.0	1.0
Stator Geometries	Stator inner radius, [mm]	R_{is}	31.0	42.3
	Magnet inner radius [mm]	$R_{mag,\,in}$	32.0	43.3
	Magnet outer radius [mm]	$R_{mag,out}$	64.0	64.0
	Stator slot bottom radius [mm]	R_{slot}	55.0	57.0
	Stator teeth width [mm]	d_{teeth}	10.0	6.5
	Magnet half thickness [mm]	$d_{mag,half}$	4.5	2.5
	Stator teeth tip length [m]	$d_{s,tip}$	1.8	N/A
	Total stack length, [mm]	L_e	80.0	65.0
Rotor Geometries	Rotor shaft radius [mm]	R_{shaft}	8.0	22.0
	Rotor inner radius [mm]	R_{ir}	19.0	33.0
	Rotor pole tip bottom radius [mm]	$R_{r,tip}$	29.0	40.0
	Rotor outer radius [mm]	R_{or}	30.0	41.3
	Rotor pole half width [mm]	$d_{pole,half}$	4.8	4.0
	Rotor pole tip length [mm]	$d_{r,tip}$	1.7	N/A
Mass and Performance Comparison	Mass of stator iron [kg]	M_{stator}	3.782	2.348
	Mass of rotor iron [kg]	M_{rotor}	1.077	1.264
	Mass of copper with end windings [kg]	M_{copper}	1.556	0.748
	Mass of NdFeB magnets [kg]	M_{mag}	1.039	0.607
	Total active mass [kg]	M_{tot}	7.453	4.966
	Torque [Nm]	T	6.439	6.532
	Specific torque density [Nm/kg]	ξ_T	0.864	1.315
	Specific power density [kW/kg]	ξ_P	1.357	2.066

6.7.2 Comparison of Loss Distribution and Efficiency

The previous analysis shows that the 12/10 FSPM machine has higher torque density and lower total weight than the dual-stator 6/4 FSPM machine, but the fundamental frequency of 12/10 topology is 2.5 times that of the dual-stator 6/4 topology. Thus, the high-pole machine will produce

more high-frequency associated losses than the low-pole machine. This section presents more performance analysis, loss distribution, and efficiency of the two machines. The two optimized designs at 10 kW and 15,000 rpm condition are compared for the key parameters as shown in TABLE 6.7. The current density of two machines is almost the same, with 4.96 A_{rms}/mm^2 for 6/4 machine and 4.98 A_{rms}/mm^2 for 12/10 machine. The PM magnetic flux linkages for dual-stator 6/4 and 12/10 are 16 mWb and 6.4 mWb respectively. Both machines have negligible saliency as identified in the d, q inductance calculations.

TABLE 6.7. PERFORMANCE AND LOSS DISTRIBUTION COMPARISON OF OPTIMIZED DUAL-STATOR 6/4 FSPM AND 12/10 FSPM MACHINES AT 10 KW, 15,000 RPM CONDITION.

Compared Parameters		Symbol	Dual-Stator 6/4 FSPM	12/10 FSPM
Performance	Magnet flux linkage [mWb]	λ_{pm}	16	6.4
	Total phase resistance @110˚C [mΩ]	R_{tot}	17.9	5.8
	d-axis inductance [mH]	L_d	0.15	0.035
	Per unit d-axis inductance	L_d^*	0.65	0.38
	q-axis inductance [mH]	L_q	0.14	0.033
	Per unit q-axis inductance	L_q^*	0.60	0.36
	Phase back-EMF @ 15,000 rpm [V_{pk}]	E_0	99.1	99.3
	Phase current [A_{rms}]	$I_{s,r}$	48.1	48.1
	Current density [A_{rms}/mm^2]	J_s	4.96	4.98
	Average Torque [Nm]	T	6.439	6.532
	Torque ripple, pp [Nm]	T_{ripple}	1.34	0.85
	Torque density [Nm/kg]	ξ_T	0.864	1.315
Loss and Efficiency	Copper loss [W]	P_{copper}	126	42
	Stator iron loss [W]	P_{stator}	168	234
	Rotor iron loss [W]	P_{rotor}	84	171
	Magnet eddy current loss [W]	P_{mag}	129	239
	Windage loss [W]	$P_{windage}$	36	70
	Total loss [W]	P_{tot}	543	756
	Efficiency	η	94.85%	92.97%
	Copper loss density [W/kg]	ζ_{cu}	80.9	56.1
	Iron loss density [W/kg]	ζ_{fe}	51.9	112.1
	Magnet loss density [W/kg]	ζ_{mag}	124.1	393.7

The loss distribution for each machine is carefully evaluated. The copper loss for dual-stator 6/4 machine is 126 W and for 12/10 machine is 42 W. This is because the dual-stator machine has more number of turns per phase and additional end windings than the 12/10 machine. The iron loss of the dual-stator 6/4 machine has 168 W in the stator and 84 W in the rotor, while the 12/10 machine has 235 W in the stator and 171 W in the rotor. The eddy current loss in the magnets should be mitigated so that axial segmentations are used for both machines. The length of each segment for two machines is chosen to be very close. Due to the different stack length of the two machines, the axial segmentation number for dual-stator 6/4 FSPM machine is 8 with 4 segmentations of magnets in each stator. The 12/10 FSPM machine has 6 axial segmentations for the magnets. So, the axial length of magnets in dual-stator 6/4 machine is 10 mm, and in 12/10 machine is 10.83 mm. The magnet eddy current loss for the dual-stator 6/4 machine is 129 W, and for the 12/10 machine is 239 W. The windage loss for both machines are also evaluated using the windage loss equations in the previous chapter. The dual-stator 6/4 and 12/10 machine has 36 W and 70 W windage loss, respectively. As a result, the dual-stator 6/4 FSPM machine has an efficiency of 94.85%, which is higher than 92.97% in the 12/10 FSPM machine.

To compare the loss density of two machines, each kind of loss density is calculated by the generated loss over the mass. Therefore, for the dual-stator 6/4 and 12/10 FSPM machines, the calculated copper loss densities are 80.9 W/kg and 56.1 W/kg, the iron loss densities are 51.9 W/kg and 112.1 W/kg, and the magnet eddy current loss densities are 124.1 W/kg and 393.7 W/kg, respectively. The low-pole dual-stator 6/4 FSPM machine has much less iron loss and magnet loss density than the 12/10 FSPM machine.

The comparison results show that the dual-stator 6/4 FSPM machine has better efficiency than the 12/10 FSPM machine at the high-speed condition, although the total weight is higher. Thus, the dual-stator 6/4 FSPM machine is suitable for applications where the weight and volume are not of primary concern, but the high efficiency at high-speed conditions is required. If the efficiency of power electronics is included, the dual-stator 6/4 FSPM machine system is expected to achieve even higher system efficiency due to the smaller switching frequency and smaller switching losses in the converter.

6.8 Summary

This chapter presents the analytical and finite element analysis of the 12/10 FSPM machine and the performance comparison of dual-stator 6/4 FSPM machine and 12/10 FSPM machine. The sizing equation, design consideration of 12/10 FSPM machine at high-speed conditions are discussed. The influence of key dimensions of 12/10 FSPM machine is studied by parametric analysis. Torque densities of both dual-stator 6/4 FSPM and 12/10 FSPM machines are compared. Both optimized machines are compared for dimensions, mass distribution, loss distribution, and efficiencies. The primary research findings are summarized below.

- The 12/10 FSPM machine at 15,000 rpm condition requires a fundamental frequency of 2.5 kHz. The fundamental iron eddy current loss frequency in stator side is proportional to the number of rotor poles, while in rotor side it is proportional to the half number of stator slot.

- The windage loss of high-speed FSPM machine is not negligible from the analytical evaluations. The salient pole structure of the rotor induces more windage loss than the round rotor structure.
- The dual-stator 6/4 FSPM machine only has 40% of the fundamental frequency as the 12/10 FSPM machine. The copper loss of the dual-stator 6/4 machine is higher, but the iron loss and magnet eddy current losses are much lower than the 12/10 FSPM machine at high-speed conditions.
- The benefits of using dual-stator 6/4 FSPM machine over 12/10 FSPM machines are higher operation speed, higher efficiency, and less converter switching frequency required.

Chapter 7

Mechanical Tolerance and Structural Dynamics Analysis of Dual-Stator 6/4 FSPM Machine

The performance of any electric machine is not only subject to design optimization, but also to the manufacturing tolerance limitation. Even a well-designed electric machine may degrade its performance under mechanical tolerance issues in some parts. There are parts that are critical in maintaining the desired tolerance such as the bearings to support the precise airgap length, and the lamination to maintain a uniform machine body. For the proposed dual-stator 6/4 FSPM machine, the mechanical tolerance analysis is an important part of the performance characterization. There are special mechanical tolerance challenges that are present in the complex dual-stator offset rotor design. This section is dedicated to the mechanical tolerance analysis and the structural analysis of the proposed machine. Torque ripple reduction by rotor step skew will be discussed in the first place to refine the torque profile. Three rotor mechanical tolerance design challenges including rotor offset angle deviation, rotor static and dynamic eccentricity are investigated. Rotor structural analysis is performed to understand the rotor dynamics property at high-speed conditions, thus designing the machine with safe margin from the critical vibrations. The mechanical stress distribution analysis is done to ensure that the designed high-speed machine operates within the material stress limitations.

7.1 Design for Torque Ripple Reduction

7.1.1 Discussion of Torque Ripple Reduction Techniques

Low torque ripple design is a desirable requirement for most the electric machines. Having a smaller torque ripple is beneficial to reducing the vibration and acoustic noise, and extending the life of bearing system. The proposed dual-stator 6/4 FSPM machine has already significantly reduced the torque ripple compared to the conventional 6/4 FSPM machine by having the offset rotor pole structure. However, there is an opportunity to further reduce the torque ripple by implementing additional techniques.

There are quite several methods developed for the cogging torque, or torque ripple minimization. The commonly used techniques of reducing the cogging torque/torque ripple includes specific rotor design such as teeth notching, teeth chamfering, changing rotor pole arc width, rotor teeth axial pairing, rotor continuous or step skewing, and rotor pole shaping [90], [91], [92], [93], [94], [95], [96], [97], [98], [99], [100], [101]. For the proposed dual-stator 6/4 FSPM machine, rotor pole and stator teeth shaping technique has already been implemented in the prior design as shown in the optimization section. The technique of stator or rotor teeth notching has tolerance challenges because a small deviation in the location and shape of the notch will significantly alter the torque ripple profile. Tight mechanical tolerance is required to achieve the desired torque ripple reduction performance if rotor pole or stator teeth notching scheme is used. Rotor teeth axial pairing technique requires multiple different rotor laminations, and there could be non-balanced magnetic forces in the rotor which increases the stress in the bearing system and potentially reduces the reliability of the machine. The torque ripple reduction method of using rotor step skew is more

straight-forward and relatively easy to implement. The behavior of torque ripple reduction is much easier to predict. Thus, this study only investigates the rotor step skewing technique to further reduce the torque ripple.

7.1.2 Torque Ripple Reduction by Rotor Step Skew

This section discusses the details of the rotor step skew design. Since the initial rotor design already has offset poles for the front and rear part, the step skewed design should pay careful attention to the step skew orientation in each rotor part. Theoretically, the number of step skew can be any number that is equal or larger than two. However, a large number of step skew complicates the design with diminishing returns. Therefore, for practical reasons, a step skew number of two is selected. Both front and rear part of the rotor pole is axially segmented into two subparts, which are offset by a step skew angle. Meanwhile, the 45˚ mechanical angle is still maintained for the corresponding offset rotor poles in the front and rear part.

The initial rotor design already has 45˚ offset poles, and the step skewed design needs to maintain this offset angle requirement when implementing the step skews. The number of skew steps per rotor pole is one variable to be selected. To begin with, the step number is chosen to be two as shown in Figure 7.1. Both front and rear rotor poles are axially segmented into two subparts, and the subpart pair F1 and R1 maintain unchanged while the subpart pair F2 and R2 are rotated by the same step angle but kept by the 45˚ offset angle. If the step number is selected as 4, each pair of the corresponding subparts (e.g. F4 and R4) maintains the 45˚ offset angle as shown in Figure 7.2. The step skew span angle is defined as the angle between the first and the last subparts

in either the front or rear poles. The variation of output torque as a function of the step skew span angle is studied below.

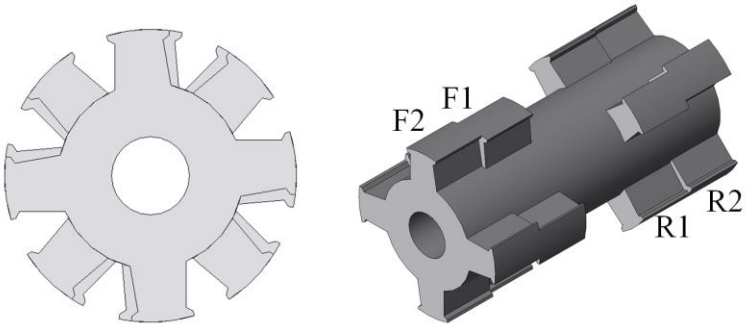

Figure 7.1. Rotor two-step skew design.

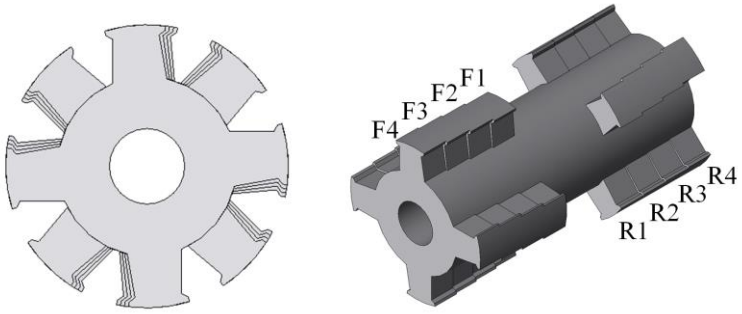

Figure 7.2. Rotor four-step skew design.

It is known that either continuous skew or step skew reduce the average torque. However, the variation of torque ripple and torque ripple percentage depends on the actual designs. Thus, the goal here is to find an optimal step skew angle that minimizes the torque ripple percentage while maintaining a sufficiently large average torque. For the two-step skew design, a parametric analysis is performed to sweep the step skew span angle from mechanical 0˚ to 7˚, with a step change of 1˚. Figure 7.3 demonstrates the variations of average torque, torque ripple, and torque ripple percentage for each of the designs. It is noted that the average torque reduces monotonically,

but the torque ripple reduces from 0˚ angle to a minimum value at 5˚ angle, and then increases after that. The design with a 5˚ step skew span angle achieves the minimum torque ripple percentage of 6.6%, with an average torque of 6.33 Nm and a torque ripple of 0.42 Nm. Compared to the initial design with an average torque of 6.45 Nm and torque ripple of 1.12 Nm, the optimal design shown in Figure 7.4 with two-step skew achieves 62.5% torque ripple reduction with only 1.9% average torque reduction.

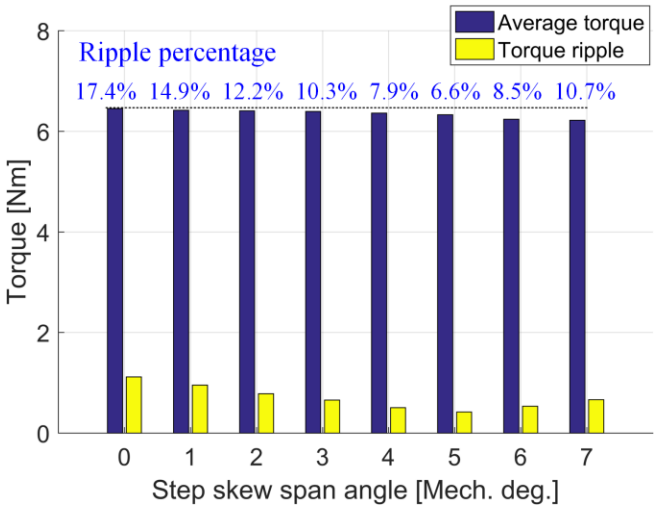

Figure 7.3. Variation of step skew span angle in the two-step skew designs and the resulting average torque, torque ripple, and ripple percentage.

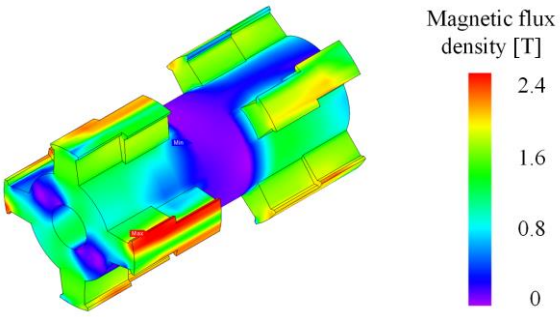

Figure 7.4. Magnetic flux density distribution at rated condition of the optimal two-step skew design with a mech. 5˚ step skew span angle.

The parametric analysis is also done for the four-step skew designs, and the torque results are shown in Figure 7.5. In this case, the average torque is larger than that in the two-step skew designs. For example, with the same step skew span angle of 5˚, the four-step skew design yields an average torque of 6.36 Nm, which is larger than the 6.33 Nm in the two-step skew design. The torque ripple in the four-step skew designs decreases from the investigated range of 0˚ to 7˚. The optimal design with minimum torque ripple percentage of 5.5% of the four-step skew design is achieved at the skew span angle of 7˚. This optimal design is shown in Figure 7.6, with an average torque of 6.33 Nm and a torque ripple of 0.35 Nm.

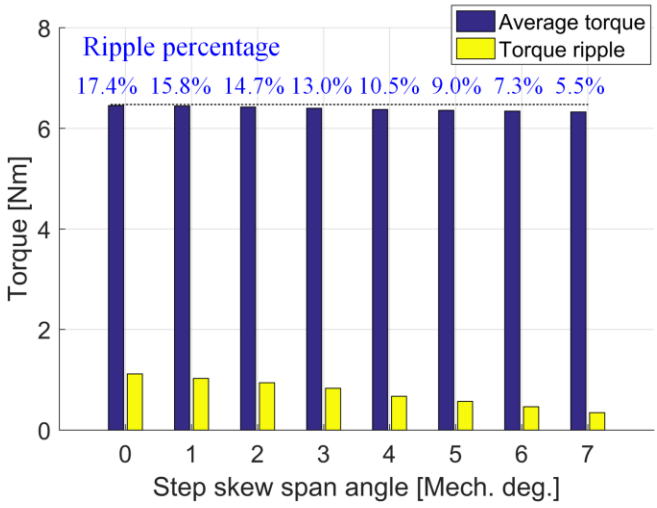

Figure 7.5. Variation of step skew span angle in the four-step skew designs and the resulting average torque, torque ripple, and ripple percentage.

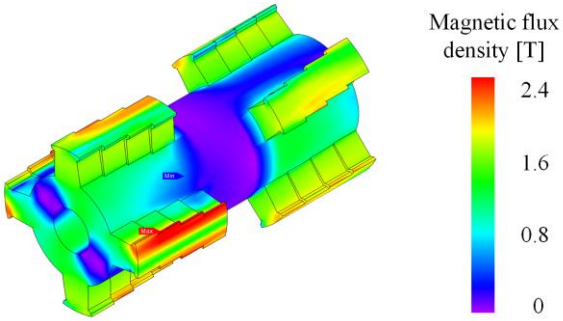

Figure 7.6. Magnetic flux density distribution at rated condition of the optimal four-step skew design with a mech. 7˚ step skew span angle.

Comparing the optimal two-step skew design with the optimal four-step skew design, both machines produce the same average torque of 6.33 Nm, but the four-step skew design has a lower torque ripple of 0.35 Nm compared to 0.42 Nm in the two-step skew design. However, the reduction of torque ripple is at the expense of significantly increased rotor structural complexity. Maintaining tight lamination tolerances in the four-step design is also much more challenging in the manufacturing process. Therefore, the optimal two-step design is chosen out of practical reasons. Figure 7.7 shows the torque waveform of the optimal two-step design and the initial design without step skew.

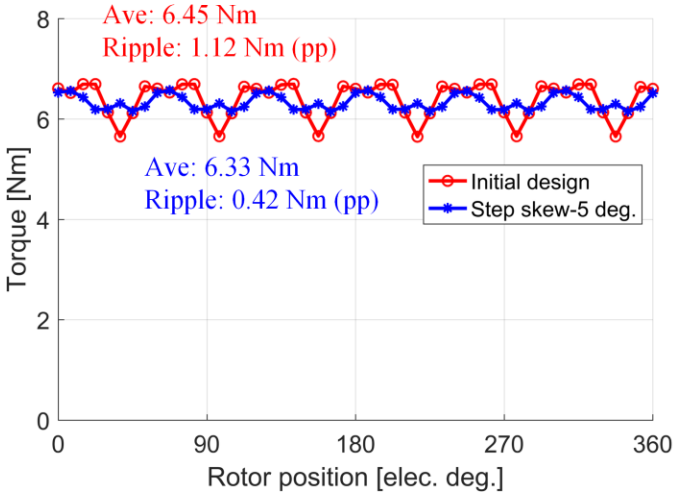

Figure 7.7. Torque waveform comparison of initial design (without step skew) and the optimal two-step skew design (5˚ step skew span angle).

7.2 Mechanical Tolerance Analysis

The performance of an electric machine cannot be maintained without appropriately controlling the mechanical tolerance in the key components. For the proposed dual-stator 6/4 FSPM machine, keeping tight mechanical tolerances in the airgap is critical in ensuring the desired performance. Therefore, it is necessary to investigate and understand the potential machine performance variations due to some possible mechanical tolerance deviations. This study focuses on three scenarios. The first scenario is that the offset angle between the front and rear rotor poles can deviate from the nominal mechanical 45˚ condition. The second and third scenarios are the rotor static eccentricity and rotor dynamic eccentricity, as the rotor may not be in perfect concentric to the center due to the manufacturing tolerances in the bearings. The previously obtained optimal

two-step skew machine is selected as the baseline design in this study. The baseline design does not have any of the mechanical tolerance deviations.

7.2.1 Deviation of Rotor Pole Offset Angle

The rotor poles of the baseline machine maintain the mechanical 45˚ angle between each pair of the subpart, i.e. F1 and R1, F2 and R2 as demonstrated in Figure 7.1. However, the front poles could deviate away by a small angle from the required 45˚ angle with respect to the rear poles due to reasons such as misalignment in the rotor stacking process. This study investigates the machine performance variation at different deviation angles. It is assumed that the rear part of the rotor poles (5˚ step skew does not change) deviates by an angle from 1˚ to 5˚ with a step change of 1˚. 3-D FEA calculated magnetic flux density contour plots are shown in Figure 7.8 for three representative cases. The average torque, torque ripple, and torque ripple percentage variations at those offset angle tolerance deviation conditions are shown in Figure 7.9. The results show that the increased deviation angle has a small reduction in the average torque, but significant increase to the torque ripple. The torque ripple is increased to an unacceptable value of 40.2% if the deviation angle is 5˚. Therefore, maintaining a tight tolerance of the offset angle is important in ensuring a low torque ripple design.

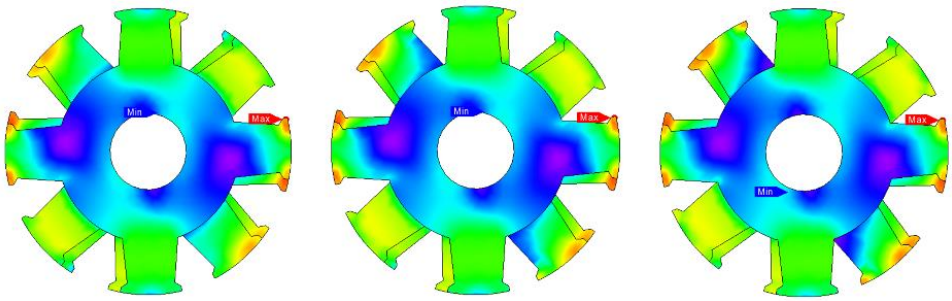

(a) (b) (c)

Figure 7.8. 3-D FEA calculated magnetic flux density distribution at different offset angle tolerance deviation. (a) tolerance offset by 1˚ mech. (b) Tolerance offset by 3˚ mech. (c) Tolerance offset by 5˚ mech.

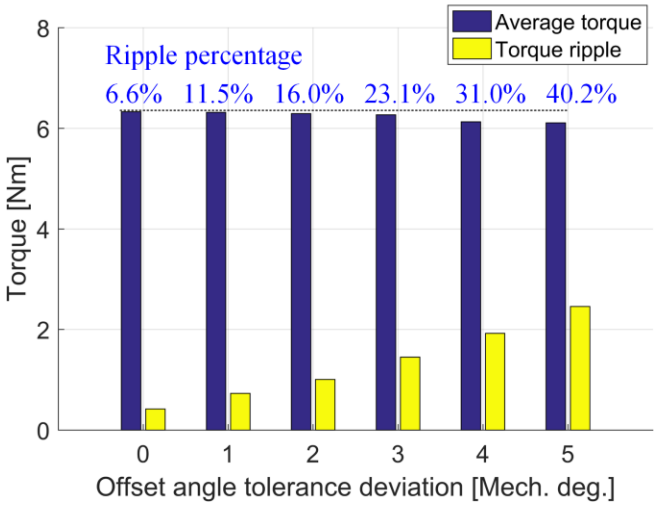

Figure 7.9. Variation of average torque and torque ripple with respect to the tolerance deviation of the offset angle.

The the flux linkage and its harmonic contents are shown in Figure 7.10 and Figure 7.11. The back-EMF waveforms at three different offset angle deviation conditions are compared to the baseline design in Figure 7.12. As the offset deviation angle increases, the amplitude of the back-EMF reduces, and the distortion of the waveform increases as demonstrated in FFT analysis in Figure 7.13. The even-order harmonics, especially the second-order harmonic, occur at increased deviation angles. Therefore, the balanced back-EMF in the dual-stator 6/4 FSPM machine can only

be achieved if the offset angle has perfect 45˚. Any deviation from this ideal angle creates imperfect cancellation of the even harmonics and leads to residue even harmonics in the phase waveforms.

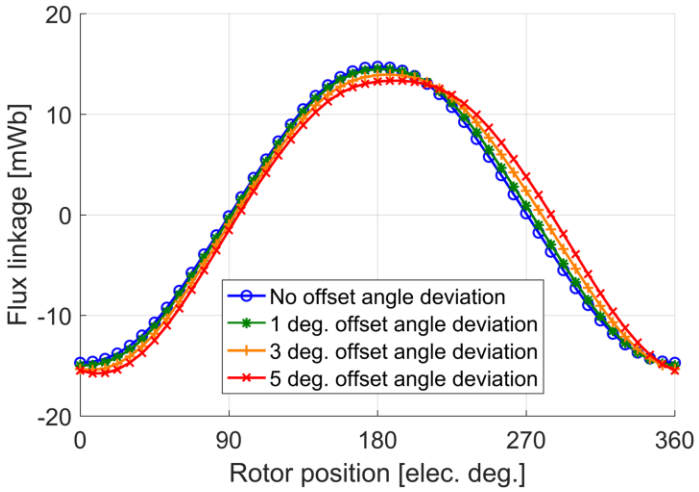

Figure 7.10. Variation of no load flux linkage waveforms for different offset angle deviation conditions.

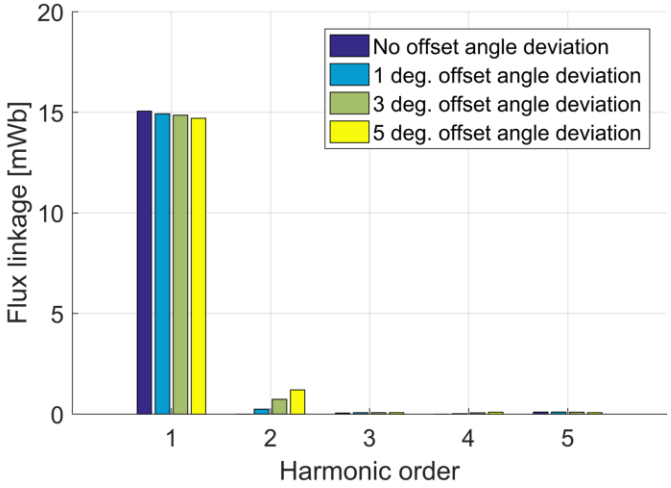

Figure 7.11. FFT harmonic contents of variation of no load flux linkage waveforms for different offset angle deviation conditions.

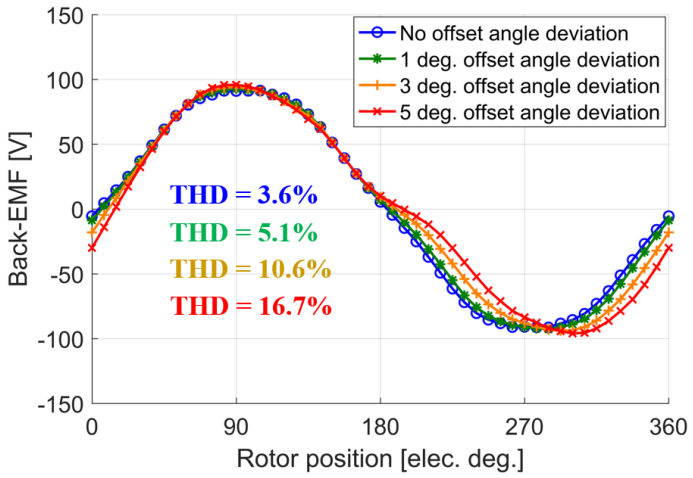

Figure 7.12. Variation of back-EMF waveforms for different offset angle deviation conditions.

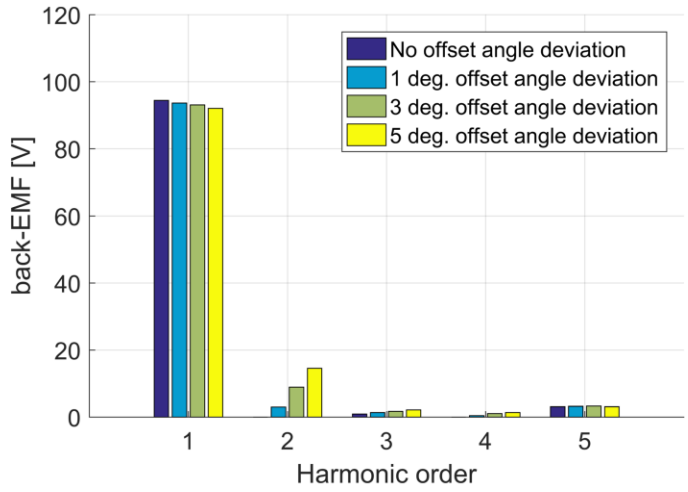

Figure 7.13. FFT harmonic contents of variation of back-EMF waveforms for different offset angle deviation conditions.

The net magnetic force map on the complete rotor for the three offset angle deviation conditions are compared to the baseline design in Figure 7.14. The calculated net rotor forces for all the deviation conditions at rated condition are small enough to be negligible. The distribution patterns in the force map are mainly attributed from the FEA discretization error, which is

influenced by factors such as mesh quality, non-linear iteration tolerance, etc. Thus, the deviation of the offset angle primarily increases the torque ripple and degrades the back-EMF waveform by reintroducing the even harmonics.

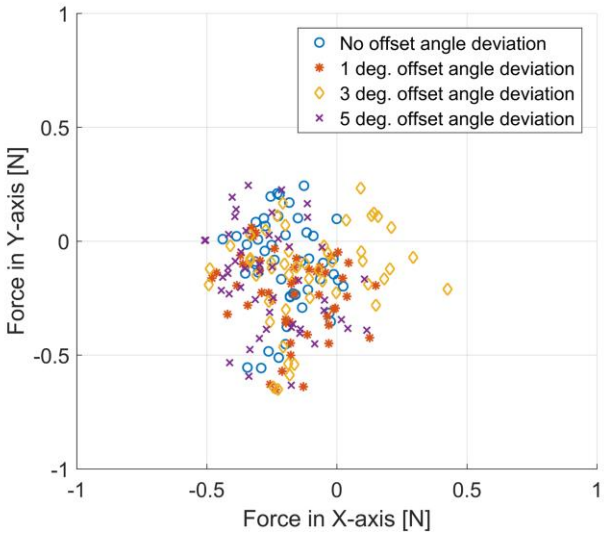

Figure 7.14. Rotor net magnetic force map under rated loading condition for different offset angle deviation conditions.

7.2.2 Rotor Static Eccentricity Analysis

The rotor of an electric machine has been assumed to rotate in perfect concentric with the stator center so far. However, the perfect concentric condition is an ideal case where the practical design can hardly achieve. In the real manufacturing and assembly of an electric machine, there is always some tolerance defined by each mechanical part, so that eccentricity conditions can hardly be avoided. Severe rotor eccentricity leads to noticeable performance degradation including vibration and noise, and reducing the life of bearing systems [280], [281], [282], [283], [284], [285].

In general, there are two types of rotor eccentricity scenarios, the rotor static eccentricity, and rotor dynamic eccentricity. To clearly differentiate these two eccentricities, an illustration using the step-skewed dual-stator 6/4 FSPM machine is shown in Figure 7.15. The perfect concentric rotor with respect to the stator inner diameter circle is drawn in Figure 7.15(a). The rotor with static eccentricity is shown in Figure 7.15(b) where the rotor rotational center is still the rotor geometric center, but the rotational center is no longer the center of stator inner diameter circle. In the rotor static eccentricity, the airgap length varies across the rotor outer periphery, but the airgap length is not influenced by the rotor rotational movement. Therefore, the relative position between the rotor and stator does not change. However, the rotor dynamic eccentricity is very different as shown in Figure 7.15(c). In this case, the rotor rotational center is not the same as the rotor geometric center. As the rotor rotates, the airgap length distribution dynamically changes depending on the rotor instantaneous position. In Figure 7.15(c), the rotor rotational center coincides with the center of stator inner diameter circle for simplicity reason, but these two centers do not have to be necessarily the same.

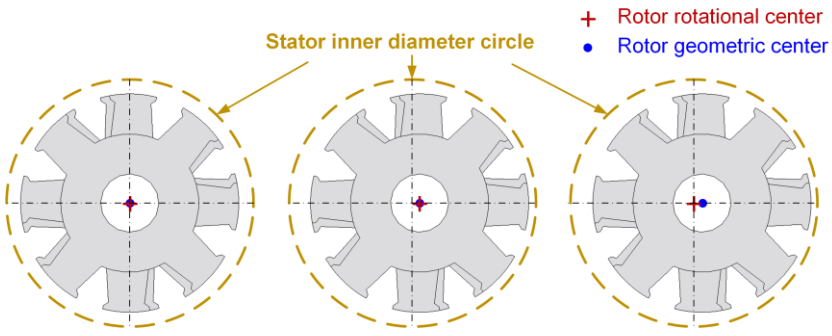

Figure 7.15. Illustration of rotor eccentricity conditions. (a) perfect concentric rotor. (b) rotor static eccentricity where the rotor rotational center is the same as the geometrical center, but this center is not the center of the stator inner diameter circle. (c) rotor dynamic eccentricity where the rotor rotational center is not the same as the geometrical center, and the rotational center can or cannot be the center of the stator inner diameter circle.

The electromagnetic stress is created in the airgap when the magnetic flux density is present under either no-load or loaded conditions. There are two components of electromagnetic stresses that can be calculated below,

$$\sigma_n = \frac{B_n^2 - B_t^2}{2\mu_0} \tag{7.1}$$

$$\sigma_t = \frac{B_n B_t}{\mu_0} \tag{7.2}$$

where σ_n and σ_t are the normal and tangential components of electromagnetic stress, respectively. B_n and B_t are the normal and tangential components of the electromagnetic flux density in the airgap, respectively. μ_0 is the permeability of free space.

The electromagnetic forces on the rotor thus can be calculated using the integration of normal and tangential magnetic flux density across a closed contour around the airgap region. If the forces on the rotor are segregated into x, y directions, the analytical expression for these two components are calculated below [115],

$$F_{mx} = \frac{rL_e}{2\mu_0}\int_0^{2\pi}[(B_t^2 - B_n^2)\cos\theta + 2B_n B_t \sin\theta]d\theta \tag{7.3}$$

$$F_{my} = \frac{rL_e}{2\mu_0}\int_0^{2\pi}[(B_t^2 - B_n^2)\cos\theta - 2B_n B_t \sin\theta]d\theta \tag{7.4}$$

where L_e is the effective stack length of the machine, r is the rotor outer radius, and θ is the mechanical angle around the airgap. The tangential and radial components of electromagnetic force can be obtained from the above two equations. The torque is produced by the tangential

electromagnetic force. The radial component of electromagnetic force does not contribute to torque production, but to pulsations in the rotor and stator structure.

This study investigates the influence of rotor static eccentricity to the torque production, back-EMF, and unbalanced rotor force. The rotor static eccentricity is assumed to be only in the x-axis. The rotor rotational center deviates from the stator center each by 0.1, 0.3, and 0.5 mm. Since the airgap length of this design is 1 mm, a 0.5 mm static eccentricity means the narrowest airgap length is 0.5 mm while the widest airgap length is 1.5 mm. The 3-D FEA flux density distribution of the most severe case is shown in Figure 7.16 with a 0.5 mm static eccentricity.

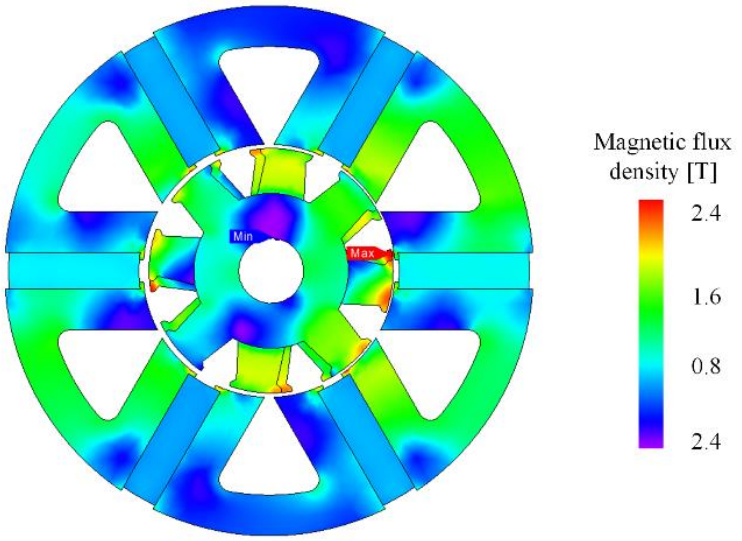

Figure 7.16. 3-D FEA calculated magnetic flux density distribution at rotor static eccentricity of 0.5 mm.

The rated torques for the three static eccentricity cases are shown in Figure 7.17. When the static eccentricity becomes larger, the average torque stays unchanged, but the torque ripple slightly increases. Therefore, the static eccentricity does not have a big impact on the produced

torque. The back-EMF waveforms shown in Figure 7.18 demonstrate that larger static eccentricity also has a slight reduction in the back-EMF amplitude, but all the waveforms remain sinusoidal shapes without noticeable distortion. The rotor force map in x, y-plane at three different static eccentricity cases is shown in Figure 7.19. The map shows that the unbalanced rotor magnetic force only occurs in the direction of deviation, and the magnitude of the force is proportional to the deviation distance. The force map of each case is plotted for one electric cycle, and the envelope of the force area increases slightly at severer static eccentricity cases.

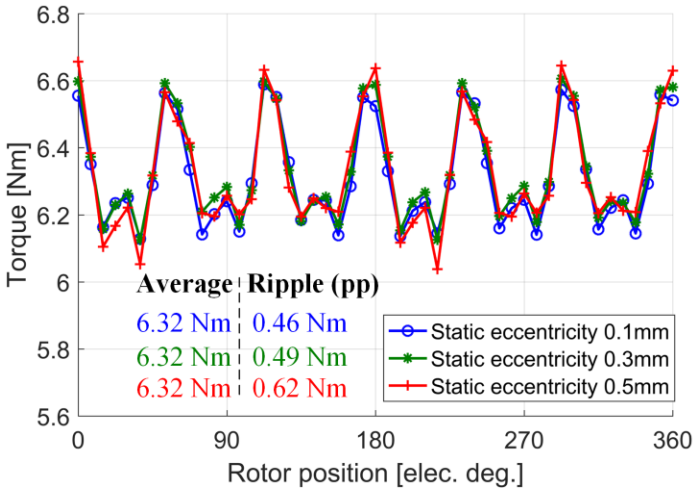

Figure 7.17. Instantaneous torque comparison of three different rotor static eccentricity conditions.

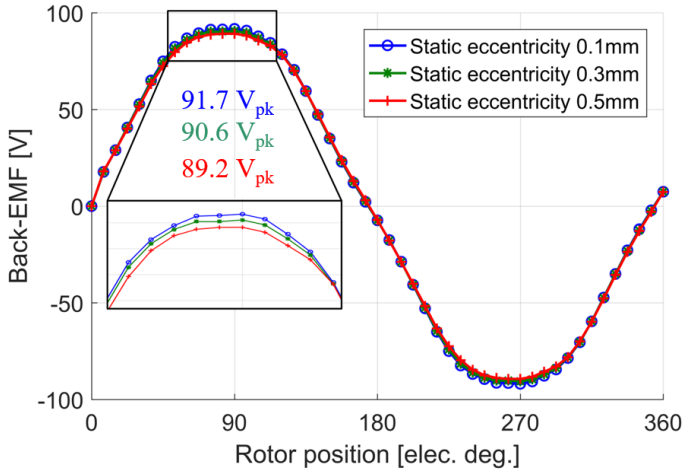

Figure 7.18. Back-EMF comparison of three different rotor static eccentricity conditions.

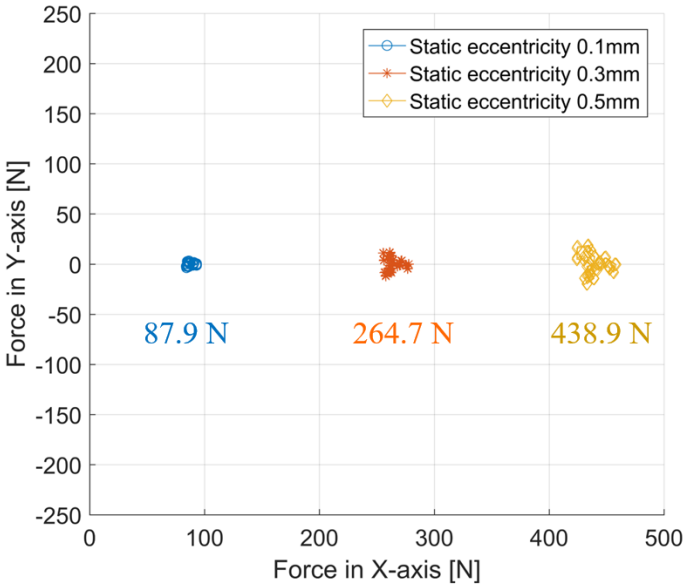

Figure 7.19. Rotor force map in x, y-planes at three different rotor static eccentricity conditions.

It is interesting to compare the rotor unbalanced magnetic force with the tangential force on the rotor that produces torque. If the average torque of the machine under this condition is

selected as 6.32 Nm, given the rotor radius of the machine being 30 mm, the calculated net tangential force on the rotor is 210.7 N. Therefore, the rotor unbalanced magnetic radial force can be much larger than the useful tangential force that produces torque.

7.2.3 Rotor Dynamic Eccentricity Analysis

Rotor dynamic eccentricity refers to the condition when rotor rotational center is not the geometric center. In this study, it is assumed that the rotor rotational center is still the center of stator inner diameter circle, but the geometric center deviates from the rotational center by 0.1, 0.3, and 0.5 mm, respectively. The rotor dynamic eccentricity has a more prominent impact on the torque waveforms as shown in Figure 7.20 than that of the rotor static eccentricity shown in Figure 7.17. As the dynamic eccentricity becomes severer, there is a noticeable decrease in average torque and an increase in the torque ripple. The back-EMF waveforms remain again sinusoidal shapes with just a minor reduction in amplitude at various dynamic eccentricity conditions shown in Figure 7.21.

The rotor force map at these three conditions is shown in Figure 7.22. In the dynamic eccentricity cases, the rotor force map has a circular shape. The reason is that the airgap length changes dynamically when the rotor rotates. Therefore, the force of rotor dynamic eccentricity has one mechanical cycle instead of one electric cycle as in the static eccentricity case.

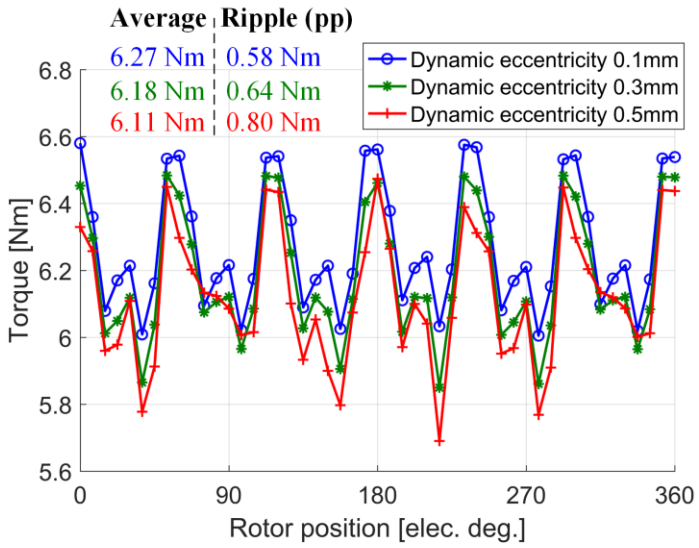

Figure 7.20. Instantaneous torque comparison of three different rotor dynamic eccentricity conditions.

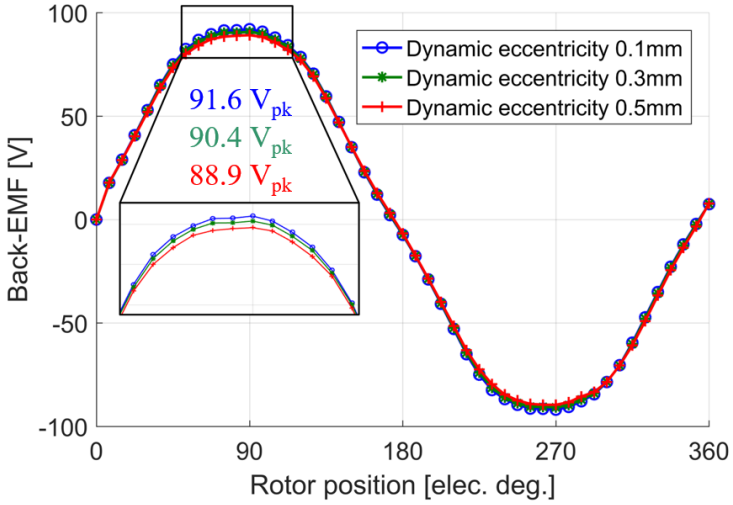

Figure 7.21. Back-EMF comparison of three different rotor dynamic eccentricity conditions.

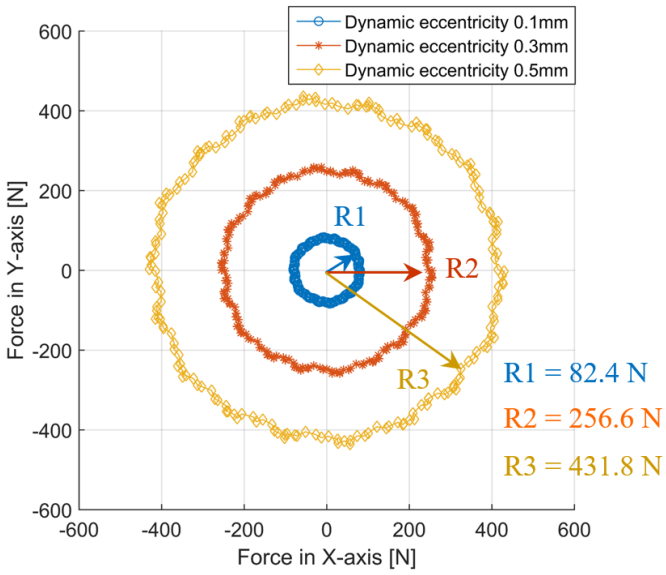

Figure 7.22. Rotor force map in x, y-planes at three different rotor dynamic eccentricity conditions.

To conclude the results from tolerance analysis, TABLE 7.1 is created to qualitatively summarize the three tolerance deviations to the influence of key machine performances including average torque, torque ripple, back-EMF waveform, and the creation of rotor unbalanced magnetic force. Tolerance deviations in offset angle and rotor dynamic eccentricity have a noticeable reduction in average torque. The rotor static eccentricity has negligible impact in the average torque. All three tolerance deviation scenarios have a large impact in increasing the torque ripple. The offset angle deviation has major harmonic degradation to the back-EMF waveform, while the rotor static and dynamic eccentricities only slightly reduce the back-EMF amplitude without introducing noticeable harmonic distortion. The rotor offset angle deviation does not incur the unbalanced rotor force, but the rotor static and dynamic eccentricity induce rotor unbalanced magnetic force. The dynamic eccentricity leads to worse force patterns than the static eccentricity

due to the circular shape of the force map that imposes higher stress and potential damage to the bearing system. From the manufacturing perspective, keeping tight tolerances in all three cases ensure that the designed dual-stator 6/4 FSPM machine maintains its desirable performances.

TABLE 7.1. INFLUENCE OF THREE TOLERANCE DEVIATION SCENARIOS INCLUDING OFFSET ANGLE DEVIATION, ROTOR STATIC AND DYNAMIC ECCENTRICITIES TO THE MACHINE PERFORMANCES

Compared Performances	Offset Angle Deviation	Rotor Static Eccentricity	Rotor Dynamic Eccentricity
Average torque reduction	Medium impact	Minor impact	Major impact
Torque ripple increase	Major impact	Major impact	Major impact
Back-EMF waveform distortion	Major impact	Minor impact	Minor impact
Rotor unbalanced force creation	Minor impact	Medium impact	Major impact

7.3 Structural Dynamics Analysis

7.3.1 Background

High-speed electric machines have many design challenges that are crucial to the performance and reliability of the system. These challenges include but not limit to machine losses and thermal regulation, bearings selection, rotor dynamics and structural integrity, and power electronics and control [286], [287]. The design of high-speed machine is a multi-physics practice that the design limitation is no longer only in electromagnetic domain. There are many design constrains that impact the speed limits of high-speed machines, particularly in thermal limit, rotor dynamics, and strength or stress limit of the material [288], [289]. The thermal property of a high-speed machine depends on both the generated heat and the implemented cooling technique. For

high-speed rotor bearing system, either resonant vibration or self-excited vibration limit the maximum rotational speed. If the rotor speed coincides with the resonant frequency of the rotor, resonant vibration occurs at this critical speed. The self-excited vibration renders the rotor unstable for rotation after a certain threshold speed. If the rotor of a machine contains permanent magnets, the tensile strength of the magnets need to be carefully considered during operation with the presented centrifugal force and electromagnetic force. Typically, a retaining sleeve is used to support the permanent magnets.

The structural property of the high-speed electric machine is closely inter-correlated with the electromagnetic performance. The electromagnetic force generated under various operating conditions influence the structural stress and strain distribution, vibrational behavior, and acoustic noise. Therefore, researchers analyzed the electromagnetic and structural aspects of the high-speed machine simultaneously [290], [291]. The analytical model to predict the noise and vibration is also derived in [292].

The electromagnetic design aspects of the proposed high-speed dual-stator 6/4 FSPM machine are elaborated previously. This section is dedicated to the structural analysis of the previously designed machine with 10 kW power rating. First, the rotor dynamics property of the dual-stator 6/4 FSPM machine is studied to investigate the vibration modes and the mode shapes. Critical speeds of the machine are identified and compared with the designed speed. The gyroscopic effects to the operating speeds are also investigated. Then, rotor forces calculated in electromagnetic FEA program are imported to the structural FEA solver to calculate the stress and strain distribution under loaded condition. The resultant maximum stress is compared to the

material yield strength to confirm that the designed machine is mechanically strong under specified operating conditions.

7.3.2 Rotor Dynamics Analysis

Rotor mechanical dynamic vibration is typically not of a great concern for medium to low speed electric machines because the operating speed of the application is usually far below the first resonance frequency of the structure. However, due to the high rotational speed nature of many high-speed electric machines, it is necessary to investigate the rotor dynamics at the operating speed region to avoid resonant vibrations that can damage the electric machine. The rotor resonance study of a high-speed PM brushless machine is presented in [293]. The influence of bearing stiffness and design parameters including the axial length of rotor lamination stack and shaft diameter to the bending mode frequency is quantified. The research shows that bearings create low-frequency vibration modes that could fall within the designed operation region of a high-speed machine. Mechanical design of a high-speed PM machine including the calculation of nature frequencies, bearing stiffness variation to the resulting bending mode, and centrifugal and interference stress analysis are presented in [294]. The evaluation of rotor dynamic analysis and characterization of the natural frequency is critical in high-speed turbo machinery applications to avoid vibration and noise as demonstrated in [295] and [296].

For the proposed dual-stator 6/4 FSPM machine designed for high-speed operation, the rotor dynamic property needs to be evaluated to ensure that the operating range of the machine does not include critical speeds which induce vibration and noise. The rotor of the proposed machine studied in this section has the same structure as the rotor shown in Figure 7.2(b) with

offset rotor poles and 5˚ two step skew implemented. For simplicity of the study, none of the rotor tolerance variations mentioned in the previous section are included. To lay a better foundation of the structural analysis, basic terms and definitions are described here.

The rotor dynamic vibration behavior essentially relates to the natural frequency of the material and the speed it operates. If the rotor is standstill without rotation, the mechanical behavior can be approximated as a beam structure. However, an electric machine needs to rotate to produce useful work, which introduces more complications to the vibrational properties. For any structure, the natural frequency at which the structure oscillates when not subjected to continuous external forces is determined by the square root of the ratio of stiffness over mass.

$$Natural \quad Frequency = \sqrt{\frac{Stiffness}{Mass}} \tag{7.5}$$

This equation describes that the natural frequency of a structure is increased by increasing the stiffness or reducing the mass. This conclusion is intuitive since we have the feeling that heavier objects tend to vibrate at lower frequency than light-weighted object, and stiff objects vibrate at higher frequency than soft objects. When the structural object vibrates at its natural frequency, the amplitude of vibration is controlled by the damping property of the system. A system with a low damping coefficient results in large vibrational amplitude. Therefore, increasing the system damping coefficient helps reduce the magnitude of vibration [297]. For a complex system like an electric machine, there is an infinite number of natural frequencies which have their own specified vibrational mode shapes.

For an electric machine system, there are several key factors that determine the natural frequencies and vibrational amplitude of the rotor dynamic property, the rotor stiffness (including

the shaft stiffness), rotor mass, and bearing stiffness. The natural frequencies of the assumed cylindrical rotor can be calculated here,

$$\omega_n = a_n \sqrt{\frac{EI}{\mu L^4}} \tag{7.6}$$

where ω_n is the rotor natural frequency in rad/sEa, a_n is the numerical constant calculated by boundary conditions, E is the Young's modulus of rotor material in GPa, I is the rotor moment of inertia in kg·m^2, μ is the mass per unit length in kg/m, and L is the axial length of the rotor [293], [294], [298]. The calculation of natural frequency for the proposed dual-stator 6/4 FSPM machine rotor becomes more complicated since there are step-skewed rotor poles with an offset angle that cannot be approximated as a simple cylinder. The rotor laminations are bounded to a shaft with bearings at each end. Detailed calculation of natural frequencies of the proposed rotor needs more sophisticated method such as structural finite element analysis.

The ratio of bearing stiffness to rotor and shaft stiffness plays a key role in shaping the vibration modes. If the rotor and shaft stiffness is much higher than the bearing stiffness (soft bearings), the rotor and shaft bending magnitudes are not very significant. This condition is typically referred to as "rigid rotor" mode. If the rotor and shaft stiffness becomes lower than the bearing stiffness (rigid bearing), the bending magnitude of rotor and shaft increases. It should be emphasized that the stiffness and damping are distinct physical properties. Stiffness is the ability of a material to resist deformation or deflection under a load. Damping is the ability to decrease the oscillation magnitude and overcome load forces by draining the energy in the system.

The rotation of the rotor introduces two general modes of vibration, the cylindrical mode and the conical mode. In the cylindrical mode, the whole rotor translates from the centerline of the

shaft and swings around the axis in a circular or elliptical shape as shown in Figure 7.23(a). In the conical mode, the rotor does not translate but rocks on the center point. The vibration pattern of the conical mode looks like two bulging cones pointing each other at the center point of the rotor as shown in Figure 7.23(b). For either cylindrical or conical mode, the rotor still rotates while it vibrates. The mode type can be further categorized into “forward whirl” or “backward whirl” depending on whether the rotation direction of the vibration is the same as or opposite to the rotation direction of the shaft. Figure 7.24 shows the illustration of the forward and backward whirls for the offset rotor.

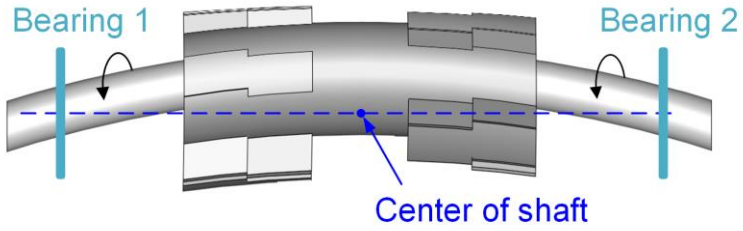

(a)

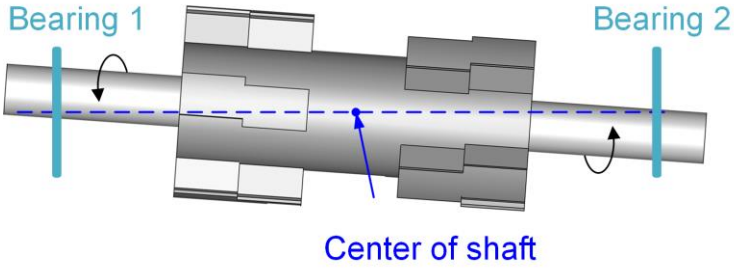

(b)

Figure 7.23. Illustration of mode shape (a) Cylindrical mode, (b) Conical mode.

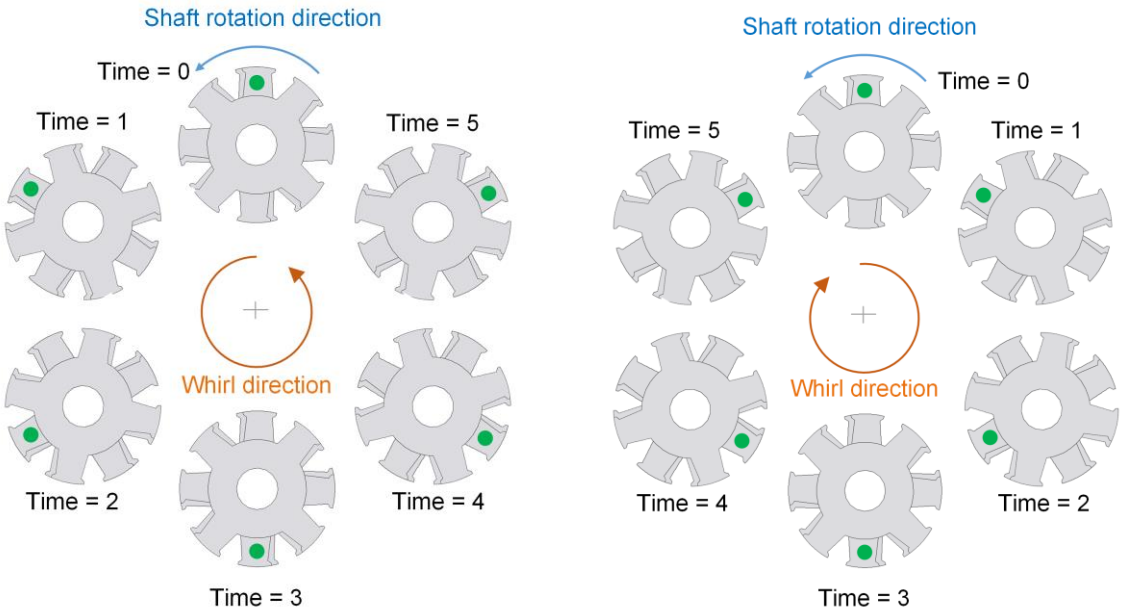

(a) (b)

Figure 7.24. Illustration of the sense of whirl (a) Forward whirl, (b) Backward whirl.

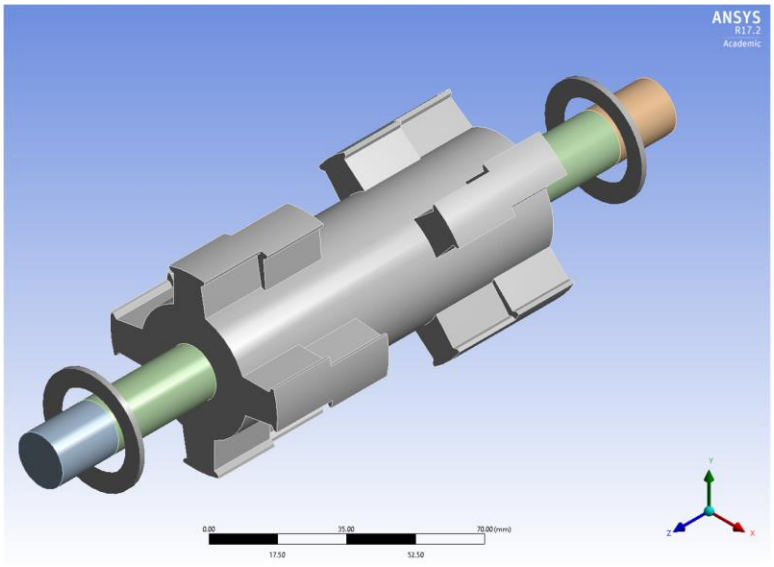

Figure 7.25. High-speed rotor system with supporting bearings in the structural modal analysis.

To investigate the influence of bearing stiffness and operating speed to various natural frequencies, modal analysis is performed in ANSYS Mechanical FEA program as shown in Figure 7.25. Given the rotor dimensions from the previous sections, the axial length of the rotor is 110 mm including the middle portion. The axial distance between the two bearings is selected to be 180 mm to give sufficient clearance to the supporting structure. Although the rotor is made of laminated steel and the shaft is made of stainless steel, most the mass for these two parts is essentially steel. Therefore, the mechanical properties of the shaft and rotor can be reasonably assumed the same as shown in TABLE 7.2.

TABLE 7.2. MECHANICAL PROPERTY OF CARBON STEEL AND ROTOR SHAFT

Mechanical Property	**Value**
Density [kg/m^3]	7850
Young's Modulus [GPa]	200
Bulk Modulus [GPa]	167
Shear Modulus [GPa]	77
Poisson's Ratio	0.3

Bearing stiffness is a crucial parameter that influences the natural frequencies and vibration modes. For a typical electric machine ball bearing, the stiffness in the horizontal direction is assumed the same as that in the vertical direction. Depending on the actual ball bearings used, the stiffness value may vary in a range. To characterize the variation of the low order natural frequencies under different bearing stiffness conditions, a parametric analysis is performed to change the bearing stiffness from 10^4 N/mm to 10^{10} N/mm while keeping the rotor speed at the rated 15,000 rpm. The damping of the bearing is set to zero for simplicity. There is a total of ten natural frequencies that are captured by the FEA program, and the result is shown in Figure 7.26.

The results show that a higher value of bearing stiffness increases the natural frequencies. Further increasing the bearing stiffness beyond a threshold does not increase the natural frequencies any more, and the threshold for lower order natural frequencies has a smaller bearing stiffness than that for the higher order natural frequencies.

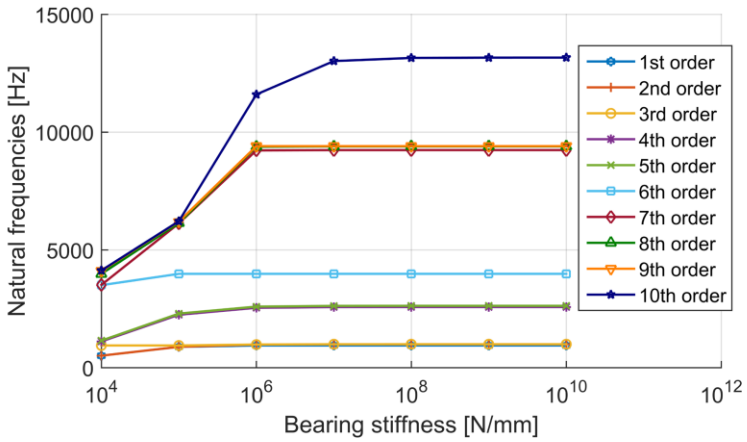

Figure 7.26. Relation of first 10 natural frequencies of rotor system to the variation of bearing stiffness at the operating speed of 15,000 rpm.

The operating speed of the rotor also influences the natural frequency. In this study, the stiffness of the bearing is selected to be a typical value of $5e^6$ N/mm, and the operating speed of the rotor is varied from zero to a sufficiently large value. Given the outer diameter of the rotor is 60 mm, the tip speed of the rotor at 15,000 rpm is 47.12 m/s. For high-speed machines, the upper tip speed limit is the speed of sound, which is about 340 m/s under normal condition. Thus, the speed limit of this analysis is chosen to be 110,000 rpm, which is approximately the speed of sound for the rotor. It should be noted that the rotor speed does not necessarily have to reach this speed limit, but the purpose of this study is to identify the potential critical speeds up to potential

maximum speed. The definition of critical speed is the shaft rotational speed that coincides with the natural frequency of the rotor system. To capture the critical speed properties, a Campbell diagram is drawn based on the FEA study results.

A Campbell diagram is used to represent the rotor system's natural frequency response spectrum under a wide range of operating speeds. The horizontal axis represents the mechanical speed of the rotor in rpm, and the vertical axis represents the natural frequencies under study. There is an additional straight line with a slope of 1/60 is added in the diagram to represent the synchronous speed. The slope of 1/60 is calculated because the value of natural frequency is equivalent to the value of rounds per second for the rotor. Therefore, 1/60 is used to convert between rounds per second and rounds per minute (rpm). The calculated Campbell diagram of the proposed machine assuming the typical bearing stiffness of $5e^6$ N/mm is shown in Figure 7.27. The evaluated speed range is from the rated 15 000 rpm up to 110 000 rpm, at which the tip speed of the rotor is close to the speed of the sound. The result shows that the first three critical speeds happen at the frequencies of 994.98 Hz, 996.17 Hz, and 1350.1 Hz. The corresponding rotational speeds are 59 593 rpm, 59 876 rpm, and 81 004 rpm, which are far beyond the designed maximum speed of 15 000 rpm. Therefore, the proposed machine does not run into any critical speeds up to nominal speed operation.

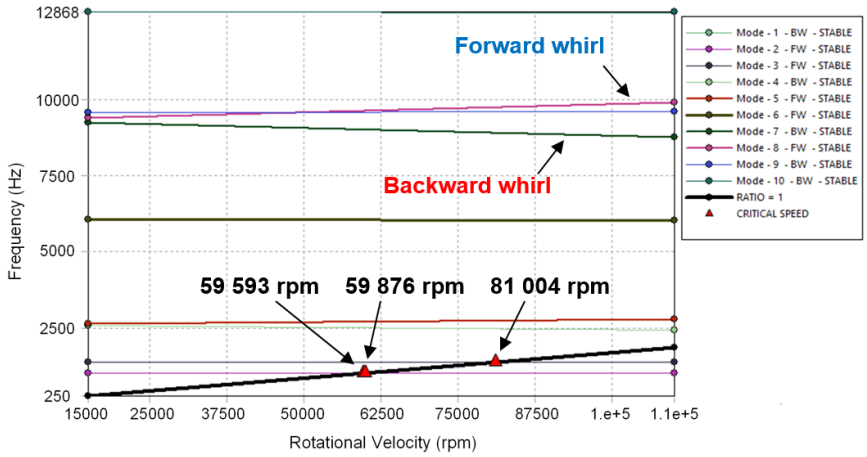

Figure 7.27. Campbell diagram of the high-speed dual-stator 6/4 FSPM machine with a bearing stiffness of $5e^6$ N/mm.

The first ten vibrational mode shapes of the rotor are calculated by the 3D structural FEA modal analysis as shown in Figure 7.28. The previously mentioned cylindrical and conical modes appear in pairs with one forward and one backward whirl mode. Mode 1 and mode 2 can also be considered as the first order bending mode. The shape property of mode 3 is rotor diameter expansion. Mode 4 and mode 5 can be considered as second order bending mode. Mode 6 has a vibrational shape of translation along the axis.

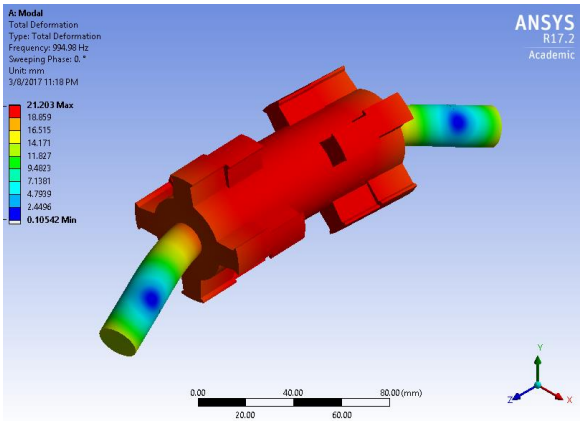

(a) Mode 1

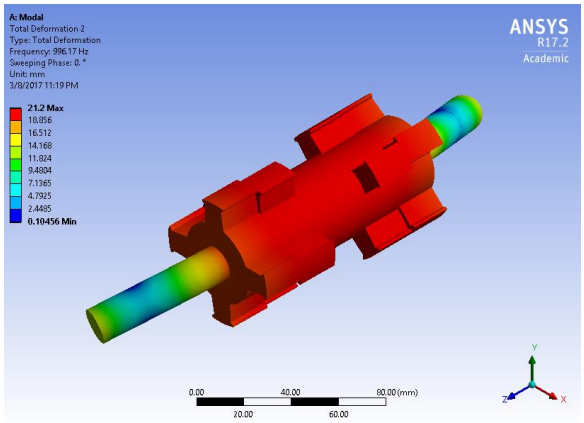

(b) Mode 2

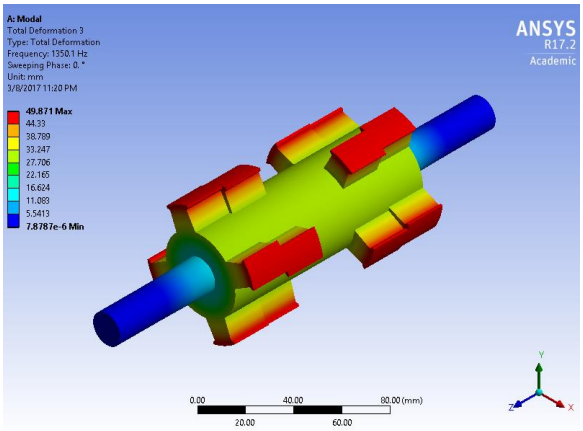

(c) Mode 3

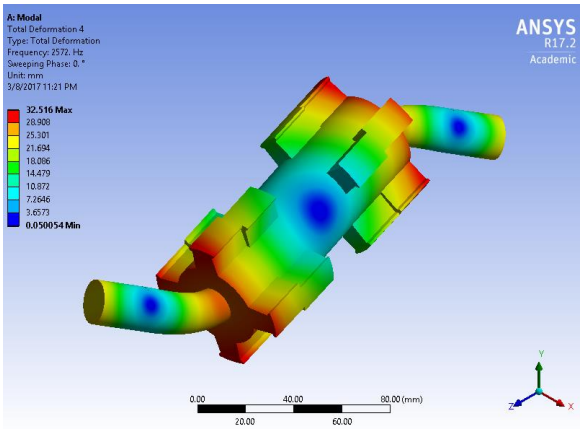

(d) Mode 4

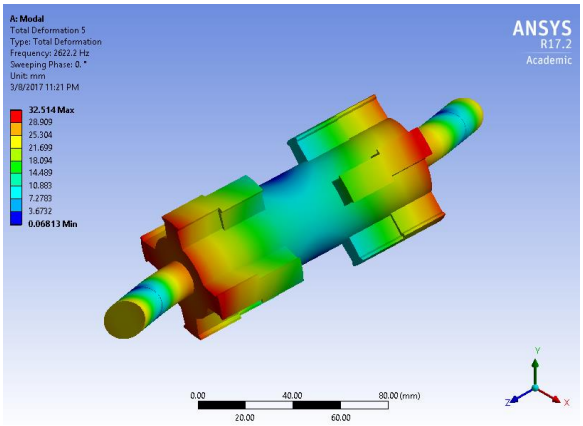

(e) Mode 5

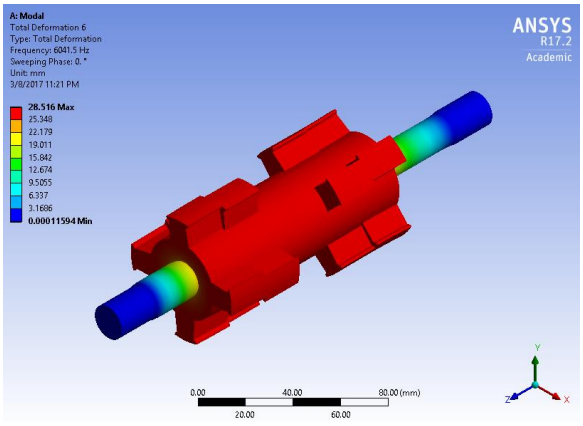

(f) Mode 6

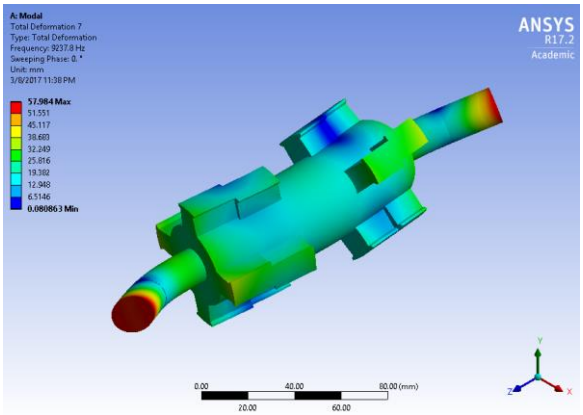

(g) Mode 7

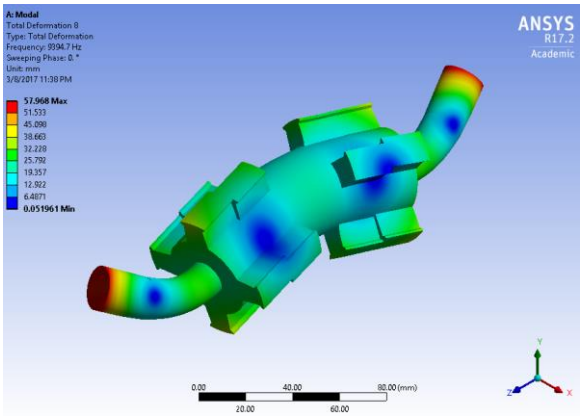

(h) Mode 8

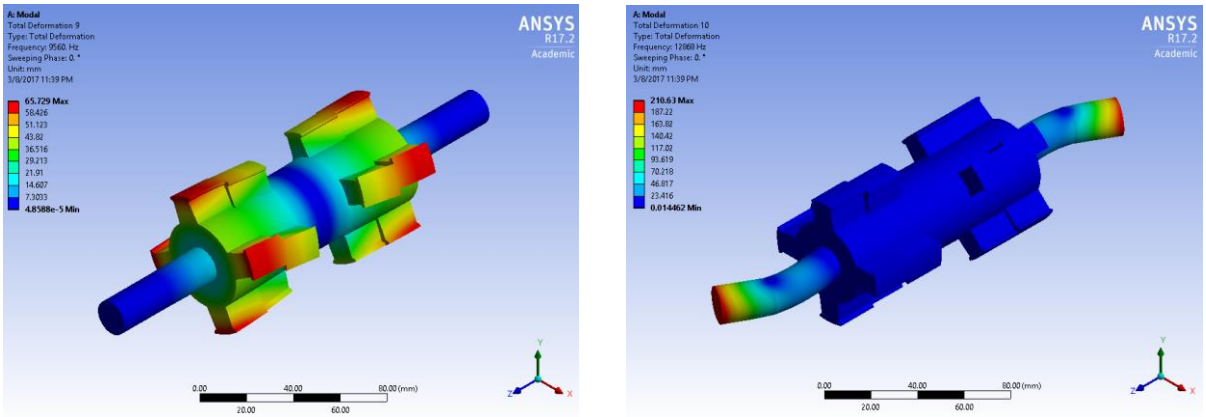

(i) Mode 9 (j) Mode 10

Figure 7.28. FEA calculated first 10 vibration mode shapes of the high-speed dual-stator 6/4 FSPM machine.

Mode 7 and mode 8 are cylindrical mode with third order bending property. Mode 9 is a torsional vibrational mode. Mode 10 is conical mode on the bearings. The vibrational mode shapes shown in the figures are the conditions that no damping is considered. In reality, there are certain damping effects in the bearing system that can mitigate the vibrational magnitudes. To summarize, the first ten vibrational mode properties are tabulated in TABLE 7.3.

TABLE 7.3. ROTOR VIBRATION MODE PROPERTIES FROM FEA RESULT

Vibration Mode Order	Whirl Direction	Critical Speed	Mode Type
Mode 1	Backward	59593 rpm	Cylindrical (1st order bending)
Mode 2	Forward	59876 rpm	Cylindrical (1st order bending)
Mode 3	Forward	81004 rpm	Diameter expansion
Mode 4	Backward	None	Conical (2nd order bending)
Mode 5	Forward	None	Conical (2nd order bending)
Mode 6	Forward	None	Translation along axis
Mode 7	Backward	None	Cylindrical (3rd order bending)
Mode 8	Forward	None	Cylindrical (3rd order bending)
Mode 9	Backward	None	Torsional
Mode 10	Backward	None	Conical on bearing

7.3.3 Rotor Stress Analysis

The electromagnetic forces on the rotor create stress on the materials that can potentially deform the mechanical structure. To ensure that the designed high-speed dual-stator 6/4 FSPM machine rotor sustains the exerted stress on normal operation, a mechanical stress analysis is investigated in this section. Stress is defined by the force per unit area, and it has a unit of Pascal. The stress on the rotor can be subdivided into shear stress and normal stress (compression or tension). The shear stress has tangential components in the airgap region and it is responsible for the production of electromagnetic torque. Shear stress is also physically calculated by the multiplication of magnetic loading (T) and electric loading (Ampere-turns/m). The normal stress does not contribute to the torque production, but instead to rotor vibrations and noise. For simplicity of this study, neither rotor static or dynamic eccentricities are considered in the stress distribution analysis.

If the application of twisting torque T (Nm) is exerted on the cylindrical rotor shaft with a length of L (m) and radius or r (m), the shear stress τ (Pa) at the radius of r is defined by the following equation,

$$\tau = \frac{T\,r}{J} \tag{7.7}$$

where J is the polar moment of inertia of an area (m^4) that characterizes the subject's ability to resist bending.

The angular deflection of a torsion rotor or shaft θ (rad) can be calculated as,

$$\theta = \frac{LT}{JG} \tag{7.8}$$

where G is the modulus of rigidity (Pa), or shear modulus.

There are many types of stress in the mechanical realm, but the von Mises stress, or equivalent tensile stress, is generally used as a guidance to determine whether a material can sustain the imposed forces or not. The von Mises stress is a scalar value that can be calculated from the Cauchy stress tensor. The von Mises stress comes from the theory of distortion energy failure, where failure occurs when the stored distortion energy is higher than the distortion energy in a simple tension case. In cases where complex multi-axis stresses are on the object, the von Mises stress is an appropriate failure criterion to consider. If the maximum von Mises stress is below the yield strength of the material, the structure will not suffer from irreversible deformation.

In this study, the FEA results from the electromagnetic program are passed to the mechanical FEA program. The body force distribution on the rotor at the rated loading condition is calculated for one electric cycle in ANSYS Maxwell program, and then the results are imported into the ANSYS transient Mechanical program. The body force density distribution on the rotor is shown in Figure 7.29. It can be noted that the radial force density is much higher than the tangential force density on the rotor, and this result is expected from the discussions in previous sections. The maximum body force density is 3.168 N/mm^2 which occurs at the tip of rotor poles. The rotor of the machine rotates counter-clockwise at the rated speed of 15 000 rpm. The rotor force distribution is studied for one electric cycle. The force vector at front rotor pole changes its magnitude and direction instantaneously than the force at the rear rotor poles. If the circumferential components of the rotor forces in the front poles are different than the force from the rear poles, torsional force (or differential force) occurs on the rotor body to create torsional stress. In the

meantime, the radial forces on the rotor poles create rotor bending stress due to the asymmetrical offset-pole structure.

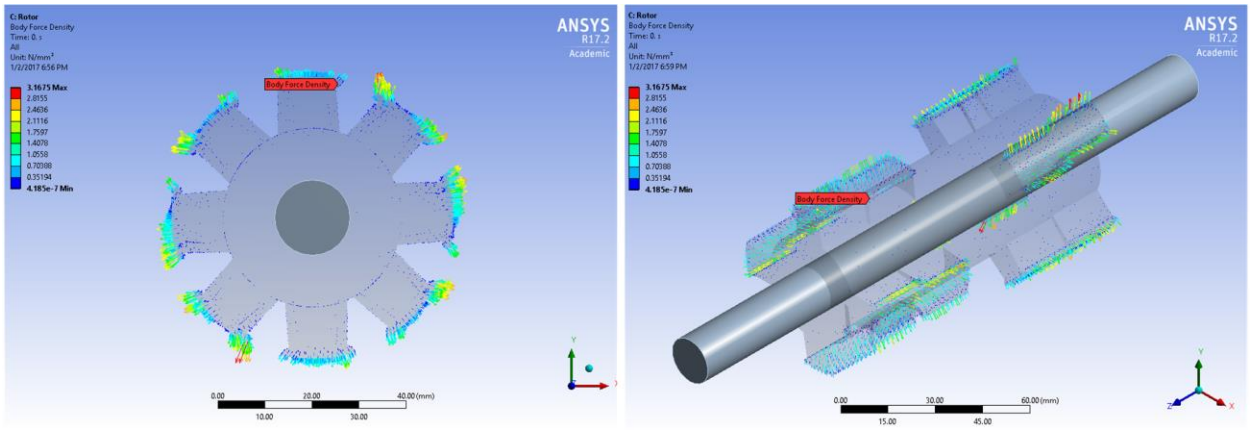

(a) (b)

Figure 7.29. Instantaneous electromagnetic forces on the rotor, (a) Front view (b) Isometric view.

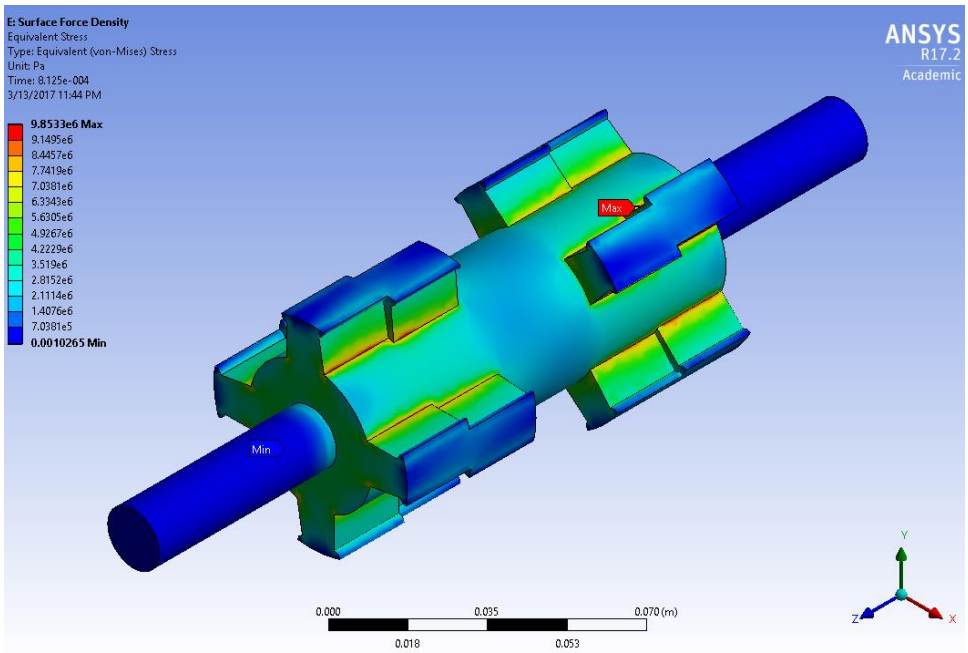

Figure 7.30. Rotor von Mises stress distribution at rated operating condition.

To evaluate the complex multi-directional stress distribution on the rotor, the von Mises stress is used and the distribution is shown in Figure 7.30. The results demonstrate that the maximum von Mises stress takes place at the corner of rotor pole where the maximum stress is around 9.85 MPa. This value is significantly lower than the maximum material tensile strength of silicon steel which is around 375 MPa. It should be noted that the von Mises stress on the middle part of the rotor is non-zero with an average value of around 1.2 MPa, which is partially contributed from the torsional stress. The two-step skew design of the rotor poles also creates differential torque on the rotor body yoke as reflected in the von Mises stress distribution. In this high-speed machine design, the mechanical integrity of the rotor is verified that the whole rotor is within large same margins of the material strength.

7.4 Summary

This chapter presents the studies on the torque ripple reduction, mechanical tolerance analysis, and structural dynamic analysis including rotor dynamics and rotor stress. The torque ripple reduction technique by step-skew is shown effective in the design practice. Mechanical tolerances including rotor pole offset angle deviation, rotor static, and rotor dynamic eccentricities are investigated to show their influence on the torque properties, harmonic distortion, and unbalanced rotor forces. Rotor dynamic vibration modes and natural frequencies are evaluated for high-speed operation. Rotor von Mises stress distribution is calculated to verify the mechanical integrity of the high-speed design. Key research findings are summarized below:

- The two-step skew design of rotor pole by the appropriate skew angle is effective in reducing the torque ripple while maintaining a sufficiently large average torque.

Compared to other torque ripple reduction method such as tooth nothing and axial pairing, the step skew method is more robust regarding the performance.

- Maintaining tight mechanical tolerances in key parts of the proposed dual-stator 6/4 FSPM machine is crucial in achieving the expected performance. The ideal rotor pole offset angle between the front and rear portions is 45˚ mechanically, and deviation from this condition reduces average torque, increases torque ripple, and significantly increases the harmonic distortion. This condition does not introduce rotor unbalanced magnetic force.
- The static and dynamic eccentricities occur when the rotor is not in perfect concentric condition with the stator inner diameter circle. Due to manufacture imperfections and wear of the machine by time, there is almost always certain amount of either type of eccentricities in the machine. Both eccentricity scenarios degrade the torque performance by reducing the average and increasing the torque ripple. The rotor unbalanced magnetic forces are also introduced in the rotor and shaft. However, the influence to increasing the harmonic distortion is negligible.
- Rotor dynamic vibrations are a critical part in the design of high-speed machine. Due to the high rotational speed limit, high-speed dual-stator 6/4 FSPM machine can potentially operate into critical speeds. To increase the low-order natural frequencies, a higher value of bearing stiffness to rotor and shaft stiffness is preferred.
- Typical vibrational modes can be categorized into cylindrical mode and conical mode. These two modes occur in pairs with forward and backward whirl properties. The

forward whirl has gyroscopic effect that tends to increase the stiffness of the system and increase the natural frequencies, while the backward whirl has the reversed effect.

- The von Mises stress considers complex multi-axis stress on the subject, and it is typically used as a criterion in structural analysis to determine material failure property. The maximum von Mises stress of the proposed offset-pole rotor occurs in the bottom of rotor poles. The middle portion of the rotor experiences non-negligible stress due to torsional stress and radial stress, but they are significantly lower than the maximum stress and material tensile stress limit.

Chapter 8
Experimental Validation

This chapter focuses on the design, fabrication, and experimental testing of a proof-of-concept dual-stator 6/4 FSPM machine. The fabrication of each machine component including the offset rotor and stator lamination stacks are described individually. The prototype machine is built using open housing pillow block bearings structure to allow visual asscess to the rotor design. The prototype machine is positioned into a dynamometer test stand for performance characterization. Measurements are taken at both no-load and various loading conditions to verify the performances, including the back-EMF, relation of output torque versus current, and various loss components.

8.1 Design of Proof-of-Concept Machine

8.1.1 Design Specifications

This section focuses on the manufacturing and experimental test setup of the proof-of-concept dual-stator 6/4 FSPM machine. The rating of the prototype machine is chosen as 1.5 kW and 1800 rpm. The reason to design and manufacture a low-speed version of the machine is to verify the even harmonic elimination effect and prove that the dual-stator 6/4 FSPM machine concept is feasible. The electromagnetic properties of the proof-of-concept machine were discussed in Chapter 4, and this chapter demonstrates the concept validation by experimental results. The experience gained during the design, fabrication, assembling, and testing process of

this proof-of-concept machine are necessary for investigating the designs for higher speed operations.

The proof-of-concept prototype is designed with the open housing structure shown in the CAD drawings in Figure 8.1. The two stators are mounted to the cubic aluminum housing with keys in each of the stators to prevent rotation. Two pillow block bearings are used to support the rotor and shaft. The housing and two pillow block bearings are mounted to the common aluminum base. By using the open housing structure, the design of the rotor and stator can be easily accessible to visually inspect the design of this machine.

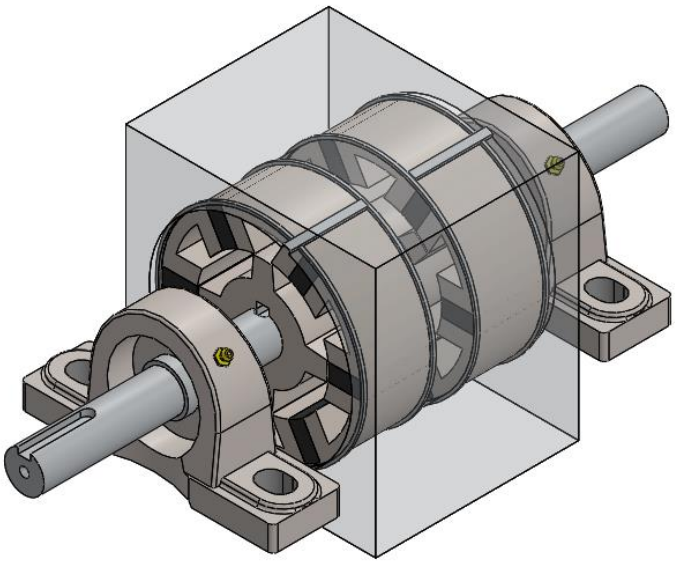

Figure 8.1. Assembling drawings of the proof-of-concept dual-stator 6/4 FSPM machine with housing and pillow block bearings in CAD program.

The fabricated rotor of the machine is shown in Figure 8.2. One of the stators is shown in Figure 8.3. The finished two stators with concentrated windings are placed side by side as shown in Figure 8.4. More detailed CAD drawing of each component are shown in the Appendix. The lamination steel used for stator and rotor is M19-29Ga, and the NdFeB permanent magnet used is N38SHT. The dimensions and materials for the prototype is shown in TABLE 8.1.

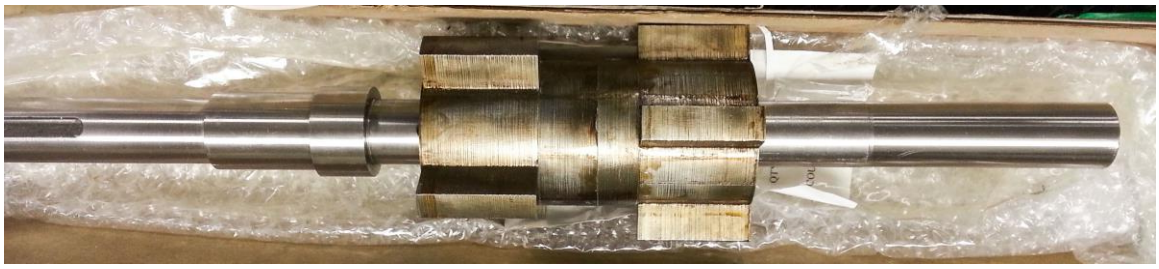

Figure 8.2. Fabricated rotor of the proof-of-concept dual-stator 6/4 FSPM machine.

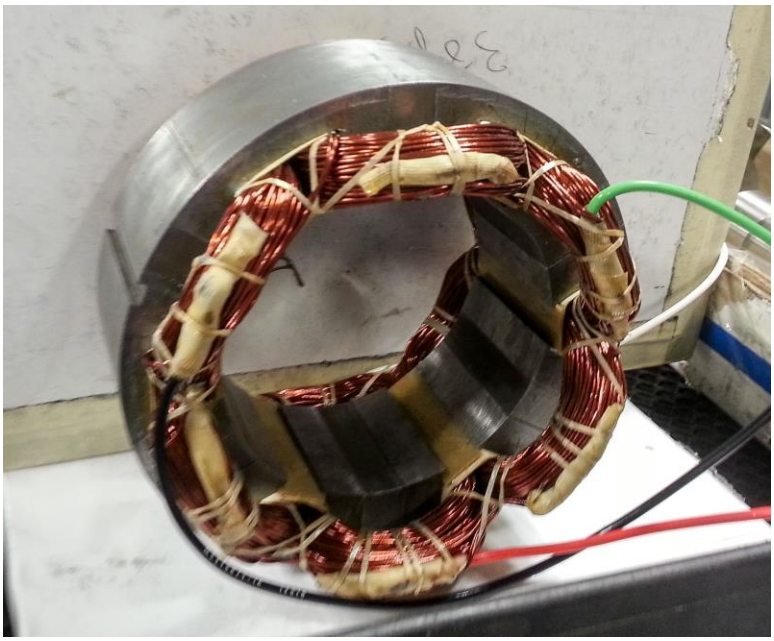

Figure 8.3. Fabricated one stator of the proof-of-concept prototype dual-stator 6/4 FSPM machine.

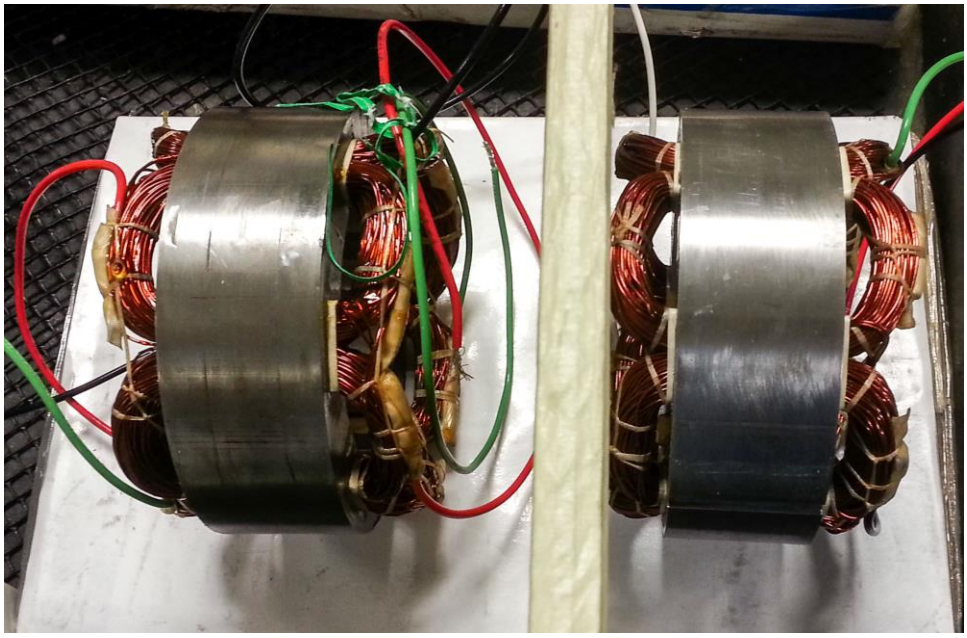

Figure 8.4. Fabricated two stators of the proof-of-concept prototype machine.

TABLE 8.1 DIMENSION AND MATERIAL USED FOR THE PROTOTYPE.

Design Parameters	**Value**
Output power, P_{out} [kW]	1.5
Rated speed, n_r [rpm]	1800
Stator outer diameter, D_{os} [mm]	130
Stator inner diameter, D_{is} [mm]	84.5
Shaft diameter, D_{shaft} [mm]	25.4
Airgap length, g [mm]	1
Magnet thickness, d_m [mm]	11
Single stator stack length, $L_{e.1/2}$, [mm]	42.5
Total effective stack length, L_e [mm]	85
Number of turns per phase per stator, N_t	120
Components	**Material**
Stator and rotor lamination	M19-29Ga
NdFeB permanent magnet	N38SHT
Windings	copper

8.1.2 Dynamometer Test Setup

The dynamometer test setup of the prototype machine is shown in Figure 8.5 with the illustrations of each component. The proof-of-concept machine is connected through a torque transducer and then to the dyno machine, which is a SPM servo motor that has a power of 2.6 kW and maximum speed of 3000 rpm. The other side of the prototype machine is connected to an incremental encoder. All the winding terminals of the prototype machine are accessible for experimental studies. There are 6 wires coming out from the front stator, and 4 wires coming out from the rear stator. The color coding for the wires are that phase A, B, and C are marked by black, red, and green individually. The neutral point of the rear stator is marked by white wire.

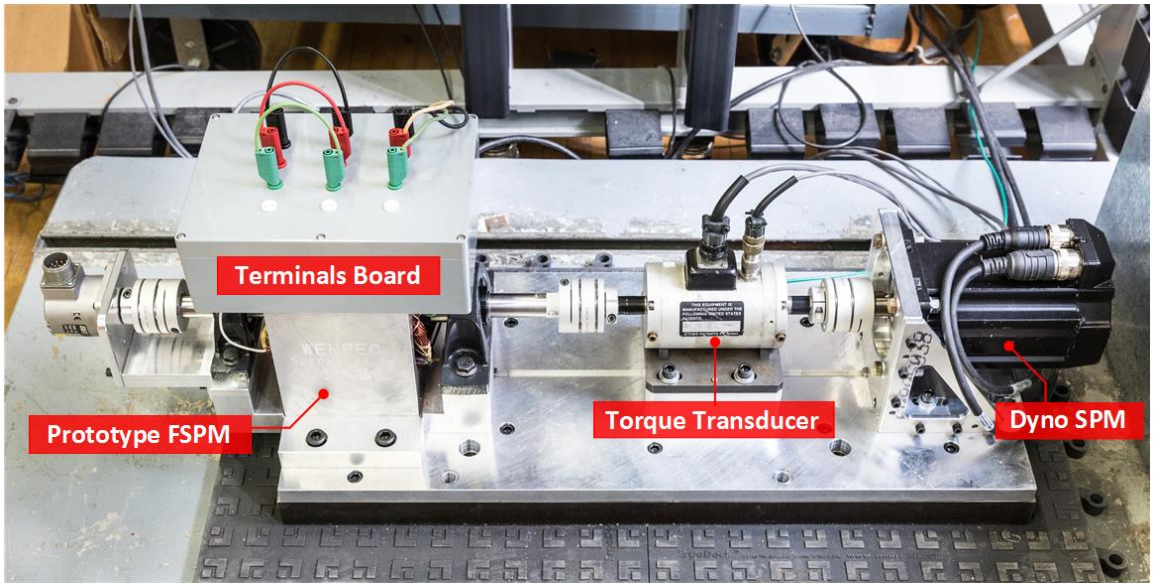

Figure 8.5. Dynamometer test stand configuration for the prototype proof-of-concept dual-stator 6/4 FSPM machine.

The wires from each of the stators are enclosed into a plastic terminal box shown in Figure 8.6. Each of the three phases in the front or rear stator can be accessed for measurement. If the terminal block TB1 and TB2 are connected as shown in the figure, the windings in the front and rear stators are connected in series. The main three-phase power is feed into the machine via TB3. The neutral point of the machine is also accessible via the white socket, so the phase-to-neutral voltage waveform can be measure during the experiments.

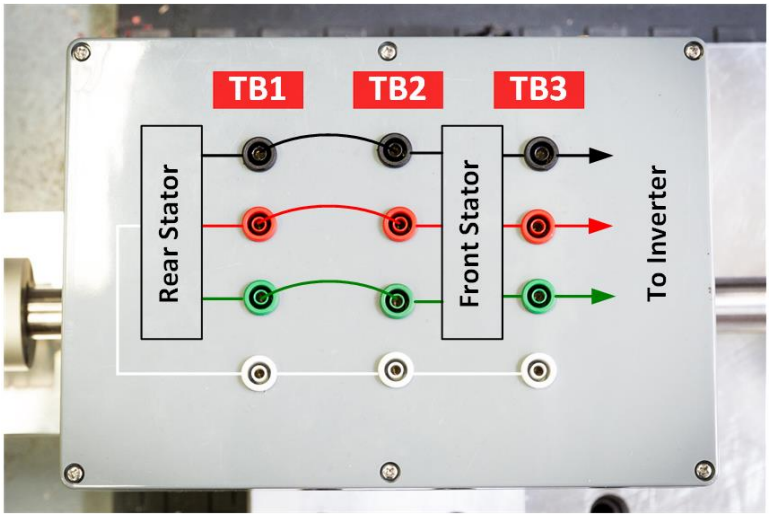

Figure 8.6. Terminal connection configuration of the prototype machine.

The inverters and controllers used for the experimental test is shown in Figure 8.7 The drive used to control the dyno SPM machine is an Allen Bradley Kinetix 5500 2198-H070-ERS drive. The digitial controller used for this drive is 1769-L18ERM-BB1B compactLogix motion controller. The type of the SPM machine is an Allen Bradley MPL-A4540F-SJ22AA 8-pole servo machine with a rated power of 2.6 kW. The drive used to control the prototype FSPM machine is

the Allen Bradley Ultra3000 2098-DSD-030 drive. The main input three-phase power has a voltage of 230 V. The dc bus of two drives are connected in parallel so that the power flows within the dynamometer system.

The Kinetix drive is used to control the speed of the dyno SPM machine, while the Ultra3000 drive is used to control the current (or the torque) of the prototype machine. To simplify the dyno test setup, the prototype machine can share the same position feedback signal with the dyno SPM machine. Therefore, the absolute Hiperface encoder embedded in the dyno SPM machine is used to provide position feedback signal to both drives. It should be mentioned that the prototype 6/4 FSPM machine performance can be considered as an 8-pole SPM machine to the drive, in the aspects of the frequency and speed relationship and only q-axis current excitation. Since the same encoder feedback is provided to both drives, the prototype machine needs to be aligned with the dyno SPM machine appropriately so that their back-EMFs should be in-phase with each other. This requirement is satisfied by adjusting the shaft connection orientation of two machines. Therefore, when the common position feedback signal is provided to two drives simultaneously, both drives produce currents that have the same phase angle. Given that the back-EMFs of two machines are also in-phase, the maximum torque per ampere condition is satisfied for both machines at the same time. The schematics of the whole system setup is shown in Figure 8.8.

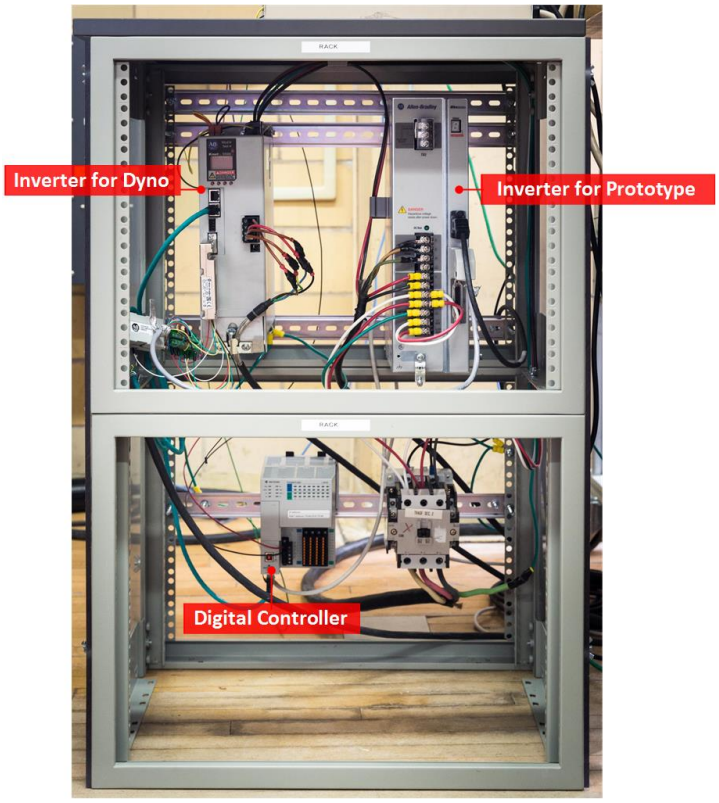

Figure 8.7. Inverter and controller rack for the dynamometer test stand.

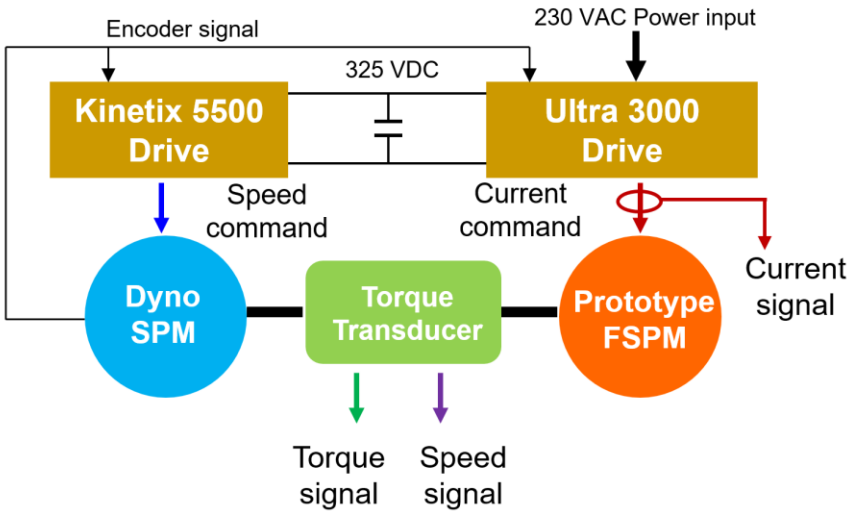

Figure 8.8. Dynamometer setup schematics.

8.2 Testing of Proof-of-Concept Machine

8.2.1 Testing of Flux Linkage and Back-EMF

This section presents the experimental results of the proof-of-concept prototype machine at open circuit condition, with comparisons to the FEA results. At open circuit condition, the prototype machine is driven by the dyno SPM machine which is controlled at a constant speed by the drive unit. To verify the flux linkage produced in each stator windings, the phase voltages (back-EMF at this no-load condition) of each stator winding are measured separately at the same speed of 900 rpm. After that, flux linkages in each individual stator winding are calculated by integrating the measured back-EMF with respect to time. The experimentally calculated flux linkage is compared with the FEA result shown in Figure 8.9 and Figure 8.10 for the front stator winding and rear stator winding, respectively. The prototype machine has slightly smaller fundamental flux linkage compared to the FEA results. The back-EMFs from the two stator windings are shown in Figure 8.11 and Figure 8.12. Then, both stator windings are connected in series and the total phase back-EMF is measured from the machine terminal to the neutral point. The measured waveform is compared with the FEA result at the same speed as shown in Figure 8.13. The experimental results show reasonably good agreement with the FEA results. The discrepancy of the results could possibly from the reasons including the difference in the saturation, fringing or other magnetic effects in the actual design. There could also be reasons such as the variations of material properties between FEA database and the actual design for permanent magnets and steel, and the precision error of the measurement equipments.

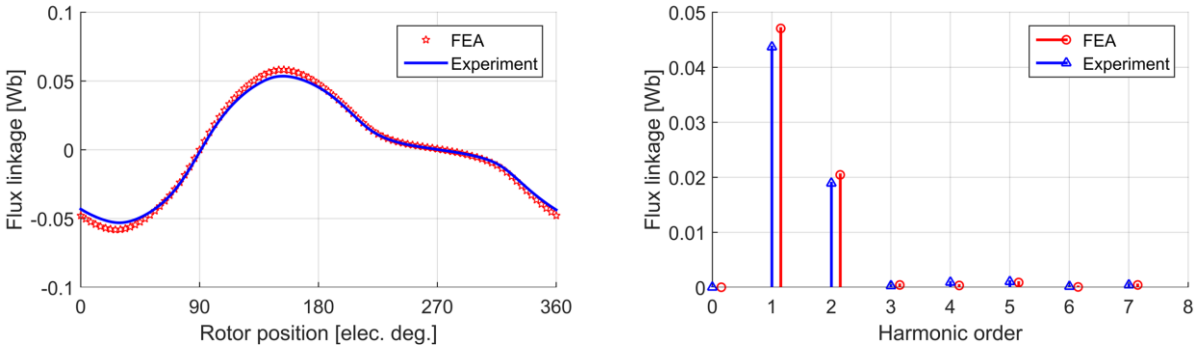

(a) (b)

Figure 8.9. Experiment and FEA result comparison of flux linkage in front stator phase winding (a) waveform and (b) harmonic components.

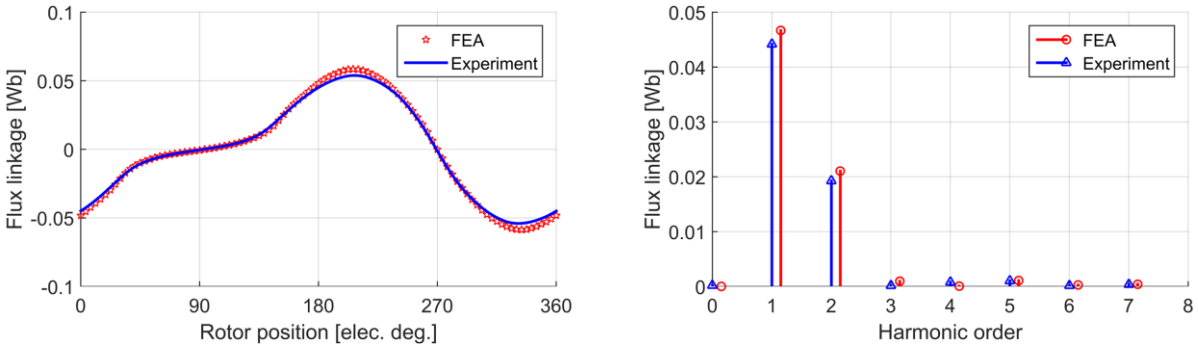

(a) (b)

Figure 8.10. Experiment and FEA result comparison of flux linkage in rear stator phase winding (a) waveform and (b) harmonic components.

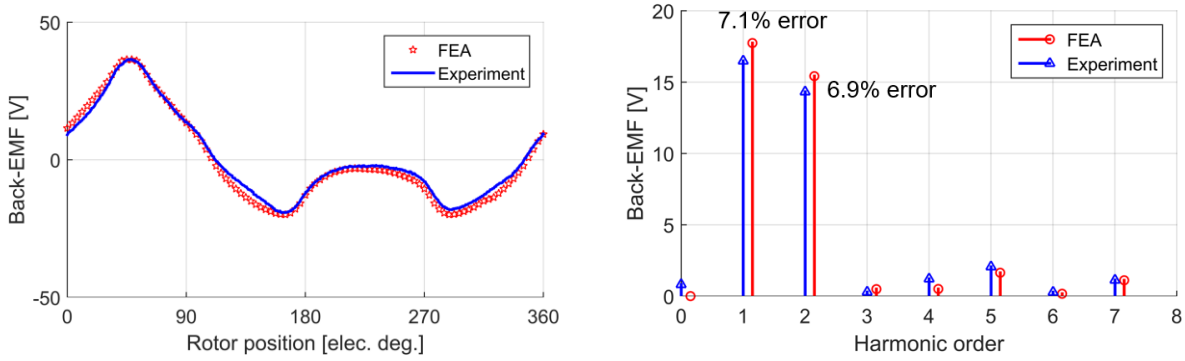

(a) (b)

Figure 8.11. Experiment and FEA result comparison of back-EMF in front stator phase winding (a) waveform and (b) harmonic components.

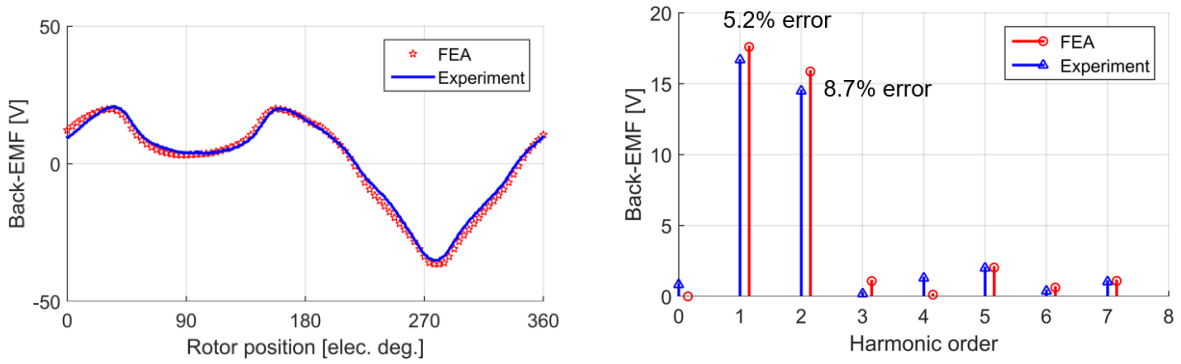

(a) (b)

Figure 8.12. Experiment and FEA result comparison of back-EMF in rear stator phase winding (a) waveform and (b) harmonic components.

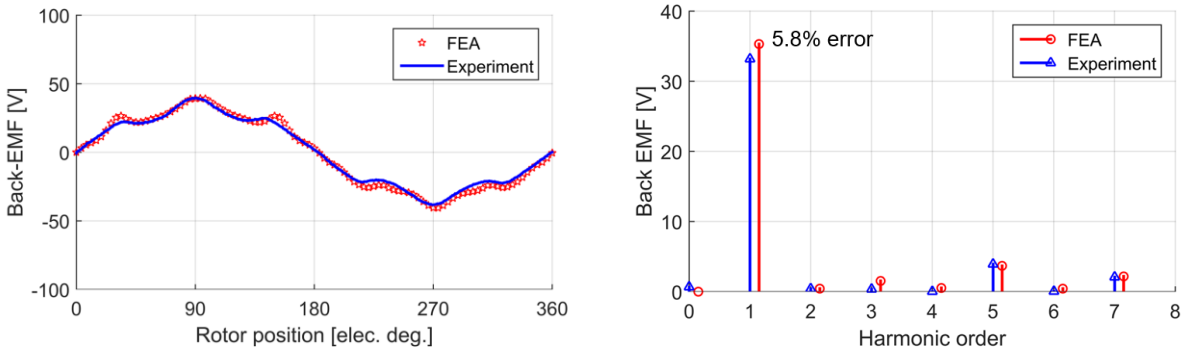

(a) (b)

Figure 8.13. Experiment and FEA result comparison of total phase back-EMF winding at 900 rpm, (a) waveform and (b) harmonic components.

8.2.2 Testing of Torque and Power Production Capability

In the loaded dynamometer test, the dyno SPM machine is given a certain constant speed command while the prototype machine is given different values of current command from no-load condition to full load current around 8 Arms. The output torque at each of the corresponding current condition is recorded. The test is performed at 900 rpm. The resulting torque current relationship from the experiments are compared to the 3D FEA results calculated at 900 rpm in

Figure 8.14. The experimental tested torque has a torque constant of 0.643 Nm/A_{rms}, while the designed machine has a torque constant of 0.701 Nm/A_{rms}. The reason is due to the lower back-EMF tested compared to FEA model. The output power and speed curve is tested under the same current loading of 7.8 A_{rms} as shown in Figure 8.15. Overall, the experimental results show reasonable agreement with the simulation results. Thus, the torque production capability of the designed machine is verified.

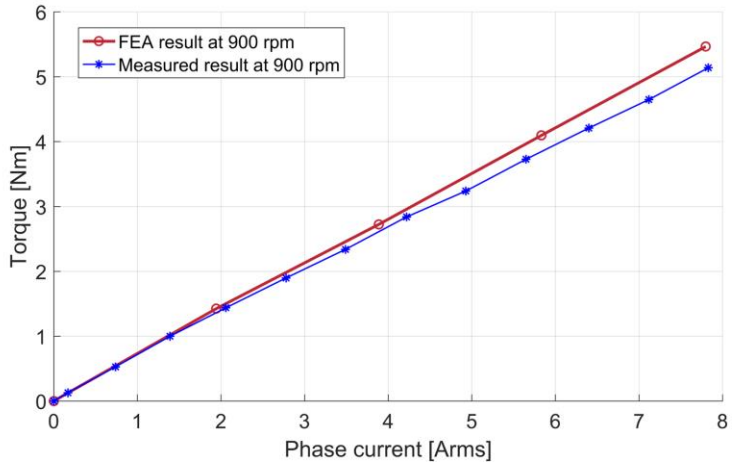

Figure 8.14. Torque current relationship comparison of FEA and experimental results.

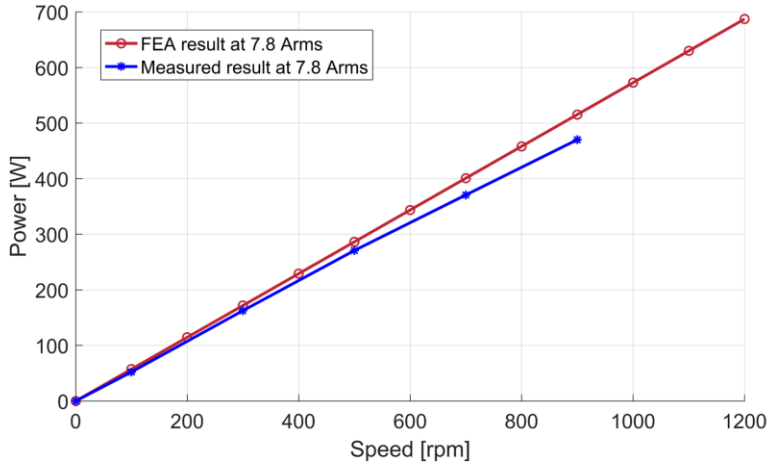

Figure 8.15. Power and speed relationship comparison of FEA and experimental results.

8.2.3 Testing of Various Machine Losses

It should be mentioned that the proof-of-concept prototype machine has several challenges in the manufacturing process. Initially, the designed prototype machine has a 50% copper fill factor with a phase winding resistance of 0.75 Ω. However, due to the difficulty in accommodating the end windings in the axial gap between the two stators, the wire design is selected as two strands with smaller diameters. The actual measured winding resistance per phase is 1 Ω instead, which is equivalent to a copper fill factor of 37%. Therefore, the winding resistance is increased by 35%. This change has an impact on the loss and efficiency measurement. The efficiency of both initial design and the actual prototype machine are compared in this section.

The other challenges in the prototype design is the interference fit issue between the shaft and rotor core. Significant acoustic noise occurred due to the sliding movement between the shaft and the rotor core. Hence, the speed of the test is limited to half the rated speed, which is 900 rpm in the lab for safty reasons. Although the measurement results are limited to 900 rpm, the loss and efficiency of the prototype machine are projected to the original full load and rated speed of 1800 rpm condition for comparison with the initial design.

The designed machine loss and efficiency is shown in TABLE 8.2. Measurement results are shown for 900 rpm and 700 rpm. Based on the output power and current relationship from 900 rpm, it can be projected that current required to produced rated 1500 W output power is 12.4 A_{rms}, which is higher than the designed rated current of 11.2 A_{rms}. Due to the increase in winding resistance of the prototype machine, the copper loss of the prototype machine at rated condition is 477 W compared to 278 W in the initial design. It is assumed that the core loss is calculated from

the 3D FEA results and the same for initial design and prototype machine. Therefore, the calculated efficiency of the designed machine is 83%, while for the prototype machine is projected to be 75%.

TABLE 8.2. COMPARISON OF DESIGNED MACHINE AND PROJECTED PROTOTYPE MACHINE

	Resistance (Ω)	Speed (rpm)	Current (A_{rms})	Copper Loss (W)	Core Loss (W)	Total Loss (W)	Input Power (W)	Output Power (W)	Efficiency	Housing Loss (W)
Designed Machine	0.74 x 3	1800	11.2	278	35*	313	1813	1500	83%	107*
Machine Received	1+1+1.1	1800	12.4**	477**	35*	512	2012	1500	75%	107*
Measured	1+1+1.1	900	7.83	190	16.1*	206	678	472	70%	55.0*
Measured	1+1+1.1	700	7.81	189	11.8*	201	572	371	65%	44.0*

* 3D FEA result

** Extrapolated from measured result

Note: Magnet eddy current loss is small to be neglected

The prototype machine under test has various losses including the copper loss, core loss, and aluminum housing loss. The magnet eddy current loss is very small at the low speed condition and it is neglected in the study. The proof-of-concept prototype FSPM machine has a rectangular-shaped alumimun housing as shown in Figure 8.1. Due to the circumferentially magnetized magnets in the stator parts, the magnetic flux leaks through the alumimum housing and generates eddy current losses in the housing during machine rotation. To better evaluate various kinds of machine losses, the housing loss needs to be estimated. Due to the difficulty in measuring the housing loss in the experiments, 3D FEA is used to calculate the housing losses at various speed and current loading conditions. The magnetic flux density contour plot at rated condition is shown in Figure 8.16. It is observed that the parts of the housing that are close to the permanent magnets

conduct non-negligible magnetic flux. The eddy current loss density contour plot of the housing at rated loading condition is shown in Figure 8.17. The 3D FEA results show that the eddy current loss concentrates on the parts that are close to the permanent magnets and end windings. The magnetic leakage flux that generate eddy current loss from the end winding portion is due to the saturation in the stator back yoke. Reducing the permanent magnet leakage flux and designing the stator yoke less saturated can potentially reduce the eddy current loss in the housing.

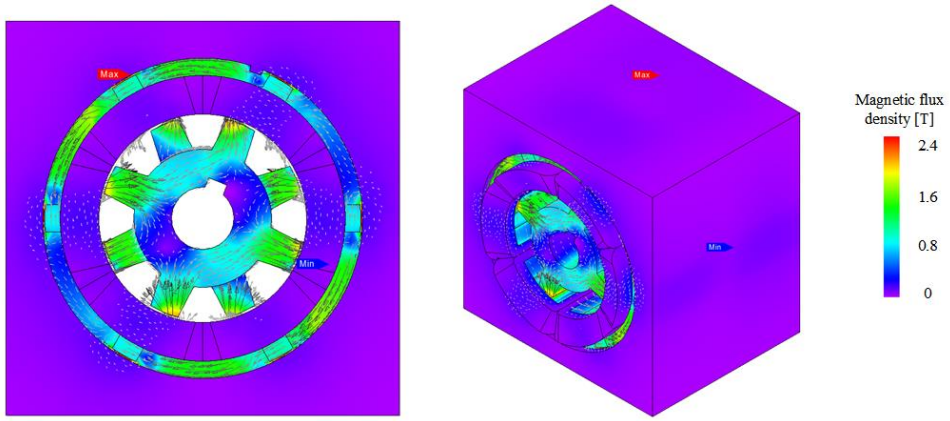

Figure 8.16. Magnetic flux density distribution at rated loading condition of the prototype machine with alumimum housing.

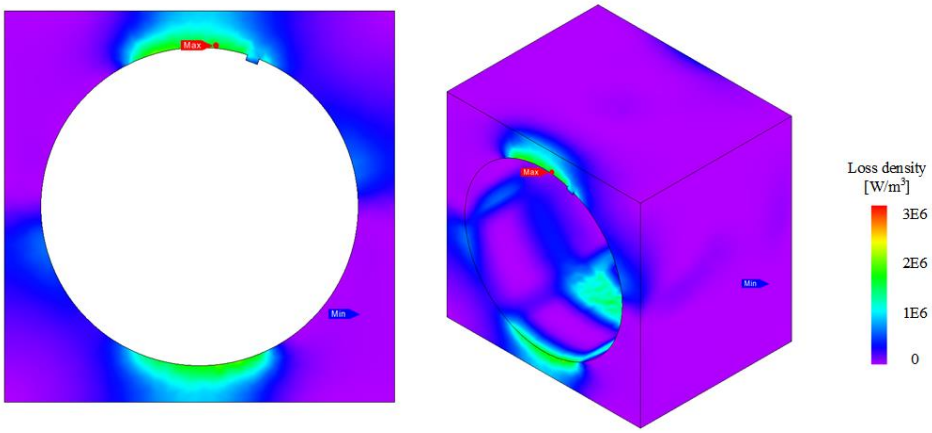

Figure 8.17. Joule loss density distribution at rated loading condition of the prototype machine with alumimum housing.

The eddy current loss in the housing is calculated at various combinations of speeds and stator excitation currents in the 3D FEA program, and the results are shown in TABLE 8.3. It should be mentioned that the housing loss at rated current and 1800 rpm condition is calculated to be 97.8 W, which is a comparatively large number considering the machine has only 1.5 kW. The calculated eddy current loss results are interpolated for other current and speed conditions, which are used in the the loss distribution test later.

TABLE 8.3. EDDY CURRENT LOSS [W] IN ALUMIMUM HOUSING CALCULATED BY 3D FEA AT VARIOUS SPEED AND CURRENT CONDITIONS

Current / Speed	0 A_{rms}	1.945 A_{rms}	3.89 A_{rms}	5.834 A_{rms}	7.778 A_{rms}
100 rpm	7.6	7.7	7.9	8.1	8.5
300 rpm	18.8	19.1	19.5	20.1	20.9
500 rpm	29.5	29.9	30.6	31.6	32.8
700 rpm	39.7	40.3	41.2	42.4	44.1
900 rpm	49.4	50.1	51.2	52.7	54.7
1800 rpm	88.5	89.7	91.6	94.3	97.8

To calculate the copper loss of the machine, the resistance of each phase is measured first. The phase resistance of the complete machine is measured at room temperature using a multimeter, and the results are in TABLE 8.4. The inductances in L_q and L_d of the prototype machine are shown in TABLE 8.5.

TABLE 8.4. MEASURED PHASE RESISTANCE OF THE PROTOTYPE MACHINE AT 20 DEGC

	Phase A	Phase B	Phase C
Resistance [Ω]	1.0	1.0	1.1

TABLE 8.5. L_Q AND L_D INDUCTANCES OF THE PROTOTYPE MACHINE

	L_q	L_d
Inductance [mH]	3.9	4.3
Per Unit	0.348	0.383

The next experiment is the loading test at various speed and current conditions. The output power and average torque of the prototype machine at each of the operating points are measured and recorded. The test is performed at 300 rpm, 500 rpm, 700 rpm and 900 rpm. In this test, the Kinetix 5500 drive is used to provide speed command to the dyno SPM machine, while the Ultra3000 drive is used to provide current command (equivalent to torque command) to the prototype FSPM machine. The currents from both the dyno SPM and the prototype FSPM machines are measured. The input power to the prototype FSPM machine is measured from an oscilloscope. The copper loss is calculated by the phase resistance and the machine current at the 20 Degree C condition, and the high frequency AC effects are not considered. The iron loss of the machine and the eddy current loss of the aluminum housing are estimated by the 3D FEA studies. The efficiency of the machine at the particular operating point is calculated by the output power over the summation of output power plus the copper and iron loss. The housing loss is not considered in the efficiency calculation. The current, torque, power, and various losses at each of the the measured speeds and loading conditions are recorded in TABLE 8.6.

TABLE 8.6. MEASURED AND PREDICTED LOADING TEST RESULTS FOR THE CURRENT, TORQUE, POWER, AND VARIOUS LOSSES AT 300 RPM, 500 RPM, 700 RPM, AND 900 RPM CONDITIONS

300 rpm												
Measured Results												
Current Prototype [Arms]	0	0.7	1.34	2	2.68	3.38	4.08	4.76	5.46	6.17	6.87	7.56
Torque [Nm]	0	0.43	0.9	1.41	1.94	2.43	2.9	3.41	3.89	4.41	4.89	5.36
Output Power [W]	0	13.5	28.4	44.4	61.1	76.3	91.2	107.2	122.5	138.8	153.7	168.6
Input Power [W]	0	32.4	53.4	74.4	98.4	128.4	161.4	185.4	233.4	266.4	317.4	362.4
Evaluated Results												
Copper loss at 20 DegC [W]	0	1.5	5.6	12.4	22.3	35.4	51.6	70.2	92.4	118	146.3	177.2
Iron loss [W]	4.36	4.36	4.37	4.37	4.37	4.38	4.38	4.38	4.39	4.39	4.4	4.41
Housing loss [W]	18.8	18.9	19	19.1	19.2	19.4	19.5	19.8	20	20.2	20.5	20.8
Efficiency	0%	70%	74%	73%	70%	66%	62%	59%	56%	53%	50%	48%

500 rpm												
Measured Results												
Current Prototype [Arms]	0	0.71	1.37	2.05	2.76	3.45	4.2	4.89	5.61	6.33	7.04	7.74
Torque [Nm]	0	0.43	0.91	1.39	1.83	2.32	2.78	3.28	3.75	4.25	4.74	5.21
Output Power [W]	0	22.5	47.4	72.8	95.9	121.3	145.6	171.6	196.4	222.5	247.9	272.7
Input Power [W]	0	57.8	87.8	123.8	162.8	204.8	243.8	288.8	351.8	399.8	456.8	519.8
Evaluated Results												
Copper loss at 20 DegC [W]	0	1.6	5.8	13	23.6	36.9	54.7	74.1	97.6	124.2	153.6	185.7
Iron loss [W]	7.73	7.73	7.74	7.74	7.74	7.75	7.75	7.77	7.78	7.79	7.8	7.82
Housing loss [W]	29.6	29.7	29.8	30	30.2	30.5	30.8	31.1	31.4	31.9	32.3	32.8
Efficiency	0%	71%	78%	78%	75%	73%	70%	68%	65%	63%	61%	58%

700 rpm												
Measured Results												
Current Prototype [Arms]	0	0.73	1.38	2.07	2.78	3.48	4.21	4.90	5.67	6.37	7.10	7.81
Torque [Nm]	0	0.44	0.91	1.37	1.84	2.27	2.79	3.21	3.7	4.14	4.6	5.06
Output Power [W]	0	32.3	67.1	100.3	135.0	166.5	204.6	235.3	271.7	304	337.1	371.1
Input Power [W]	0	84.6	126.6	171.6	219.6	273.6	324.6	381.6	450.6	522.6	591.6	663.6
Evaluated Results												
Copper loss at 20 DegC [W]	0	1.6	5.9	13.3	24.0	37.5	54.9	74.4	99.7	125.8	156.3	189.1
Iron loss [W]	11.66	11.67	11.67	11.68	11.69	11.70	11.71	11.72	11.74	11.76	11.79	11.82
Housing loss [W]	39.8	39.9	40.1	40.3	40.7	41.0	41.4	41.8	42.3	42.9	43.5	44.0
Efficiency	0	71%	79%	80%	79%	77%	75%	73%	71%	69%	67%	65%

900 rpm												
Measured Results												
Current Prototype [Arms]	0	0.74	1.39	2.06	2.78	3.49	4.22	4.93	5.65	6.40	7.12	7.83
Torque [Nm]	0	0.4	0.87	1.32	1.78	2.22	2.72	3.11	3.61	4.08	4.52	5.01
Output Power [W]	0	37.3	82	123.6	167.2	208.7	255.6	292.9	339.7	384.4	426	471.8
Input Power [W]	0	109.8	160.8	217.8	277.8	343.8	412.8	481.8	553.8	634.8	718.8	802.8
Evaluated Results												
Copper loss at 20 DegC [W]	0	1.7	6.0	13.2	24.0	37.8	55.2	75.3	99.0	127.0	157.2	190.1
Iron loss [W]	15.87	15.88	15.88	15.89	15.91	15.93	15.95	15.98	16.00	16.03	16.05	16.08
Housing loss [W]	49.5	49.7	49.9	50.2	50.6	51.0	51.5	52.0	52.6	53.3	54.1	55.0
Efficiency	0	68%	79%	81%	81%	80%	78%	76%	75%	73%	71%	70%

To better understand the difference between the predicted losses and the measured losses, the loss distribution results at each of the speed condition are visualized in Figure 8.18, Figure 8.19, Figure 8.20, and Figure 8.21. The rms current of the machine is plotted in the horizontal axis, while the loss is plotted in the vertical axis. The predicted losses of the prototype are the summation of the copper loss, iron loss, and the housing loss. The measured loss is from the calculation of input power minus the output power.

When the operating speed of the prototype is 300 rpm or 500 rpm, the total predicted losses are higher than the measured losses at all tested the current conditions. When the operating speed of the prototype is at 700 rpm and 900 rpm, the measured losses are smaller than the predicted total losses at low current conditions, but are larger than the predicted total losses at high current conditions. The reason why the measured losses are increasingly higher than the predicted losses is that the prototype machine becomes much more saturated at hign loading conditions. Thus, there are more parasitic losses in the prototype system that are not modeled in the FEA program. Overall, the measured losses demonstrate reasonably good agreement with the predicted losses.

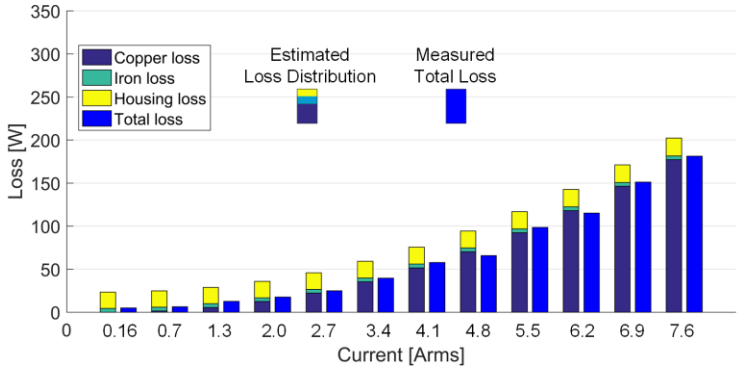

Figure 8.18. Comparison of predicted loss distribution and measured total loss of the prototype machine at 300 rpm.

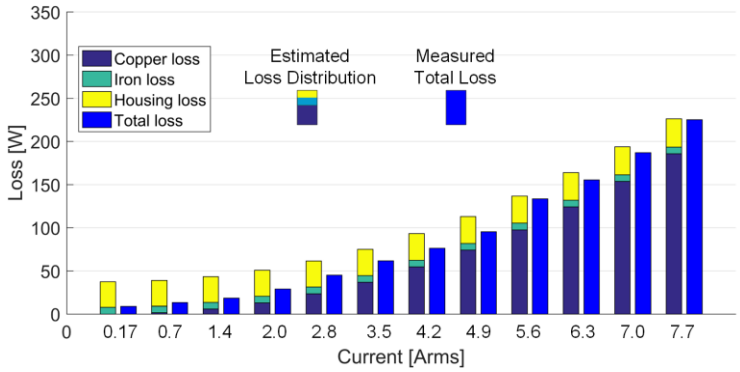

Figure 8.19. Comparison of predicted loss distribution and measured total loss of the prototype machine at 500 rpm.

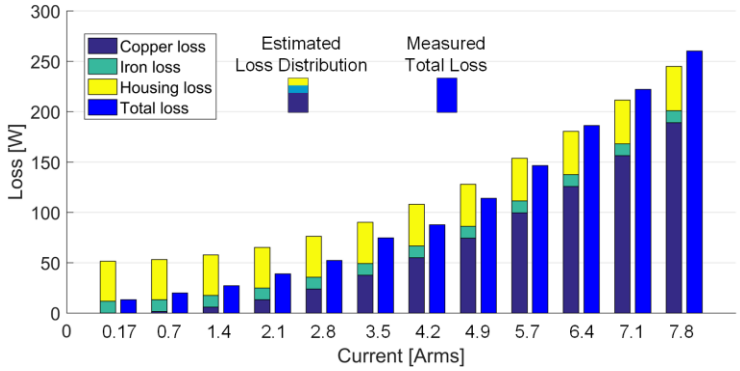

Figure 8.20. Comparison of predicted loss distribution and measured total loss of the prototype machine at 700 rpm.

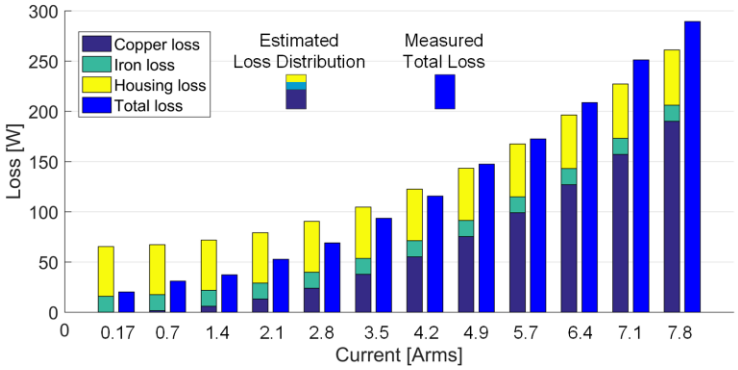

Figure 8.21. Comparison of predicted loss distribution and measured total loss of the prototype machine at 900 rpm.

The fabrication and test of the proof-of-concept prototype machine offers design insights of the proposed dual-stator 6/4 FSPM machine. The observations are summarized here. The copper loss the prototype machine accounts for a large percentage of the total loss due to the large phase resistance in the dual winding design. To reduce the copper loss and the phase resistance, the alternative topology with single winding coil that wraps around two stators needs to be used. The housing eddy current loss is also a non-negligible part of the total loss. To reduce the housing eddy current loss, designs with less magnetic flux leakage need to be considered. In addition, the end winding leakage flux also contributes to eddy current loss in the housing which needs to be carefully managed during design process.

8.3 Design Experiences Learned from the Prototype

There are design experiences learned from manufacturing of this proof-of-concept prototype which can be summaried as the follows. The copper loss accounts for most the total loss due to the excessive winding resistance of the machine.

- The topology with separate windings in each stator produces additional end windings that increase the total resistance. To reduce the winding resistance, the alternative topology where single coil wraps around two stators needs to be used.
- Although the proposed dual-stator 6/4 flux-switching PM machine has concentrated winding, the copper fill factor should be designed conservatively with margins. Therefore, the copper fill factor is assumed to be 35% to 40% for normal manufacturing capability.
- The proof-of-concept prototype machine uses iron bridges to connect the highly segmented stator pieces. However, this method increases magnetic flux leakage in the outside aluminum housing and reduces the torque production capability. To increase the torque production capability, a ring frame can be used instead of the iron bridge to connect the stator pieces together.
- The circumferentially magnetized permanent magnets produce circumferential flux leakage in the aluminum housing and generates eddy current loss in the housing. To reduce the aluminum housing loss and increase the efficiency, the magnetic leakage flux needs to be reduced. One technique is to cut the outer and inner circumferences of the permanent magnets to reduce the leakage flux by creating air gaps in these regions. In addition, this technique also helps to reduce the magnet eddy current loss as the loss concentrates on the two ends of the permanent magnets.

8.4 Summary

This chapter presents the design, fabrication, and experimental test of the proof-of-concept prototype dual-stator 6/4 FSPM machine. The detailed design for each of the component and the

whole machine setup are discussed. Experimental dynamometer test stand is demonstrated. The prototype machine is tested under open circuit condition first. Flux linkages in each individual stator windings are calculated based on the measured terminal voltages, and the harmonic components comparison show good agreement with FEA results. The measured total phase back-EMF is close to the sinusoidal waveform as predicted by the FEA simulation. The prototype machine is also tested under loaded condition. The average torque and phase current relationship is close to the FEA results. Dynamometer test is done for various speeds and current loading conditions, and various losses are segregated. The measured total loss matches with the predicted total loss within reasonable range of accuracy. The validity of the dual-stator 6/4 FSPM machine design is verified.

Chapter 9

Conclusions, Contributions, and Future Work

9.1 Conclusions

The following subsections summarize the main conclusions of this thesis. This research study identified the viable low-pole FSPM machine topologies and proposed a novel dual-stator 6/4 FSPM machine concept. The design and operation principles of the proposed novel machine are investigated. Performance comparison of dual-stator 6/4 FSPM machine is compared with the conventional 6/4 FSPM machine and the 12/10 FSPM machine. Analysis and optimization are performed for various designs at different power and speed ratings. The principle of scalability is discussed and proven by the sizing equation. Mechanical tolerance analysis is performed to understand three major rotor tolerance deviation to the machine performance. Structural dynamic analysis including rotor dynamics at medium and high-speed conditions and rotor mechanical stress are studied to ensure that the designed medium-speed machine operates within safe regions. A prototype machine is fabricated and tested to validate the expected performances.

9.1.1 Low-Pole FSPM Machine Topologies

- There are limited number of viable stator slot/rotor pole combinations of flux-switching machines. The topologies with 6 stator slots and 5 or 7 rotor poles have unbalanced magnetic forces that are detrimental to the life of bearings and are not desirable for high-speed operations. The lowest possible three phase topology of flux-switching machine is with 6 stator slots and 4 rotor poles. The conventional single-stator-single-rotor form of the 6/4 FSPM machine is not feasible to use due to the unacceptably large harmonic distortions in the flux linkage and back-EMF.
- The large harmonic distortion in the flux linkage and back-EMF of conventional 6/4 FSPM machine is caused by the 2^{nd} order harmonic content. The harmonics that are higher than 2^{nd} order are small enough compared to the 2^{nd} harmonic that they can be neglected. The presence of such 2^{nd} harmonic is due to the asymmetrical airgap harmonic permeance variation, and the lack of corresponding coils to compensate the even harmonics, as is the case for some high-pole FSPM machines.
- The proposed dual-stator 6/4 FSPM machine can eliminate all the even harmonics of flux linkage in the phase winding and notably reduce the harmonic distortion in the back-EMF. The reason is that the coils in the other introduced stator provide flux linkage that changes all the phases of even order harmonics by 180˚ electrically. The whole machine has nearly sinusoidal total flux linkage and performs like a normal FSPM machine.
- There are multiple alternative configurations of the dual-stator 6/4 FSPM machine that all achieve the same even harmonic cancellation property. One of the topologies is with

offset rotor poles, opposite magnet directions, and single winding that wraps around two stators (Topology-I). The other topology is with offset rotor poles, separated windings with opposite directions that warp two stators individually (Topology-II). The last one is with non-offset rotor poles, but the rear portion of the stator is rotated by 45˚ mechanically (Topology-III).

- The topology with offset rotor poles and opposite magnet direction (Topology-I) has the least amount of material consumption and most compact structure. The topology with offset rotor poles and opposite winding direction (Topology-II) has the highest torque density and modular design advantage, but with increased total weight and volume due to a larger separation distance between two stators. The topology with non-offset rotor poles and rotated rear stators (Topology-III) has the conventional rotor design and modular stator design, but with highest material consumption and weight.

9.1.2 Design and Operation Principle of Dual-Stator 6/4 FSPM Machine

- The winding MMF harmonics of the dual-stator 6/4 FSPM machine have odd orders. The lowest winding MMF harmonic is the 1st order component, which means that the MMF have a one pole-pair pattern. There are positively and negatively rotating winding MMF harmonics as identified by the analytical equations.
- The proposed dual-stator 6/4 FSPM machine operates based on the principle of flux modulation by the magnet MMF harmonics and the airgap permeance harmonics. When both stator and rotor sides of the permeances are considered, the airgap flux

density components can be categorized into three types, which are the stationary components, rotational components, and modulational components.

- The proposed dual-stator 6/4 FSPM machine has multiple coupled harmonics to produce non-zero average torque. The harmonic components of winding MMF have the same harmonic order, rotational speed, rotational direction, and the phases are always orthogonal to the corresponding harmonic orders in the airgap flux density harmonic orders. Positive torque is produced by the positively rotating coupled harmonics, and the negative torque is produced by the negatively rotating coupled harmonics.
- The proposed dual-stator 6/4 FSPM machine can be designed for traction motor with a characteristic current that is close to the rated current to achieve nearly optimal flux weakening condition. The low fundamental frequency requirement in this machine is beneficial in reducing the high-frequency losses including the iron loss, magnet eddy current loss. High efficiency is retained at the constant power operating trajectory.
- The sizing equation of the proposed dual-stator 6/4 FSPM machine demonstrates that the output torque of the machine can be increased by reducing the 2^{nd} order harmonic content, reducing the leakage flux, and increasing the magnetic and electrical loading.
- The proposed dual-stator 6/4 FSPM machine can be scaled to various power and speed ratings with reasonably good accuracy by using the proposed sizing equations. For first principle design and validation of the proposed machine, the key dimensions of airgap diameter and the axial length of the machine can be predicted by using the sizing equation.

9.1.3 Parametric Analysis and Optimization of the Dual-Stator 6/4 FSPM Machine

- There are several key dimensional parameters that influence the overall performance of the dual-stator 6/4 FSPM machine, and those parameters are the split ratio, the width of the stator teeth, the width of the magnet, and the width of the rotor poles. The split ratio is responsible for splitting the electrical and magnetic loading of a machine design. The widths of the stator teeth, magnet, and rotor poles affect the airgap flux modulation effects of the machine.
- The study shows that wider total width of stator teeth and magnet thickness is beneficial to increased output torque. Generally, the width of stator teeth is larger than the magnet thickness when rare earth magnets are used.
- Rotor pole width has a big influence on both the average torque and the cogging torque. Wider rotor pole width generally enables more produced average torque, but the torque ripple can be also increased if the rotor pole width is too large. The design of rotor pole width should be optimized with the design of stator teeth width and magnet thickness.
- The torque density profiles from parametric studies show that torque density is a function of applied current density. The higher the current density in the windings, the larger torque density the machine can produce. However, the torque density and current density relationship is not linear, and the non-linearity is mainly attributed to the saturation in the steel at high current loading conditions.
- Design objectives of maximizing average torque and minimizing torque ripple are conflicting requirements of the dual-stator 6/4 FSPM machine. The 3D structure of the

dual-stator machine further complicates the problem. The generalized method is to use 2D FEA optimization study to optimize the single stator structure, and use 3D FEA study to validate the designs.

- The torque ripple of the dual-stator 6/4 FSPM machine is not negligible. To reduce the torque ripple effectively, the methods of stator tooth and rotor pole shaping technique is implemented. The rotor two step skew is also demonstrated to be practical in reducing the torque ripple while maintaining a sufficiently large average torque. Rotor four step skew reduces the torque ripple slightly better than two step skew design, but with the tradeoff of significantly increased manufacturing complexity.

9.1.4 Comparison of Proposed Machine with Conventional 6/4 FSPM and 12/10 FSPM Machines

- The dual-stator 6/4 FSPM machine achieves about 30% reduction of THD in the flux linkage, 55% reduction in the back-EMF, and 76% reduction of cogging torque compared to the conventional 6/4 FSPM machine. The introduction of dual-stator structure only increases the total weight by about 11.5% compared with the conventional structure, the output average torque is increased by 12.1%. The torque density is slightly increased than the conventional 6/4 FSPM machine.
- The dual-stator 6/4 FSPM machine requires only 40% of the fundamental frequency as that of the 12/10 FSPM machine at same operating speed. If the operating speed is 15,000 rpm, the fundamental frequency for the 12/10 FSPM machine is 2.5 kHz, while for the dual-stator 6/4 FSPM machine is only 1 kHz.

- The stator and rotor part of the FSPM machine has different iron fundamental eddy current loss frequencies. The fundamental eddy current loss frequency for stator iron is proportional to the number of rotor poles, while for rotor iron is proportional to the half number of stator slots. Thus, for the same 15,000 rpm speed condition, the 12/10 FSPM machine has 2.5 kHz and 1.5 kHz fundamental eddy current loss frequencies in the stator and rotor laminations, and the dual-stator 6/4 FSPM machine has 1 kHz and 0.75 kHz for stator and rotor laminations respectively.
- For high-speed designs, the dual-stator 6/4 FSPM machine achieves higher efficiency than the 12/10 FSPM machine due to the reduction of high-frequency associated losses. The iron loss and magnet eddy current loss in the dual-stator 6/4 FSPM machine is much lower than that in the 12/10 FSPM machine. The dual-stator 6/4 FSPM machine has less windage loss than 12/10 FSPM machine. The copper loss of dual-stator 6/4 FSPM machine could be higher than 12/10 FSPM machine, but the copper loss is small compared with the dominant iron loss at high-speed conditions.
- Compared with the 12/10 FSPM machine, the dual-stator 6/4 FSPM machine is suitable for applications where the high-speed and high-efficiency operation is required. The required inverter switching frequency is also reduced so that the inverter can operate at higher efficiency due to the reduction of switching losses.

9.1.5 Mechanical Tolerance and Structural Dynamics Analysis

- Maintaining tight mechanical tolerances in key parts of the proposed dual-stator 6/4 FSPM machine is crucial in achieving the expected performance. For the proposed

machine, the variation of rotor mechanical tolerances directly impact the uniformity of the airgap region, thus influence the machine performance.

- The ideal rotor pole offset angle between the front and rear portions is 45˚ mechanically, and deviation from this optimal condition results in reduced average torque, increased torque ripple, and significantly increased the harmonic distortion. However, the offset angle deviation condition does not introduce rotor unbalanced magnetic force.
- The rotor static and dynamic eccentricities occur when the rotor is not in perfect concentric condition with the stator inner diameter circle. Both eccentricity scenarios degrade the torque performance by reducing the average torque and increasing the torque ripple. The rotor unbalanced magnetic forces are also induced in either of the eccentricity cases. However, the rotor static and dynamic eccentricities have negligible effect in increasing the harmonic distortions in the back-EMF.
- Rotor dynamic vibrations are a critical part in high-speed machine design. Due to the high rotational speed nature, high-speed dual-stator 6/4 FSPM machine can potentially operate into regions that contain critical speeds. To increase the low-order natural frequencies and increase the low order critical speeds, a higher value of bearing stiffness to rotor and shaft stiffness is preferred.
- Typical vibrational modes can be categorized into the cylindrical mode and conical mode. These two modes occur in pairs with forward and backward whirl properties. The forward whirl has gyroscopic effect that tends to increase the stiffness of the

system and increase the natural frequencies, while the backward whirl has the reversed effect.

- The von Mises stress considers complex multi-axis stress on the subject, and it is typically used as a criterion in structural analysis to determine material failure property. The maximum von Mises stress of the proposed offset-pole rotor occurs in the bottom of rotor poles. The middle portion of the rotor experiences non-negligible stress due to torsional stress and radial stress, but they are significantly lower than the maximum stress and material tensile stress limit.

9.2 Contributions

The primary contributions of this research are summarized below.

9.2.1 Proposed Dual-Stator 6/4 FSPM Machines

- **Analyzed the viable low-pole topologies of flux-switching machines**

  This research presents the viable stator slot/rotor pole combinations of flux-switching machines to show that the topologies with six stator slots have unbalanced back-EMF (for 6/4 and 6/8) and unbalanced magnetic forces (6/5 and 6/7). The reason for having a large harmonic distortion in the flux linkage of 6/4 FSPM machine is identified because of the 2^{nd} order harmonic and some higher order even harmonics. The mechanism of producing the 2^{nd} order harmonic is explained by airgap permeance variations.

- **Proposed a novel concept of flux-coupling dual-stator 6/4 FSPM machine**

  A novel concept of dual-stator 6/4 FSPM machine is proposed to eliminate the even harmonics in the flux linkage to make the 6/4 FSPM machine topology feasible to use. The resultant back-EMF of the proposed dual-stator 6/4 FSPM machine is balanced and close to sinusoidal waveforms.

- **Proposed three alternative dual-stator 6/4 FSPM machines, and generalized the structure features of possible topology variations**

  Three alternative topologies of the dual-stator 6/4 FSPM machines that achieve the same even harmonic elimination effect are proposed for completeness. The structural differences between each of the alternative topologies are explained. The performances including flux linkage, back-EMF, cogging torque, weight distribution, and torque density of the three alternative topologies are compared. The manufacturing simplicities of each topology is also discussed.

9.2.2 Operation Principle and Characterization of Dual-Stator 6/4 FSPM Machine

- **Analyzed the even order harmonic elimination scheme in the proposed machine**

  This research explains the reasons for even order harmonic elimination in the proposed dual-stator 6/4 FSPM machine by harmonic decomposition of the flux linkage in each of the stator windings. It is discovered that the phase angles of all the even harmonics in the second stator winding are exactly opposite to the first stator winding, so the total phase winding does not have the even harmonics when two stator windings are connected in series.

- **Investigated the operating principle and torque production of proposed machine by harmonic analysis**

  This research presents the operating principles of the dual-stator 6/4 FSPM machine by harmonic analysis of the winding MMF and airgap flux density. The Fourier analysis is performed for winding MMF, magnet MMF, and stator and rotor side permeances. The flux modulation effect of the machine is studied in detail. The complex airgap flux density harmonic components are analytically derived to show that there are stationary and rotational harmonics. It is explained that the non-zero average torque production of the proposed dual-stator 6/4 FSPM machine is due to the multiple harmonic coupling effects, which means that multiple winding MMF harmonics are coupled with the corresponding airgap flux density harmonics to produce torque.

- **Developed the sizing equations for the proposed dual-stator 6/4 FSPM machine**

  This work mathematically derives the sizing equations of the dual-stator 6/4 FSPM machine based on the generalized sizing equations for electric machines. The key parameters in the sizing equations are discussed, and ways to increasing the torque density is discussed such as to reduce the 2^{nd} order harmonic contents, reduce the leakage flux, and to improve the magnetic and electrical loadings.

- **Characterized the performance of a proof-of-concept 6/4 FSPM machine**

  A dual-stator 6/4 FSPM machine with a relatively low power and low speed for lab testing is designed and analyzed by FEA studies. The basic electromagnetic properties including flux linkage, back-EMF, inductance, rotor forces, and magnet operating

points are evaluated at both open circuit and loaded conditions. The loss distribution and efficiency are also characterized by FEA simulation.

- **Designed a dual-stator 6/4 FSPM machine for traction application**

  The proposed dual-stator 6/4 FSPM machine is designed for traction application with a wide constant power speed range. The characteristic current can be designed close to the rated current. High efficiency across the constant power speed range is demonstrated due to the reduction of high-frequency losses in this low-pole machine.

- **Investigated the principle of scalability of the proposed dual-stator 6/4 FSPM machine**

  The proposed dual-stator 6/4 FSPM machine can be scaled to various power and speed ratings. Key dimensions of the machine can be calculated by the proposed sizing equations with reasonable accuracy. Four different designs are compared to verify that the sizing equation holds true for each of the cases.

9.2.3 Performance Optimization and Comparison of Proposed Machine with Conventional 6/4 FSPM and 12/10 FSPM Machines

- **Investigated the performance comparison between conventional 6/4 FSPM machine and dual-stator 6/4 FSPM machine**

  The dual-stator 6/4 FSPM machine is compared with the conventional 6/4 FSPM machine for performances including THD reduction in flux linkage, back-EMF, cogging torque, and torque ripple. The mass distribution and torque density of two machines are also evaluated to show that the proposed dual-stator 6/4 FSPM machine

achieves slightly higher torque density than conventional 6/4 FSPM machine, and the harmonic distortion is notably reduced.

- **Implemented the parametric analysis and optimization of the dual-stator 6/4 and 12/10 FSPM machines**

  The key parameters in the design of dual-stator 6/4 and 12/10 FSPM machines are identified which are the split ratio, the width of flux modulation components including stator teeth, magnet thickness, and rotor poles. Parametric analysis is done to evaluate the variation of each of the parameters to the performance of the machines. Optimization by finite element analysis is also investigated for both dual-stator 6/4 and 12/10 FSPM machine to maximize average torque and minimizing torque ripple.

- **Evaluated the torque density of dual-stator 6/4 and 12/10 FSPM machines**

  The torque density profiles of both dual-stator 6/4 and 12/10 FSPM machines are characterized and compared. The study shows that the torque density profile is a function of current density in the windings. The study also presents that for a specific current density, the design with maximum torque density is related to the optimal split ratio. The torque profiles for the two machines are compared and results show 12/10 FSPM machine has higher torque density.

- **Investigated the loss and efficiency comparison of dual-stator 6/4 and 12/10 FSPM machines**

  Both the proposed dual-stator 6/4 FSPM and 12/10 FSPM machines are designed for the same relatively high power and high speed operating condition for performance comparison. The optimized two machines are designed with almost same current

density. Comprehensive comparison studies are shown for the mass distribution, torque density, loss distribution, and efficiency. The design benefits of reduced high-frequency associated losses, high efficiency of the dual-stator 6/4 FSPM machine are highlighted.

- **Investigated the torque ripple minimization technique by stator tooth rotor pole shaping and rotor step skew**

  The stator tooth and rotor pole shaping technique are effective in modifying the airgap permeance distribution and reducing the torque ripple. The appropriate shaping geometry is determined by optimization. Rotor step skew is also an effective technique to reduce the torque ripple while maintaining a large average torque. Two-step skew design is investigated and the optimal skew angle is found versus the more complicated four-step skew design.

9.2.4 Mechanical Tolerance and Structural Dynamics Studies

- **Investigated mechanical tolerance deviation scenarios of rotor offset angle deviation, rotor static and dynamic eccentricities to the machine performance**

  It is demonstrated that the mechanical tolerance deviation in the airgap region leads to performance degradation. Three common rotor mechanical tolerance deviations are investigated to show the impact to averaget torque, torque ripple, back-EMF harmonic distortion, and rotor unbalanced magnetic forces.

- **Investigated rotor dynamics property including natural frequency and vibration modes of the proposed dual-stator 6/4 FSPM machine**

The natural frequencies of the designed high-speed dual-stator 6/4 FSPM machine are characterized for a wide speed range. The critical speeds corresponding to each of the natural frequencies are estimated. The distinct vibrational modes at each natural frequency are demonstrated to show the mode shape and whirl properties.

- **Investigated the rotor stress property of the proposed dual-stator 6/4 FSPM machine**

  The rotor magnetic forces and the generated mechanical stress are estimated by 3D structural analysis for the designed high-speed dual-stator 6/4 FSPM machine. Von Mises stress distribution is calculated for the rated loading condition to show that the machine is within safe operation range of the material strength limit.

9.2.5 Experimental Study of the Prototype Machine

- **Designed and fabricated a proof-of-concept prototype machine**

  The proof-of-concept dual-stator 6/4 FSPM machine is designed, fabricated, and assembled for experimental study. The prototype machine is designed with open housing structure, and all the terminals from two stators can be accessed for tests.

- **Developed the dynamometer test setup for the prototype machine**

  The dynamometer test setup is built. The terminals for the prototype machine is enclosed in a terminal box, and the windings in the two machines and be connected or disconnected for various test purposes. The inverters for both the dyno machine and the prototype machine are configured to provide speed and torque control.

- **Experimentally validated the back-EMF and torque production capability of the prototype**

  The proof-of-concept prototype machine is tested under open circuit condition to measure the phase winding back-EMF. Then, the prototype machine is loaded to test the torque and current relationship. Both results from open circuit test and loaded test show reasonably good agreements with the finite element analysis results. The experiments verified the validity of the proposed concept and the design.

- **Experimentally validated various losses distribution of the prototype machine**

  The predicted losses including copper loss, iron loss, and housing loss are compared with the measured total loss. The comparison results show reasonably good agreement with the predicted results.

9.3 Future Work

The future work proposed by the author for this research program is summarized below.

- **Investigate the thermal aspects including the advanced cooling technique of the dual-stator 6/4 FSPM machine**

  The design of advanced cooling technique is important for high torque density designs with aggressive current loading requirements. Cooling techniques including water jacket housing, direct winding cooling, or other advanced cooling methods can be investigated to increase the thermal performance of the machine.

- **Investigate the acoustic noise of the dual-stator 6/4 FSPM machine**

  The force distribution and vibrational property of the stator of the proposed machine lead to acoustic noise. The investigation of acoustic noise reduction of the proposed machine is crucial in applications that require low noise emission.

- **Investigate the multi-physics co-optimization including electromagnetic, thermal, and structural domains of the dual-stator 6/4 FSPM machine**

  The multi-physics co-optimization of the proposed machine is a further step in ensuring that the performance of the proposed machine satisfies the safety and performance requirements in electromagnetic, thermal, and structural domain simultaneously. This multi-physics approach is necessary for demanding applications.

- **Investigate the performance comparison of proposed dual-stator 6/4 FSPM machine with baseline low-pole surface permanent magnet machines for high-speed conditions**

  The performance comparison of the proposed dual-stator 6/4 FSPM machine with a baseline low-pole SPM machine is meaningful in understanding the benefits of the proposed FSPM machine system. The comparison can be focused on aspects including magnet thermal regulation, torque density, operating cycle total loss, and total cost, etc.

- **Investigate the system performance optimization of dual-stator 6/4 FSPM machine driven by SiC-based inverter**

  The design of high-speed dual-stator 6/4 FSPM machine and SiC-based inverter system have opportunities to optimize the overall performance on a system level. System

optimization favors either the machine design or inverter design brings its opportunities and challenges that need to be identified.

- **Investigate the fault-tolerant capability of the dual-stator 6/4 FSPM machine**

  Fault-tolerant operation capability is an essential part of the machine design in applications where high reliability and low failure tolerance are demanded. There are opportunities to investigate fault mode and techniques to increase the fault-tolerant capability of the proposed dual-stator 6/4 FSPM machine.

Bibliography

[1] Z. Q. Zhu and D. Howe, "Electrical machines and drives for electric, hybrid and fuel cell vehicles," *Proc. IEEE*, vol. 95, no. 4, pp. 746–765, Apr. 2007.

[2] K. Wang, Z. Q. Zhu, and G. Ombach, "Synthesis of High Performance Fractional-Slot Permanent-Magnet Machines with Coil-Pitch of Two Slot-Pitches," *IEEE Trans. Ener. Conv*., vol. 29, no. 3, pp. 758-770, 2014.

[3] K. T. Chau, C. C. Chan, and C. Liu, "Overview of permanent-magnet brushless drives for electric and hybrid electric vehicles," *IEEE Trans. Ind. Electron.*, vol. 55, no. 6, pp. 2246–2257, Jun. 2008.

[4] P. Reddy, A. EI-Refaie, K. K. Huh, J. Tangudu, and T. Jahns, "Comparison of Interior and Surface PM Machines Equipped with Fractional-Slot Concentrated Windings for Hybrid Traction Applications," *IEEE Trans. Ener. Conv*., vol. 27, no. 3, pp. 593-602, 2014.

[5] D. Ishak, Z. Q. Zhu, and D. Howe, "Comparison of PM brushless motors, having either all teeth or alternate teeth wound," *IEEE Trans. Ener. Conv*., vol. 21, no. 1, pp. 95-103, 2006.

[6] G. Pellegrine, P. Guglielmi, A. Vagati, and F. Villata, "Core Losses and Torque Ripple in IPM Machines- Dedicated Modeling and Design Tradeoff," *IEEE Trans. Ind. Appl*., vol. 46, no. 6, pp. 2381-2391, 2010.

[7] S. Han, T. Jahns, and Z. Q. Zhu, "Design Tradeoffs Between Stator Core Loss and Torque Ripple in IPM Machines," *IEEE Trans. Ind*. Appl., vol. 46, no. 1, pp. 187-195, 2010.

[8] S. Galioto, P. Reddy, and A. EI-Refaie, "Effect of Magnet Types on Performance of High-Speed Spoke Interior-Permanent-Magnet Machines Designed for Traction Applications," *IEEE Trans. Ind. Appl*., vol. 51, no. 3, pp. 2148-2160, 2015.

[9] P. Reddy, A. EI-Refaie, K. Hun, "Effect of Number of Layers on Performance of Fractional-Slot Concentrated-Windings Interior Permanent Magnet Machines," *IEEE Trans. Pow. Electron*., vol. 30, no. 4, pp. 2205-2218, 2015.

[10] Y. Wang, R. Qu, and J. Li, "Multilayer Windings Effect on Interior PM Machines for EV Applications," *IEEE Trans. Ind. Appl*., vol. 51, no. 3, pp. 2208-2215, 2015.

[11] P. Reddy, K. Huh, and A. EI-Refaie, "Generalized Approach of Stator Shifting in Interior Permanent-Magnet Machines Equipped with Fractional-Slot Concentrated Windings," *IEEE Trans. Ind. Electron*., vol. 61, no. 9, pp. 5035-5046, 2014.

[12] A. EI-Refaie and T. Jahns, "Impact of Winding Layer Number and Magnet Type on Synchronous Surface PM Machines Designed for Wide Constant-Power Speed Range Operation," *IEEE Trans. Ener. Conv.*, vol. 23, no. 1, pp. 53-60, 2008.

[13] M. Barcaro and N. Bianchi, "Interior PM Machines Using Ferrite to Replace Rare-Earth Surface PM Machines," *IEEE Trans. Ind. Appl.*, vol. 50, no. 2, pp. 979-985, 2014.

[14] S. Han, T. Jahns, W. Soong, M. Guven, and M. Illindala, "Torque Ripple Reduction in Interior Permanent Magnet Synchronous Machines Using Stators With Odd Number of Slots Per Pole Pair," *IEEE Trans. Ener. Conv.*, vol. 25, no. 1, pp. 118-127, 2010.

[15] J. K. Tangudu, T. M. Jahns, A. El-Refaie, and Z. Q. Zhu, "Lumped parameter magnetic circuit model for fractional-slot concentrated-*winding* interior permanent magnet machines," in *Proc. IEEE Energy Conversion Congr. Expo. (ECCE2009)*, San Jose, CA, Sep. 20–24, 2009, pp. 2423–2430.

[16] J. K. Tangudu and T. M. Jahns, "Comparison of interior PM machines with concentrated and distributed stator windings for traction applications," in Proc. *IEEE Vehicle Power and Propulsion Conference*, 2011, pp. 1-8.

[17] T. Fukushige, N. Limsuwan, T. Kato, K. Akatsu, and R. D. Lorenz, "Efficiency contours and loss minimization over a driving cycle of a variable flux-intensifying machine," *IEEE Trans. Ind. Appl.*, vol. 51, no. 4, pp. 2984-2989, 2015.

[18] N. Limsuwan, T. Kato, K. Akatsu, and R. D. Lorenz, "Design and evaluation of a variable-flux flux-intensifying interior permanent-magnet machine," *IEEE Trans. Ind. Appl.*, vol. 50, no. 2, pp. 1015-1024, 2014.

[19] T. Kato, N. Limsuwan, C. Y. Yu, K. Akatsu, and R. D. Lorenz, "Rare earth reduction using a novel variable magnetomotive force flux-intensified IPM machine," IEEE Trans. Ind. Appl., vol. 50, no. 3, pp. 1748-1756, 2014.

[20] Nicola Bianchi, S. Bolognani, and F. Luise, "Potentials and limits of high-speed PM motors," *IEEE Trans. Ind. Appl.*, vol. 40, no. 6, pp. 1570-1578, 2004.

[21] Z. Kolondzovski, A. Arkkio, J. Larjola, and P. Sallinen, "Power Limits of High-Speed Permanent-Magnet Electrical Machines for Compressor Applications," *IEEE Trans. Ener. Conv.*, vol. 26, no. 1, pp. 73-82, 2011.

[22] W. Li, H. Qiu, X. Zhang, J. Cao, and R. Yi, "Analyses on electromagnetic and temperature fields of super high-speed permanent-magnet generator with different sleeve materials," *IEEE Trans. Ind. Electron.*, vol. 61, no. 6, pp. 3056–3063, 2014.

[23] M. Caprio, V. Lelos, J. Herbst, and J. Upshaw, "Advanced induction motor endring design features for high speed applications," in *Proc. IEMDC*, May 2005, vol. 1, pp. 993–998.

[24] D. Gerada, A. Mebarki, N. Brown, C. Gerada, A. Cavagnino, and A. Boglietti, "High-Speed Electrical Machines- Technologies, Trends, and Developments," *IEEE Trans. Ind. Electron*., vol. 61, no. 6, pp. 2946-2959, 2014.

[25] A. Borisavljevic, H. Polinder, and J. Ferreira, "On the speed limits of permanent-magnet machines," *IEEE Trans. Ind. Elec*., vol. 57, no. 1, pp. 220-227, 2010.

[26] N. Bianchi, S. Bolognani, and F. Luise, "High Speed Drive Using a Slotless PM Motor," *IEEE Trans. Pow. Electron*., vol. 21, no. 4, pp. 1083–1090, 2006.

[27] M. Cheng, W. Hua, J. Zhang, and W. Zhao, "Overview of Stator-Permanent Magnet Brushless Machines," *IEEE Trans. Ind. Electron*., vol. 58, no. 11, pp. 5087-5101, 2011.

[28] M. Chen, W. Hua, X. Zhu, X. Kong, J. Zhang, and W. Zhao, "Stator-permanent magnet brushless machines: Concepts, developments and applications," in *International Conference on Electric Machines and Systems (ICEMS)*, 2008.

[29] C. Liu, K. Chau, J. Jiang, and S. Niu, "Comparison of Stator-Permanent-Magnet Brushless Machines," *IEEE Trans. Magn*., vol. 44, no. 11, pp. 4405-4408, 2008.

[30] Y. Liao, F. Liang, and T. Lipo, "A Novel Permanent Magnet Motor with Doubly Salient Structure," *IEEE Trans. Ind. Appl*., vol. 31, no. 5, pp. 1069-1078, 1995.

[31] M. Chen, K. Chau, and C. C. Chan, "Design and analysis of a new doubly salient permanent magnet motor," *IEEE Trans. Magn*., vol. 37, no. 4, pp. 3012-3020, 2001.

[32] K. T. Chau, M. Cheng, and C. C. Chan, "Performance analysis of 8/6-pole doubly salient permanent magnet motor," *Elect. Mach. Power Syst*., vol. 27, no. 10, pp. 1055–1067, Oct. 1999.

[33] M. Cheng, K. T. Chau, C. C. Chan, and Q. Sun, "Control and operation of a new 8/6-pole doubly salient permanent magnet motor drive," *IEEE Trans. Ind. Appl*., vol. 39, no. 5, pp. 1363–1372, Sep. 2003.

[34] Y. Li and C. C. Mi, "Doubly salient permanent-magnet machine with skewed rotor and six-state commutating mode," *IEEE Trans. Magn*., vol. 43, no. 9, pp. 3623–3629, Sep. 2007.

[35] B. Sarlioglu, Y. Zhao, and T. A. Lipo, "A novel doubly salient single phase permanent magnet generator," in *Conf. Rec. IEEE IAS Annu. Meeting*, 1994, pp. 8–15.

[36] M. Lin, M. Cheng, and E. Zhou, "Design and performance analysis of new 12/8-pole doubly salient permanent-magnet motor," in *Proc. Int. Conf. Elect. Mach. Syst*., 2003, pp. 21–25.

[37] B. Sarlioglu and T. A. Lipo, “Assessment of power generation capability of doubly-salient PM generator,” in *Proc. Int. Conf. Elect. Mach. Drives*, 1999, pp. 549–552.

[38] R. P. Deodhar, S. Andersson, I. Boldea, and T. J. E. Miller, “The flux reversal machine: A new brushless doubly-salient permanent-magnet machine,” in *Conf. Rec. IEEE IAS Annu. Meeting*, 1996, pp. 786–793.

[39] R. P. Deodhar, S. Andersson, I. Boldea, and T. J. E. Miller, “The flux reversal machine: A new brushless doubly-salient permanent-magnet machine,” *IEEE Trans. Ind. Appl*., vol. 33, no. 4, pp. 925-934, 1997.

[40] C. Wang, S. A. Nasar, and I. Boldea, “Three-phase flux reversal machine (FRM),” *IEEE Proc. Elec. Power Appl*. vol. 146, no. 2, pp. 139-146, 1999.

[41] C. X. Wang, I. Boldea, and S. A. Nasar, “Characterization of three phase flux reversal machine as an automotive generator,” *IEEE Trans. Ener. Conv*., vol. 16, no. 1, pp. 74–80, Mar. 2001.

[42] I. Boldea, L. Zhang, and S. A. Nasar, “Theoretical characterization of flux reversal machine in low-speed servo drives-the pole-PM configuration,” *IEEE Trans. Ind. Appl*., vol. 38, no. 6, pp. 1549–1557, Nov./Dec. 2002.

[43] D. G. Dorrell, I. Chindurza, and F. Butt, “Operation, theory and comparison of the flux reversal machine—Is it a viable proposition?” in *Proc. Int. Conf. Power Electron. Drive Syst*., 2003, pp. 253–258.

[44] T. H. Kim, S. H. Won, K. Bong, and J. Lee, “Reduction of cogging torque in flux-reversal machine by rotor teeth pairing,” *IEEE Trans. Magn*., vol. 41, no. 10, pp. 3964–3966, Oct. 2005.

[45] K. B. Jang, S. H. Won, T. H. Kim, and J. Lee, “Starting and high-speed driving of single-phase flux-reversal motor for vacuum cleaner,” *IEEE Trans. Magn*., vol. 41, no. 10, pp. 3967–3969, Oct. 2005.

[46] T. H. Kim and J. Lee, “A study of the design for the flux reversal machine,” *IEEE Trans. Magn*., vol. 40, no. 4, pp. 2053–2055, Jul. 2004.

[47] T. H. Kim, “A Study on the Design of an Inset-Permanent-Magnet-Type Flux-Reversal Machine,” *IEEE Trans. Magn*., vol. 45, no. 16 pp. 2859-2862, Jun. 2009.

[48] Y. Yang, X. Wang, and Z. Zhang, “Analytical calculation of magnetic field and electromagnetic performance of flux reversal machines,” *IET Electric Power Applications*, vol. 8, no. 5, pp. 178-188, 2014.

[49] J. Zhang, M. Chen, Z. Chen, and W. Hua, "Comparison of Stator-Mounted Permanent-Magnet Machines Based on a General Power Equation," *IEEE Trans. Ener. Conv*., vol. 24, no. 4, pp. 826-834, 2009.

[50] W. Hua, M. Cheng, Z. Q. Zhu, W. Zhao, and X. Kong, "Comparison of electromagnetic performance of brushless PM machine having magnets in stator and rotor," *J. Appl. Phys.*, vol. 103, no. 7, pp. 07F124:1–07F124:3, Apr. 2008.

[51] S. E. Rauch and L. J. Johnson, "Design Principles of Flux-Switch Alternators," *AIEE Trans., Power App.* Syst. Part III, vol. 74, no. 3, pp.1261-1268, Jan. 1955.

[52] E. Hoang, A. H. Ben-Ahmed, and J. Lucidarme, "Switching flux PM polyphased synchronous machines," in *Proc. 7th Eur. Conf. Power Electron. Appl*., vol. 3, pp. 903-908, Sep. 1997.

[53] Z. Q. Zhu and J. T. Chen, "Advanced flux-switching permanent magnet brushless machines," *IEEE* Trans. Magn., vol. 46, no. 6, pp. 1447–1453, Jun. 2010.

[54] Z. Q. Zhu, "Switched flux permanent magnet-machines – innovation continues," in *Proc. Int. Conf. Elec. Mach. Syst*., Aug. 2011, pp. 1-10.

[55] J. X. Shen and W. Z. Fei, "Permanent magnet flux switching machines — Topologies analysis and optimization," *Power Engr. Energy and Elec. Drives (POWERENG)*, pp. 352-366, 2013.

[56] W. Hua, M. Cheng, Z. Q. Zhu, and D. Howe, "Design of flux-switching permanent magnet machine considering the limitation of inverter and flux weakening capability," in *Conf. Rec. IEEE IAS Annu. Meeting*, 2006, pp. 2403–2410.

[57] L. E. Somesan, K. Hameyer, E. Padurariu, I.-A. Viorel, and C. Martis, "Sizing-designing procedure of the permanent magnet flux-switching machine based on a simplified analytical model," in *Proc. Int. Conf. Optimization of Elec. And Electron. Equipment*, May 2012, pp.653-658.

[58] J. Zhang, M. Cheng, and Z. Chen, "Investigation of a new stator interior PM machine," *Proc. IET Elec.* Power Appl., vol. 2, no. 2, pp. 77–87, 2008.

[59] Z. Z. Wu and Z. Q. Zhu, "Analysis of Air-Gap Field Modulation and Magnetic Gearing Effects in Switched Flux Permanent Magnet Machines," *IEEE Trans. Magn*. vol. 51, no. 5, 2015.

[60] J.D. McFarland, T.M. Jahns, and A.M. EI-Refaie, "Analysis of the torque production mechanism for flux-switching permanent magnet machines," *IEEE Trans. Ind. Appl*. vol. 51, no. 4, pp. 3041-3049, 2015.

[61] J.D. McFarland, T.M. Jahns, and A.M. EI-Refaie, "Demagnetization performance characteristics of flux switching permanent magnet machines," in *Proc. International Conference on Electrical Machines (ICEM)*, Sept. 2014.

[62] B. Gaussen, E. Hoang, O. de la Barriere, J. Saint-Michel, M. Lecrivain, and M. Gabsi, "Analytical Approach for Air-Gap Modeling of Field-Excited Flux-Switching Machine No-Load Operation," *IEEE Trans. Magn*. vol, 48, no. 9, pp. 2505-2517, 2012.

[63] W. Hua, M. Cheng, Z. Q. Zhu, and D. Howe, "Analysis and optimization of back EMF waveform of a flux-switching permanent magnet motor," *IEEE Trans. Energy Convers*., vol. 23, no. 3, pp. 727–733, Sep. 2008.

[64] Z. Q. Zhu, Y. Pang, J. T. Chen, Z. P. Xia, and D. Howe, "Influence of design parameters on output torque of flux-switching PM machines," in *Proc. IEEE Vehicle Power Propulsion Conf.*, China, Sep. 3–5, 2008, pp. 1–6.

[65] W. Hua, and M. Cheng, "Inductance characteristics of 3-phase flux-switching permanent magnet machine with doubly-salient structure," *IEEE Int. Power Electronics and Motion Control Conf*., 2006, pp. 1-5.

[66] E. Ilhan, M. F. J. Kremers, E. T. Motoasca, J. J. H. Paulides, and E. A. Lomonova, "Sensitivity analysis for phase inductances in flux-switching PM machines," in *Proc. Int. Conf. Elec. Mach*., Sep. 2012, pp.763-768.

[67] G. Qi, J. T. Chen, Z. Q. Zhu, D. Howe, L. B. Zhou, and C. L. Gu ''Influence of skew and cross-coupling on d- and q-axis inductances and flux-weakening performance of PM brushless AC machines,'' *IEEE Trans. Ind. Appl*., vol. 45, no. 5, pp. 1681-1691, May 2009.

[68] D. Li, R. Qu, X. Zhang, and Y. Liu, "Optimal split ratio in switched flux permanent magnet machines," in *Proc. IEEE Energy Convers. Congr. Expo*., Sep. 2012, pp.1925-1931.

[69] Z. Q. Zhu, Y. Pang, W. Hua, M. Cheng, and D. Howe, "Investigation of end-effect in PM brushless machines having magnets in the stator," *J. Appl. Phys*., vol. 99, no. 8, pp. 08R319:1–08R319:3, Apr. 2006.

[70] Z. Q. Zhu, J.T. Chen, Y. Pang, D. Howe, S. Iwasaki, and R. Deodhar, "Modelling of end-effect on electromagnetic torque in flux-switching permanent magnet machine," Int. *Conf. Electrical Machines and Systems (ICEMS2007)*, 8-11 October, 2007, Seoul, Korea, CDROM, paper PMP-36, pp.943-948.

[71] Z. Q. Zhu and Z. Azar, "Influence of end-effect and cross-coupling on torque-speed characteristics of switched flux permanent magnet machines," *IEEE 8th Int. Conf. Power Electron. and ECCE Asia*, pp. 145-152, 2011.

[72] Z. Q. Zhu, M. AL-Ani, B. Lee, and X. Liu, “Comparative study of the electromagnetic performance of switched flux permanent magnet machines,” I*ET Electric Power Appl*. vol. 9, no. 4, pp. 297-306, 2015.

[73] W. Xu, J. Zhu, Y. Zhang, and T. Wang, “Electromagnetic design and performance evaluation on 75kW axially laminated flux switching permanent magnet machine,” in *Proc. Int. Conf. Elec. Mach. Syst*., Aug. 2011, pp. 1-6.

[74] G. Li, J. Ojeda, E. Hoang, M. Gabsi, and M. Lecrivain, “Thermal-electromagnetic analysis for driving cycles of embedded flux-switching permanent-magnet motors,” *IEEE Trans. Veh. Technol*., vol. 61, no. 1, pp.140-151, Jan. 2012.

[75] C. Hwang, C. M. Chang, S. S. Hung, and C. T. Liu, “Design of High Performance Flux Switching PM Machines with Concentrated Windings,” *IEEE Trans. Magn.* vol. 50, no. 1, 2014.

[76] G. Zhang, M. Cheng, W. Hua, and X. Sun, “Analysis of flux-switching permanent-magnet machine by an improved nonlinear magnetic network model considering saturation,” *14th Biennial IEEE Conf. Electromagnetic Field Computation (CEFC)*, Chicago, IL, 2010, Paper CEFC2010-1049.

[77] G. Zhang, M. Cheng, W. Hua, “Analysis of flux-switching permanent-magnet machine by nonlinear magnetic network model with bypass-bridges,” *2010 Int. Conf. Electrical Machines and Systems*, 2010, pp. 1787-1791.

[78] W. Hua, G. Zhang, M. Cheng, and J. Dong, “Electromagnetic Performance Analysis of Hybrid-Excited Flux-Switching Machines by a Nonlinear Magnetic Network Model,” *IEEE Trans. Magn*. vol. 47, no. 10, pp. 3216-3219, 2011.

[79] Z. Q. Zhu, Y. Pang, D. Howe, S. Iwasaki, R. Deodhar, and A. Pride, “Analysis of electromagnetic performance of flux-switching permanent magnet machines by non-linear adaptive lumped parameter magnetic circuit model,” *IEEE Trans. Magn.*, vol. 41, no. 11, pp. 4277–4287, Nov. 2005.

[80] Y. Chen, Z. Q. Zhu, and D. Howe, “Three-dimensional lumped-parameter magnetic circuit analysis of single-phase flux-switching permanent magnet motor,” *IEEE Trans. Magn*., vol. 44, no. 6, pp. 1701–1710, Nov. 2008.

[81] J.T. Chen, and Z.Q. Zhu, “Influence of rotor pole number on optimal parameters in flux-switching PM brushless AC machines by lumped parameter magnetic circuit model,” *IEEE Trans. Ind. Appl.*, vol.46, no.4, pp.1381-1388, 2010.

[82] J.T. Chen, Z.Q. Zhu, and D. Howe, “A dual-lumped parameter magnetic circuit model accounting for the cross-coupling effect, with particular reference to flux-switching

permanent magnet machines," *IET, power Electronics, Machines and Drives*, 2-4 April, 2008, York, UK, pp.111-115.

[83] A. Chen, R. Nilssen, and A. Nysveen, "Analytical design of a high-torque flux-switching permanent magnet machine by a simplified lumped parameter magnetic circuit model," *Int. Conf. Electrical Machines*, 2010, pp. 1-6.

[84] Y. Tang, T. E. Motoasca, J. J. H. Paulides, and E. A. Lomonova, "Analytical modeling of flux-switching machines using variable global reluctance networks," in *Proc. Int. Conf. Elec. Mach.*, Sep. 2012, pp.2792-2798.

[85] Z. Xu, S. Xie, P. Mao, "Analytical Design of Flux-Switching Hybrid Excitation Machine by a Nonlinear Magnetic Circuit Method," *IEEE Trans. Magn.*, vol. 49, no. 6, pp. 3002-3008, 2013.

[86] S. Zhou, H. Yu, M. Hu, C. Jiang, and L. Huang, "Nonlinear equivalent magnetic circuit analysis for linear flux-switching permanent magnet machines," *IEEE Trans. Magn.*, vol. 48, no. 2, pp. 883-886, Feb. 2012.

[87] B. L. J. Gysen, E. Ilhan, K. J. Meessen, J. J. H. Paulides, and E. A. Lomonova, "Modeling of flux switching permanent magnet machines with Fourier analysis," *IEEE Trans. Magn.*, vol. 46, no. 6, pp. 1499–1502, Jun. 2010.

[88] E. Ilhan, B. L. J. Gysen, J. J. H. Paulides, and E. A. Lomonova, "Analytical hybrid model for flux switching permanent magnet machines," *IEEE Trans. Magn.*, vol. 46, no. 6, pp. 1762–1765, Jun. 2010.

[89] D. C. J. Krop, L. Encica, and E. A. Lomonova, "Hybrid modeling method for the analysis of a linear flux switching machine," *14th Biennial IEEE Conf. Electromagnetic Field Computation*, 2010, pp. 1-1.

[90] W. Hua and M. Cheng, "Cogging torque reduction of flux-switching permanent magnet machines without skewing," in *Proc. Int. Conf. Elect. Mach. Syst.*, 2008, pp. 3020–3025.

[91] Z. Q. Zhu, A. S. Thomas, J. T. Chen, and G. W. Jewell, "Cogging torque in flux-switching PM machines," *IEEE Trans. Magn.*, vol. 45, no. 10, pp. 4708–4711, 2009.

[92] W. Fei, P. C. K. Luk, J. X. Shen, B. Xia, and Y. Wang, "Permanent-magnet flux-switching integrated starter generator with different rotor configurations for cogging torque and torque ripple mitigations," *IEEE Ind. Appl.*, vol. 47, pp. 1247-1256, May/Jun. 2011.

[93] W. Fei, P. C. K. Luk, B. Xia, Y. Wang, and J. X. Shen, "Permanent magnet flux switching integrated-starter-generator with different rotor configurations for cogging torque and torque ripple mitigations," *IEEE Energy Conversion Congress and Exposition*, 2010, pp. 1715-1722.

[94] Y. Wang, M. J. Jin, W. Z. Fei, and J. X. Shen, "Cogging torque reduction in permanent magnet flux-switching machines by rotor teeth axial pairing," *IET Electric Power Applications*, vol. 4, pp. 500-506, 2010.

[95] M. J. Jin, Y. Wang, J. X. Shen, P. C. K. Luk, W. Z. Fei, and C. F. Wang, "Cogging torque suppression in a permanent magnet flux-switching integrated-starter-generator," *IET Electric Power Applications*, vol. 4, pp. 647-656, 2010.

[96] J. Yang, Y. Deng, Q. Ma, and W. Zhao, "Cogging torque analysis of flux-switching permanent magnet motor," Int. *Conf. E-Product E-Service and E-Entertainment*, 2010, pp. 1-4.

[97] D. Wang, X. Wang, and S.-Y. Jung, "Reduction on cogging torque in flux-switching permanent magnet machine by teeth notching schemes," *IEEE Trans. Magn*., vol. 48, no. 11, pp. 4228-4231, Nov. 2012.

[98] W. Xu, J. Zhu, Y. Zhang, and J. Hu, "Cogging torque reduction for radially laminated flux-switching permanent magnet machine with 12/14 poles," in *Proc. 37th Annu. Conf. IEEE Ind. Electron. Society*, Nov. 2011, pp.3590-3595.

[99] S. Zhou, H. Yu, M. Hu, C. Jiang, and L. Hao, "Reduction of cogging force in a linear flux-switching permanent magnet brushless AC machine for direct-drive applications," *IEEE Trans. Magn*., vol. 47, no. 10, pp. 3252-3255, Oct. 2011.

[100] W. Fei, P. C. K. Luk, and J. X. Shen, "Torque analysis of permanent magnet flux switching machines with rotor step skewing," *IEEE Trans. Magn*., vol. 48, no. 10, pp. 2664-2673, Oct. 2012.

[101] C. Sikder, I. Husain, and W. Ouyang, "Cogging torque reduction in flux-switching permanent magnet machines by rotor pole shaping," *IEEE Trans. Ind. Appl*. vol. 51, no. 6, pp. 3609-3619, 2015.

[102] X. Zhu, M. Cheng, K. T. Chau, and C. Yu, "Torque ripple minimization of flux-controllable stator-permanent magnet brushless motors using harmonic current injection," *J. Appl. Phys*., vol. 105, no. 7, pp. 07F102:1– 07F102:3, Feb. 2009.

[103] H. Jia, M. Cheng, W. Hua, W. Zhao, and W. Li, "Torque ripple suppression in flux-switching PM motor by harmonic current injection based on voltage space-vector modulation," *IEEE Trans. Magn*., vol. 46, no. 6, pp. 1527–1530, Jun. 2010.

[104] H. Jia, M. Cheng, W. Hua, Z. Yang, and Y. Zhang, "Compensation of cogging torque for flux-switching permanent magnet motor based on current harmonics injection," *IEEE Int. Electric Machines and Drives Conf*., 2009, pp. 286-291.

[105] N. Larsen, A. Gesior, and P. Hein, “Torque ripple reduction based on current control for a flux switching permanent magnet machine,” in *Proc. Int. Symp. Power Electron., Elect. Drives, Automation and Motion*, Jun. 2012, pp. 712-717.

[106] K. S. Chai and C. Pollock, “Using genetic algorithms in design optimization of the flux switching motor,” *Int. Conf. on Power Electronics, Machines and Drives*, 2002, pp. 540-545.

[107] Z.Q. Zhu, and X. Liu, “Individual and global optimization of switched flux permanent magnet motors,” *Int. Conf. Electrical Machines and Systems (ICEMS)* 2011, 20-23 August 2011, Beijing, China.

[108] W. Z. Fei and J. X. Shen, “Comparative study and optimal design of PM switching flux motors,” *Proc. 41st Int. Universities Power Engineering Conf.*, 2006, pp. 695-699.

[109] L. Jung Ho, L. Tae Hoon, and J. Ah Ram, “Optimum design criteria for maximum torque density and minimum torque ripple of flux switching motor using response surface methodology,” *IEEE Conf. Electromagnetic Field Computation*, 2010, pp. 1848-1851.

[110] J. T. Chen, Z. Q. Zhu, A. S. Thomas, and D. Howe, “Optimal combination of stator and rotor pole numbers in flux-switching PM brushless ac machines,” in *Proc. Int. Conf. Elect. Mach. Syst.*, 2008, pp. 2905–2910.

[111] J. T. Chen and Z. Q. Zhu, “Winding configurations and optimal stator and rotor pole combination of flux-switching PM brushless ac machines,” *IEEE Trans. Energy Convers*., vol. 25, no. 2, pp. 293–302, Jun. 2010.

[112] J. T. Chen, Z. Q. Zhu, and Z. P. Xia, “Coil connections and winding factors in flux-switching PM brushless AC machines,” *Int. J. for Computation and Mathematics in Electrical and Electronic Engineering (COMPEL)*, vol.30, no. 1, pp.84-97, 2011.

[113] J. T. Chen and Z. Q. Zhu, “Influence of rotor pole number on optimal parameters in flux-switching PM brushless AC machines by lumped parameter magnetic circuit model,” in *Proc. IEEE Int. Electric Mach. Drives Conf. (IEMDC2009)*, Miami, FL, May 3–6, 2009, pp. 1216–1223.

[114] J. T. Chen and Z. Q. Zhu, “Comparison of all and alternate poles wound flux-switching PM machines having different stator and rotor pole numbers,” in *Proc. IEEE Energy Conversion Congr. Expo. (ECCE2009)*, San Jose, CA, Sep. 20–24, 2009, pp. 1705–1712.

[115] J.T. Chen and Z.Q. Zhu, “Comparison of all and alternate poles wound flux-switching PM machines having different stator and rotor pole numbers,” *IEEE Trans. Industry Applications*, vol.46, no.4, pp.1406-1415, 2010.

[116] J. T. Chen, Z. Q. Zhu, S. Iwasaki, R. Deodhar, "Influence of slot opening on optimal stator and rotor pole combination and electromagnetic performance of flux-switching PM brushless AC machines," *IEEE Trans. Industry Applications*, vol. 47, no. 4, pp. 1681-1691, 2011.

[117] Y. Wang, Z. W. Huang, J. X. Shen, and C. F. Wang, "Comparison and study of 6/5- and 12/10-pole permanent magnet flux-switching motors considering flux-weakening capability," in *Proc. Int. Conf. Elect. Mach. Syst.*, 2008, pp. 3262–3265.

[118] R. L. Owen, Z. Q. Zhu, A. S. Thomas, G. W. Jewell, and D. Howe, "Alternate poles wound flux-switching permanent-magnet brushless ac machines," *IEEE Trans. Ind. Appl.*, vol. 46, no. 2, pp. 790–797, Mar./Apr. 2010.

[119] A. S. Thomas, Z. Q. Zhu, G. W. Jewell, and D. Howe, "Flux-switching PM brushless machines with alternative stator and rotor pole combinations," in *Proc. Int. Conf. Elec. Mach. Syst.*, Oct. 2008, pp. 2986-2991.

[120] Z. Q. Zhu, M. M. AI-Ani, X. Liu, M. Hasegawa, A. Pride, and R. Deodhar, "Comparative study of torque-speed characteristics of alternate switched-flux permanent magnet machine topologies," 6th Int. Conf. *Power Electron. Mach. and Drives (PEMD)*, pp. 1-6, 2012.

[121] J. T. Chen, Z. Q. Zhu, S. Iwasaki, R. Deodhar, "A novel E-core switched-flux PM brushless AC machine," *IEEE Trans. Industry Applications*, vol.47, no.3, pp.1273-1282, 2011.

[122] Z. Q. Zhu, J. T. Chen, Y. Pang, D. Howe, S. Iwasaki, and R. Deodhar, "Analysis of a novel multi-tooth flux-switching PM brushless ac machine for high torque direct-drive applications," *IEEE Trans. Magn.*, vol. 44, no. 11, pp. 4313–4316, Nov. 2008.

[123] J. T. Chen, Z. Q. Zhu, and D. Howe, "Stator and rotor pole combinations for multi-tooth flux-switching PM brushless ac machines," *IEEE Trans. Magn.*, vol. 44, no. 12, pp. 4659–4667, 2008.

[124] J. T. Chen, Z. Q. Zhu, and D. Howe, "Optimization of multi-tooth flux-switching PM brushless AC machines," in *Proc. Int. Conf. Elec. Mach.*, Sep. 2008, pp.1-6.

[125] Y. Tang, J. J. Paulides, T. E. Motoasca, and E. A. Lomonova, "Flux-switching machine with DC excitation," *IEEE Trans. Magn.*, vol. 48, no. 11, pp. 3583-3586, 2012.

[126] Y. Tang, E. Ilhan, J. J. Paulides, and E. A. Lomonova, "Design considerations of flux-switching machines with permanent magnet or DC excitation," *15th European Conference on Power Electron. and Appl. (EPE)*, pp. 1-10, 2013.

[127] J. T. Chen, Z. Q. Zhu, S. Iwasaki, and R. Deodhar, "Low cost flux-switching brushless AC machines," *IEEE Vehicle Power and Propulsion Conf.*, 1-3 Sept., 2010, Lille, Fracnce, VPPC 2010, Paper RT6/95-13475.

[128] Y. J. Zhou and Z. Q. Zhu, "Comparison of low-cost wound-field switched-flux machines," in *Proc. IEEE ECCE*, 2013, pp. 904-911.

[129] Y. J. Zhou and Z. Q. Zhu, "Comparison of Low-Cost Single-Phase Wound-Field Switched-Flux Machines," *IEEE Trans. Ind. Appl*. vo. 50, no. 5, pp. 3335-3345, 2014.

[130] Y. J. Zhou and Z. Q. Zhu, "Comparison of Low-Cost Single-Phase Wound-Field Switched-Flux Machines," *IEEE Int. Elec. Mach. & Drives Conf. (IEMDC),* pp. 1275-1282, 2013.

[131] E. Hoang, M. Lecrivain, and M. Gabsi, "A new structure of a switching flux synchronous polyphased machine with hybrid excitation," in *Proc. 12th Eur. Conf. Power Electron. Appl*., 2007, pp. 1–8.

[132] E. Hoang, S. Hlioui, M. Lecrivain, and M. Gabsi, "Experimental comparison of lamination material case of switching flux synchronous machine with hybrid excitation," *European Conf. Power Electronics and Applications*, 2009, pp. 1-7.

[133] E. Hoang, M. Lecrivain, S. Hlioui, and M. Gabsi, "Hybrid excitation permanent magnet synchronous machines optimally designed for hybrid and full electric vehicles," *Int Conf on Power Electronics (ICPE2011) – ECCE-Asia,* 2011, Paper TuD1-2.

[134] W. Hua, M. Cheng, and G. Zhang, "A novel hybrid excitation flux switching motor for hybrid vehicles," *IEEE Trans. Magn*., vol. 45, no. 10, pp. 4728–4731, Oct. 2009.

[135] W. Hua, G. Zhang, X. Yin, and M. Cheng, "Flux-regulation capability of hybrid-excited flux-switching machines," in *Proc. Int. Conf. Elec. Mach.,* Sep. 2012, pp.2909-2913

[136] W. Hua, G. Zhang, and M. Cheng, "Flux-Regulation Theories and Principles of Hybrid-Excited Flux-Switching Machines," *IEEE Trans. Ind. Elec*. vol. 62, no. 9, pp. 5359-5369, 2015.

[137] W. Hua, G. Zhang, M. Cheng, and X. Sun, "Comparison of flux-regulation capability of a hybrid-excited flux-switching machine with different magnet materials," *14th Biennial IEEE Conf. Electromagnetic Field Computation*, 9-12 May 2010.

[138] W. Hua, G. Zhang, and M. Cheng, "Electromagnetic performance analysis of hybrid-excited flux-switching machines for electrical vehicles by an improved magnetic network model," *IEEE Vehicle Power and Propulsion Conf.,* 2010, pp. 1-5.

[139] G. Zhang, W. Hua, M. Cheng, J. Zhang, and W. Jiang, "Investigation of an Improved Hybrid-Excitation Flux Switching Brushless Machine for HEV-EV Applications," *IEEE ECCE,* 2014, pp. 5852-5857.

[140] G. Zhang, M. Cheng, W. Hua, and J. Dong, "Analysis of the oversaturated effect in hybrid excited flux-switching machines," *IEEE Trans. Magn*., vol. 47, no. 10, pp. 2827-2830, Oct. 2011.

[141] Y. Wang, and Z. Deng, "Comparison of hybrid excitation topologies for flux switching machines," *IEEE Trans. Magn*., vol. 48, no. 9, pp. 2518- 2527, Sep. 2012.

[142] Y. Wang, Z. Deng, and X. Wang, "A parallel hybrid excitation flux-switching generator DC power system based on direct torque linear control," *IEEE Trans. Energy Convers*., vol. 27, no. 2, pp. 308-317, Jun. 2012.

[143] R. L. Owen, Z. Q. Zhu, and G. W. Jewell, "Hybrid excited flux-switching permanent magnet machines," in *Proc. 13th Eur. Conf. Power Electron*. Appl., 2009, pp. 1–10.

[144] R L. Owen, Z.Q. Zhu, and G. W. Jewell, "Novel hybrid-excited flux-switching permanent-magnet machines with iron bridges," *IEEE Trans. Magnetics*, vol.46, no.6, pp.1726-1729, 2010.

[145] J. T. Chen, Z. Q. Zhu, S. Iwasaki, R. Deodhar, "A novel hybrid excited switched-flux brushless AC machine for EV/HEV applications," *IEEE Trans. Vehicular Technology*, vol.60, no.4, pp.1365-1373, 2011.

[146] E. Sulaiman, T. Kosaka, Y. Tsujimori, and N. Matsui, "Design of 12-slot 10-pole permanent magnet flux-switching machine with hybrid excitation for hybrid electric vehicle," *Int. Conf. Power Electronics, Machines and Drives*, 2010, pp. 1-5.

[147] E. Sulainman, T. Kosaka, N. Matsui, and M. Z. Ahmad, "Design studies on high torque and high power density hybrid excitation flux switching synchronous motor for HEV applications," in *Proc. IEEE Int. Power Engineering and Optimization Conf*., Jun. 2012, pp. 333-338.

[148] E. Sulaiman, T. Kosaka, N. Matsui, and M. Z. Ahmad, "Design improvement and performance analysis of 12slot-10pole permanent magnet flux switching machine with field excitation coils," in *Proc. IEEE 8th Int. Conf. Power Electron. and ECCE Asia*, Jun. 2011, pp.1913-1920.

[149] E. Sulaiman, T. Kosaka, and N. Mstsui, "A novel hybrid excitation flux switching synchronous machine for a high-speed hybrid electric vehicle applications," in *Proc. Int. Conf. Elec. Mach. Syst*., Aug. 2011, pp. 1-6.

[150] E. Sulaiman, T. Kosaka, and N. Matsui, "High power density design of 6-slot-8-pole hybrid excitation flux switching machine for hybrid electric vehicles," *IEEE Trans. Magn*., vol. 47, no. 10, pp. 4453-4456, Oct. 2011.

[151] B. Gaussens, E. Hoang, P. Manfe, M. Lecrivain, and M. Gabsi, "Improved output power capability of hybrid excited flux-switching DC-alternators: analysis and experiments," in *Proc. IEEE Int. Conf. Ind. Tech*., Mar. 2012, pp.960-965.

[152] B. Gaussens, E.Hoang, M. Lecrivain, P. Manfe, and M. Gabsi, "A new hybrid-excited flux-switching machine with excitation coils in stator slots," in *Proc. Int. Conf. Elec. Mach. Syst.*, Oct. 2012, pp. 1-6.

[153] M. Z. Ahmad, E. Sulaiman, Z. A. Haron, and T. Kosaka, "Preliminary studies on a new outer-rotor permanent magnet flux switching machine with hybrid excitation flux for direct drive EV applications," in *Proc. IEEE Int. Conf. Power and Energy*, Dec. 2012, pp.928-933.

[154] L. Mo, L. Quan, Y. Chen, and H. Qiu, "Sandwiched Flux-Switching Permanent-Magnet Brushless AC Machines Using V-Shape Magnets," *Vehicle Power and Propulsion Conference (VPPC)*, 2013.

[155] Y. J. Zhou and Z. Q. Zhu, "Torque Density and Magnet Usage Efficiency Enhancement of Sandwiched Switched Flux Permanent Magnet Machines Using V-Shaped Magnets," *IEEE Trans. Magn*. Vol. 49, no. 7, pp. 3834-3837, 2013.

[156] T. Raminosoa, A. El-Refaie, D. Pan, K. K. Huh, J. Alexander, K. Grace, S. Grubic, S. Galioto, P. Reddy, and X. Shen, "Reduced rare-earth flux-switching machines for traction applications," *IEEE Trans. Appl*. vol. 41, no. 4, pp. 2959-2971, 2015.

[157] T. Raminosoa, A. El-Refaie, D. Pan, K. K. Huh, J. Alexander, K. Grace, S. Grubic, S. Galioto, P. Reddy, and X. Shen, "Reduced rare-earth flux-switching machines for traction applications," in *Proc. IEEE ECCE*, 2014 pp. 318-327.

[158] H. Yang, H. Lin, J. Dong, J. Yan, Y. Huang, and S. Fang, "Analysis of a Novel Switched-Flux Memory Motor Employing a Time-Divisional Magnetization Strategy," *IEEE Trans. Magn*. vol. 50, no. 2, 2014.

[159] H. Yang, Z. Q. Zhu, H. Lin, S. Fang, and Y. Huang, "Comparative Study of Novel Variable-Flux Memory Machines Having Stator Permanent Magnet Topologies," *IEEE Trans. Magn*. 2015 DOI: 10.1109/INTMAG.2015.7156983.

[160] H. Yang, H. Lin, S. Fang, Y. Huang, Z. Q. Zhu, D. Wu, and H. Hua, "Novel alternative switched flux memory machines having hybrid magnet topologies," *10th Int. Conf. Ecological Vehi. and Renew. Ener. (EVER)*, pp. 1-9, 2015.

[161] H. Yang, H. Lin, Z. Q. Zhu, D. Wang, S. Fang, and Y. Huang, "Novel switched-flux hybrid permanent magnet memory machines for EV/HEV applications," *17th Int. Conf. Elec. Mach. and Sys. (ICEMS)*, pp. 1191-1195, 2014.

[162] H. Yang, H. Lin, Y. Feng, and X Lu, "Design and quantitative comparison of switched-flux memory integrated-starter-generators for hybrid electric vehicles," *Int. Conf. Renewable Energy Research and Applications (ICRERA)*, pp. 757-762, 2013.

[163] X. Liu, D. Wu, Z. Q. Zhu, A. Pride, R. P. Deodhar, and T. Sasaki, "Efficiency Improvement of Switched Flux PM Memory Machine Over Interior PM Machine for EV-HEV Applications," *IEEE Trans. Magn*. vol. 50, no. 11, 2014.

[164] D. Wu, Z. Q. Zhu, and X. Liu, "Novel external rotor switched flux memory motor with hybrid magnets," *17th Int. Conf. Elec. Mach. and Sys. (ICEMS)*, pp. 3324-3300, 2014.

[165] D. Wu, X. Liu, Z. Q. Zhu, A. Pride, R. Deodhar, and T. Sasaki, "Switched flux hybrid magnet memory machine," *IET Electric Power Appl*. vol. 9, no. 2, pp. 160-170, 2015.

[166] D. Wu, X. Liu, Z. Q. Zhu, A. Pride, R. Deodhar, and T. Sasaki, "Novel switched flux hybrid magnet memory motor," *7th IET Conf. Power Elec. Mach. and Drives (PEMD)*, pp. 1-6, 2014.

[167] R. Owen, Z.Q. Zhu, J.B. Wang, D. A. Stone, and I. Urquhart, "Mechanically adjusted variable-flux concept for switched-flux permanent-magnet machines," *Int. Conf. Electrical Machines and Systems*, ICEMS 2011, 20-23 August 2011, Beijing, China.

[168] Z. Q. Zhu, M. M. J. Al-Ani, X. Liu, M. Hasegawa, A. Pride, and R. Deodhar, "Comparison of alternate mechanically adjusted variable flux switched flux permanent magnet machines," in *Proc. IEEE Energy Convers. Congr. Expo*., Sep. 2012, pp.3655-3662.

[169] Z. Q. Zhu, M. M. J. Al-Ani, X. Liu, M. Hasegawa, A. Pride, and R. Deohar, "Comparison of flux weakening capability in alternative switched flux permanent magnet machines by mechanical adjusters," in *Proc. Int. Conf. Elec. Mach*., Sep. 2012, pp.2889-2895.

[170] Z. Q. Zhu, M. M. Al-Ani, X. Liu, and B. Lee, "A Mechanical Flux Weakening Method for Switched Flux Permanent Magnet Machines," *IEEE Trans. Ener. Convs.*, vol. 30, no. 2, pp. 806-815, 2015.

[171] A. S. Thomas, Z. Q. Zhu, R. L. Owen, G.W. Jewell, and D. Howe, "Multiphase flux-switching permanent-magnet brushless machine for aerospace application," *IEEE Trans. Ind. Appl*., vol. 45, no. 6, pp. 1971–1981, Nov./Dec. 2009.

[172] R. L. Owen, Z. Q. Zhu, A. S. Thomas, G. W. Jewell, and D. Howe, "Fault tolerant flux switching PM brushless AC machines," in *Proc. IEEE Ind. Appl. Soc. Annu. Meeting*, Edmonton, AB, Canada, Oct. 5–9, pp. 1–8, 2008.

[173] A. Gandhi and L. Parsa, "Thrust optimization of a five-phase fault-tolerant flux-switching linear synchronous motor," in *Proc. 38th Annu. Conf. IEEE Ind. Electron. Society*, Oct. 2012, pp.2067-2073.

[174] E. Ben Sedrine, J. Ojeda, I. Slama-Belkhodja, and M. Gabsi, "Five-phase flux switching machine: optimal current waveforms in order to improve open phase operation," in *Proc. 38th Annu. Conf. IEEE Ind. Electron. Society*, Oct. 2012, pp.1805-1910.

[175] X. Xue, W. Zhao, J. Zhu, G. Liu, X. Zhu, and M. Chen, "Design of Five-Phase Modular Flux-Switching Permanent-Magnet Machines for High Reliability Applications," *IEEE Trans. Magn*. vol. 49, no. 7, pp. 3941-3944, 2013.

[176] W. W. Yang, W. Xu, and X. Y. Xiao, "Research on fault diagnosis and tolerant operation of redundant flux-switching permanent-magnet motors," in *Proc. Int. Conf. Applied Superconductivity and electromagnetic Devices*, Dec. 2011, pp. 164-168.

[177] W. Zhao, M. Cheng, W. Hua, H. Jia, and R. Cao, "Back-EMF harmonic analysis and fault-tolerant control of flux-switching permanent-magnet machine with redundancy," *IEEE Trans. Ind. Electron*., vol. 58, no. 5, pp. 1926–1935, May 2011.

[178] W. Zhao, M. Cheng, W. Hua, H. Jia, R. Cao, and W. Wang, "Remedial operation of a fault-tolerant flux-switching permanent magnet motor for electric vehicle applications," *IEEE Vehicle Power and Propulsion Conf*., 1-3 Sept. 2010, pp. 1-6.

[179] W. Zhao, M. Cheng, K. T. Chau, J. Ji, W. Hua, and R. Cao, "A new modular flux-switching permanent-magnet machine using fault-tolerant teeth," *14th Biennial IEEE Conf. Electromagnetic Field Computation,* 9-12 May 2010, pp.1.

[180] W. Zhao, M. Cheng, W. Hua, and H. Jia, "A redundant flux-switching permanent magnet motor drive for fault-tolerant applications," *IEEE Vehicle Power and Propulsion Conference,* 2008, pp. 1-6.

[181] W. Zhao, M. Cheng, K. T. Chau, W. Hua, H. Jia, J. Ji, and W. Li, "Stator-flux-oriented fault-tolerant control of flux-switching permanent-magnet motors," *IEEE Trans. Magn*., vol. 47, no. 10, pp. 4191-4194, Oct. 2011.

[182] W. Zhao, M. Cheng, K. T. Chau, and C. C. Chan, "Control and operation of fault-tolerant flux-switching permanent-magnet motor drive with second harmonic current injection," *IET Elect. Power Appl*., vol.6, no. 9, pp.707-715, Nov. 2012.

[183] M. Jin, C. Wang, J. Shen, and B. Xia, "A modular permanent-magnet flux-switching linear machine with fault-tolerant capability," *IEEE Trans. Magn*., vol. 45, no. 8, pp. 3179–3186, Aug. 2009.

[184] Z. Q. Zhu, X. Chen, J. T. Chen, D. Howe, and J. S. Dai, "Novel linear fault-tolerant flux-switching PM machines," *Int. Conf. Elec. Mach. Syst*., China, Oct. 17–20, 2008, Paper SMO-48.

[185] X. Ojeda, G. J. Li, and M. Gabsi, "Fault diagnosis using vibration measurements of a flux-switching permanent magnet motor," *IEEE Int. Symp. Industrial Electronics*, 2010, pp. 2091-2096.

[186] M. O. E. Aboelhassan, T. Raminosoa, A. Goodman, L. De Lillo, and C. Gerada, "A fault-tolerant control scheme for a dual flux-switching permanent magnet motor drive," in *Proc. Int. Conf. Elec. Mach. Syst*., Aug. 2011, pp. 868-872.

[187] T. Raminosoa, C. Gerada, and M. Galea, "Design considerations for a fault-tolerant flux-switching permanent-magnet machine," *IEEE Trans. Industrial Electronics*, vol. 58, no.7, pp. 2818-2825, Jul. 2011.

[188] T. Raminosoa and C. Gerada, "A comparative study of permanent magnet - synchronous and permanent magnet - flux switching machines for fault tolerant drive systems," *IEEE Energy Conversion Congress and Exposition*, 12-16 Sept. 2010, pp. 2471-2478.

[189] T. Raminosoa and C. Gerada, "Novel fault tolerant design of flux switching machines," *Int. Conf. Power Electronics, Machines and Drives*, 5th IET , Apr. 2010, pp. 1-6.

[190] T. Raminosoa and C. Gerada, "Fault tolerant winding technology comparison for flux switching machine," *Int. Conf. Electrical Machines*, 6-8 Sept. 2012, pp. 1-6.

[191] G. J. Li, J. Ojeda, E. Hoang, and Gabsi, "Double and single layers flux-switching permanent magnet motors: fault tolerant model for critical applications," in *Proc. Int. Conf. Elec. Mach. Syst.*, Aug. 2011, pp. 1-6.

[192] G. J. Li, J. Ojeda, E. Hoang, and M. Gabsi, "Thermal-electromagnetic analysis of a fault-tolerant dual-star flux-switching permanent magnet motor for critical applications," *IET Elect. Power Appl*., vol.5, no. 6, pp.503-513, Jul. 2011.

[193] L. Huang, H. Yu, M. Hu, S. Zhou, and L. Hao, "Fault-tolerant performance of a novel flux-switching permanent magnet linear machine based on harmonic current injection," *IEEE Trans. Magn*., vol. 47, no. 10, pp. 3224-3227, Oct. 2011.

[194] A. S. Thomas, Z. Q. Zhu, and L. J. Wu, "Novel modular-rotor switched-flux permanent magnet machines," *IEEE* Trans. Ind. Appl., vol.48, no.6, pp. 2249-2258, Nov./Dec. 2012.

[195] A. Zulu, "Flux switching machines using segmental rotors," Ph.D. Thesis, Newcastle University, 2010.

[196] A. Zulu, B. C. Mecrow, and M. Armstrong, "Topologies for wound-field three-phase segmented-rotor flux-switching machines," *IET Int. Conf. Power Electronics, Machines and Drives (PEMD 2010)*, 2010, pp. 1-6.

[197] A. Zulu, B. Mecrow, and M. Armstrong, “A wound-field three-phase flux switching synchronous motor with all excitation sources on the stator,” in *Proc. IEEE ECCE*, 2009, pp. 1502–1509.

[198] A. Zulu, B. Mecrow, and A. Armstrong, “A wound-field three-phase flux-switching synchronous motor with all excitation sources on the stator,” *IEEE Trans. Industry Applications*, vol. 46, pp. 2363-2371, 2010.

[199] A. Zulu, B. C. Mecrow, and M. Armstrong, “Prediction of performance of a wound-field segmented-rotor flux-switching synchronous motor using a dq-equivalent model,” *Int. Conf. on Electrical Machines*, 2010, pp. 1-6.

[200] A. Zulu, B. C. Mecrow, and M. Armstrong, “Permanent-magnet flux-switching synchronous motor employing a segmental rotor,” *IEEE Trans. Ind. Appl*., vol.48, no.6, pp. 2259-2267, Nov./Dec. 2012.

[201] A. Zulu, B. C. Mecrow, and M. Armstrong, “Investigation of the dq -Equivalent Model for Performance Prediction of Flux-Switching Synchronous Motors With Segmented Rotors,” *IEEE Trans. Ind. Electron*., vol.59, no.6, pp. 2392-2402, 2012.

[202] D. J. Evans and Z. Q. Zhu, “Novel Partitioned Stator Switched Flux Permanent Magnet Machines,” *IEEE Trans. Magn*. vol. 51, no. 1, 2015.

[203] C. C. Awah, Z. Q. Zhu, Z. Wu, H. Zhan, J. Shi, D. Wu, and X. Ge, “Comparison of Partitioned Stator Switched Flux Permanent Magnet Machines Having Single- or Double-layer Windings,” *IEEE Trans. Magn*. vol. 52, no. 1, 2016.

[204] C. C. Awah, Z. Q. Zhu, Z. Wu, and D. Wu, “High torque density magnetically-geared switched flux permanent magnet machines,” *10th Int. Conf. Ecological Vehicles and Renewable Energies (EVER)*, pp. 1-6, 2015.

[205] H. Hua and Z. Q. Zhu, “Novel hybrid excited switched flux machine having separate field winding stator,” *IEEE Trans. Magn*. 2016. DOI: 10.1109/TMAG.2016.2522920.

[206] Z. Wu, Z. Q. Zhu, and D. Evans, “Comparison of globally optimized partitioned stator SFPM machines with different stator/rotor pole combinations,” *IEEE InterMag*, 2015.

[207] Z. Q. Zhu, Z. Z. Wu, D. J. Evans, and W. Q. Chu, “A Wound Field Switched Flux Machine With Field and Armature Windings Separately Wound in Double Stators,” *IEEE Trans. Ener. Conv*. Vol. 30, no. 2, pp. 772-783, 2015.

[208] Z. Q. Zhu, Y. J. Zhou, and J. T. Chen, “Investigation of axial field partitioned stator switched flux machines,” *10th Int. Conf. Ecological Vehicles and Renewable Energies (EVER)*, pp. 1-7, 2015.

[209] W. Hua, P. Su, G. Zhang, and M. Cheng, "A novel rotor-permanent magnet flux-switching machine," *10th International Conference on Ecological Vehicles and Renewable Energies (EVER)*, pp. 1-10, 2015.

[210] J. X. Shen, "Permanent magnet flux switching linear machines: theory, optimization and prospective applications," in *Proc. Conf. and Exhib. Ecological Vehicles and Renewable Energies*, March. 2012, pp. 1-11.

[211] Z. Q. Zhu, X. Chen, J. T. Chen, D. Howe, and J. S. Dai, "Novel linear flux-switching permanent magnet machines," in *Proc. Int. Conf. Elect. Mach. Syst*., 2008, pp. 2948–2953.

[212] C. F. Wang, J. X. Shen, Y. Wang, L. L. Wang, and M. J. Jin, "A new method for reduction of detent force in PM flux-switching linear motors," *IEEE Trans. Magn*., vol. 45, no. 6, pp. 2843–2846, 2009.

[213] C. F. Wang, J. X. Shen, Y. Wang, L. L. Wang, and M. J. Jin, "A new method for reduction of detent force in permanent magnet flux-switching linear motors," *IEEE Trans. Magn.*, vol. 45, pp. 2843-2846, 2009.

[214] C. F. Wang and J. X. Shen, "A method to segregate detent force components in permanent-magnet flux-switching linear machines," *IEEE Trans. Magn*., vol. 48, no. 5, pp. 1948-1955, May 2012.

[215] C. F. Wang, J. X. Shen, L. L. Wang, and K. Wang, "A novel permanent magnet flux-switching linear motor," *4th IET Conf. Power Electronics, Machines and Drives*, 2008, pp. 116-119.

[216] W. Min, J. T. Chen, Z. Q. Zhu, Y. Zhu, M. Zhang, G. H. Duan, "Optimization and comparison of novel E-core and C-core linear switched flux PM machines," *IEEE Trans. Magn.*, vol. 47, no. 8, pp. 2134-2141, 2011.

[217] W. Min, J. T. Chen, Z. Q. Zhu, Y.Zhu, and G. H. Duan, "Optimization of linear flux switching permanent magnet motor," *IEEE Vehicle Power and Propulsion Conf*., 1-3 Sept., 2010, Lille, Fracnce, VPPC 2010, Paper RT6/95-93051.

[218] L. Huang, H. Yu, M. Hu, J. Zhao, and Z. Cheng, "A novel flux-switching permanent-magnet linear generator for wave energy extraction application," *IEEE Trans. Magnetics*, vol. 47, pp. 1034-1037, 2011.

[219] D. C. J. Krop, L. Encica, and E. A. Lomonova, "Analysis of a novel double sided flux switching linear motor topology," *Int. Conf. Electrical Machines*, 2010, pp. 1-5.

[220] J. Cai, Q. Lu, Y. Jin, C. Chen, and Y. Ye, "Performance investigation of multi-tooth flux-switching PM linear motor," ," in *Proc. Int. Conf. Elec. Mach. Syst*., Aug. 2011, pp. 1-6.

[221] R. Cao, M. Cheng, C. Mi, W. Hua, X. Wang, and W. Zhao, "Modeling of a complementary and modular linear flux-switching permanent magnet motor for urban rail transit applications," *IEEE Trans. Energy Convers*., vol. 27, no. 2, pp. 489-497, Jun. 2012.

[222] R. Cao, M. Cheng, C. Mi, W. Hua, and W. Zhao, "A hybrid excitation flux-switching permanent magnet linear motor for urban rail transit," in *Proc. IEEE Veh. Power and Propulsion Conf.,* Sep. 2011, pp. 1-5.

[223] C. Hwang, P. Li, and C. Liu, "Design and analysis of a novel hybrid excited linear flux switching permanent magnet motor," *IEEE Trans. Magn*., vol. 48, no. 11, pp. 2969-2972, Nov. 2012.

[224] M. Lin and Z. Q. Zhu, "Axial-field flux-switching PM brushless machines," China Chinese Patent No: 200810019783.2, 2008.

[225] M. Lin, L. Hao, X. Li, X. Zhao, and Z. Q. Zhu, "A novel axial field flux-switching permanent magnet wind power generator," *IEEE Trans. Magn*., vol. 47, no. 10, pp. 4457-4460, Oct. 2011.

[226] L. Hao, M. Lin, X. Zhao, X. Fu, Z. Q. Zhu, and P. Jin, "Static characteristics analysis and experimental study of a novel axial field flux-switching permanent magnet generator," *IEEE Trans. Magn*., vol. 48, no. 11, pp. 4212-4215, Nov. 2012.

[227] L. Hao, M. Lin, W. Li, H. Luo, X. Fu, and P. Jin, "Novel dual-rotor axial field flux-switching permanent magnet machine," *IEEE Trans. Magn*., vol. 48, no. 11, pp. 4232-4235, Nov. 2012.

[228] W. Zhao, T. A. Lipo, and B. Kwon, "A novel dual-rotor, axial field, fault-tolerant flux-switching permanent magnet machine with high-torque performance," *IEEE Trans. Magn*. vol. 51, no. 11, 2015.

[229] L. Hao, M. Lin, X. Zhao, and H. Luo, "Analysis and optimization of EMF waveform of a novel axial field flux-switching permanent magnet machine," in *Proc. Int. Conf. Elec. Mach. Syst*., Aug. 2011, pp. 1-6.

[230] X. Liu, A. Zheng, and C. Wang, "Design of a stator-separated axial flux-switching hybrid excitation synchronous machine," in *Proc. Int. Conf. Elec. Mach. Syst*., Aug. 2011, pp. 1-4.

[231] X. Liu, C. Wang, and A. Zheng, "Operation principle and topology structures of axial flux-switching hybrid excitation synchronous machine," in *Proc. Int. Conf. Elec. Mach. Syst*., Aug. 2011, pp. 1-7.

[232] J. Yan, H. Lin, Y. Huang, H. Liu, and Z. Q. Zhu, "Magnetic field analysis of a novel flux switching transverse flux permanent magnet wind generator with 3-D FEM," in *Proc. Int. Conf. PEDS*, 2009, pp. 332–335.

[233] J. B. Wang, W. Y. Wang, K. Atallah, and D. Howe, "Design considerations for tubular flux-switching PM machines," *IEEE Trans. Magn.*, vol. 44, no. 11, pp. 4026–4032, 2008.

[234] W. Fei, P. Luk, J. Shen, and Y. Wang, "A novel outer-rotor PM flux-switching machine for urban electric vehicle propulsion," in *Proc. 3rd Int. Conf. Power Electron. Syst. Appl*., May 2009, pp. 1–6.

[235] Y. Wang, M. J. Jin, J. X. Shen, W. Z. Fei, and P. C. K. Luk, "An outer-rotor flux-switching permanent magnet machine for traction applications," *IEEE Energy Conversion Congress and Exposition*, 2010, pp. 1723-1730.

[236] Y. Wang and Z. Deng, "A multi-tooth fault-tolerant flux-switching permanent-magnet machine with twisted-rotor," *IEEE Trans. Magn.*, vol. 48, no. 10, pp. 2674-2684, Oct. 2012.

[237] Y. Pang, Z. Q. Zhu, D. Howe, S. Iwasaki, R. Deodhar, and A. Pride, "Comparatively study of flux-switching and interior permanent magnet machines," in *Proc. Int. Conf. Elect. Mach. Syst.*, 2007, pp. 757–762.

[238] A. Fasolo, L. Alberti, and N. Bianchi, "Performance comparison between switching-flux and IPM machine with rare earth and ferrite PMs," in *Proc. Int. Conf. Elec. Mach*., Sep. 2012, pp.731-737.

[239] A. Fasolo, L. Alberti, and N. Bianchi, "Performance comparison between switching-flux and IPM machine with rare earth and ferrite PMs," *IEEE Trans. Ind. Appl*. vol. 50, no. 6, pp. 3708-3716, 2014.

[240] R. Cao, C. Mi, and M. Cheng, "Quantitative comparison of flux-switching permanent-magnet motors with interior permanent magnet motor for EV, HEV, and PHEV applications," *IEEE Trans. Magn.*, vol. 48, no. 8, pp. 2374-2384, Aug. 2012.

[241] J. D. McFarland, T. M. Jahns, and A. M. El-Refaie, "Performance and efficiency comparisons for interior PM and flux-switching PM machines with ferrite magnets for automotive traction applications," in *Proc. IEEE ECCE*, 2015, pp. 6529-6536.

[242] T. Raminosoa, A. M. EI-Refaie, D. Pan, K. K. Huh, J. P. Alexander, K. Grace, S. Grubic, S. Galioto, P. B. Reddy, and X. Shen, "Reduced Rare-Earth Flux Switching Machines for Traction Applications," *IEEE Trans. Ind. Appl.* vol. 51, no. 4, pp. 2959-2971, 2015.

[243] A.S. Thomas, Z.Q. Zhu, G.W. Jewell, "Comparison of switched flux and surface mounted permanent magnet generators for high speed applications," *Proc. IET, Electrical Systems in Transportation*, vol. 1, no. 3, pp. 111-116, 2011.

[244] A.S. Thomas, Z.Q. Zhu, G.W. Jewell, "Comparison of switched flux and surface mounted permanent magnet generators for high speed applications," *Proc.5th IET International Conference on Power Electronics, Machines and Drives (PEMD 2010), pp. 1-5, 2010.*

[245] A.S. Thomas, "Novel flux switching permanent magnet machines for aerospace applications," PhD thesis, University of Sheffield, 2009.

[246] W. Hua, Z. Q. Zhu, M. Cheng, Y. Pang, and D. Howe, "Comparison of flux-switching and doubly salient permanent magnet brushless machines," in *Proc. Int. Conf. Elect. Mach. Syst.*, 2005, pp. 165–170.

[247] W. Hua, M. Cheng, Z.Q. Zhu, and D. Howe, "Comparative study of 2-phase flux-switching and doubly-salient permanent magnet brushless machines," *Proc. Int. Conf. Elec. Machines, (ICEM2006),* Crete Island, Greece, 2-5 Sept. 2006, paper no: OMM1-1, 6 pages.

[248] W. Hua, M. Cheng, H. Jia, and X. Fu, "Comparative study of flux-switching and doubly-salient PM machines particularly on torque capability," *IEEE Industry Applications Society Annual Meeting,* 2008, pp. 1-8.

[249] W. Hua and M. Cheng, "A comprehensive comparison of flux-switching and flux-reversal brushless PM machines," *Int. Magnetics Conf.,* Madrid, Spain, 2008, Paper GM-08.

[250] C. Pollock and M. Brackley, "Comparison of the acoustic noise of flux-switching and a switched reluctance drives," *IEEE Trans. Ind. Appl*., vol. 39, no. 3, pp. 826–834, 2003.

[251] C. Pollock and M. Brackley, "Comparison of the acoustic noise of flux-switching and a switched reluctance drives," *36th IAS Annual Meeting,* pp. 2089-2096, 2001.

[252] G. Lian, G. Gu, Y. Cheng, J. Tao, S. Wang, and X. Chen, "Comparative study on switched reluctance and flux-switching machines with segmented rotors," *IEEE 18th International Conference on Electrical Machines and Systems (ICEMS)*, Oct. 25-28, Pattaya City, Thailand.

[253] C. Pollock, H. Pollock, and M. Brackley, "Electronically controlled flux switching motors: a comparison with an induction motor driving an axial fan," *The 29th Annual Conference of the IEEE Industrial Electronics Society, IECON* '03, 2003, pp. 2465-2470.

[254] A. S. Thomas, Z. Q. Zhu, and G. W. Jewell, "Proximity loss study in high speed flux-switching permanent magnet machine," *IEEE Trans. Magn*., vol. 45, no. 10, pp. 4748–4751, Oct. 2009.

[255] S. Iwasaki, R. Deodhar, Y. Liu, A. Pride, Z. Q. Zhu, and J. Bremner, "Influence of PWM on proximity loss in PM brushless AC machines," *IEEE Trans. Ind. Appl*., vol. 45, no. 3, pp. 1359–1367, 2009.

[256] Y. Pang, Z. Q. Zhu, D. Howe, S. Iwasaki, R. Deodhar, and A. Pride, "Investigation of iron loss in flux-switching PM machines," in *Proc. IET Power Electron., Mach. Drives*, U.K., Apr. 2–4, 2008, pp. 460–464.

[257] Y. Li, S. Li, Y. Yang, and B. Sarlioglu, "Analysis of flux switching permanent magnet machine design for high-speed applications," *IEEE ECCE*, 2014.

[258] Z. Q. Zhu, Y. Pang, J. T. Chen, R. Owen, D. Howe, S. Iwasaki, R. Deodhar, and A. Pride, "Analysis and reduction of magnet eddy current loss in flux-switching PM machines," in *Proc. IET Power Electron., Mach. Drives*, York, U.K., Apr. 2–4, 2008, pp. 120–124.

[259] Y. Pang, Z. Q. Zhu, D. Howe, S. Iwasaki, R. Deodhar, and A. Pride, "Eddy current loss in the frame of a flux-switching permanent magnet machine," *IEEE Trans. Magn.*, vol. 42, no. 10, pp. 3413–3415, Oct. 2006.

[260] E. Hoang, M. Lecrivain, and M. Gabsi, "3-D thermal model of an hybrid excitation flux switching synchronous machine using a 2-D FE method software," *Int. Symposium Power Electronics Electrical Drives Automation and Motion (SPEEDAM)*, 2010, pp. 101-104.

[261] J. T. Chen, Z. Q. Zhu, S. Iwasaki, and R. Deodhar, "Comparison of losses and efficiency in alternate flux-switching permanent magnet machines," *XIX Int. Conf. on Elec. Machines, ICEM*,6-8 Sept. 2010, Rome, Italy, paper RF-002259-PMM2.

[262] J. Yang, Q. Ma, Y. Deng, and Y. Liu, "Flux-weakening capability of flux-switching permanent magnet motor," *Int. Conf. E-Product E-Service and E-Entertainment*, 2010, pp. 1-4.

[263] W. Xu, J. Zhu, Y. Zhang, Y. Guo, and G. Lei, "New axial laminated structure flux-switching permanent magnet machine with 6/7 poles," *IEEE Trans. Magn.*, vol. 47, no. 10, pp. 2823-2826, Oct. 2011.

[264] W. Xu, G. Le, T. Wang, X. Yu, J. Zhu, and Y. Guo, "Theoretical research on new laminated structure flux switching permanent magnet machine for novel topologic plug-in hybrid electrical vehicle," *IEEE Trans. Magn.*, vol. 48, no. 11, pp. 4050-4053, Nov. 2012.

[265] D. Wu, J. T. Shi, Z. Q. Zhu, and X. Liu, "Electromagnetic performance of novel synchronous machines with permanent magnets in stator yoke," *IEEE Trans. Magn*. vol. 50, no. 9, 2014.

[266] D. Xie, Y. Wang, Z. Deng, "FSPM machines with twisted-rotor structure," *IEEE 9th Conference on Industrial Electronics and Applications (ICIEA)*, 2014.

[267] D. Xie, Y. Wang, Z. Deng, "Torque ripple reduction of flux-switching machines with twisted-rotor structure," *17th International Conference on Electrical Machines and Systems (ICEMS)*, 2014.

[268] Y. J. Zhou and Z. Q. Zhu, "Comparison of wound-field switched-flux machines," *IEEE Trans. Ind. Appl*. vol. 50, no. 5, 2014.

[269] E. Ben Sedrine, J. Ojeda, M. Gabsi, and I. Slama-Belkhodja, "Fault-Tolerant Control Using the GA Optimization Considering the Reluctance Torque of a Five-Phase Flux Switching Machine," *IEEE Trans. Ener. Conv*. vol. 30, no. 3, pp. 927-938, 2015.

[270] H. Jia, M. Cheng, W. Hua, W. Lu, and X. Fu, "Investigation and implementation of control strategies for flux-switching permanent magnet motor drives," in *Conf. Rec. IEEE IAS Annu. Meeting*, 2008, pp. 1747–1752.

[271] H. Jia, M. Cheng, W. Hua, W. Zhao, and W. Lu, "A new stator flux orientation strategy for flux-switching permanent motor drive based on voltage space-vector," in *Proc. Int. Conf. Elect. Mach. Syst*., 2008, pp. 3032–3036.

[272] W. Hua, M. Cheng, W. Lu, and H. Jia, "A new stator-flux orientation strategy for flux-switching permanent magnet motor based on current-hysteresis control," *J. Appl. Phys*., vol. 105, no. 7, pp. 07F112:1–07F112:3, Feb. 2009.

[273] K. Wang, J. X. Shen, and S. Z. Dong, "Sensorless control and initial position estimation of permanent magnet flux switching motor," *Int. Conf. Electrical Machines and Systems*, pp. 487-491.

[274] Y. Wang and Z. Deng, "A position sensorless method for direct torque control with space vector modulation of hybrid excitation flux-switching generator," *IEEE Trans. Energy Convers*., vol. 27, no. 4, pp. 912-921, Dec. 2012.

[275] T. C. Lin, L. M. Gong, and Z. Q. Zhu, "Saliency investigation of switched-flux PM brushless AC machine for saliency-tracking-based sensorless control," in *Proc. Int. Conf. Elec. Mach*., Sep. 2012, pp.2238- 2244.

[276] S. Huang, J. Luo, F. Leonardi, and T. A. Lipo, "A general approach to sizing and power density equations for comparison of electrical machines," *IEEE Trans. Ind. Appl*., vol. 34, no. 1, 1998.

[277] S. Kunihiro, N. Misao, H. Yasuyuki, "Electrical steels for advanced automobiles – core materials for motors, generators, and high frequency reactors," *JFE Technical Report*, no.4, 2004.

[278] J.E. Vrancik, "Prediction of windage power loss in alternators," *NASA-Langley*, Report No. TND-4849, 1968.

[279] K. Srinivas and R. Arumugam, "Analysis and characterization of switched reluctance motors: Part II. Flow, thermal, and vibration analyses," *IEEE Transaction on Magnetics*, vol. 41, no. 4, pp. 1321–1332, 2005.

[280] D. Dorrell, M. Popescu, and D. Ionel, “Unbalanced magnetic pull due to asymmetry and low-level static rotor eccentricity in fractional slot brushless permanent-magnet motors with surface-magnet and consequent-pole,” *IEEE Trans. Magnet.*, Vol. 46, No. 7, pp. 2675–2685, 2010.

[281] Islam, M. S., Islam, R., and Sebastian, T., “Noise and vibration characteristics of permanent-magnet synchronous motors using electromagnetic and structural analyses,” *IEEE Trans. Ind. Appl.*, Vol. 50, No. 5, pp. 3214–3222, September 2014.

[282] Arkkio, A., “Unbalanced magnetic pull in cage induction motors—dynamic and static eccentricity,” *Proceedings of the* International *Conference on Electrical Machines*, pp. 192–197, Vigo, Spain, 10–12 September 1996.

[283] Wallin, M., Bladh, J., and Lundin, U., “Damper winding influence on unbalanced magnetic pull in salient pole generators with rotor eccentricity,” *IEEE Trans. Magnet.*, Vol. 49, No. 9, pp. 5158–5165, 2013.

[284] Ko, H.-S., and Kim, K.-J., “Characterization of noise and vibration sources in interior permanent-magnet brushless DC motors,” *IEEE Trans. Magnet.*, Vol. 40, No. 6, pp. 3482–3489, November 2004.

[285] Boisson, J., Louf, F., Ojeda, J., Mininger, X., and Gabsi, M., “Magnetic forces and vibrational behavior analysis for flux switching permanent magnet machines,” *XXth International Conference on Electrical Machines (ICEM)*, pp. 2988–2993, Marseille, France, 2–5 September 2012.

[286] S. Li, Y. Li, W. Choi, and B. Sarlioglu, “High-speed electric machines: challenges and design considerations,” *IEEE Trans. Transportation Electrification*, vol. 2, no. 1, March 2016.

[287] Alberto Tenconi, Silvio Vaschetto, Alessandro Vigliani, "Electrical Machines for High-Speed Applications: Design Considerations and Tradeoffs", *Industrial Electronics IEEE Transactions on*, vol. 61, pp. 3022-3029, 2014.

[288] A. Borisavljevic, H. Polinder, J. Ferreira, "On the speed limits of permanent-magnet machines", *IEEE Trans. Ind. Electron.*, vol. 57, no. 1, pp. 220-227, Jan. 2010.

[289] A. Borisavljevic, H. Polinder, and J. A. Ferreira, “Overcoming limits of high-speed PM machines,” in *Proc. ICEM*, Vilamoura, Portugal, Sep. 2008, pp. 1–6.

[290] D. Fodorean, M. Sarrazin, C. Martis, J. Anthonis, and H. Auweraer, “Electromagnetic and structural analysis for a surface-mounted PMSM used for light-EV,” *IEEE Trans. Ind. Appl.* vol. 52, no. 4, pp. 2892-2899, 2016.

[291] Z. Yang, M. Krishnamurthy, I. P. Brown, "Electromagnetic and vibrational characteristic of IPM over full torque–speed range", *Proc. IEEE Int. Elect. Mach. Drives Conf. (IEMDC'13)*, pp. 295-302, May 2013.

[292] R. Islam, I. Husain, "Analytical model for predicting noise and vibration in permanent-magnet synchronous motors", *IEEE Trans. Ind. Appl.*, vol. 46, no. 6, pp. 2346-2354, Nov./Dec. 2010.

[293] J. Ede, Z. Zhu, D. Howe, "Rotor resonances of high-speed permanent-magnet brushless machines", *IEEE Trans. Ind. Appl.*, vol. 38, no. 6, pp. 1542-1548, Nov. 2002.

[294] D. Gerada, A. Mebarki, R. P. Mokhadkar, N. L. Brown, C. Gerada, "Design issues of high-speed permanent magnet machines for high-temperature applications", *Proc. Int. Elect. Mach. Drives Conf.*, pp. 1036-1042, 2009.

[295] J. M. Vance, *Rotor Dynamics of Turbo Machinery*. New York: Wiley, 1988.

[296] Han-Wook Cho, Kyoung-Jin Ko, Jang-Young Choi, Hyun-Jae Shin, Seok-Myeong Jang, "Rotor Natural Frequency in High-Speed Permanent-Magnet Synchronous Motor for Turbo-Compressor Application", Magnetics *IEEE Transactions on*, vol. 47, pp. 4258-4261, 2011, ISSN 0018-9464.

[297] E. Swanson, C. Powell, and S. Weissman, "A practical review of rotating machinery critical speeds and modes," *Sound & Vibration* 39(5): 10-17, May 2005.

[298] E. Schubert and B. Sarlioglu, "Mechanical design method for a high-speed surface permanent magnet rotor," *Proc. IEEE Energy Conversion Congress and Expo.*, Milwaukee, WI, 2016, 6 pp.

Appendix

Prototype Proof-of-Concept Machine Assembling

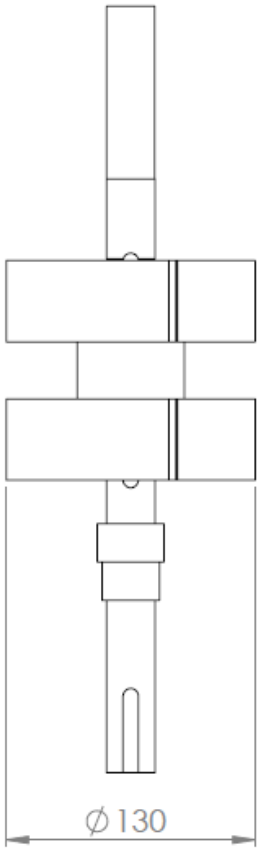

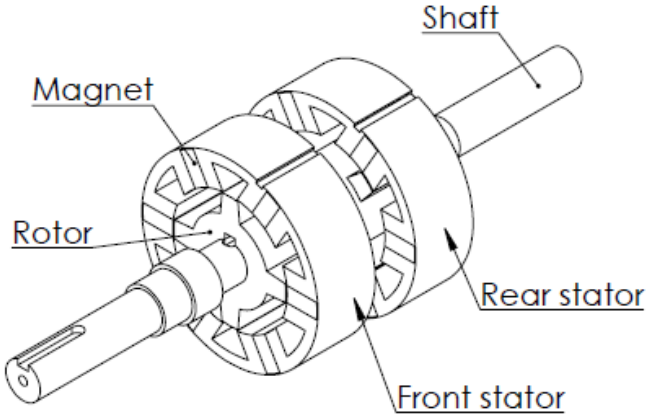

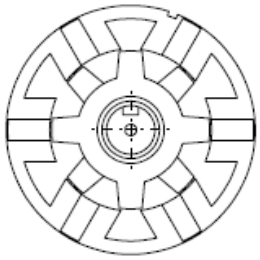

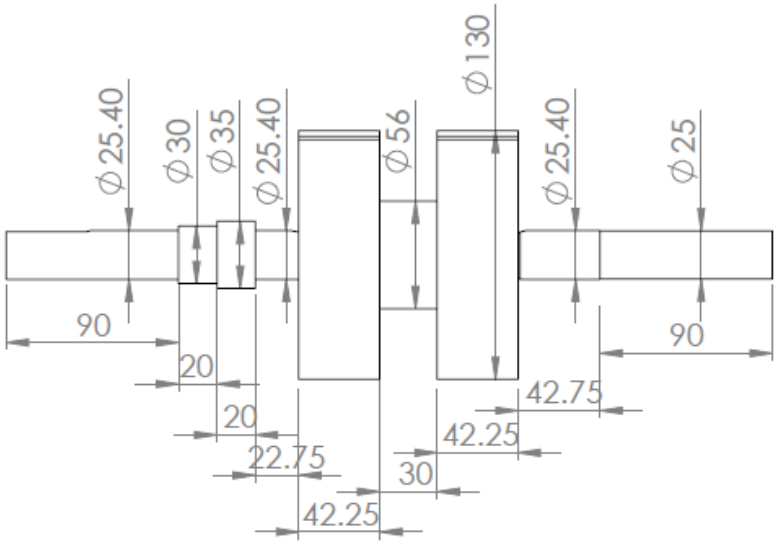

Prototype Stator Design

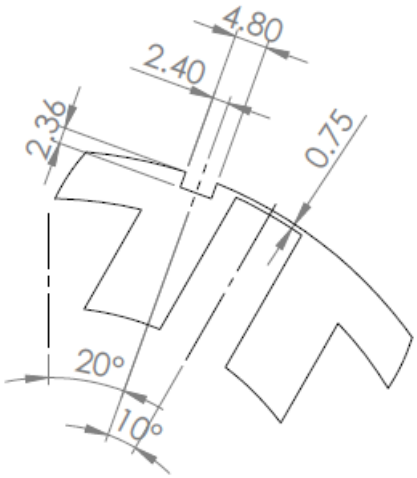

DETAIL A
SCALE 1 : 1

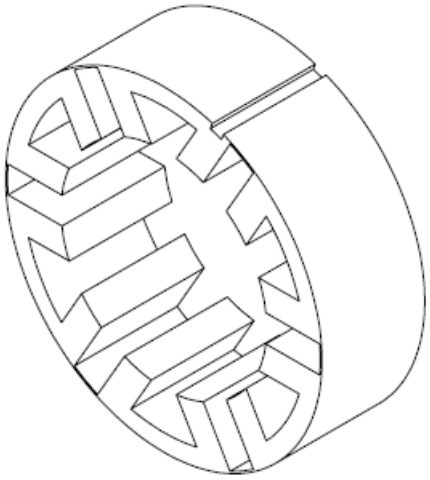

Unit: mm
Tolerance: +/- 0.01mm
Tolerance: +/- 0.05 Deg.

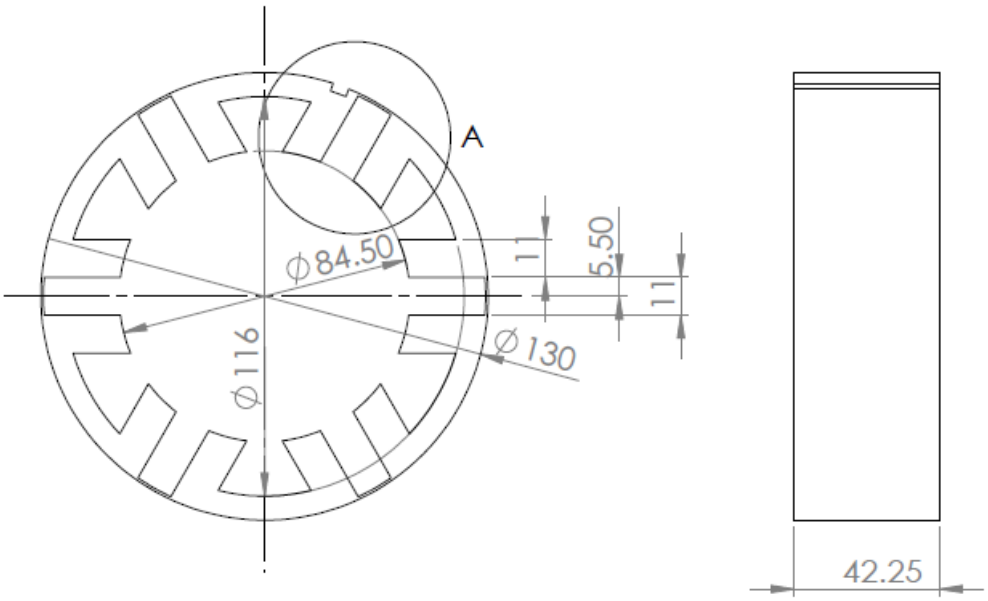

Prototype Rotor Design

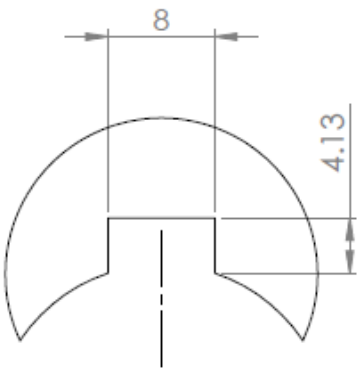

DETAIL A
SCALE 2 : 1

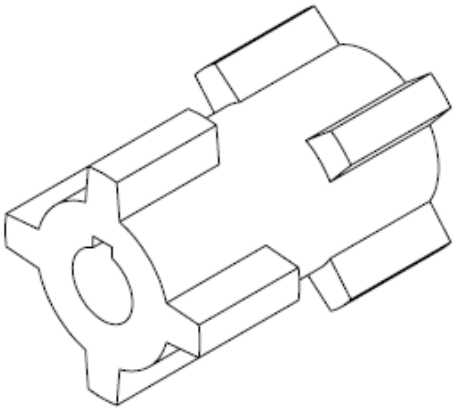

Isometric View

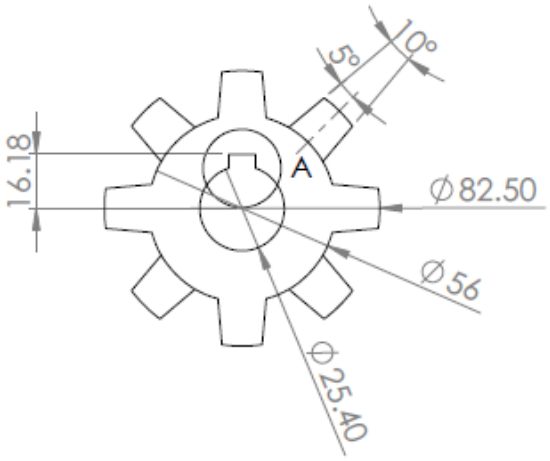

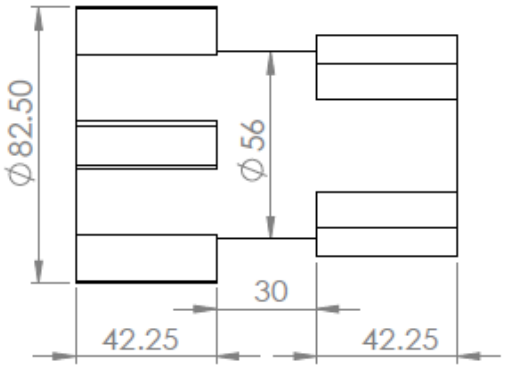

Unit: mm
Tolerance: +/- 0.01mm
Tolerance: +/- 0.05 Deg.

Prototype Rotor Front Part Lamination

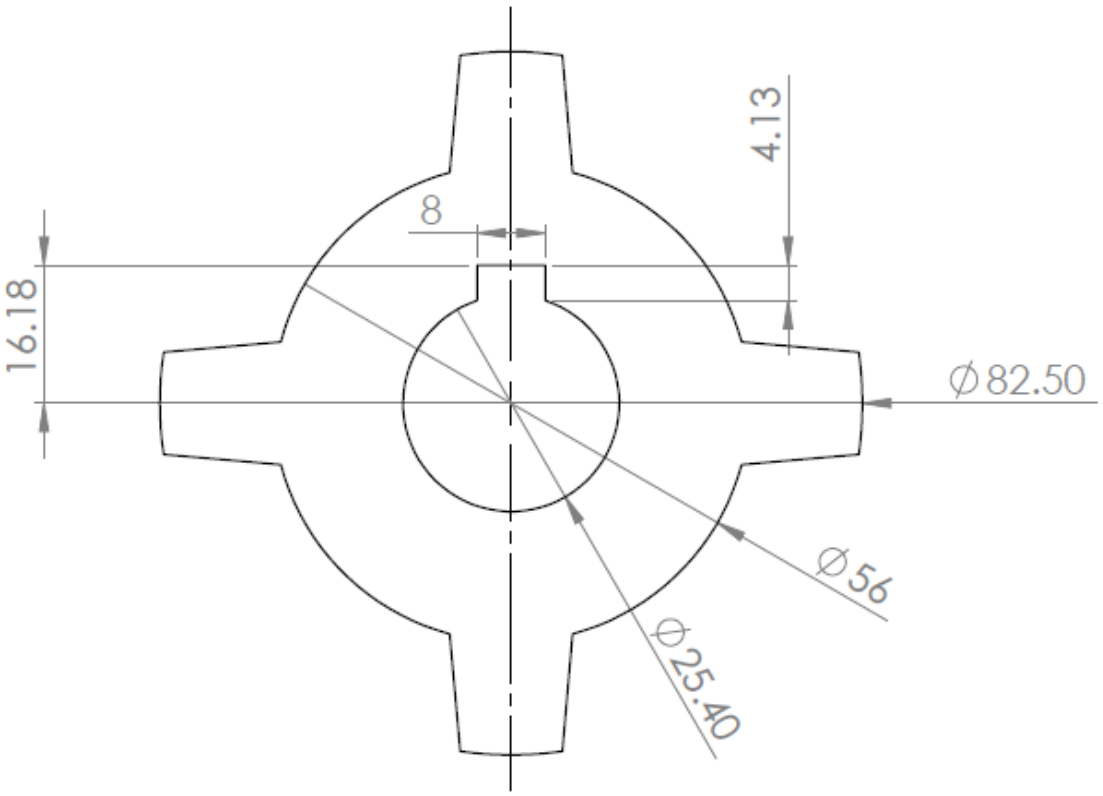

Prototype Rotor Middle Part Lamination

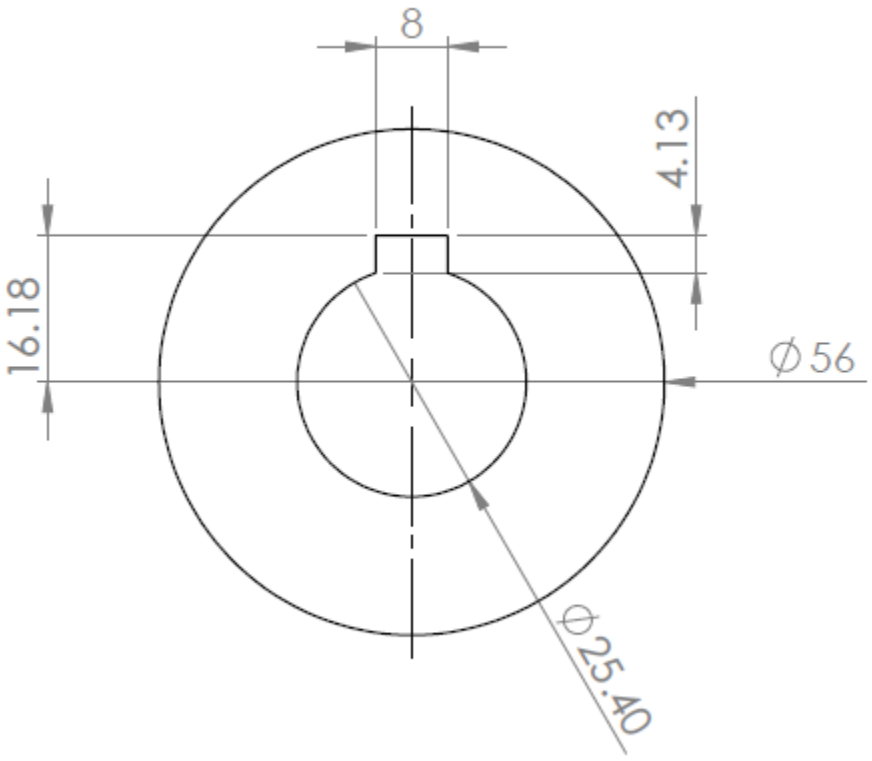

Prototype Rotor Rear Part Lamination

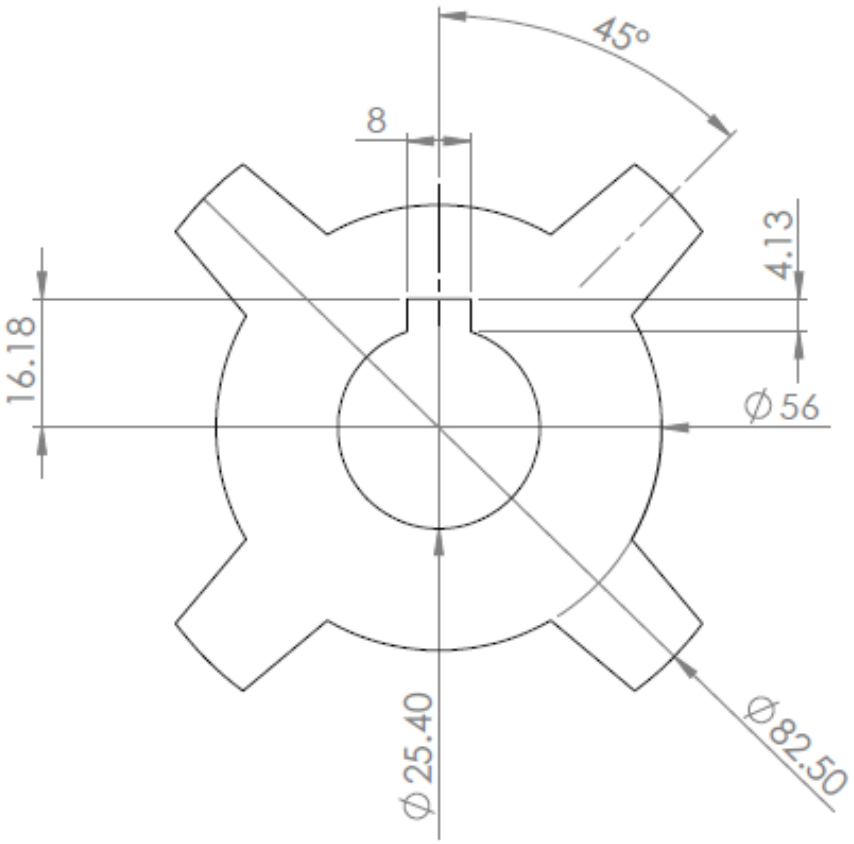

Prototype Machine Shaft Design

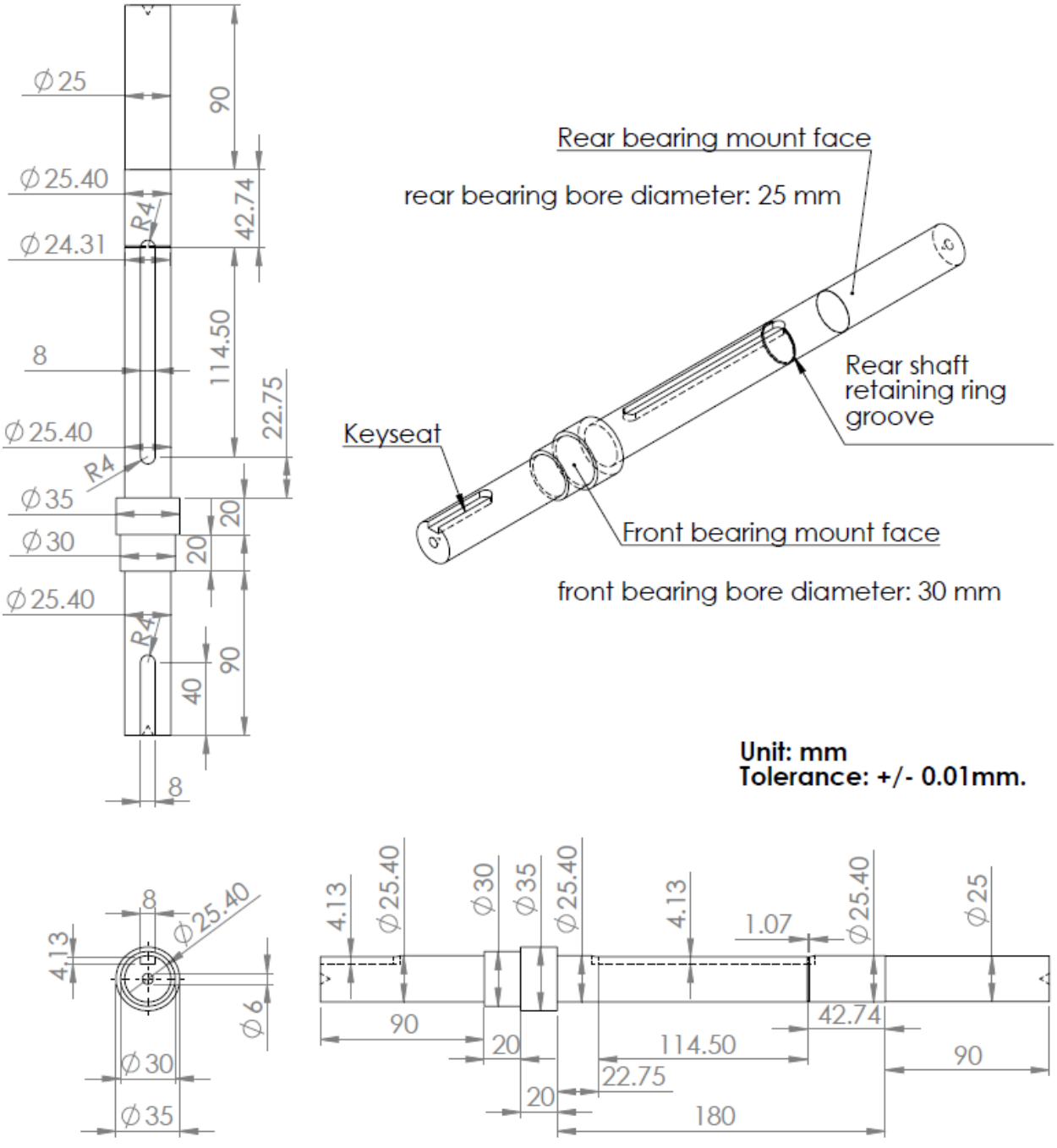

Prototype Machine Housing Design

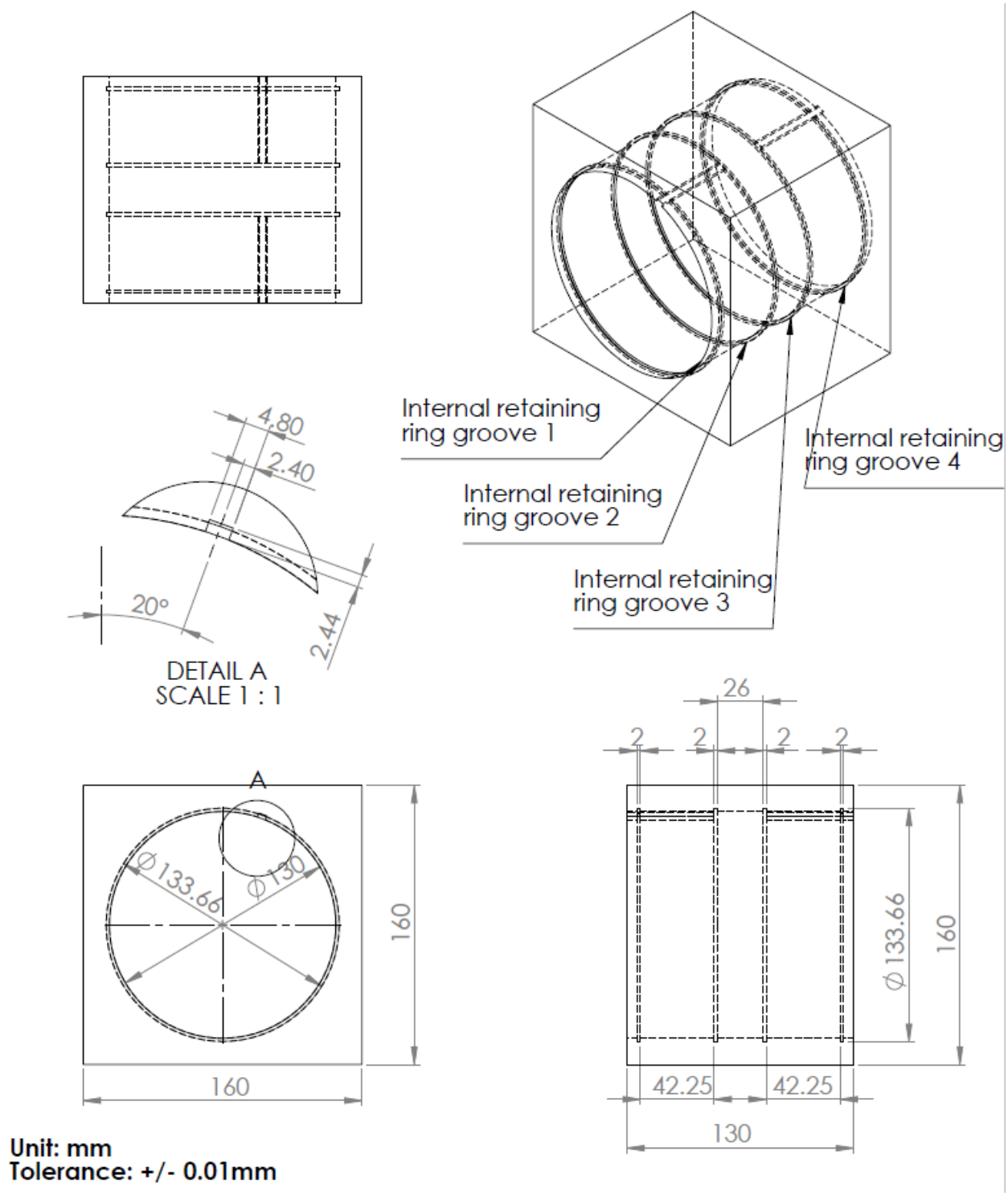

Unit: mm
Tolerance: +/- 0.01mm

Instruction of Assembling Magnets for the two Prototypes

1. Prototype one (magnets in front and rear stators have the same orientation)

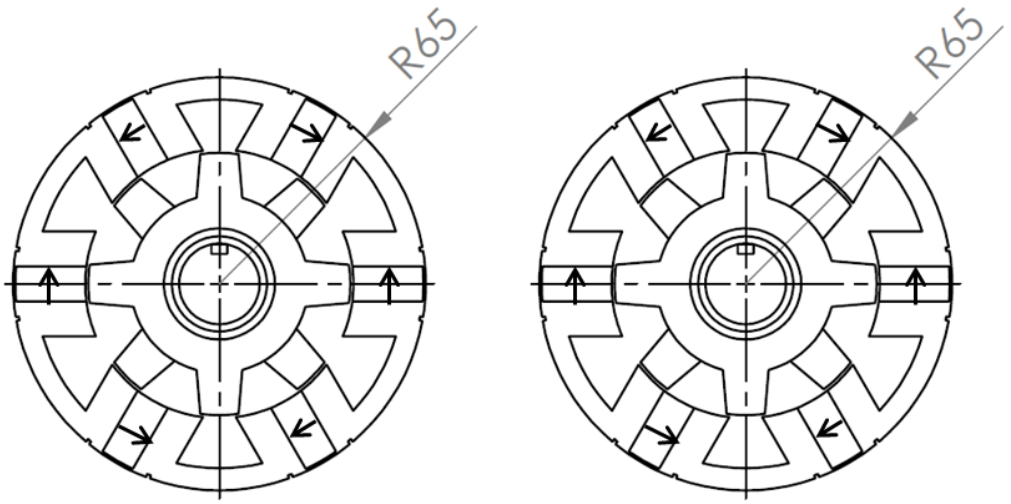

Front Stator Rear Stator

2. Prototype two (magnets in front and rear stators have the opposite orientation)

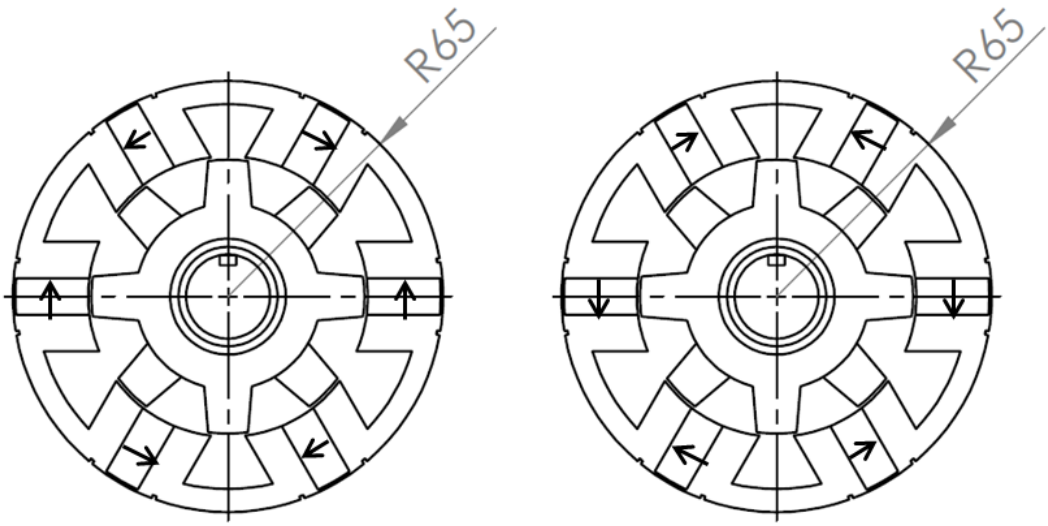

Front Stator Rear Stator

Winding Diagram for Prototype One

3D view

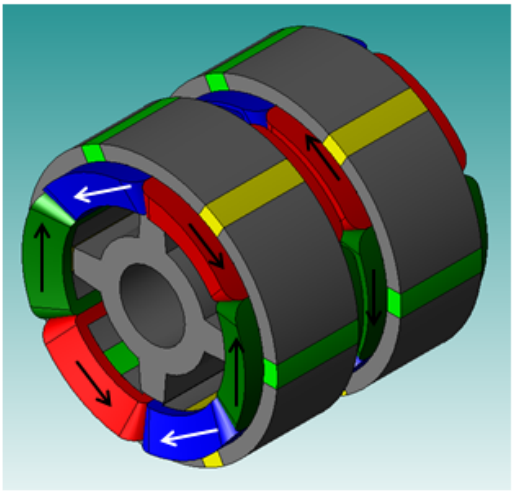

Right view

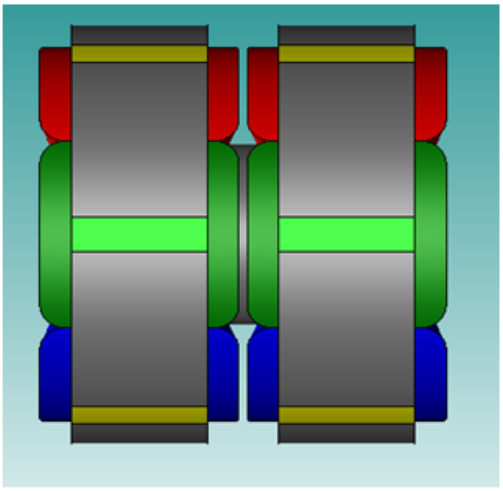

Arrows are the direction of current flow

Winding connections for front the rear stator

Front stator

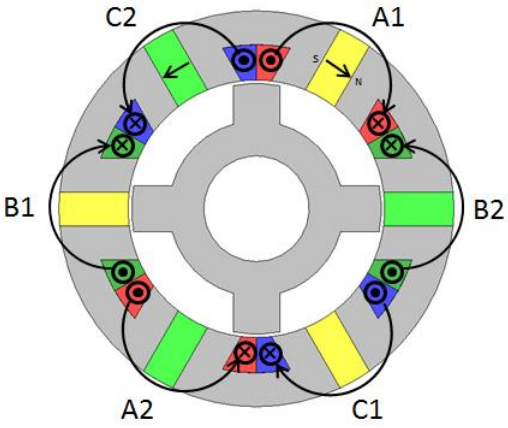

Rear stator

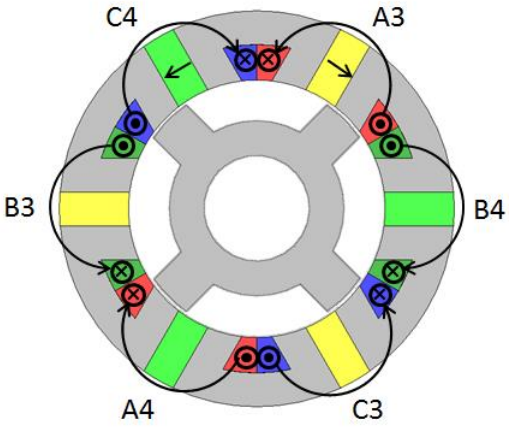

Note: Color “red” “green” and “blue” represents phase A B and C respectively. The direction of current flow is show by “dot” (flow outwards perpendicular to the paper) and “cross” (flow inwards perpendicular to the paper.

Winding connections for the whole machine

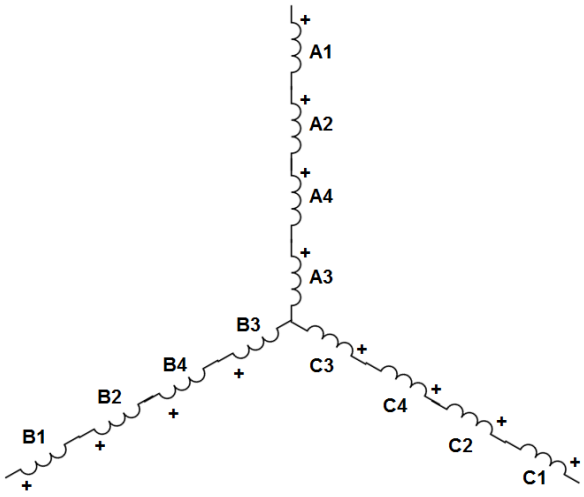

Note: There are a total of 4 coils connected in series per phase. The windings are connected in star configuration.

Circuit connection in JMAG-Designer

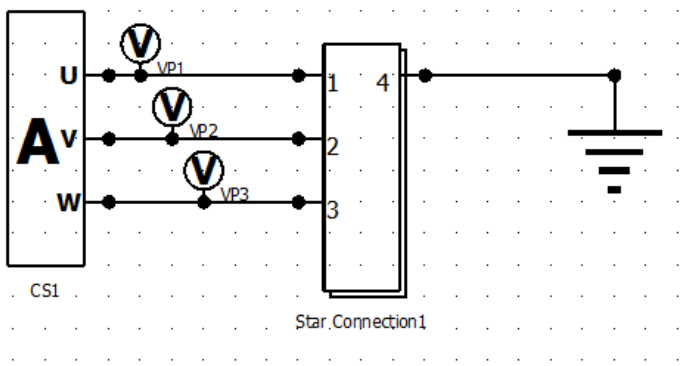

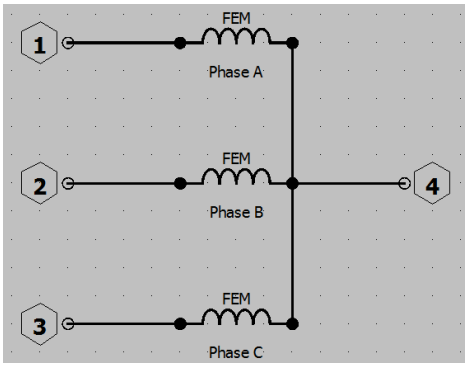

Winding parameters:

a. Number of coils connected in series per phase: 4

b. Number of turns per coil: 60

c. AWG for a single turn is #17 (assuming slot fill factor roughly 50%)

Pillow Block Bearings for the prototype

Bearing brand: Link-Belt 200 Series Ball Bearing

Bearing type: pillow block bearing

Bearing bore diameter: 30 mm for the front bearing; 25 mm for the rear bearing

Specs for the **front bearing** and **rear bearing**

P3U200

Photo Shows a 2-Bolt Ball Bearing Pillow Block Unit

Product Features

- Corrosion-resistant powder coating
- Cast iron housing
- Broad range of sealing options
- Wide inner ring for increased shaft stability
- Spring locking setscrew mount
- Alignable & relubricatable
- See Features & Benefits for additional info.

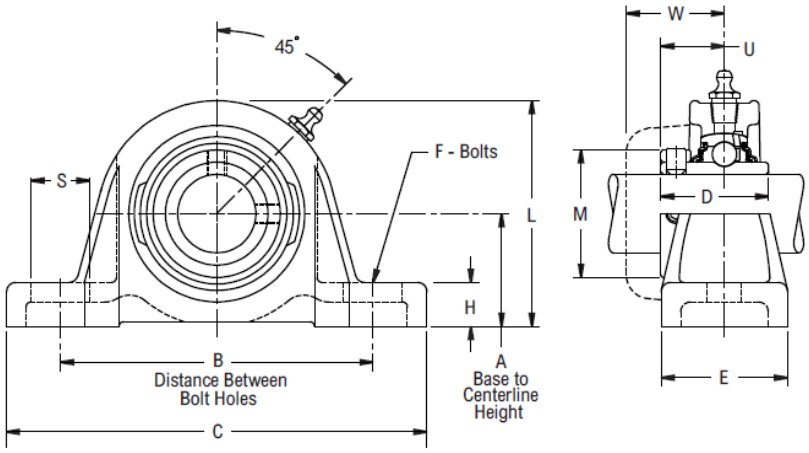

Bearing Dimensions

Size Code	Shaft Diameter	Part Number	A Base to Centerline Height	B Distance Between Bolt Holes	C	D	E	F	H	L	M	S	U	W	Approx. Weight
205	7/8	P3U214N Δ*	1 7/16	4	5 3/8	1 23/64	1 5/8	3/8	9/16	2 7/8	-	11/16	51/64	1 9/32	1.90
	15/16	P3U215N Δ*													
	1	P3U216N Δ*													
	25.00	*P3U2M25N Δ*	*36.51*	*101.60*	*136.50*	*34.53*	*41.30*	*10.00*	*14.30*	*73.00*	*-*	*17.50*	*20.20*	*32.50*	*0.86*
206	1 1/8	P3U218N *	1 11/16	4 5/8	6 5/16	1 9/16	1 3/4	1/2	11/16	3 5/16	-	15/16	61/64	1 29/64	2.70
	1 3/16	P3U219N *													
	1 1/4	P3U2E20N *													
	30.00	*P3U2M30N **	*42.86*	*117.50*	*160.30*	*39.69*	*44.40*	*12.00*	*17.50*	*84.10*	*-*	*23.80*	*24.20*	*36.90*	*1.22*

Additional Notes

Please call 1-866-REXNORD for availability
Lubrication fitting tap size, 1/8 in PT
Base to centerline tolerance, +.000 in/-.010 in *(+0.00 mm/-0.25 mm)*
* N lip seals standard
■ Available with H labyrinth seals
Δ Available with E3 triple lip seals
For the Selection Guide, Load Ratings and Speed Limits, see the Link-Belt 200 Series Ball Bearing Engineering section

Note: the units for these two bearings are in mm instead of inch.